Seasonal and under-ice dynamics of the La Grande River plume and their influence on eelgrass habitats in northeastern James Bay

By Christopher Peck

A thesis submitted to the Faculty of Graduate and Postdoctoral Studies of The University of Manitoba in partial fulfillment of the degree of:

DOCTOR OF PHILOSOPHY

Department of Environment and Geography University of Manitoba Winnipeg, Manitoba, Canada

Supervised by

Assoc. Prof. Dr. Jens Ehn

Department of Environment and Geography
Clayton H. Riddell Faculty of Environment, Earth, and Resources University of Manitoba
Winnipeg, MB R3T 2N2, Canada

Assoc. Prof. Dr. Zou Zou Kuzyk
Department of Earth Sciences
Clayton H. Riddell Faculty of Environment, Earth, and Resources University of Manitoba
Winnipeg, MB R3T 2N2, Canada

Advisory committee

Res. Prof. Dr. Igor Dmitrenko
Department of Environment and Geography
Clayton H. Riddell Faculty of Environment, Earth, and Resources University of Manitoba
Winnipeg, MB R3T 2N2, Canada

Prof. Dr. Urs Neumeier
Institut des sciences de la mer de Rimouski
Université du Québec à Rimouski, QC G5L 3A1, Canada

External Examiner

Assoc. Prof. Dr. Lars Chresten Lund-Hansen
Department of Biology
Arctic Research Centre, University of Aarhus, Ole Worms Allé 1, 1135, 8000 Aarhus C, Denmark

Abstract

A river plume is a buoyant, freshened surface layer often turbid or colored formed by mixing river discharge with saline coastal waters. Its structure and extent are shaped by wind, tides, ice cover, and discharge variability, though plume dynamics remain less understood in seasonally ice-covered environments. Under continuous landfast ice, plumes may expand further than in open water due to reduced wind mixing but can be constrained by ice bottom topography. This thesis investigates the seasonal dynamics and short-term variability of the La Grande River (LGR) plume in relation to discharge regulation, ice conditions, and their combined influence on coastal plume extent and key ecological properties within eelgrass (*Zostera marina*) habitats. The LGR plume is the primary freshwater source in James Bay (subarctic Canada) during winter, and its discharge has increased due to hydroelectric development. Observations from 2016–2017 showed the under-ice plume did not expand significantly despite rising discharge since 1987. Narrowing landfast ice and coastal topography limited northward spread, while bottom-mounted moorings confirmed southward expansion despite prevailing northward currents. Persistent westerly winds lowered salinity in eelgrass embayments, indicating wind affects plume extent even when direct wind forcing is blocked by landfast ice. Two locations CH4 (north) and CH33 (south of the LGR), named after local hunting traplines, were studied for seasonal ice breakup effects on eelgrass habitat conditions. During ice cover, high discharge lowered salinity at both sites, with tidal salinity oscillations of 15 PSU at CH33 and more stable brackish conditions (1–2 PSU variation) at CH4. Ice breakup in late May–early June caused brief salinity drops and temperature increases. During open water, salinity stabilized, and temperature and photosynthetically active radiation (PAR) levels rose, initiating eelgrass growth. Site-specific differences persisted: CH33 exceeded the optimal salinity for growth (>15 PSU) 44% (ice-covered) and 89% (open water) of the time, compared to 25% and 82% at CH4. Open-water PAR exceeded the eelgrass compensation point 26% of the time at CH33 and 15% at CH4. However, CH33's higher PAR was offset by suboptimal salinity and temperature, potentially limiting growth relative to CH4's more stable conditions.

Acknowledgements

Throughout my PhD program, I have been blessed with the support of so many great people. First, I would like to thank my two co-supervisors, Jens Ehn and Zou Zou Kuzyk, for their guidance, encouragement, and funding throughout my studies. You both gave me the opportunity to work in the Arctic environment and the opportunity to integrate and work with local Cree communities. The experience of working in remote environments and with northern community members has been invaluable and offered me a new perspective on people living and working in the Arctic. Both of you also always made the time for discussion on results or upcoming field campaigns, whether they be quick five-minute chats or meetings for several hours. Most importantly, the support did not waver throughout the covid pandemic.

My PhD research was part of a large multidisciplinary study called the Coastal Habitat Comprehensive Research Project (CHCRP), conducted on the Northeast coast of James Bay. I would like to acknowledge the Cree Nation of the Chisasibi and Niskamoon Corporation for their help in funding this project. The University of Manitoba Graduate Fund and the Government of Canada Northern Scientific Training Program supported student participation and travel.

My time in Winnipeg has been filled with many great research experiences and conference trips. I would like to thank the staff and faculty at the Center of Earth Observation Science for their support in these endeavors. Special thanks must go to the administrative staff for helping me with my endless travel claims and shipping equipment to Chisasibi. I’m also very thankful to Maddy Stocking, Devin Hammett, Kaushik Gupta and Alessia Guzzi for your help all up and down the James Bay coast. You helped me deploy moorings, take ice cores, CTD casts, deploy and recover the AUV, and were my diving helpers on the surface. I would like to thank the community members and tallymen of the Chisasibi and Wemindji communities. Without you, none of this work would have been possible. I would particularly like to thank Ernie Rabbitskin for handling the logistics within the communities.

In my personal life, I have met many people whom I would like to thank. It was an absolute pleasure to captain and be the president of the Winnipeg Wasps Rugby Club. I would like to thank all the members past and present for taking me in and giving me an outlet (Black and Gold Forever). I would also like the thank the following people for their support and friendship throughout my 6 years in Winnipeg: Sean Hancock (and family), Tonya Burgers, Lisa Matthes, Campbell Hennessey, David Babb (and family), Frankie Beaudet, Alexe Mayette, Cody Carlyle, Wesley Ogloff and Kevin Scharffenberg. To my Mum

and Dad, thank you for your continued support and encouragement throughout my life and education, even while I was on the other side of the Atlantic. Last but most certainly not least, I would like to express my deepest gratitude to my wife Kasey Peck. You have been with me since the beginning of my postgraduate work, sharing all the highs and lows. From keeping me fed and sane during my candidacy in the height of lockdown to listening to me partake in the favorite British pastime of complaining. I could not have done this without your unwavering love and support.

Table of Contents

List of tables

List of supplemental tables

List of figures

List of supplemental figures

List of acronyms

ROFI	Region of freshwater influence
CDOM	Colored dissolved organic matter
LGR	La Grande River
NE	Northeast
CTD	Conductivity temperature depth
CT	Conductivity temperature
ADCP	Acoustic Doppler Current Profiler
YD	Year Day
CHCRP	Coastal Habitat Comprehensive Research Project
PAR	Photosynthetically active radiation
AUV	Autonomous underwater vehicle
GPS	Global positioning system
INS	Internal navigation system
DVL	Doppler velocity logger
USBL	Ultra-short baseline acoustic positioning system
USV	Uncrewed Surface Vehicle

Use of copyrighted materials

Figure 2.1: Adapted and originally published in Horner-Devine, A. R., Hetland, R. D. and MacDonald, D. G. (2015) ‘Mixing and transport in coastal river plumes’, Annual Review of Fluid Mechanics, 47, pp. 569–594. doi: 10.1146/annurev-fluid-010313-141408.

Figure 2.2: Originally published Horner-Devine, A. R., Hetland, R. D. and MacDonald, D. G. (2015) ‘Mixing and transport in coastal river plumes’, Annual Review of Fluid Mechanics, 47, pp. 569–594. doi: 10.1146/annurev-fluid-010313-141408.

Figure 2.3: Based upon the findings of Yankovsky, A.E. and Chapman, D.C., 1998. A simple theory for the fate of buoyant coastal discharges. Journal of Physical oceanography, 27(7), pp.1386-1401.

Figure 2.4: Originally published in Fong, D. A. and Geyer, W. (2001) ‘Response of a river plume during an upwelling favorable wind event’, Journal of Geophysical Research: Oceans, 106(C1), pp. 1067–1084. doi: 10.1029/2000JC900134.

Figure 2.5: Recreated from Brown, E. (2002) Waves, Tides and Shallow-Water Processes. 2nd edn, Waves, Tides and Shallow-Water Processes. 2nd edn. Gulf Professional Publishing. doi: 10.1016/b978-0-08-036372-1.x5000-4.

Figure 2.6: Originally published in Osadchiev, A., Medvedev, I., Shchuka, S., Kulikov, M., Spivak, E., Pisareva, M. and Semiletov, I. (2020) ‘Influence of estuarine tidal mixing on structure and spatial scales of large river plumes’, Ocean Science, 16, pp. 781–798. doi: 10.5194/os-16-781-2020.

Figure 2.7: Originally published in Yuan, Y., Horner-Devine, A. R., Avener, M. and Bevan, S. (2018) ‘The role of periodically varying discharge on river plume structure and transport’, Continental Shelf Research, 158, pp. 15–25. doi: 10.1016/j.csr.2018.02.009.

Figure 2.8: Originally published in Macdonald, R. W. and Carmack, E. C. (1991) ‘The role of large-scale under-ice topography in separating estuary and ocean on an Arctic shelf’, Atmosphere - Ocean, 29(1), pp. 37–53. doi: 10.1080/07055900.1991.9649391

Figure 2.9: Modified from Kuzyk, ZA. and Candlish, LM. 2019. From Science to Policy in the Greater Hudson Bay Marine Region: An Integrated Regional Impact Study (IRIS) of Climate Change and Modernization. ArcticNet, Québec City, 424 pp.

Figure 2.10: Modified from Leblanc, M.-L., O'Connor, M., Noisette, F., Leblon, B., Davis, K., Clyne, K., LaRocque, A., Olatunji, A. & Humphries, M., 2023a. *Coastal Habitat Comprehensive Project: Eelgrass Team Final Report*. Niskamoon Corporation, July 21, 2023.

Chapter 3 of this thesis was reproduced with minor modifications from Peck, C.J., Kuzyk, Z.A., Heath, J.P., Lameboy, J., Ehn, J.K. (2022). Under-ice hydrography of the La Grande River plume in relation to a ten-fold increase in wintertime discharge. Journal of Geophysical Research: Oceans, p. e2021JC018341. Available at: https://doi.org/10.1029/2021JC018341.

Chapter 4 of this thesis was reproduced with minor modifications from Peck, C.J., Kuzyk, Z.A., Kirillov, S., Neumeier, U., Rabbitskin, E., Ehn, J.K. (2025). 'On the upcoast intrusion of the La Grande River under-ice plume under wind forcing. Continental Shelf Research.

Chapter 5 of this thesis was reproduced with minor modifications from Peck, C.J., Kuzyk, Z.A., O'Conner, M., Leblanc, M., Ehn, J.K. (2024). Winter-to-summer transition in seawater salinity, temperature, and light at eelgrass bed habitats in northeastern James Bay. 'In prep'

Contributions of authors

Chapter 3: Peck, C.J., Kuzyk, Z.A., Heath, J.P., Lameboy, J., Ehn, J.K. (2022) 'Under-ice hydrography of the La Grande River plume in relation to a ten-fold increase in wintertime discharge', Journal of Geophysical Research: Oceans, p.e2021JC018341. https://doi.org/10.1029/2021JC018341.

Contributions

Survey design: J.P. Heath, J. Lameboy Z.AA. Kuzyk, and J.K. Ehn

Data collection: C.J. Peck (2017 only), J.P. Heath, J. Lameboy Z.A. Kuzyk, and J.K. Ehn

Data analysis and Interpretations: C.J. Peck, Z.A. Kuzyk, and J.K. Ehn

Manuscript preparation*: C.J. Peck, J.P. Heath, J. Lameboy, Z.A. Kuzyk, and J.K. Ehn

*The manuscript was drafted by C.J. Peck and revised by every co-author.

Chapter 4: Peck, C.J., Kuzyk, Z.Z., Kirillov, S., Neumeier, U., Rabbitskin, E. Ehn, J.K. (2024) On the response of the La Grande River under-ice plume to wind forcing. 'Accepted' Continental shelf research

Contributions

Survey design: C.J. Peck, E. Rabbitskin, Z.A. Kuzyk, and J.K. Ehn

Data collection: C.J. Peck, E. Rabbitskin, U. Neumeier

Data analysis and Interpretations: C.J. Peck, S. Kirillov, Z.Z Kuzyk, and J.K, Ehn

Manuscript preparation*: C.J. Peck, S. Kirillov, U. Neumeier, E. Rabbitskin, Z.A. Kuzyk, and J.K. Ehn

*The manuscript was drafted by C.J. Peck and revised by every co-author.

Chapter 5: Peck, C.J., Kuzyk, Z.AA., O'Conner, M., Leblanc, M., Ehn, J.K. (2024) Winter-to-summer transition in seawater salinity, temperature, and light at eelgrass bed habitats in northeastern James Bay. 'In prep'

Contributions

Survey design: C.J. Peck, Z.A. Kuzyk, and J.K. Ehn

Data collection: C.J. Peck

Data analysis and Interpretations: C.J. Peck, M. O'Conner, M. Leblanc, Z.A. Kuzyk, and J.K. Ehn

Manuscript preparation*: C.J. Peck, M. O'Conner, M. Leblanc, Z.A. Kuzyk, and J.K. Ehn

*The manuscript was drafted by me and revised by every co-author

Chapter 1 Introduction

1.1 Motivation

Freshwater runoff or discharge from the continents is a large and important part of the global water cycle, with rivers carrying more than one-third of land-based precipitation to the ocean (Trenberth et al., 2007). The large amounts of freshwater released by the world's major rivers into the coastal ocean form river plumes. These freshwater plumes impact ocean circulation patterns at local and regional scales through their momentum and lower density compared to seawater (Carton, 1991; Milliman and Farnsworth, 2013). This discharge from rivers also comes with a large quantity of terrestrial particles, dissolved minerals, and nutrients that shape the characteristics of ecosystems in coastal waters. Therefore, river discharge plays a vital role in ecosystem productivity and coastal ocean biogeochemical cycles (Horner-Devine et al., 2009; Horner-Devine et al., 2015). Freshwater discharge that enters the coastal ocean not only forms distinct river plumes of very low salinity and other distinct characteristics but also dilute salinity and modify other water properties across larger regions known as regions of freshwater influence (ROFIs). The impact of river plumes and the materials they carry on the surrounding coastal waters varies with the physical processes that transport and mix the plume with the surrounding, more saline, coastal ocean (Chant, 2011; Horner-Devine et al., 2015).

Understanding the impacts of freshwater plumes within the coastal environment is vital because these habitats are host to some of the most diverse ecosystems on the planet, such as floodplains, estuaries, dune systems, mangrove forests, seagrass beds, and coral reefs (Hinrichsen, 2013). The habitats, ecosystems, natural resources, and ecosystem services provided by coastal areas are of great human importance, with 75% of the world's population living and working in coastal watersheds (Chant, 2011). They are a vital resource, as they provide a platform for food, industry, and leisure for the general population (Carter, 2013). However, coastlines are extremely fragile and face many threats associated with climate change and anthropogenic forcing (Carter, 2013).

One area that is particularly vulnerable is the vast Canadian Arctic and subarctic, where climate warming is occurring at unprecedented rates (Barber et al., 2008; Steiner et al., 2015). Arctic coasts and ecosystems are on the front lines of environmental responses to climate change, undergoing changes that include shortening of the sea ice season, rising sea surface temperatures, increased coastal erosion, sea level rise, altered freshwater runoff, and expanding human development (Forbes, 2011). With many northern communities located on or close to Arctic coastlines and relying on coastal ecosystems for their food security and traditional practices, it is imperative that these threats and changes are understood. River plumes are controlled by a number of factors that can change their size, structure, and distribution along the coast. Coastal topography and the shape of the river mouth provide physical constraints on plumes (Horner-Devine et al., 2015), whereas discharge controls the plume shape and distribution because of buoyancy and momentum (Garvine 1995; Horner-Devine et al., 2015). Additionally, factors such as tides and wind forcing alter plumes through mixing (Fong and Geyer, 2001; Chant, 2011; Halverson and Pawlowicz, 2008). These factors are often omitted from the numerical models of plumes because of their short-term variations and added complexity, particularly when it comes to wind forcing. There have been some modelling studies examining the alteration of plume distribution via wind forcing, the results of which were consistent with Ekman transport, whereby upwelling winds move the plume offshore and downwelling winds move the plume towards the coast (Fong and Geyer, 2001; Chant, 2011). Overall, most factors influencing river plume dynamics including wind forcing have been studied extensively using models and to a lesser degree using in situ observations. Indeed, in situ observations of river plume dynamics are mostly limited to areas that do not experience much if any sea-ice cover, that is, areas outside of the polar regions, with a few notable exceptions, as discussed below.

The Arctic is host to some of the largest rivers in the world and receives more than 10% of the global freshwater discharge (Bianchi et al., 2013). North American and Eurasian Arctic rivers deliver ~538 km^3 y^{-1} and ~2683 km^3 y^{-1}, respectively, into the Arctic Ocean proper (Alkire et al., 2017), and the Subarctic region known as Hudson Bay adds another ~635 km^3 y^{-1} to the Arctic Ocean outflow that reaches the North Atlantic Ocean via the Hudson Strait (St-Laurent et al., 2011). Despite the large magnitude of Arctic and Subarctic river-runoff, most of the studies on Arctic and Subarctic rivers were conducted in the summer, when discharge is low, but the areas are ice-free and thus more accessible for research conducted from ships. During winter, many of the small and medium-sized rivers are frozen or characterized by minimal discharge. However, some larger rivers, such as the Mackenzie and Yenisei, still flow during winter. The Mackenzie River, which discharges into the Western Arctic Ocean, is among the best studied in terms of river plume dynamics during both the ice-free and ice-covered seasons. Macdonald et al. (1995) documented how the Mackenzie River water spread under landfast sea ice at rates of about 0.2 cm s^{-1} away from the coast and 1.3 cm s^{-1} along the coast in the Canadian Beaufort Sea, ultimately impounding most of the winter inflow from the river under the ice and shutting down convection driven by brine production in this area of impounded freshwater. Eicken et al. (2005) described how the influence of the Lena River discharge produced a 2000–3000 km^2 under-ice plume with surface water salinities <5 and north, northeastward spreading rates of 1.0–2.7 cm s^{-1} In recent decades, some Arctic and Subarctic rivers such as the La Grande, Eastmain, Caniapiscau, Rupert, Churchill, and Nelson Rivers have undergone hydroelectric development that modified both the amount of discharge and the timing, leading in some cases to substantially increased winter flows (Stadnyk et al., 2021). For the La Grande River (northern Québec, Canada), which had its natural flow augmented by flows diverted from the Eastmain, Rupert, and Caniapiscau Rivers, the highest amount of discharge now occurs during the winter, when the most power generation is required (de Melo et al., 2022). Consequently, a large amount of freshwater is discharged by the regulated La Grande River into the ice-covered environment of James Bay, a southern extension of Hudson Bay (~5000 m^3 s^{-1}, forming an under-ice river plume on par with the river plumes of the Mackenzie River and other great Arctic rivers. While the average annual discharge of the La Grande River is much lower than that of the great Arctic rivers, its average winter discharge ranks among the highest in the Arctic region, due to hydroelectric regulation. Table 1.1 compares average annual and winter discharge volumes across key Arctic and Subarctic rivers to contextualize the magnitude and timing of freshwater input.

The in situ studies that have been conducted on under-ice river plumes across Arctic and Subarctic areas generally have shown that they have a much larger extent than plumes developed from equivalent discharge during the open water period (cf., Kuzyk et al., 2008; Macdonald et al., 1995, Ingram and Larouche, 1987). This increase in size occurs because ice cover reduces the amount of wind-driven mixing (Ingram, 1981; Freeman, 1983; Ingram and Larouche, 1987). The extent of under-ice plumes can also be modified or 'steered' by under-ice topography, such as stamukhi zones, confining the freshwater along the coast (Kuzyk et al., 2008; Macdonald et al., 1995). River water also may be incorporated into growing landfast ice cover (Kuzyk et al., 2008; Macdonald et al., 1995; Eicken et al., 2005; Diaz et al., 2024). However, these studies do not incorporate the kinds of continuous observations that would allow detailed study of how an under-ice plume might be affected by time-dependent factors such as winds and tides, and how multiple factors might combine to impact plume structure and extent from year to year and throughout the course of a single winter.

Table 1.1: Average annual discharge and the typical winter discharge for the major rivers in the Arctic compared to the La Grande river.

River	Average annual discharge ($m^3 s^{-1}$)	Typical Winter Discharge ($m^3 s^{-1}$)	Source
Mackenzie	~9870	~1095	Shiklomano et al., 2021
Lena	~19,180	~1650	Shiklomano et al., 2021
Yenisei	~19,500	~4060	Shiklomano et al., 2021
Ob	~13,230	~2340	Shiklomano et al., 2021
Nelson	~3240	~460	Déry et al., 2016
La Grande River (LGR)	~4,100	~4800	Peck et al., 2022

Understanding how under-ice plumes behave throughout the period from ice formation to melt and ice breakup is important because of the potentially significant impacts of plumes on salinity, water temperature, nutrients, and light availability in coastal ecosystems, driven by the mixing and transport processes of freshwater inputs along the coast. The salinity distribution around a river mouth is heavily influenced by factors such as coastal topography, ice zonation, river discharge, wind, and tides, which collectively can create stratified conditions that limit vertical mixing and produce very low surface salinities below 5 (cf., Eicken et al., 2005). Changes in salinity can disrupt local biota, such as near-shore coral reefs and seagrass growth (Lirman and Cropper, 2003; Huang et al., 2014). Riverine sediments can produce turbidity in coastal waters, which can be detrimental to primary producers (Cloern and Jassby, 2012). While river discharge can be a source of nutrients that limit coastal vegetation growth, stratification of coastal waters by river water addition can also have the net effect of decreasing nutrient availability for phytoplankton (Harrison et al., 2008; Guzzi et al., 2024). Additionally, high loads of colored dissolved organic matter (CDOM) delivered by rivers to coastal areas absorb light within the water column and reduce photosynthetically active radiation (PAR) availability at the seabed, thereby affecting seagrass and macroalgal primary production (Blough and Del Vecchio, 2002). The complex and seasonally varying interactions between river discharge and ice coverage that affect river plume dispersion and consequently salinity, temperature, nutrients, and light availability shape coastal ecosystems and, in part, determine their resilience when they experience environmental changes (Kemp et al., 2005; Raymond and Spencer, 2015).

In general, the established knowledge on how river plumes behave under certain conditions has come from numerical models, which typically focus on one influencing factor at a time, for example, wind forcing or topography. Furthermore, the vast majority of observational studies on the behavior of river plumes have been conducted outside of the Arctic and Subarctic or in open-water conditions. The few studies that have been conducted on under-ice river plumes have not addressed how a plume's extent and structure might vary over temporal and spatial scales as a function of the combined effects of landfast ice morphology, the horizontal extent of landfast ice cover, tides, wind forcing, and variations in discharge.

1.2 Thesis objectives

The aim of this thesis is to investigate and improve the understanding of oceanographic processes in the coastal domain of northeast James Bay, where the regulated La Grande River (LGR) discharges freshwater at, on average, twice its natural rate into the coastal habitat, with peak flows during winter. Because of limited modelling of under-ice river plumes in complex coastal settings, the focus is on observing processes that are important for river plume dynamics during the ice-cover season. Fieldwork opportunities in this setting were made possible by a comprehensive research program launched to investigate the coastal habitat. This provided opportunities to collect and analyze new time-series measurements to establish the controls on the LGR plume dynamics, and examine the way it interacts with the nearshore coastal waters, which are home to ecosystems sensitive to freshwater discharge. In particular, the coastal habitat that receives LGR discharge in eastern James Bay hosts a habitat of eelgrass *(Zostera marina),* which was once among the largest expanses of eelgrass in North America, estimated at ~250 km^2 (Lalumière et al., 1994). The eastern James Bay eelgrass ecosystem underwent a massive collapse in the late 1990s, nearly 20 years after the start of LGR development, and questions remain about the role of the hydropower development and associated freshwater changes in bringing about the eelgrass decline (Leblanc et al., 2023; Idrobo et al., 2024).

To address these aims, add to our general understanding of frozen estuaries and under-ice river plumes, and contribute to investigations of environmental change in this regionally important coastal habitat, the following three research questions were generated:

1. How has the LGR plume changed in response to discharge regulation and changes in ice conditions?

2. What are the short-term drivers of variations in the LGR plume characteristics especially horizontal extent along the coast?
3. How does the influence of the LGR plume, local stream discharge, and evolution of the surface ice cover influence key eelgrass habitat properties during the seasonal transition from winter to summer?

1.3 Thesis outline

This thesis consists of six chapters, including this introduction. Chapter 2 outlines the scientific background of the research studies. Chapter 3 contains a separate original full-length research paper that has been published in a peer-reviewed journal. Chapters 4 and 5 each contain original, full-length research papers. The first of these papers (Chapter 4) has been submitted to a peer-reviewed journal for consideration for publication and a revision requested, and the second paper (Chapter 5) is almost ready for submission. Chapter 6 summarizes the key findings of this thesis with respect to the research questions stated above and offers recommendations for future work.

Chapter 2 addresses the background on how a river plume is established, the factors that control river plume dynamics, what is known about under-ice river plumes, including the under-ice river plume of the La Grande River, and finally, the ecological setting in northeast James Bay and the timeline of past studies documenting the expansion of the river plume in association with the decline of eelgrass (*Zostera marina*).

Chapter 3 addresses research questions 1 & 2 by analyzing a large newly collected dataset of salinity, temperature, and water current data from along the northeast coast of James Bay including from both summer and winter. This data allowed us to investigate the current extent of the LGR plume under landfast ice since the most recent phase of hydroelectric development was completed bringing winter discharges to ~5000 m^3 s^{-1}. Data were collected in 2016 and 2017. The findings are presented in a peer-reviewed manuscript in the Journal of Geophysical Research: Oceans. The citation for this manuscript is as follows:

Peck, C.J., Kuzyk, Z.A., Heath, J.P., Lameboy, J., Ehn, J.K. (2022) Under-ice hydrography of the La Grande River plume in relation to a ten-fold increase in wintertime discharge', Journal of Geophysical Research: Oceans, p. e2021JC018341. Available at: https://doi.org/10.1029/2021JC018341.

Chapter 4 addresses research questions 2 & 3 by analyzing data from instruments placed in embayments to the north and south of the LGR river mouth, which monitored temperature, salinity, and two-dimensional current data throughout a full year. The data were collected from August 2019 to August 2020, and the findings are presented in a manuscript submitted to Continental Shelf Research:

Peck, C.J., Kuzyk, Z.A., Kirillov, S., Neumeier, U., Rabbitskin, E., Ehn, J.K. (2025) On the upcoast intrusion of the La Grande River under-ice plume under wind forcing, Continental Shelf Research. (accepted)

Chapter 5 addresses research question 3 by describing temperature, salinity, and photosynthetically active radiation (PAR) variation in relation to decreases in LGR discharge and melting and breakup of the coastal landfast ice. The continuous measurements of water properties important for eelgrass health were collected using bottom-mounted moorings deployed from March 2019 to August 2019. The findings are currently being prepared for submission to Estuaries and Coasts.

Peck, C.J., Kuzyk, Z.A., Ehn, J.K. (2024) Variations in salinity, temperature, and light in eelgrass bed habitats in northeastern James Bay over the seasonal transition from winter to summer. 'In prep'

Chapter 6 provides a summary of the key findings, drawing together the different aspects of the research in relation to the stated research questions, and makes recommendations for future work.

1.4 References

Alkire, M.B., Morison, J., Schweiger, A., Zhang, J., Steele, M., Peralta-Ferriz, C., Dickinson, S., 2017. A Meteoric Water Budget for the Arctic Ocean. Journal of Geophysical Research: Oceans 122, 10020–10041. https://doi.org/10.1002/2017JC012807

Barber, D.G., Lukovich, J.V., Keogak, J., Baryluk, S., Fortier, L., Henry, G.H.R., 2008. The changing climate of the Arctic. Arctic 7–26.

Bianchi, T.S., Allison, M.A., Cai, W.-J., 2013. Biogeochemical Dynamics at Major River-Coastal Interfaces: Linkages with Global Change. Cambridge University Press.

Blough, N.V., Del Vecchio, R., 2002. Chromophoric DOM in the Coastal Environment, in: Biogeochemistry of Marine Dissolved Organic Matter. Elsevier, pp. 509–546. https://doi.org/10.1016/B978-012323841-2/50012-9

Carter, R.W.G., 2013. Coastal Environments: An Introduction to the Physical, Ecological, and Cultural Systems of Coastlines. Elsevier.

Carton, J.A., 1991. Effect of seasonal surface freshwater flux on sea surface temperature in the tropical Atlantic Ocean. Journal of Geophysical Research: Oceans 96, 12593–12598. https://doi.org/10.1029/91JC01256

Chant, R.J., 2011. 2.11 - Interactions between Estuaries and Coasts: River Plumes – Their Formation, Transport, and Dispersal, in: Wolanski, E., McLusky, D. (Eds.), Treatise on Estuarine and Coastal Science. Academic Press, Waltham, pp. 213–235. https://doi.org/10.1016/B978-0-12-374711-2.00209-6

Cloern, J.E., Jassby, A.D., 2012. Drivers of change in estuarine-coastal ecosystems: Discoveries from four decades of study in San Francisco Bay. Reviews of Geophysics 50. https://doi.org/10.1029/2012RG000397

de Melo, M.L., Gérardin, M.-L., Fink-Mercier, C., del Giorgio, P.A., 2022. Patterns in riverine carbon, nutrient and suspended solids export to the Eastern James Bay: links to climate, hydrology and landscape. Biogeochemistry 161, 291–314. https://doi.org/10.1007/s10533-022-00983-z

Diaz, A., Kuzyk, Z.Z.A., Guzzi, A., Gupta, K., Papakyriakou, T., Ehn, J.K., 2024. Stable isotopes of landfast sea ice as a record of La Grande River under-ice plume dispersal. Arctic Science 10, 698–712. https://doi.org/10.1139/as-2024-0003

Eicken, H., Dmitrenko, I., Tyshko, K., Darovskikh, A., Dierking, W., Blahak, U., Groves, J., Kassens, H., 2005. Zonation of the Laptev Sea landfast ice cover and its importance in a frozen estuary. Global and Planetary Change, Arctic Siberian Shelf Environments 48, 55–83. https://doi.org/10.1016/j.gloplacha.2004.12.005

Fong, D.A., Geyer, W.R., 2001. Response of a river plume during an upwelling favorable wind event. Journal of Geophysical Research: Oceans 106, 1067–1084. https://doi.org/10.1029/2000JC900134

Forbes, D.L.E., 2011. State of the Arctic Coast 2010 - Scientific Review and Outlook [WWW Document]. URL http://www.arcticcoasts.org/ (accessed 9.10.25).

Freeman N.G., 1982. Measurement and Modelling of Freshwater Plumes Under an Ice Cover. PhD dissertation, University of Waterloo, Canada.

Garvine, R.W., 1995. A dynamical system for classifying buoyant coastal discharges. Continental Shelf Research, Nearshore and Coastal Oceanography 15, 1585–1596. https://doi.org/10.1016/0278-4343(94)00065-U

Guzzi, A.C., Ehn, J.K., Michel, C., Tremblay, J.-É., Heath, J.P., Kuzyk, Z.Z.A., 2024. Influence of altered freshwater discharge on the seasonality of nutrient distributions near La Grande River, northeastern James Bay, Québec. Elementa: Science of the Anthropocene 12, 00133. https://doi.org/10.1525/elementa.2023.00133

Halverson, M.J., Pawlowicz, R., 2008. Estuarine forcing of a river plume by river flow and tides. Journal of Geophysical Research: Oceans 113. https://doi.org/10.1029/2008JC004844

Harrison, P.J., Yin, K., Lee, J.H.W., Gan, J., Liu, H., 2008. Physical–biological coupling in the Pearl River Estuary. Continental Shelf Research, Coastal Ecosystem Responses to Changing Nutrient Inputs from Large Temperate and Subtropical Rivers 28, 1405–1415. https://doi.org/10.1016/j.csr.2007.02.011

Hinrichsen, D., 2013. Coastal Waters of the World: Trends, Threats, and Strategies. Island Press.

Horner-Devine, A.R., Hetland, R.D., MacDonald, D.G., 2015. Mixing and Transport in Coastal River Plumes. Annual Review of Fluid Mechanics 47, 569–594. https://doi.org/10.1146/annurev-fluid-010313-141408

Horner-Devine, A.R., Jay, D.A., Orton, P.M., Spahn, E.Y., 2009. A conceptual model of the strongly tidal Columbia River plume. Journal of Marine Systems 78, 460–475. https://doi.org/10.1016/j.jmarsys.2008.11.025

Huang, H., Yang, Y., Li, X., Yang, J., Lian, J., Lei, X., Wang, D., Zhang, J., 2014. Benthic community changes following the 2010 Hainan flood: Implications for reef resilience. Marine Biology Research 10, 601–611. https://doi.org/10.1080/17451000.2013.841942

Idrobo, C.J., Leblanc, M.-L., O’Connor, M.I., 2024. The “Turning Point” for the Fall Goose Hunt in Eeyou Istchee: A Social-Ecological Regime Shift from an Indigenous Knowledge Perspective. Human Ecology 52, 617–636. https://doi.org/10.1007/s10745-024-00499-0

Ingram, R.G., 1981. Characteristics of the Great Whale River plume. Journal of Geophysical Research: Oceans 86, 2017–2023. https://doi.org/10.1029/JC086iC03p02017

Ingram, R.G., Larouche, P., 1987. Changes in the under-ice characteristics of La Grande Rivière plume due to discharge variations*. Atmosphere-Ocean 25, 242–250. https://doi.org/10.1080/07055900.1987.9649273

Kemp, W.M., Boynton, W.R., Adolf, J.E., Boesch, D.F., Boicourt, W.C., Brush, G., Cornwell, J.C., Fisher, T.R., Glibert, P.M., Hagy, J.D., Harding, L.W., Houde, E.D., Kimmel, D.G., Miller, W.D., Newell, R.I.E., Roman, M.R., Smith, E.M., Stevenson, J.C., 2005. Eutrophication of Chesapeake Bay: historical trends and ecological interactions. Marine Ecology Progress Series 303, 1–29. https://doi.org/10.3354/meps303001

Kuzyk, Z.A., Macdonald, R.W., Granskog, M.A., Scharien, R.K., Galley, R.J., Michel, C., Barber, D., Stern, G., 2008. Sea ice, hydrological, and biological processes in the Churchill River estuary region, Hudson Bay. Estuarine, Coastal and Shelf Science 77, 369–384. https://doi.org/10.1016/j.ecss.2007.09.030

Lalumière, R., Messier, D., Fournier, J.-J., Peter McRoy, C., 1994. Eelgrass meadows in a low Arctic environment, the northeast coast of James Bay, Québec. Aquatic Botany 47, 303–315. https://doi.org/10.1016/0304-3770(94)90060-4

Leblanc, M.-L., O'Connor, M.I., Kuzyk, Z.Z.A., Noisette, F., Davis, K.E., Rabbitskin, E., Sam, L.-L., Neumeier, U., Costanzo, R., Ehn, J.K., Babb, D., Idrobo, C.J., Gilbert, J.-P., Leblon, B., Humphries, M.M., 2023. Limited recovery following a massive seagrass decline in subarctic eastern Canada. Global Change Biology 29, 432–450. https://doi.org/10.1111/gcb.16499

Lirman, D., Cropper, W.P., 2003. The influence of salinity on seagrass growth, survivorship, and distribution within Biscayne Bay, Florida: Field, experimental, and modelling studies. Estuaries 26, 131–141. https://doi.org/10.1007/BF02691700

Macdonald, R.W., Paton, D.W., Carmack, E.C., Omstedt, A., 1995. The freshwater budget and under-ice spreading of Mackenzie River water in the Canadian Beaufort Sea based on salinity and 18O/16O measurements in water and ice. Journal of Geophysical Research: Oceans 100, 895–919. https://doi.org/10.1029/94JC02700

Raymond, P.A., Spencer, R.G.M., 2015. Riverine DOM, in: Biogeochemistry of Marine Dissolved Organic Matter. Elsevier, pp. 509–533. https://doi.org/10.1016/B978-0-12-405940-5.00011-X

Stadnyk, T.A., Tefs, A., Broesky, M., Déry, S.J., Myers, P.G., Ridenour, N.A., Koenig, K., Vonderbank, L., Gustafsson, D., 2021. Changing freshwater contributions to the Arctic: A 90-year trend analysis (1981–2070). Elementa: Science of the Anthropocene 9, 00098. https://doi.org/10.1525/elementa.2020.00098

Steiner, N., Azetsu-Scott, K., Hamilton, J., Hedges, K., Hu, X., Janjua, M.Y., Lavoie, D., Loder, J., Melling, H., Merzouk, A., Perrie, W., Peterson, I., Scarratt, M., Sou, T., Tallmann, R., 2015. Observed trends and climate projections affecting marine ecosystems in the Canadian Arctic. Environmental Reviews 23, 191–239. https://doi.org/10.1139/er-2014-0066

St-Laurent, P., Straneo, F., Dumais, J.-F., Barber, D.G., 2011. What is the fate of the river waters of Hudson Bay? Journal of Marine Systems, The Hudson Bay System 88, 352–361. https://doi.org/10.1016/j.jmarsys.2011.02.004

Trenberth, K.E., Smith, L., Qian, T., Dai, A., Fasullo, J., 2007. Estimates of the Global Water Budget and Its Annual Cycle Using Observational and Model Data. Journal of Hydrometeorology 8, 758–769. https://doi.org/10.1175/JHM600.1

Chapter 2 Background

2.1 Structure of buoyant river plumes and coastal currents

When the mouth of a river meets the coast, it releases lower density freshwater into the higher density saline ambient oceanic water and therefore is a source of both momentum and buoyancy. The structure that is formed from the difference in density is referred to as a buoyant river plume (Kourafalou et al., 1996). This plume, along with its mixing zone and associated coastal currents, is part of what is broadly termed a region of freshwater influence (ROFI), defined as the spatial domain where freshwater input significantly alters the salinity, density structure, and circulation of the coastal ocean (Simpson, 1997; Horner-Devine et al., 2015). ROFIs can vary in extent from tens to hundreds of kilometers and encompass both the dynamic inner plume and its broader influence on shelf circulation. River plumes are complex structures with dynamic balance changing as they extend away from the shore before mixing with the ocean. Because of these changes, the structure of a river plume can be split into four dynamic regions: the source region and liftoff, near-field region, mid-field region, and far- field region (Garvine, 1984; Hetland, 2005; Horner-Devine et al., 2009).

2.1.1 Source region and plume liftoff

The source region is where a river plume is initiated and is located within the river mouth. The buoyancy and momentum of the plume are determined in this area and have a profound effect on the dynamics of the plume as it enters the surrounding ocean (Horner-Devine et al., 2015). In a river with a high velocity, the plume will exhibit 'liftoff' from the seabed near the river mouth and form a buoyant layer, becoming advected at the surface (Figure 2.1a). When rivers have a low discharge velocity, the plume can detach from the seabed within the estuary or, in some cases, remain attached to the bottom (Chant, 2011; Branch et al., 2020).

The process of plume liftoff is governed by two-layer hydraulics theory (Armi and Farmer, 1986) and is typically described using the upper layer internal Froude number (Horner-Devine et al., 2015; Branch et al., 2020). The internal Froude number (Fr_1) is a ratio of the depth-averaged freshwater velocity, u1, to the propagation speed of the gravity current, where g' is the reduced gravity and h_1 is the depth of the freshwater flow:

$$\mathrm{Fr}_1 = \frac{u_1}{\sqrt{g' h_1}}$$

The reduced gravity is defined as:

$$g' = g\left(\frac{\Delta\rho}{\rho_o}\right)$$

here g is the acceleration due to gravity and Δρ is the density difference relative to the ambient ocean water density ρo (MacDonald and Geyer, 2004; Macdonald and Geyer, 2005; Geyer and Ralston, 2011). The internal Froude number decreases as the flow propagates offshore and loses its momentum. Liftoff occurs when the internal Froude number is equal to 1, as the hydrostatic pressure of the ocean overcomes the dynamic pressure of the river, forcing freshwater off the bottom (MacDonald and Geyer, 2004; Macdonald and Geyer, 2005; Geyer and Ralston, 2011).

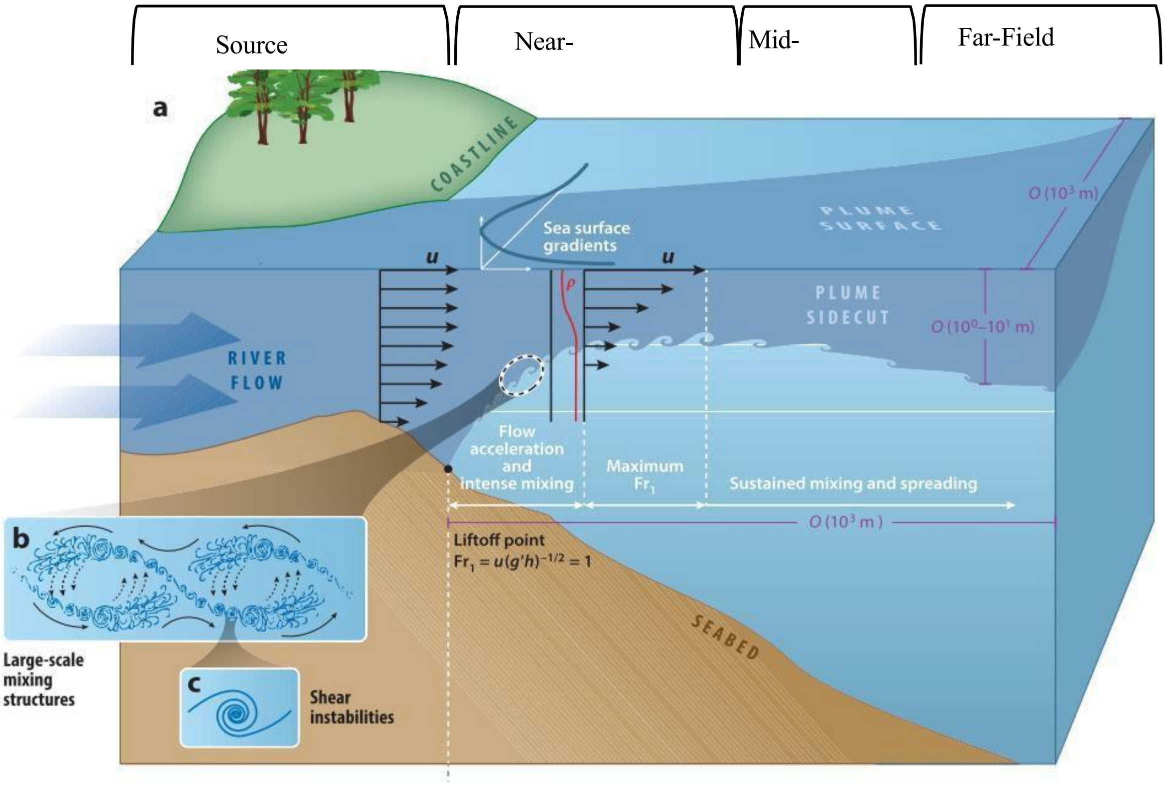

Figure 2.1:(a) Diagram of the plume lift-off process and subsequent regions: near-field, mid-field, and far-field. (b) Mixing structures within a flow. (c) Shear instabilities that exist within the large-scale mixing structures. Taken and adapted from (Horner-Devine et al., 2015).

2.1.2 Dynamic regions of river plumes: near- to far-field

The near-field region begins at the point of liftoff or at the river mouth if liftoff has occurred further upstream in the river, and it is where the velocity of discharge exceeds the buoyancy of the plume and acts like a buoyant jet (Jirka et al., 1981). The near-field region is extremely dynamic due to both tidal currents and the initial velocity of the plume as it enters the surrounding ocean (Chant, 2011). The plume usually begins to shoal in the near-field region, as the strong density difference between the plume and the ambient ocean water causes lateral gravitational spreading. The momentum carried from the source region also initiates turbulent mixing at the interface of the upper and lower layers (Figure 2.1b) (Hetland, 2005; Chen et al., 2009). Vertically, the near-field region is characterized by a sharp density gradient, with a surface-trapped freshwater layer above denser saline water, and strong shear at the interface (Figure 2.1c) (MacDonald and Geyer, 2004; Horner-Devine et al., 2009). The near-field region does not exist in all plumes. The likelihood of the near-field region being present can sometimes be determined by the ratio of the width of the river mouth to the Rossby radius. The Rossby radius is the length scale at which the rotational effects of the Coriolis effect are as important as the effects of buoyancy waves (Nurser and Bacon, 2014). River mouths that are wide compared to the Rossby radius will not have a near-field region and will instead transition straight into a far-field plume as the discharge exits the river mouth.

The mid-field region is the transition zone from the jet-like near-field into a geostrophic or wind-driven far-field plume (Figure 2.1a). In this region, the rotation of the Earth becomes an important factor in the dynamics of a river plume, as the lateral spreading of the plume is slowing and the momentum from the source region is reduced. As the Earth's rotation (Coriolis effect) plays more of a role, the plume, although initially directed offshore, forms a shore-parallel coastal current and is associated with a corresponding increase in centripetal force (Garvnie 1987, McCabe 2009). The mid-field region often displays a well-developed two-layer structure of a fresher surface layer of variable thickness underlain by more saline ocean water, with reduced mixing across the halocline except in regions influenced by wind (Fong and Geyer, 2002; Horner-Devine et al., 2015).

As the buoyant river plume transitions away from the jet-like dynamics of the near-field region, its structure evolves under the increasing influence of Earth's rotation and ambient ocean conditions. In this mid-field region, the lateral spreading of the plume slows as momentum from the source region is dissipated, and the Coriolis effect begins to deflect the plume, steering it into a shore-parallel coastal current (Figure 2.1a). This region is often characterized by complex structures such as recirculating (anticyclonic) bulges or unsteady anticyclonic eddies, which form when wind forcing is weak (Horner-Devine et al., 2015). A series of more detailed numerical models and field observations have confirmed the existence of freshwater-retaining bulges (Fong and Geyer, 2002; Chant et al., 2008; Horner-Devine et al., 2009). In previous models, they were often purposefully eliminated by inducing an ambient current, as bulges were rarely observed in the real world. A series of model simulations run by Fong and Geyer (2002) without the input of a strong ambient current showed that a growing recirculating bulge formed in front of the mouth and limited the transport of freshwater down the coast. The bulges are characterized by anticyclonic flow, with the strongest current located on the offshore edge. The discharge initially travels offshore and then turns in a clockwise motion continually until the flow collides with the coast. At this point, some of the flow is directed down the coast and feeds into the coastal current, but the majority of the flow reenters the bulge and circulates again (Fong and Geyer, 2002). In these bulges, the vertical structure may become more stratified, with suppressed vertical mixing due to the weak surface wind stress (McCabe et al., 2009).

Beyond the bulge, in the far-field region, the influence of source momentum becomes negligible, and plume dynamics are dominated by a balance between buoyancy, wind stress, and Coriolis forcing. This geostrophic adjustment leads to the development of coastal currents, where the cross-shore pressure gradient created by the freshwater lens is balanced by the Coriolis acceleration directed toward the coast (Kourafalou et al., 1996). The resulting density-driven currents extend the plume along the coastline rightward in the Northern Hemisphere and leftward in the Southern Hemisphere. These coastal currents can persist over distances ranging from tens to hundreds of kilometers, particularly when ambient ocean currents and wind-driven offshore forcing are weak or absent. As the plume advances, the freshwater layer gradually becomes thinner and more uniform due to ongoing mixing and adjustment to surrounding oceanic conditions, while entrainment processes diminish (Horner-Devine et al., 2015). A well-studied example is the Columbia River plume, which generates a buoyant coastal current that traces the Pacific Northwest coast of the United States (Hickey et al., 1998; Nash and Moum, 2005). In high-latitude environments, such as the Arctic, it is these plume-formed coastal current components that form the coastal riverine domain. This domain is a narrow band of low-salinity surface water that follows the continental margins and exerts a significant influence on regional stratification, circulation, and biological productivity (Carmack et al., 2015). Together, the mid-field and far-field regions illustrate how buoyant river plumes transition from jet-like discharge to rotationally dominated coastal flows, with their shape and extent heavily modulated by a number of factors including but not limited to bathymetry and wind forcing (Figure 2.1a).

2.2 Consistent controls on buoyant river plumes

As demonstrated above, several factors influence the extent and size of a buoyant river plume, and these vary in different settings. Some of these factors only vary over long timescales and are referred to as consistent controls. Other factors vary on shorter timescales and are defined as inconsistent controls. This section describes the controls that are consistent across all river plumes: the Coriolis effect, ambient coastal currents, bottom topography, and the shape and orientation of the river mouth.

2.2.1 Coriolis effect and ambient coastal currents

The Earth's rotation (Coriolis effect) causes ocean currents to be deflected to the right in the northern hemisphere and to the left in the southern hemisphere, increasing in strength as you move to high latitudes. The Coriolis effect directs buoyant river plumes shoreward, and when they are in balance with the force from the pressure gradient, it creates a geostrophic coastal current that can carry the plume over large distances (Carmack et al., 2015; Horner-Devine et al., 2015). A box model created by Kourafalou et al. (1996) examined plume characteristics with and without the Coriolis effect, and found that without the rotating influence, a plume would spread symmetrically from the mouth. With rotation, asymmetry in the spread and velocity of the plume occurs in one direction. This asymmetric behavior is also associated with the formation of anticyclonic bulges (section 2.1.2), which occur when rotational effects are present but not yet dominant enough to fully constrain the flow into a coastal current.

The Coriolis effect can influence the type of plume that is formed. For example, the small Coriolis effect at the equator means that the Amazon plume spreads radially, a key characteristic of small-scale plumes in Garvine's classification of plumes (O'Donnell, 2010; Chant, 2011; Horner-Devine et al., 2015), despite the large discharge of the Amazon River. In contrast, the riverine coastal domain that extends along western Greenland, northeastern –Canada (Baffin Island to Newfoundland), and the eastern United States, which receives ~10-times less freshwater than the region influenced by the Amazon, is characterized by a buoyancy-driven coastal current influenced by strong Coriolis forces. The Amazon River plume is a good example of a non-rotational plume (Figure 2.2b) that has no mid-field region or geostrophic coastal currents (Horner-Devine et al., 2015). Non-rotational plumes can occur at higher latitudes despite the stronger Coriolis effect if the river is sufficiently small, for example, the River Teign on the southern coast of England (Pritchard and Huntley, 2006). With the relatively low discharge, non-rotational plumes tend to be short-lived and spatially limited, particularly in energetic environments with strong tides or wind forcing enhance vertical and horizontal mixing (Osadchiev & Zavialov, 2020; Lentz & Helfrich, 2002).

At the latitude of northeast James Bay (~54°N), low density surface water flowing northward towards Hudson Bay is typically deflected towards the east by the Coriolis effect (El-Sabh and Koutitonsky, 1977). However, seasonal variations can arise because of interactions with buoyancy and wind forcing. For example, during spring and summer when freshwater inputs from rivers and ice melt are high, a sea surface height pressure gradient between western and eastern Hudson Bay induces a westward flow of low-density surface water, which is deflected to the right by the Coriolis effect, producing a geostrophic flow directed through the center of Hudson Bay (Ridenour et al., 2019). Ambient coastal currents have also been shown to significantly influence how a plume is transported. If moving in the same direction, an ambient current as small as 0.2 m s-1 is significant enough to increase the alongshore transport of a plume (Fong and Geyer, 2002).

2.2.2 Mouth of the river

The mouth of a river is the point where freshwater discharge exits the river channel and enters a larger body of water, such as an ocean, sea, or lake, initiating the formation of a buoyant plume. The size, relative angle to the coast, and presence of topography can greatly influence the shape of the plume. When the river mouth is perpendicular to the coast, the resulting plume is relatively straightforward and would be classed as a rotational plume (section 2.1). It will be influenced by the Coriolis effect and is likely to form a prototypical plume) (Figure 2.2a) (Horner-Devine et al., 2015). However, a plume can sometimes enter the coastal ocean at an angle, such as the Eel River on the northern Californian coast (Figure 2.2d) (Geyer et al., 2000). If the river mouth is oriented with the ambient coastal current, there will not be a bulge, and the plume's momentum will carry it into the coastal current. The width of the river mouth is also an important factor. Due to Earth's rotation, a plume can detach from one side of a river with an extremely large mouth. This essentially becomes a coastal current that starts at the river mouth and turns the corner into the coastal ocean, meaning that there is no near-field or mid-field region (Figure 2.2c) (Horner-Devine et al., 2015). An example of such a plume is the Delaware Bay plume (Whitney and Garvine, 2006). Narrower river mouths are associated with higher velocity but lower volume discharges, and can create small river plumes that only exist for a matter of days or hours (Osadchiev and Zavialov, 2019). Narrow river mouths are mainly associated with non- rotational plumes because the discharge is generally lower (Figure 2.2b).

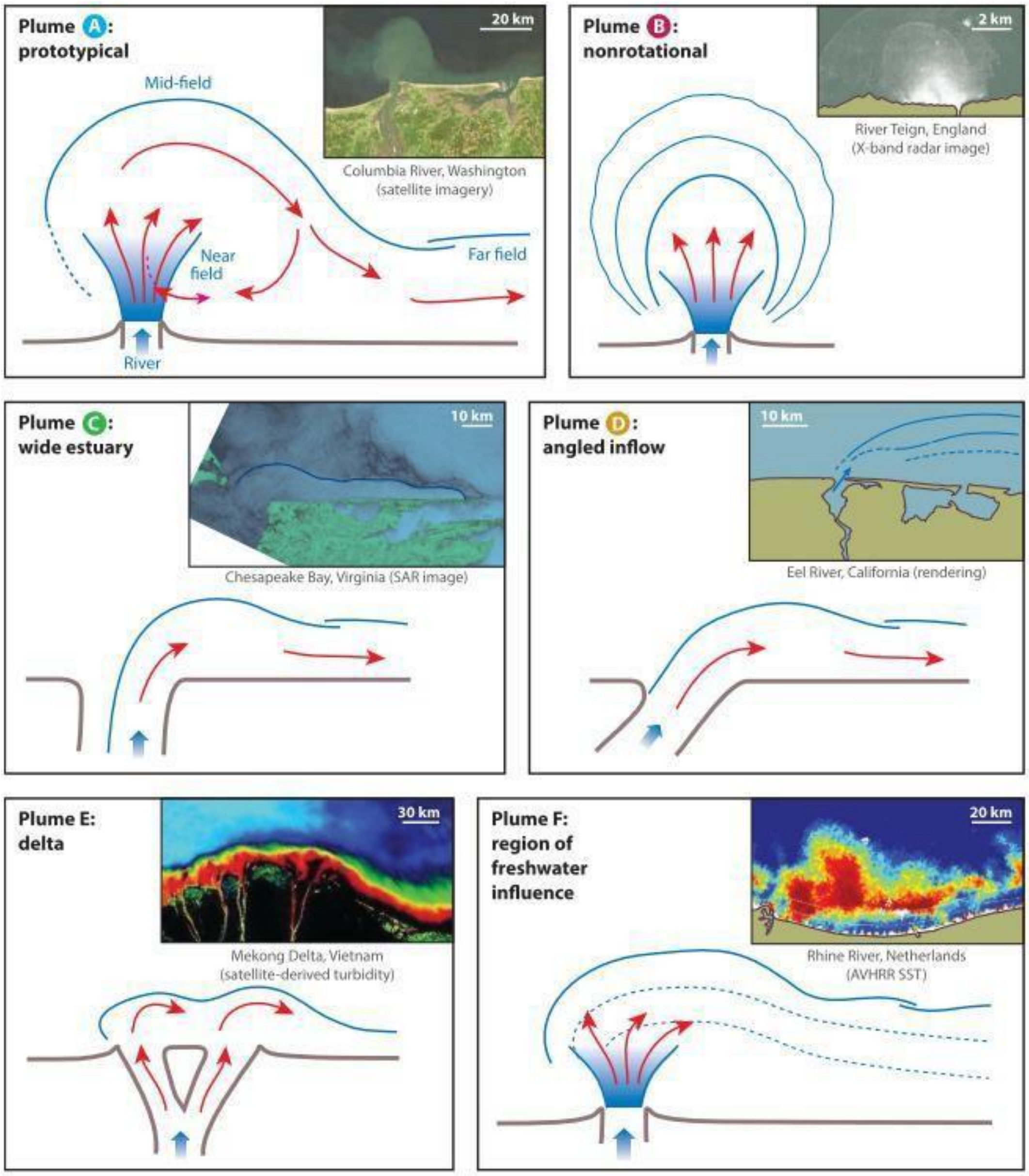

Figure 2.2 Typical plume morphologies with real world examples: Prototypical (plume A), nonrotational (plume B), wide estuary (plume C), angled inflow (plume D), delta plume (plume E) and a region of freshwater influence (plume F). Taken from Horner-Devine, Hetland and MacDonald 2015).

2.2.3 Bottom topography

Although buoyant plumes are commonly surface advected, the underwater topography can still have a significant impact on a plume's distribution. First, in the case of a semi-enclosed basin (such as a gulf or fjord) or a bathymetric sill being present, freshwater may be strongly retained due to limited exchange with the open ocean. This was found to be the case in the Clyde Sea, where vertical mixing is limited and the water column remains stratified throughout the majority of the year (Rippeth and Simpson, 1996). A box model by Rippeth and Simpson (1996) found that cross-sill exchange is limited, and over the six years modeled, there were only four instances of complete vertical mixing throughout the water column.

In the open coastal ocean, the presence of a slope away from the shore can have a profound effect. Kourafalou et al. (1996) used a box model to determine the importance of the slope under the following conditions: no ambient currents or external forcing (e.g. winds and tides), a consistent bathymetry (i.e., no slope), a coast with a 'flat bottom', and a vertical wall at the shore. They showed that under these conditions, a plume will spread radially from the source, and a weak meandering coastal current may be established by the Earth's rotation (Figure 2.2b & f). The model then introduced a small slope and found that the plume became elongated and trapped against the coast; as the slope angle increased, the plume narrowed. The box model also showed that if the depth increases too quickly, the plume detaches from the bottom and spreads radially. A model, with realistic bathymetry, of the Mississippi River by (Androulidakis et al., 2015) characterized the Mississippi plume with a flat bottom and realistic topography of a sloping bottom. The model produced similar results to others in that with a slope, the plume extent was limited in the offshore direction owing to potential vorticity constraints and elongation along the shore (Kourafalou et al., 1996; Androulidakis et al., 2015).

The presence of a slope, and how steep it is, can influence whether a plume is bottom-attached or surface-advected. Yankovsky and Chapman (1997) built upon the findings of Chapman and Lentz, (1994) to find the conditions needed to form a bottom-advected plume in a rotating ocean, and the results have been used in research on buoyant plumes thereafter (Lentz and Helfirch, 2002; Avicola and Huq, 2002). From the model, Yankovsky and Chapman (1997) produced two lengths (i.e., bottom depths) that are important in determining whether a plume remains attached to the bottom. The first length is the equilibrium depth (hb) which refers to the depth (and corresponding offshore distance) at which the plume becomes trapped nearshore and can no longer continue to flow offshore along the seabed. This trapping of the plume close to shore occurs when the offshore geostrophic front, assuming a uniform vertical shear along the front velocity, is in balance with the horizontal density gradients across the front (Yankovsky and Chapman, 1997; Horner- Devine et al., 2015). This is the distance to which a plume can spread along the surface without being affected by contact with the bottom (ys), assuming the plume has a uniform thickness. Three possible scenarios were identified using these two lengths: The first scenario is when the distance to the equilibrium depth (hb) is longer than the spread of the surface plume (i.e. $hb > ys$) (Figure 2.3a). In this case, a bottom-attached plume will be formed and is characterized by a surface to bottom front that is more buoyant than the surrounding ocean. These types of plumes are typically formed when the water column is well mixed and the density difference with the ambient ocean is small. The second scenario is when the depth of hb is shallower than the inflow. Here, the bottom has no influence, and a surface-advected plume is formed, which spreads radially offshore (Figure 2.3b). This is most common when inflow is deposited directly into the ocean. The third and final scenario occurs when the depth of hb is greater than the inflow, but its distance offshore is shorter than the ys length (i.e. $hb < ys$) (Figure 2.3c). This is known as an intermediate plume, which has some properties of both surface-advected and bottom-attached plumes. A frontal zone will be created at the depth of hb and extend along the coast. The inflow at the surface will extend seawards, rotating anticlockwise, past the length of hb.

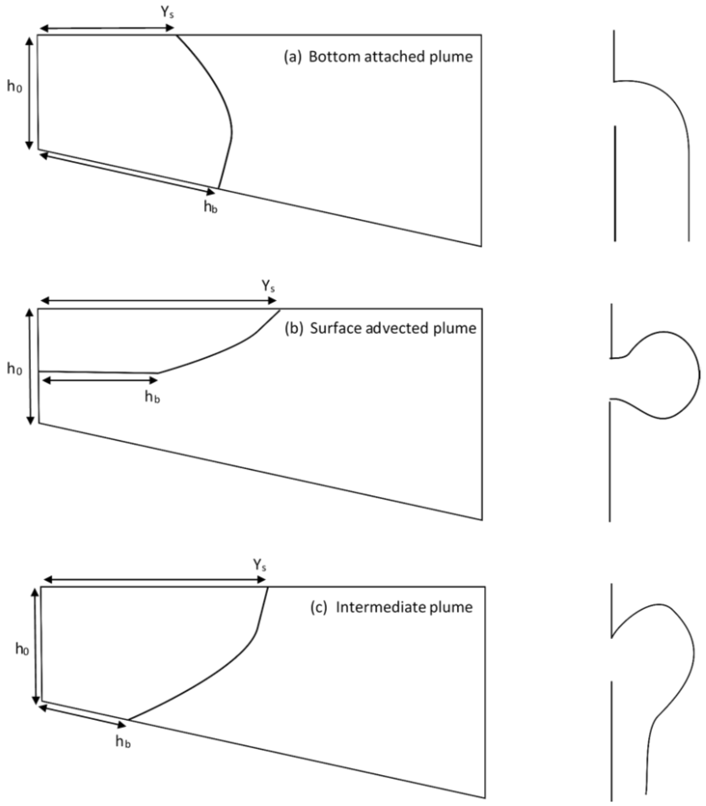

Figure 2.3: Diagrams of the types of plume attachment that results from a sloping bottom as cross section (left) and bird's eye view (right): (a) Bottom attached plume, (b) Surface advected plume, (c) Intermediate plume. Where h0 is the inflow depth, hb is the equilibrium depth of the plume that corresponds to its horizontal offshore location, and Ys is the maximum distance the plume travels at the surface. Based upon the findings of Yankovsky and Chapman (1998).

2.3 Inconsistent controls on buoyant river plumes

A major issue in studying and classifying river plumes is that several factors occur inconsistently or on short timescales that greatly influence a plume and significantly change its characteristics. These inconsistent controls are wind forcing, tidal influence, variations in discharge, and the influence of ice.

2.3.1 Wind forcing

In many of the model studies cited in section 2.2, the influence of wind forcing is omitted because it is inconsistent over time. However, wind forcing can profoundly change the structure and extent of buoyant river plumes. It is key driver for wave generation and vertical mixing by providing the required kinetic energy. In the majority of the ocean, the impact of wind is to also drive the processes of Ekman transport (Ekman, 1905; Horner-Devine et al., 2015). Thus, the influence of wind forcing on a plume can be divided into three categories: upwelling wind conditions, downwelling wind conditions, and wind wave-induced mixing.

Wind driven coastal upwelling is the process by which deep waters are brought to the surface to replace surface waters that are transported offshore by Ekman transport. Numerous observational studies have shown that river plumes tend to detach from the coast and mix with the ambient ocean waters when under the influence of upwelling-favorable wind conditions (Fong et al., 1997; Hickey et al., 1998; Androulidakis et al., 2015). Upwelling favorable wind directions are such that they blow from land to sea pushing water offshore directly, or in a direction parallel to the coastline on the left-hand side in the northern hemisphere such that the Coriolis effect pushes the Ekman surface layer offshore, or in a direction in between these two. The detachment and mixing of a buoyant coastal current into ambient ocean waters is important for the distribution of entrained materials, such as sediments and nutrients (Horner-Devine et al., 2015).

Fong and Geyer (2001) created a three-dimensional model to describe a plume's response to upwelling wind conditions. In a model setup with an ambient current of 10 cm s^{-1}, which prevents the formation of a bulge at the river mouth (Garvine, 1999), a freshwater inflow of 1500 m^3 s^{-1} and an adjustment period of 36 days, they simulated an elongated, coastally trapped plume (Figure 2.4a). The plume was then subjected to 72 hours of moderate upwelling wind forcing, and after just 24 hours, the plume detached from the coast and began to widen. Over the subsequent 48 hours, the plume was transported further offshore, became even wider in shape, and its salinity increased (Figure 2.4c). The plume widened because the Ekman velocity was faster on the offshore side of the plume than on the coastal side, causing the plume to spread laterally (Fong and Geyer, 2001; Chant, 2011). Stratification, although weak in their model, persisted for a short period as the plume was transported offshore. Mixing occurred at the edge of the plume and caused horizontal stratification. However, because upwelling occurred, the net Ekman transport of bottom waters was towards the shore and the isohalines bent, maintaining vertical stratification as the plume moved offshore (Fong and Geyer, 2001; Chant, 2011).

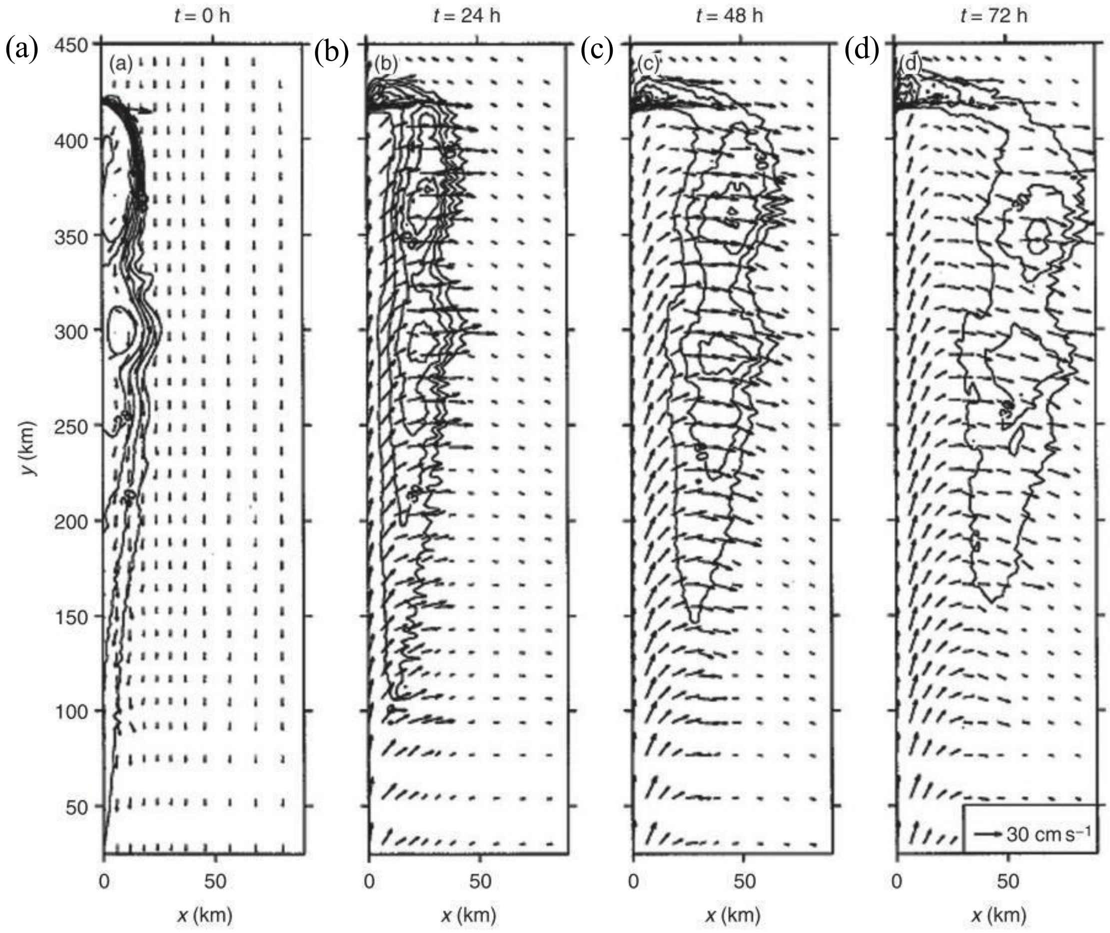

Figure 2.4: Surface salinity of a river plume, contours represent 1 PSUintervals, under forcing from a moderate upwelling wind. (a) Initial plume structure after 1 month of discharge with no winds. (b)-(d) represents the plume structure after wind forcing for 24, 48 and 72 hours, respectively. The discharge is steady at 1500 m^3 s^{-1} *and an ambient southward current (from top to bottom in the plots) is introduced at y=450 km. Surface current velocity is represented by the vector arrows. Originally published in Fong and Geyer (2001).*

Coastal downwelling occurs when winds blow from sea to land, or parallel to the coastline with the coast on the right-hand side in the Northern Hemisphere, causing Ekman transport to move surface waters toward the shore. The response of river plumes to downwelling-favorable winds is also consistent with convergence against the shore. A buoyant plume is pushed up against the coastline and narrows, resulting in the plume thickening (Fong and Geyer, 2001). If the plume becomes thick enough, it may even transition from a surface-advected plume to a bottom-attached plume (Yankovsky and Chapman, 1998; Chant, 2011). Because vertical salt flux requires stratification, it will likely be greatly diminished once the plume is attached to the bottom. However, as the plume is attached to the bottom, there will likely be significant turbulent mixing and resuspension of sediments (Chant, 2011).

The response of a river plume to cross-shore winds has not been well studied, despite the fact that it is very likely to modify the structure and extent of a plume, through the generation of surface waves (Fewings et al., 2008; Chant, 2011). Wind originating from the coast produces similar results to Ekman upwelling in that the surface waters move offshore resulting in coastal surface waters being replaced by upwelled bottom waters (Fewings et al., 2008; Jurisa and Chant, 2013). Similarly, in onshore wind conditions, the plume and surface waters will be pushed up against the shore, and the lower water column will move offshore, similar to the conditions during Ekman downwelling (Fewings et al., 2008).

As wind acts on the ocean surface, surface waves are inevitably generated. The crosswind processes described above in Fewings et al. (2008) were observed under small-wave conditions. When winds were strong enough to produce large waves, onshore winds induced the entire water column to move in an onshore direction increasing the height of the sea level. In offshore winds, the transport direction remained the same as under small waves, but the velocity of transport increased (Fewings et al., 2008). The influence of waves from along-shore winds was less significant as the net transport of water was either towards or away from the coast. However, wave breaking generates intense turbulent mixing at the surface. The impact of wave mixing on a plume depends on the wave height; plumes might only be strongly influenced by breaking waves when the wave height is similar to the plume's thickness (Horner-Devine et al., 2015). Work conducted by Gerbi et al., (2013) showed that when wave breaking is included in a model, the plume will react by narrowing, thickening, and propagating offshore slower than a plume with no wave breaking in upwelling conditions. They also found that the vertical salinity gradient of the plume was smaller and/or more homogeneous when wave breaking was included.

2.3.2 Tidal influence

As with wind in the previous section, the influence of tides on buoyant river plumes is often omitted from models investigating how river plumes act along the coast and was entirely omitted in Garvine's (1995) classification scheme. Tidal processes mostly influence the near-field and source region of a river plume, linking them closely with estuarine dynamics and processes (Halverson and Pawlowicz, 2008). The interaction between river discharge and tidal mixing determines the type of estuary that is present, which in turn influences the salinity of plume that is discharged and transported along the coast. When the tidal influence is low and the river discharge is dominant, a highly stratified estuary will form, depositing water of lower initial salinity into the coastal ocean. The less dense freshwater discharge flows over the top of the denser ocean water to form what is known as a salt wedge (Figure 2.5a) (Brown, 2002). The salt wedge penetrates further into the estuary when the river discharge is low and retreats to the ocean when the discharge is high (Brown, 2002).

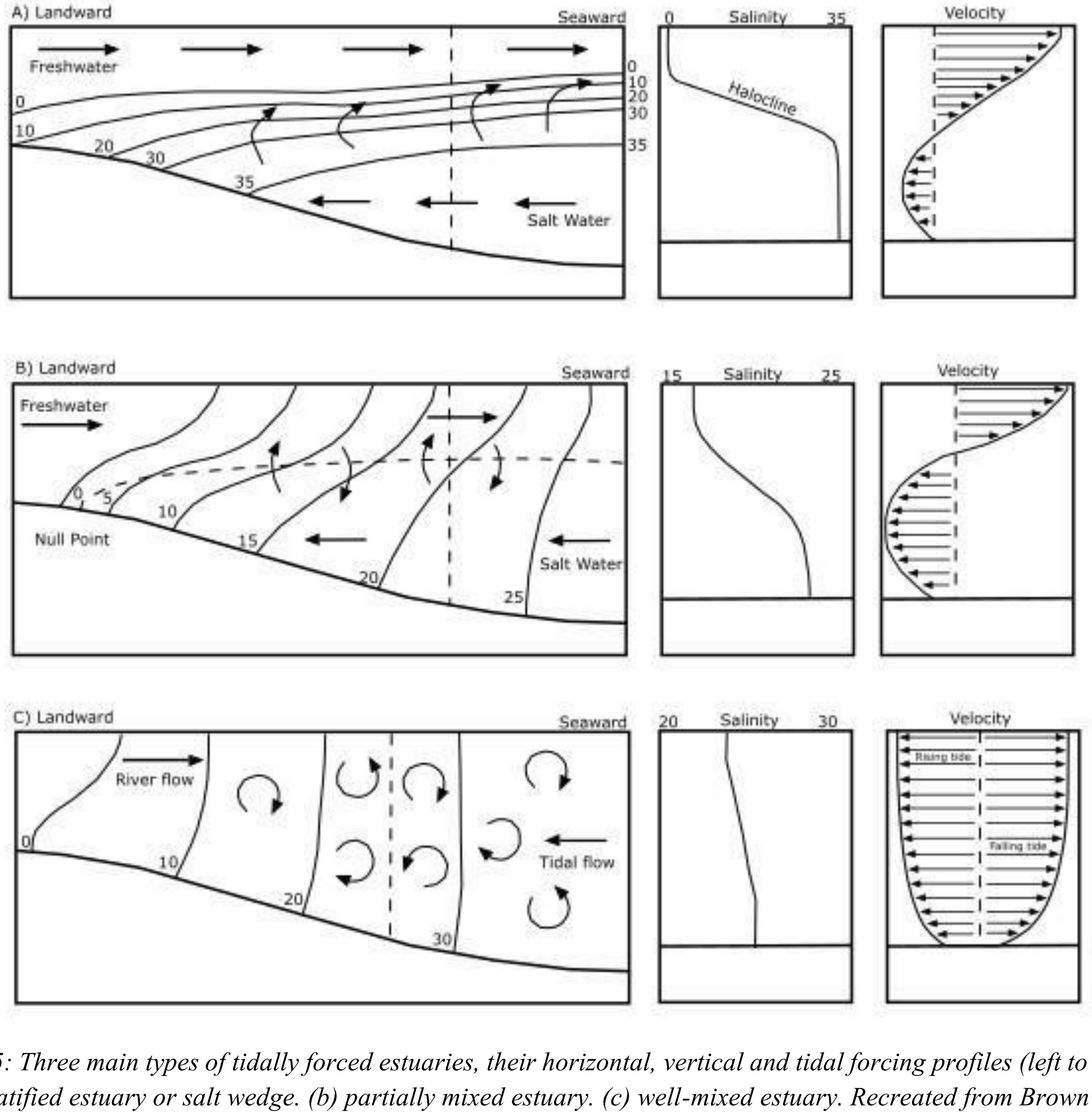

Figure 2.5: Three main types of tidally forced estuaries, their horizontal, vertical and tidal forcing profiles (left to right). (a) highly-stratified estuary or salt wedge. (b) partially mixed estuary. (c) well-mixed estuary. Recreated from Brown (2002).

In areas with larger tidal ranges, estuaries are usually weakly stratified or sometimes well mixed (Brown, 2002). The surface height of the water rises and falls with the flood and ebb of the tide, and the friction between the water and estuary bottom creates turbulence that mixes the water more easily than the entrainment of salt alone. In a partially mixed water column, the stratification is weak, and the isohalines are more steeply inclined (Figure 2.5b) (Brown, 2002). When tidal influence increases even further, a well-mixed estuary is established (Figure 2.5c) (Brown, 2002). The salinity within the estuary varies with the state of the tide, with it being fresher during the ebb and a higher salinity as the ocean water entrains during the flood. The tide can sometimes be so strong during a flood that it forces a plume back down the estuary and creates a tidal intrusion front in the shape of a V, severely limiting the extent of freshwater in the coastal ocean (Brown, 2002). Finally, because tides also vary on a bi-weekly scale between spring and neap, the estuary type can fluctuate on this timescale. During the stronger spring tide, more mixing occurs from turbulence and breaks down the stratification. When a weaker neap tide occurs, stratification can be strengthened, and sometimes a temporary salt wedge can be established, resulting in the export of more freshwater offshore (Brown, 2002). An example of the effect of a neap tide is the Strait of Georgia, Canada, where the expansion of freshwater was greatest during the neap tide, when mixing was lowest (Griffin and Leblond, 1990).

An example of how tidal mixing can vary between two estuaries and affect the extent and structure of a plume can be found in a recent study by Osadchiev et al. (2020). The study compared the spatial scales of plumes from the Yenisei and Khatanga Rivers. Osadchiev et al. (2020) found that the two river plumes had similar spatial extents, despite the Yenisei's discharge being larger by one order of magnitude, because of the differences in the tidal mixing conditions. The Yenisei, which is the larger river, estuary experiences relatively low tidal velocity (maximum of 24.2 cm s^{-1}) and therefore was subject to less mixing. The low tidal forcing and high discharge resulted in more freshwater retention and a highly stratified plume with an average thickness of approximately 12 m, extending 450-500 km offshore from the mouth of the river (Figure 2.6a) (Osadchiev et al., 2020). On the other hand, the Khatanga estuary experiences a large tidal forcing (maximum of 80–100 cm s^{-1}) in the inner estuary, resulting in significant surface-to-bottom tidal mixing. The Khatanga plume is much more well-mixed, less freshwater is retained on the surface, and its vertical structure is similar to that of a partially mixed plume (Figure 2.5b). Despite intense mixing, river discharge was still large enough to create a very small surface layer that propagated into the ocean and could be found 400–500 km from the mouth of the river, although it was extremely diluted (Figure 2.6b) (Osadchiev et al., 2020).

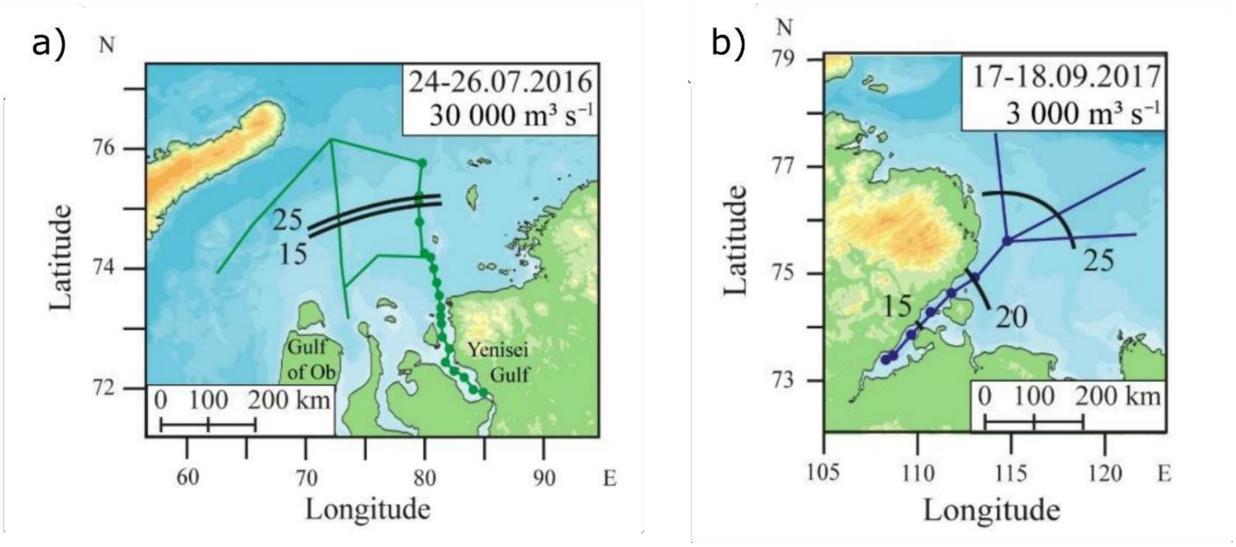

Figure 2.6: Spatial extent of the Yenisei (a) and Khatanga (b) rivers with the locations of isohalines 15, 20 and 25 at the surface of the water column. Originally published in Osadchiev et al., (2020).

2.3.3 Variations in river discharge

The discharge of a river sets the initial conditions for a buoyant plume. Its volume and velocity can significantly affect how a plume enters the surrounding ocean (Horner-Devine et al., 2015). As discussed in Section 2.1, a high-velocity plume will immediately become surface advected, whereas lower-velocity plumes will likely remain bottom-attached. The discharge of a river is also not constant as most of the world's rivers have a seasonal cycle; for example, the Amazon River peaks in May-June, the Orinoco River peaks in August, and Arctic rivers such as the Yenisei and the Lena River peak in June (Dai and Trenberth, 2002). The June peak of Arctic rivers is related to the importance of snowmelt in augmenting river discharge. On a continental scale, the peak of river discharge into the Arctic Ocean is in June, whereas the peak of river discharge into the Indian Ocean, which is less affected by snowmelt, is in August (Dai and Trenberth, 2002). A study conducted on the world's largest 16 rivers found that, generally, as the discharges increased, so did the area of the associated river plume (Kang et al., 2013). However, the linear relationship was weak for 15 of the rivers, implying the influence of other factors, such as winds or tides (Kang et al., 2013). An exception to this trend was observed in under-ice conditions; Ingram and Larouche (1987) found a strong linear relationship between increasing discharge and plume area beneath landfast ice, likely due to the suppression of wind-driven mixing and the more constrained lateral spread of the plume. The influence of ice on river plumes will be explored further in section 2.3.4.

The discharge of a river can vary on short timescales owing to external forcing, such as rainfall increasing discharge or tidal action, arresting the flow of water and temporarily reducing discharge. This variation in discharge can significantly impact the structure of a plume (Yuan et al., 2018). When the discharge is low, the plume bulge extends mainly in the alongshore direction, reattaching to the coast at a shallower incidence (attachment) angle (Figure 2.7a). Typically, when the discharge is high, the plume forms a large bulge that spreads mainly in the offshore direction before reattaching to the coast on the downstream side. This is known as a circular plume (Figure 2.7b) (Avicola and Huq, 2003; Horner-Devine et al., 2006; Rogowski et al., 2014; Yuan et al., 2018). If the incidence angle is less than 0, the plume bulge becomes unstable and detaches from the coastline (Yankovsky et al., 2001).

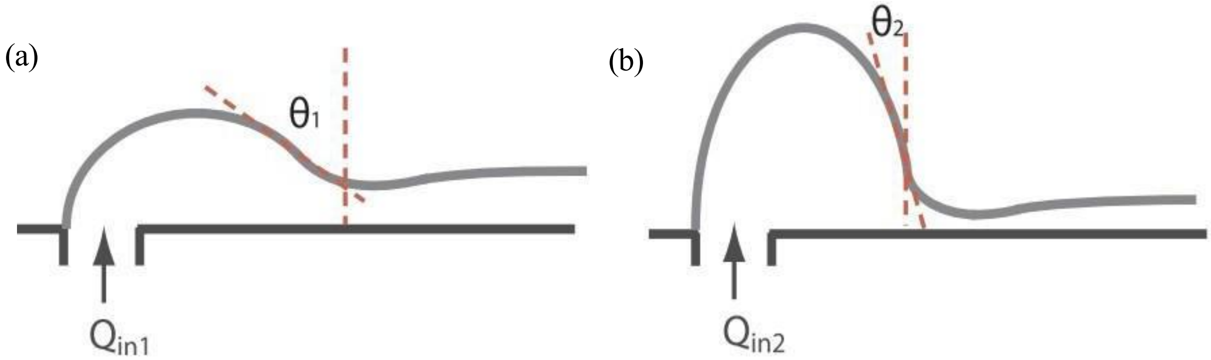

Figure 2.7: Diagram of a (a) compressed plume structure with a high incidence angle (θ) and a low discharge (Qin1). (b) rotational plume structure with a shallow incidence angle from greater discharge (Qin2). Originally published in Yuan et al., 2018).

A larger and more circular bulge retains more freshwater in front of the river mouth and prevents its distribution down the coast. Conversely, when the bulge is smaller and elongated, more freshwater is transported into the coastal current and down the coast (Fong and Geyer, 2002). This indicates that the distance from the coast to the center of the bulge is critical to the distribution of freshwater along the coast, similar to how an eddy current interacts with a coastal wall (Nof, 1988; Chant, 2011). Fong and Geyer (2002) suggested that an outflow Rossby number (Ro) is the main control on how far the center of the bulge will travel. Ro is a dimensionless parameter that compares the inertial force of the river outflow to the Coriolis force, defined as

$$Ro = \frac{u_r}{fL_r}$$

where ur is the discharge velocity, f is the Coriolis effect and Lr is the width of the estuary. It differs from the Rossby radius of deformation, which is a length scale representing how far a buoyancy-driven disturbance can travel before being deflected by Earth's rotation. The simulations found that when the Rossby number was small (0.01), approximately 80% of the freshwater was transported along the coast. When the Rossby number was larger (4), only 30% of the freshwater was distributed into the coastal current (Fong and Geyer, 2002). Further analysis of their results suggests that wide outflows tend to form coastal currents, and narrow outflows create circulating bulges. This is because the distance the bulge spreads across the shore is controlled by ur/f and the alongshore distance of the bulge is controlled by Lr. In addition, the Froude number has been identified as important for bulge formation, as a bottom-attached plume is unlikely to form a bulge (Horner-Devine et al., 2006).

The impact of damming a river should not be ignored as a factor influencing plume shape, size, and impact on coastal environments, as the construction of dams can influence the total amount of discharge and water quality (Hu et al., 2008; Yan et al., 2010; Gain and Giupponi, 2014). For example, the Colorado River, prior to the construction of the Hoover Dam, would likely have induced brackish conditions from the river mouth to the Upper Gulf of California (Carbajal et al., 1997). Since the development of the Hoover Dam, the discharge has been all but eliminated, creating an inverse estuary with evaporation rates exceeding the inflow of freshwater (Lavín et al., 1998). Damming a river and regulating flow can also change seasonal discharge patterns and impact the environment downstream, such as the Three Gorges Dam. The discharge of the Yangtze River is now the highest during the dry winter period (January-March) and decreases during the rainy season (June-August) (Cheng et al., 2018). Not only has the discharge regime been altered, but the Three Gorges Dam has also significantly altered the hydrological and ecological dynamics of the Yangtze River basin. The altered seasonal discharge has changed aquatic habitats that are critical for fish, including the four major species of carp that reside in the river (Cheng et al., 2018). The reduced and irregular flow rates have been shown to disrupt the spawning behavior of carp species, and the number of eggs is significantly reduced (Cheng et al., 2018).

2.3.4 The influence of ice

The majority of research on river plumes has been conducted in open water conditions, and very few researchers have investigated how the presence of ice might affect a plume's structure, extent and dynamics. A few observational studies in high-latitude settings have shown that in ice-covered conditions, a river plume can extend much further than in open-water conditions for a similar amount of discharge (Ingram, 1981; Freeman, 1982; Ingram and Larouche, 1987). An observational study conducted by Ingram (1981) on the Great Whale River in eastern Hudson Bay confirmed this trend by comparing the river plume conditions in open water and ice-covered conditions. During the summer, the plume was observed to have an area of 100 km^2 and an average thickness of 1-2 m. During ice-covered conditions, the plume was much thicker and larger in extent despite reduced freshwater input. This is thought to have been a result of the ice acting as a shield and reducing the influence of direct wind and wave mixing (Ingram, 1981). The increase in the under-ice plume extent has also been shown in a numerical model by Kasper and Weingartner (2015). The model had a decreasing river discharge over 30 days, with a peak of 6000 m^3 s^{-1} in the first 10 days, and simulated ice-free, partial ice cover, and full ice-covered conditions. After 10 days, the plumes were similar in coastal alongshore extent. However, the plume extended approximately 20 km further offshore by day 10 in fully ice-covered conditions compared to ice-free and partial cover conditions. After 30 days, the plume extent doubled under ice-covered conditions compared to ice-free conditions. The plume structure also varied. Under ice-free conditions, an anticyclonic bulge formed almost immediately before the plume was transported down the coast; after 30 days, a second smaller anticyclonic bulge formed, slowing the transport of freshwater down the coast. In ice-covered conditions, there was just one large bulge that formed and extended both down the coast and offshore.

The presence of rough ice can also arrest the offshore or alongshore advancement of the plume, as under-ice topography has been shown to trap freshwater in the coastal zone (Macdonald and Carmack, 1991; Macdonald et al., 1995; Kuzyk et al., 2008). Ice morphology can be split into three regions (Reimnitz et al., 1978; Barnes et al., 1987). The first is landfast ice, which exists along the coastline and is characterized by generally flat, smooth, and immobile ice. The deeper waters offshore are where mobile pack ice forms, creating the second region. The third region is where mobile ice and landfast ice collide. The result of the collision of mobile ice and landfast ice is a region of mechanically deformed ice composed of rubble ice and pressure ridges. This rubble zone has been referred to as the Stamukhi zone (cf., Macdonald and Carmack, 1991). Here, the ice can reach heights of over 10 m above the surface of the landfast ice, and the subsequent supporting structure under the ice can also be very large, and in some cases grounding out between 20 and 50 m (Weeks, 2010). In Canada, such a structure exists on the southern Beaufort Sea shelf during winter, and it halts the offshore advancement of the buoyant river plume from the Mackenzie River. The buoyant freshwater from the river pools behind the ‘wall’ of the Stamukhi in the coastal zone which prevents the immediate dilution of the surrounding coastal water (Figure 2.8). Under-ice plumes can also be limited to landfast ice areas that lack a Stamukhi zone. For example, it has been suggested that, as downwelling inducing wind action can be transferred to the water column through forcing of the mobile pack ice thereby allowing onshore winds to push a plume up against the shore (Schulze and Pickart, 2012).

Interestingly, offshore of the Stamukhi zone, salinity also increases as the continued ice formation introduces brine to the water column (Macdonald and Carmack, 1991). Especially when the wind blows from the shore and push ice floes offshore, an open water or new ice area can form known as flaw-lead polynya (e.g., Bruneau et al., 2021). These polynyas are hotspots for the vertical mixing of fresh surface water and the underlying saltwater layer, preventing river plumes from spreading past the ice edge (Messier, 2002). Vertical mixing is enhanced in polynyas as the lack of sea ice exposes the surface to wind forcing and heat loss into the atmosphere, which in turn drive convective overturning (Muench et al., 2001; Winsor and Björk, 2000; Morales Maqueda et al., 2004). These processes enhance vertical mixing, break down stratification and mix buoyant freshwater with the saline layer below, limiting the offshore spread of surface plumes.

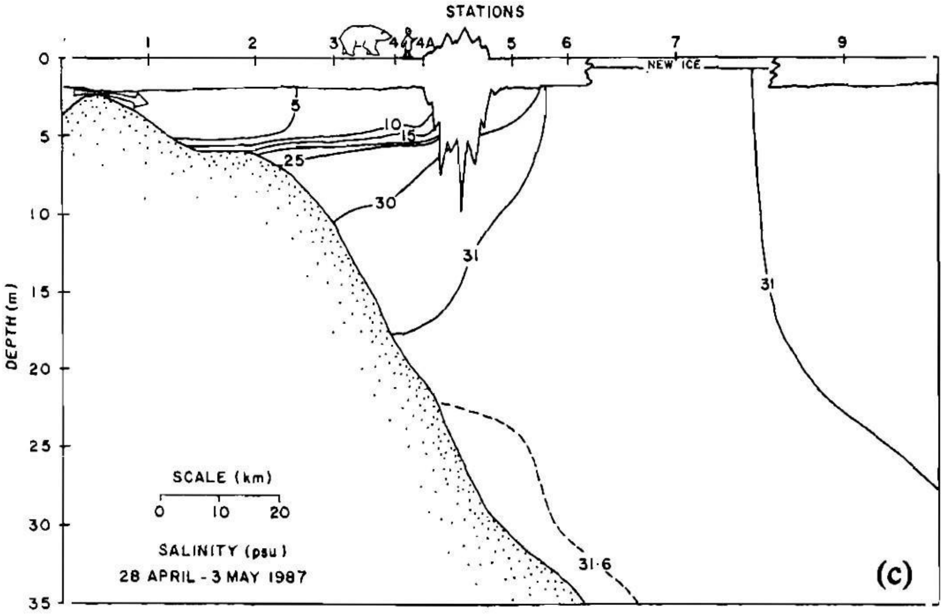

Figure 2.8: Section of under-ice salinity from the 28th April- 3rd May in 1987 with a large Stamukhi zone. Originally published in Macdonald and Carmack (1991).

2.4 Study area

2.4.1 Hudson Bay, James Bay and the La Grande River under-ice plume

The work for this thesis was conducted on the northeast coast of James Bay, an embayment in the southern part of the Hudson Bay marine region. Hudson Bay is host to forty coastal communities in total, with four of them situated on the east coast of James Bay (Figure 2.9). All of these coastal communities rely heavily on the coastal zone for food, culture and identity, mobility, and livelihoods (Kuzyk and Candlish, 2019). The four coastal communities in eastern James Bay (Chisasibi, Wemindji, Eastmain, and Waskaganish) have been particularly impacted by the widespread loss, since the late 1990s, of eelgrass (*Zostera marina*) meadows along the coast (cf., Leblanc et al., 2023).

Hudson Bay and James Bay are located at the southern limit of the Arctic and are considered a subarctic region. However, the region experiences a climate and sea-ice cycle similar to those of coastal shelves in the Arctic Ocean (Hochhiem and Barber, 2010; Andrews et al., 2018). Hudson Bay is the largest body of water in the world that experiences ice cover during the winter and then becomes ice-free during the summer (Prinsenberg 1980). The overall freeze-up period for Hudson and James Bay begins in early November, with the ice beginning to break up in late May to early June (Taha et al., 2019). With surface air temperatures rising by approximately 0.26–0.30°C per decade since the 1960s (Hochhiem and Barber, 2010), the overall sea ice extent has shown a clear trend toward earlier break-up and delayed freeze-up in recent decades, with ice-free seasons increasing by up to 0.9 days per year (Kowal et al., 2017). The landfast ice has exhibited contrasting changes across the region; western Hudson Bay and James Bay have shown a trend of delayed freeze-up and earlier breakup, resulting in a shorter ice season. However, the eastern sector of Hudson Bay has seen slightly prolonged ice persistence due to the coastal morphology and ice stability (Gupta et al., 2022). Ice breakup dates and sea surface temperatures in eastern James Bay underwent a step change in 1998 signaled by increased variability and longer, more intense temperature extremes called marine heat waves (MHWs) (Bruneau et al., 2025). After only two MHW events between 1982 and 1997, five events occurred in 1998 and four or more in each of 2001, 2005, 2010, 2012. Events in May and October 2021 lasted over a month in duration, with the former reaching intensities of between 2.5 and 3°C (Bruneau et al., 2025).

The water enters (and exits) Hudson Bay through Foxe Basin and Hudson Strait and then flows in a cyclonic direction (Prinsenberg, 1982; Rindenour et al., 2019). The water circulates down into James Bay from the western coast and then exits along the east coast. The circulation in Hudson and James Bay is found to change seasonally, with weak anticyclonic circulation occurring in the spring and summer near the mouth of James Bay in eastern Hudson Bay (Rindenour et al., 2019). More details on the circulation and ice patterns for James Bay are provided in the study area sections of Chapters 3-5.

Figure 2.9: Location of the communities near or on the coast of Hudson Bay with the four coastal communities of East James Bay and Sanikiluaq highlighted in red. Modified from Kuzyk and Candlish (2019).

The drainage basin of Hudson Bay covers an area of 3.1 x 10^6 km^2 and is the largest drainage system in Canada, consisting of a large number of rivers. Rivers that discharge into Hudson Bay have relatively low discharge rates compared to larger rivers in the Mackenzie and Siberian drainage basins (Dery et al., 2005). For example, the annual discharge rate of the Nelson River in western Hudson Bay is only 2219 m^3 s^{-1} whereas the Yenisei, Lena, Ob, and Mackenzie Rivers have an average annual discharge between 9,800 and 19,500 m^3 s^{-1} (Table 1.1) (Shiklomano et al., 2021). Despite the low discharge rates, the Hudson Bay drainage system accounts for 18% (23,940 m^3 s^{-1}) of the total continental freshwater input to the Arctic and subarctic seas (~133,000 m^3 s^{-1}), a contribution greater than that of any single river basin in Eurasia or North America (Shiklomanov et al., 2000). Furthermore, the peak winter discharge from the regulated La Grande River in northeastern James Bay of 5000-6000 m^3 s^{-1} is among the largest winter discharges in the circumpolar north (Table 1.1).

James Bay, the southern subset of Hudson Bay, is around 150 km wide and 400 km long with an average depth of 28 m but has a drainage basin of 0.68 x 106 km^2 and receives a mean annual discharge of 10,100 m^3 s^{-1}. The runoff into James Bay makes up around 40% of the total runoff of the Hudson Bay/James Bay system. The large river discharge and relative proximity to industrial activity in central Canada make southern Hudson Bay and James Bay prime locations for hydroelectric development. During the late 1970s and the 1980s, major rivers such as the Nelson and the La Grande underwent large-scale hydroelectric developments that significantly modified the discharge of both rivers. The La Grande River previously had the second largest discharge into Hudson Bay; however, after development, its mean annual discharge roughly doubled to 3780 m^3 s^{-1} and it became the river with the largest discharge (Dery et al. 2005; de Melo et al., 2022).

The La Grande hydroelectric complex was built in several stages to address the increasing electricity demand from the Québec province of Canada. The development effectively doubled the size of the La Grande drainage basin to over 200,000 km^2 (Roy and Messier, 1989). One of the major developments that occurred in the early 1980s saw the diversion of flows from the Eastmain, Opinaca, and Caniapiscau rivers into the La Grande Complex. The diversion reduced the discharge of the Eastmain River by 79% (Prinsenberg 1980) and transferred 45% of the Caniapiscau River discharge from eastern Hudson Strait to eastern James Bay (Roy and Messier, 1989). Further expansion of the complex came with the Rupert River diversion, completed in 2012, during which approximately 53% of the Rupert River's flow was redirected westward toward the La Grande system (de Melo et al., 2022). Prior to development, the peak discharge from the La Grande River occurred in June and the minimum discharge occurred in March

(Dery et al. 2005). After the developments, the peak discharge shifted to the winter months, with an average winter discharge of 4500 m^3 s^{-1} and peaks exceeding 5000 m^3 s^{-1} (Messier 2002; de Melo et al., 2022).

With the highest discharge now occurring in the ice-covered season, the La Grande River (LGR) plume is, in winter, much larger than before development. The initial surface area covered by the center of the plume (salinity ≤ 5) before any flow augmentation or regulation was estimated at about 200 km^2 based on observations collected in winter 1976 (Ingram and Larouche, 1987). Ingram and Larouche (1987) also characterized the freshwater plume of the LGR both in the offshore and downcoast directions in February 1984, when the discharge rates were about six times the winter 1976 rate, with a mean of about 2560 m^3 s^{-1}. They found that the plume extended 70 km north of the La Grande River mouth during the winter, with an observed area of reduced salinity roughly 20 km wide along the coast.)

A more recent study by Messier (2002) characterized the extent of the La Grande River plume in 1987, 1989, 1993, and 1995, although the data for 1987 and 1989 were combined. During 1987 and 1989, the discharge values varied between 3700 and 4000 m^3 s^{-1}, and the area of the plume as defined by the 10 PSU isohaline extended to 1600 km^2, while the area enclosed by the 5 PSU isohaline reached 1200 km^2. The center of the plume (salinity ≤ 5 PSU) extended from 35 km south of the mouth to 30 km north of the mouth. The outer edge of the plume (salinity of 20) extended 60 km south and 50 km north of the mouth (Messier, 2002). In 1993, the discharge was 4600 m^3 $s^{-1}$and the plume covered an area between 3200 and 3500 km^2, with the center covering 1637 km^2. In 1995, the discharge was 4400 m^3 s^{-1}, and the area of the plume varied from 2100 to 2800 km^2, with the center covering a maximum area of 1600 km2 (Messier 2002).

One of the earliest sets of measurements of the LGR plume was conducted by Freeman (1982), who described its structure as well as its spatial extent, and divided it into three distinct sections. The first 5 to 10 km describes the first section with a thinning of the halocline and a reduction in flow speed. In the second section, the next 25 to 30 km offshore, thinning continues and a frontal zone is created where the horizontal salinity gradients are at a maximum. In the third section, mixing is substantially increased, and the water column becomes more homogenous. The structure and extent of the LGR under-ice plume in the 1980s and the 1990s is further discussed in Chapters 3-5.

2.4.2 Status of eelgrass on the northeast coast of James Bay

Eelgrass (*Zostera marina*) is a marine flowering plant that is the most distributed seagrass species in the Northern hemisphere, found in tropical, temperate, subarctic and Arctic regions. Existing in different climates means eelgrass can survive in a variety of growing conditions, including under sea ice (McRoy 1969). Eelgrass provides a critical habitat for marine wildlife and waterfowl, and reliable, nearshore wildlife harvesting opportunities for many Indigenous Peoples (Unsworth and Butterworth, 2021; Murphy et al., 2021). However, like other seagrasses, eelgrass has declined in many locations during the past century and, in spite of restoration efforts, rarely recovered to its original state (Dunic et al., 2021). A limited understanding of environmental variation and change in coastal habitats is among the factors believed to be holding back successful eelgrass management and restoration efforts (Turschwell et al., 2021).

Environmental factors affecting eelgrass health include light, nutrients, salinity, temperature, physical disturbances such as ice scour, and suitability of sediment substrate (Figure 2.10). Eelgrass typically grows in sandy mud substrates and requires clear water to receive sufficient light for photosynthesis to thrive (McRoy 1969, Hemminga and Duarte 2000). Although eelgrass can survive a wide range of oceanographic conditions, there are some thresholds that can impact eelgrass survival. For example, eelgrass experiences higher mortality at temperatures above 25°C, with the optimal range for growth being 10–25°C (Nejrup and Pedersen, 2008) (Figure 2.10). The optimal salinity for eelgrass growth is >15 PSU, but it can also withstand a range of salinities and can survive short periods of low salinity (<5 PSU). However, at low salinity, seed germination and shoot survival rates were reduced (Nejrup and Pedersen 2008; Salo et al., 2014) (Figure 2.10). Nutrient availability also plays a crucial role in eelgrass growth. Typically, eelgrass requires a nitrate to phosphate ratio of 24:1 for optimal growth (Durate, 1990) (Figure 2.10). If the nutrient levels are too low, growth can be restricted. On the other hand, excessive nutrient enrichment and eutrophication of coastal waters can lead to light limitation and an overgrowth of algae (Hauxwell et al. 2003; Schmidt et al. 2012). For eelgrass beds in subarctic and Arctic areas, ice cover can affect eelgrass as it not only reduces light availability but can also damage eelgrass beds through scouring (Robertson and Mann 1984; Moksnes et al., 2018). Eelgrass has a higher light requirement for growth than macroalgae and phytoplankton, requiring a minimum of 11% to 29.4% surface irradiance (Lee et al., 2007) (Figure 2.10).

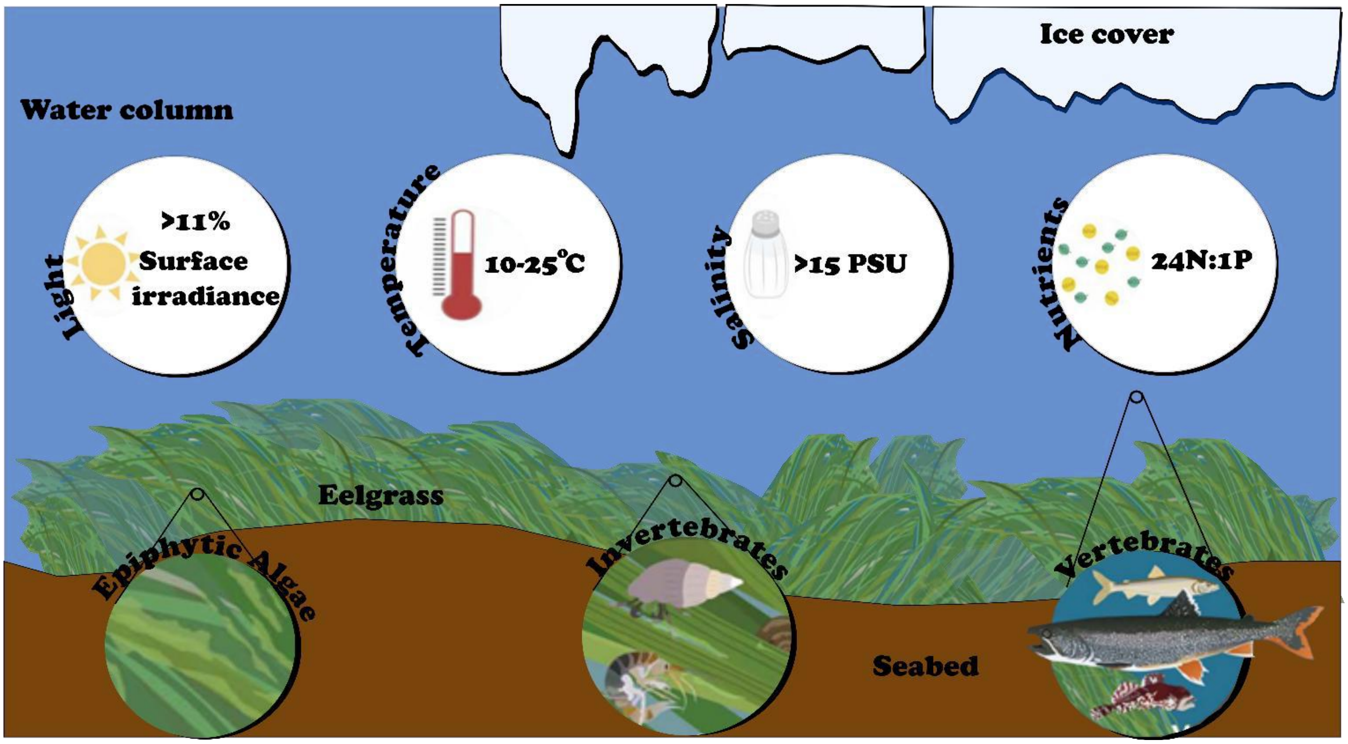

Figure 2.10: Stylized eelgrass habitat on the North East coast of James Bay with the optimal light, temperature, salinity and nutrient contents for eelgrass growth. Modified from Leblanc et al., (2023a) originally by Align Illustration.

As previously mentioned, the northeast coast of James Bay was host to extensive eelgrass beds prior to a massive decline in the late 1990s, from which it has been slow to recover (Leblanc et al., 2023b). Shoots measured over 2017-2021 were ≤1 m, compared to 2 m or more in the 1980s and early 1990s (Lalumière et al., 1994), and the surviving eelgrass beds occupy a narrower and shallower water depth range (~0.5-2.5 m compared to ~0.5-4 m before the decline). Quantitative data and eelgrass cover classifications from eelgrass surveys conducted from 1982 onwards were compiled and synthesized by Leblanc et al. (2023b). They showed that between 1996 and 2019, the number of sites with eelgrass cover greater than 50% declined by 40%, and aboveground biomass dropped by approximately 80% from 185.3 ± 13.3 g dry weight m^{-2} in 1995 to just 35.9 ± 3.3 g dry weight m^{-2} in 2019 (Leblanc et al., 2023b). As of 2023, only partial and localized regrowth has been documented, with eelgrass density and biomass remaining well below historical levels in most locations (Leblanc et al., 2023b). In some areas, eelgrass was also found to be shorter, discolored, and patchy, indicating ongoing stress or incomplete recovery.

In view of the region's long period of seasonal sea-ice cover, the eelgrass likely has a strong seasonal growth regime, similar to that described for other eelgrass populations found under ice. The eelgrass starts to grow quickly from late May to mid-June as the ice begins to melt and daylight hours increase, allowing more light to penetrate the water column for photosynthesis (McRoy 1969; Davis et al., 2024). The eelgrass then likely reaches its maximum biomass in the summer months (Lalumière et al. 1994). The rapid increase in biomass during the summer is critical to the plants' survival as the eelgrass will build and store carbohydrates in their roots and rhizomes, which are vital for the plants' growth and survival during winter (McRoy 1969).

Eelgrass meadows in James Bay play a vital ecological role, supporting a diverse range of epiphytes, benthic/epibenthic organisms, and several species of fish (Lalumière, 1988) (Figure 2.10). Moreover, these mature and productive eelgrass ecosystems serve as crucial migration stopover spots for Canadian geese (*Branta canadensis*) and Atlantic brants (*Branta bernicla hrota*). In the 1970s and the 1980s, large numbers of geese, exceeding 10,000, congregated in shallow embayments with extensive eelgrass meadows (Curtis 1976; Reed et al. 1996). For Cree First Nation hunters, this presented an opportunity to secure food and practice traditional activities, as they organized their hunting around the geese's use of eelgrass beds during low tide (Idrobo et al., 2024).

In response to the loss and slow recovery of eelgrass in northeast James Bay (Dickey, 2015, Leblanc et al., 2023) and a decline in migratory waterfowl, particularly Canada geese (*Branta canadensis*), a large multidisciplinary research program called the Eeyou Coastal Habitat Comprehensive Research Program (CHCRP) was launched in 2017 with the aim of improving our understanding of the ecology of eelgrass and characteristics of the coastal habitat that impact eelgrass health (see https://www.eeyoucoastalhabitat.ca/ for more information). This PhD research contributed to this overall project. The coastal Cree First Nations were partners throughout the project and provided input to study design, execution, and interpretation of results (Fink-Mercier et al., 2024). The field work was facilitated by Cree Land Users, who provided expertise about the coastal habitat and the ways it has changed over time, including eelgrass distribution, ice, and water quality. The Eeyou Istchee territory is organized into land management units, called traplines, for use by designated groups of individuals or families. The mooring sites use the traplines on which they were located for the name scheme.

2.5 References

Andrews, J., Babb, D., Barber, D.G., 2018. Climate change and sea ice: Shipping in Hudson Bay, Hudson Strait, and Foxe Basin (1980–2016). Elementa: Science of the Anthropocene 6, 19. https://doi.org/10.1525/elementa.281

Androulidakis, Y.S., Kourafalou, V.H., Schiller, R.V., 2015. Process studies on the evolution of the Mississippi River plume: Impact of topography, wind and discharge conditions. Continental Shelf Research 107, 33–49. https://doi.org/10.1016/j.csr.2015.07.014

Armi, L., Farmer, D.M., 1986. Maximal two-layer exchange through a contraction with barotropic net flow. Journal of Fluid Mechanics 164, 27–51. https://doi.org/10.1017/S0022112086002458

Avicola, G., Huq, P., 2003. The characteristics of the recirculating bulge region in coastal buoyant outflows. Journal of Marine Research 61(4), 435–463.

Avicola, G., Huq, P., 2002. Scaling analysis for the interaction between a buoyant coastal current and the continental shelf: experiments and observations. Journal of Physical Oceanography 32(11), 3233–3248. https://doi.org/10.1175/1520-0485(2002)032<3233:SAFTIB>2.0.CO;

Barnes, P.W., Asbury, J.L., Rearic, D.M., Ross, C.R., 1987. Ice erosion of a sea-floor knickpoint at the inner edge of the stamukhi zone, Beaufort Sea, Alaska. Marine Geology 76, 207–222. https://doi.org/10.1016/0025-3227(87)90030-2

Branch, R.A., Horner-Devine, A.R., Kumar, N., Poggioli, A.R., 2020. River Plume Liftoff Dynamics and Surface Expressions. Water Resources Research 56, e2019WR026475. https://doi.org/10.1029/2019WR026475

Brown, 2002. Open University oceanography series. Pergamon/Butterworth Heinemann, Oxford.

Bruneau, J., Babb, D., Chan, W., Kirillov, S., Ehn, J., Hanesiak, J., Barber, D.G., 2021. The ice factory of Hudson Bay: Spatiotemporal variability of the Kivalliq Polynya. Elementa: Science of the Anthropocene 9, 00168. https://doi.org/10.1525/elementa.2020.00168

Bruneau, J.A., Ehn, J.K., Kuzyk, Z.Z.A., Crawford, A.D., Leblanc, M.L., 2025. Step change in sea surface temperatures brings marine heat waves to sub-Arctic James Bay, Canada. Frontiers in Marine Science 12, 1549329. https://doi.org/10.3389/fmars.2025.1549329

Carbajal, N., Souza, A., Durazo, R., 1997. A numerical study of the ex-ROFI of the Colorado River. Journal of Marine Systems 12, 17–33. https://doi.org/10.1016/S0924-7963(96)00086-3

Carmack, E., Winsor, P., Williams, W., 2015. The contiguous panarctic Riverine Coastal Domain: A unifying concept. Progress in Oceanography, Overarching perspectives of contemporary and future ecosystems in the Arctic Ocean 139, 13–23. https://doi.org/10.1016/j.pocean.2015.07.014

Carmack, E.C., 2000. The Arctic Ocean's Freshwater Budget: Sources, Storage and Export, in: Lewis, E.L., Jones, E.P., Lemke, P., Prowse, T.D., Wadhams, P. (Eds.), The Freshwater Budget of the Arctic Ocean. Springer Netherlands, Dordrecht, pp. 91–126. https://doi.org/10.1007/978-94-011-4132-1_5

Chant, R.J., 2011. 2.11 - Interactions between Estuaries and Coasts: River Plumes – Their Formation, Transport, and Dispersal, in: Wolanski, E., McLusky, D. (Eds.), Treatise on Estuarine and Coastal Science. Academic Press, Waltham, pp. 213–235. https://doi.org/10.1016/B978-0-12-374711-2.00209-6

Chant, R.J., Glenn, S.M., Hunter, E., Kohut, J., Chen, R.F., Houghton, R.W., Bosch, J., Schofield, O., 2008. Bulge Formation of a Buoyant River Outflow. Journal of Geophysical Research: Oceans 113. https://doi.org/10.1029/2007JC004100

Chapman, D.C. and Lentz, S.J., 1994. Trapping of a coastal density front by the bottom boundary layer. Journal of Physical Oceanography 24(7), 1464–1479. https://doi.org/10.1175/1520-0485(1994)024<1464:TOACDF>2.0.CO;2

Chen, F., MacDonald, D.G., Hetland, R.D., 2009. Lateral spreading of a near-field river plume: Observations and numerical simulations. Journal of Geophysical Research: Oceans 114. https://doi.org/10.1029/2008JC004893

Cheng, L., Opperman, J.J., Tickner, D., Speed, R., Guo, Q., Chen, D., 2018. Managing the Three Gorges Dam to Implement Environmental Flows in the Yangtze River. Frontiers in Environmental Science 6, 64. https://doi.org/10.3389/fenvs.2018.00064

Curtis, S., Allen, L., 1976. Waterfowl ecology of the Quebec coast of James Bay, in: Proceedings of the James Bay Environment 1976 Symposium. Environment Canada, Canada Wildlife Service, Ottawa, Canada, pp. 701–724.

Dai, A. and Trenberth, K.E., 2002. Estimates of freshwater discharge from continents: latitudinal and seasonal variations. Journal of Hydrometeorology 3(6), 660–687. https://doi.org/10.1175/1525-7541(2002)003<0660:EOFDFC>2.0.CO;2

Davis, K., Noisette, F., Ehn, J., Kuzyk, Z., Peck, C., O'Connor, M., 2024. Effects of light and water column nutrient availability on eelgrass *Zostera marina* productivity in Eeyou Istchee, eastern James Bay, Quebec. Marine Ecology Progress Series 738, 103–117. https://doi.org/10.3354/meps14605 de Melo, M.L., Gérardin, M.-L., Fink-Mercier, C., del Giorgio, P.A., 2022. Patterns in riverine carbon, nutrient and suspended solids export to the Eastern James Bay: links to climate, hydrology and landscape. Biogeochemistry 161, 291–314. https://doi.org/10.1007/s10533-022-00983-z

Déry, S.J., Stieglitz, M., McKenna, E.C., Wood, E.F., 2005. Characteristics and Trends of River Discharge into Hudson, James, and Ungava Bays, 1964–2000. https://doi.org/10.1175/JCLI3440.1

Dickey, M.-H., 2015. Status of eelgrass beds on the east coast of James Bay. Internal Environment Canada Report.

Dunic, J.C., Brown, C.J., Connolly, R.M., Turschwell, M.P., Côté, I.M., 2021. Long-term declines and recovery of meadow areas across the world's seagrass bioregions. Global Change Biology 27, 4096–4109. https://doi.org/10.1111/gcb.15684

Duarte, C., 1990. Seagrass nutrient content. Marine Ecology Progress Series 67, 201–207. https://doi.org/10.3354/meps067201

Ekman, V.W., 1905. On the influence of the earth's rotation on ocean-currents. Arkiv för Matematik, Astronomi och Fysik, 2(11), pp. 1–52

El-Sabh, M.I., Koutitonsky, V.G., 1977. An Oceanographic Study of James Bay before the Completion of the La Grande Hydroelectric Complex. Arctic 30, 169–186.

Fewings, M., Lentz, S.J., Fredericks, J., 2008. Observations of Cross-Shelf Flow Driven by Cross-Shelf Winds on the Inner Continental Shelf. Journal of Physical Oceanography 38(11), 2358–2378. https://doi.org/10.1175/2008JPO3990.1

Fink-Mercier, C., Leblanc, M.L., Noisette, F., O'Connor, M., Idrobo, J., Bélanger, S., del Giorgio, P.A., de Melo, M., Ehn, J.K., Giroux, J.-F., Gosselin, M., Leblon, B., Neumeier, U., Sorais, M., Humphries, M.M., Peck, C., Davis, K.E., Guzzi, A., Galindo, V., LaRocque, A., Dunn, M., Courcelles, R., Durocher, C., Gilbert, J.-P., Tapiatic, R., Rabbitskin, E., Kuzyk, Z.Z.A., 2024. Cree-driven community-partnered research on coastal ecosystem change in subarctic Canada: a multiple knowledge approach. Arctic Science 10, 731–748. https://doi.org/10.1139/as-2023-0061

Fong, D.A., Geyer, W.R., 2002. The alongshore transport of freshwater in a surface-trapped river plume. Journal of Physical Oceanography 32(3), 957–972.

Fong, D.A., Geyer, W.R., 2001. Response of a river plume during an upwelling favorable wind event. Journal of Geophysical Research: Oceans 106, 1067–1084. https://doi.org/10.1029/2000JC900134

Fong, D.A., Geyer, W.R., Signell, R.P., 1997. The wind-forced response on a buoyant coastal current: Observations of the western Gulf of Maine plume. Journal of Marine Systems 12, 69–81. https://doi.org/10.1016/S0924-7963(96)00089-9

Freeman N.G., 1982. Measurement and Modelling of Freshwater Plumes Under an Ice Cover. PhD dissertation, University of Waterloo, Canada

Gain, A.K., Giupponi, C., 2014. Impact of the Farakka Dam on Thresholds of the Hydrologic Flow Regime in the Lower Ganges River Basin (Bangladesh). Water 6, 2501–2518. https://doi.org/10.3390/w6082501

Garvine, R.W., 1999. Penetration of buoyant coastal discharge onto the continental shelf: A numerical model experiment. Journal of Physical Oceanography 29(8), 1892-1909.

Garvine, R.W., 1995. A dynamical system for classifying buoyant coastal discharges. Continental Shelf Research, Nearshore and Coastal Oceanography 15, 1585–1596. https://doi.org/10.1016/0278-4343(94)00065-U

Garvine, R.W., 1987. Estuary Plumes and Fronts in Shelf Waters: A Layer Model. Journal of Physical Oceanography 17(11), 1877–1896.

Garvine, R.W., 1984. Radial spreading of buoyant, surface plumes in coastal waters. Journal of Geophysical Research: Oceans 89, 1989–1996. https://doi.org/10.1029/JC089iC02p01989

Gerbi, G.P., Chant, R.J., Wilkin, J.L., 2013. Breaking Surface Wave Effects on River Plume Dynamics during Upwelling-Favorable Winds. Journal of Physical Oceanography 43(9), 1959–1980. https://doi.org/10.1175/JPO-D-12-0185.1

Geyer, W.R., Hill, P., Milligan, T., Traykovski, P., 2000. The structure of the Eel River plume during floods. Continental Shelf Research, Oceanic Flood Sedimentation 20, 2067–2093. https://doi.org/10.1016/S0278-4343(00)00063-7

Geyer, W.R., Ralston, D.K., 2011. The Dynamics of Strongly Stratified Estuaries, in: Treatise on Estuarine and Coastal Science. Elsevier, pp. 37–51. https://doi.org/10.1016/B978-0-12-374711-2.00206-0

Granskog, M.A., Ehn, J., Niemelä, M., 2005. Characteristics and potential impacts of under-ice river plumes in the seasonally ice-covered Bothnian Bay (Baltic Sea). Journal of Marine Systems 53, 187–196. https://doi.org/10.1016/j.jmarsys.2004.06.005

Griffin, D.A., LeBlond, P.H., 1990. Estuary/ocean exchange controlled by spring-neap tidal mixing. Estuarine, Coastal and Shelf Science 30, 275–297. https://doi.org/10.1016/0272-7714(90)90052-S

Gupta, K., Mukhopadhyay, A., Babb, D.G., Barber, D.G., Ehn, J.K., 2022. Landfast sea ice in Hudson Bay and James Bay: Annual cycle, variability and trends, 2000–2019. Elementa: Science of the Anthropocene 10, 00073. https://doi.org/10.1525/elementa.2021.00073

Halverson, M.J., Pawlowicz, R., 2008. Estuarine forcing of a river plume by river flow and tides. Journal of Geophysical Research: Oceans 113. https://doi.org/10.1029/2008JC004844

Hauxwell, J., Cebrian, J., Valiela, I., 2003. Eelgrass *Zostera marina* loss in temperate estuaries: relationship to land-derived nitrogen loads and effect of light limitation imposed by algae. Marine Ecology Progress Series 247, 59–73. https://doi.org/10.3354/meps247059

Hemminga, M.A., Duarte, C.M., 2000. Seagrass Ecology. Cambridge University Press.

Hetland, R.D., 2005. Relating River Plume Structure to Vertical Mixing. Journal of Physical Oceanography 35(9), 1667–1688. https://doi.org/10.1175/JPO2774.1

Hickey, B.M., Pietrafesa, L.J., Jay, D.A., Boicourt, W.C., 1998. The Columbia River Plume Study: Subtidal variability in the velocity and salinity fields. Journal of Geophysical Research: Oceans 103, 10339–10368. https://doi.org/10.1029/97JC03290

Hochheim, K.P., Barber, D.G., 2010. Atmospheric forcing of sea ice in Hudson Bay during the fall period, 1980–2005. Journal of Geophysical Research: Oceans 115. https://doi.org/10.1029/2009JC005334

Horner-Devine, A.R., Fong, D.A., Monismith, S.G., Maxworthy, T., 2006. Laboratory experiments simulating a coastal river inflow. Journal of Fluid Mechanics 555, 203–232. https://doi.org/10.1017/S0022112006008937

Horner-Devine, A.R., Hetland, R.D., MacDonald, D.G., 2015. Mixing and Transport in Coastal River Plumes. Annual Review of Fluid Mechanics 47, 569–594. https://doi.org/10.1146/annurev-fluid-010313-141408

Horner-Devine, A.R., Jay, D.A., Orton, P.M., Spahn, E.Y., 2009. A conceptual model of the strongly tidal Columbia River plume. Journal of Marine Systems, Special Issue on Observational Studies of Oceanic Fronts 78, 460–475. https://doi.org/10.1016/j.jmarsys.2008.11.025

Hu, W., Wang, G., Deng, W., Li, S., 2008. The influence of dams on ecohydrological conditions in the Huaihe River basin, China. Ecological Engineering 33, 233–241. https://doi.org/10.1016/j.ecoleng.2008.04.003

Idrobo, C.J., Leblanc, M.-L., O'Connor, M.I., 2024. The "Turning Point" for the Fall Goose Hunt in Eeyou Istchee: A Social-Ecological Regime Shift from an Indigenous Knowledge Perspective. Human Ecology 52, 617–636. https://doi.org/10.1007/s10745-024-00499-0

Ingram, R.G., 1981. Characteristics of the Great Whale River plume. Journal of Geophysical Research: Oceans 86, 2017–2023. https://doi.org/10.1029/JC086iC03p02017

Ingram, R.G., Larouche, P., 1987. Changes in the under-ice characteristics of La Grande Rivière plume due to discharge variations. Atmosphere-Ocean 25, 242–250. https://doi.org/10.1080/07055900.1987.9649273

Jirka, G.H., Stolzenbach, K.D., Adams, E.E., 1981. Buoyant Surface Jets. Journal of the Hydraulics Division 107, 1467–1487. https://doi.org/10.1061/JYCEAJ.0005764

Jurisa, J.T., Chant, R.J., 2013. Impact of Offshore Winds on a Buoyant River Plume System. Journal of Physical Oceanography 43(12), 2571–2587. https://doi.org/10.1175/JPO-D-12-0118.1

Kang, Y., Pan, D., Bai, Y., He, X., Chen, X., Chen, C.-T.A., Wang, D., 2013. Areas of the global major river plumes. Acta Oceanologica Sinica 32, 79–88. https://doi.org/10.1007/s13131-013-0269-5

Kasper, J.L., Weingartner, T.J., 2015. The Spreading of a Buoyant Plume Beneath a Landfast Ice Cover. Journal of Physical Oceanography 45(2), 478–494. https://doi.org/10.1175/JPO-D-14-0101.1

Kourafalou, V.H., Oey, L.-Y., Wang, J.D., Lee, T.N., 1996. The fate of river discharge on the continental shelf: 1. Modeling the river plume and the inner shelf coastal current. Journal of Geophysical Research: Oceans 101, 3415–3434. https://doi.org/10.1029/95JC03024

Kowal, S., Gough, W.A., Butler, K., 2017. Temporal evolution of Hudson Bay Sea Ice (1971–2011). Theoretical and Applied Climatology 127, 753–760. https://doi.org/10.1007/s00704-015-1666-9

Kuzyk, Z.A., Macdonald, R.W., Granskog, M.A., Scharien, R.K., Galley, R.J., Michel, C., Barber, D., Stern, G., 2008. Sea ice, hydrological, and biological processes in the Churchill River estuary region, Hudson Bay. Estuarine, Coastal and Shelf Science 77, 369–384. https://doi.org/10.1016/j.ecss.2007.09.030

Lalumière, R., Messier, D., Fournier, J.-J., Peter McRoy, C., 1994. Eelgrass meadows in a low Arctic environment, the northeast coast of James Bay, Québec. Aquatic Botany 47, 303–315. https://doi.org/10.1016/0304-3770(94)90060-4

Lavín, M.F., Godínez, V.M., Alvarez, L.G., 1998. Inverse-estuarine Features of the Upper Gulf of California. Estuarine, Coastal and Shelf Science 47, 769–795. https://doi.org/10.1006/ecss.1998.0387

Leblanc, M.-L., O'Connor, M., Noisette, F., Leblon, B., Davis, K., Clyne, K., LaRocque, A., Olatunji, A. & Humphries, M., 2023a. *Coastal Habitat Comprehensive Project: Eelgrass Team Final Report*. Niskamoon Corporation, July 21, 2023.

Leblanc, M.-L., O'Connor, M.I., Kuzyk, Z.Z.A., Noisette, F., Davis, K.E., Rabbitskin, E., Sam, L.-L., Neumeier, U., Costanzo, R., Ehn, J.K., Babb, D., Idrobo, C.J., Gilbert, J.-P., Leblon, B., Humphries, M.M., 2023b. Limited recovery following a massive seagrass decline in subarctic eastern Canada. Global Change Biology 29, 432–450. https://doi.org/10.1111/gcb.16499

Lee, K.-S., Park, S.R., Kim, Y.K., 2007. Effects of irradiance, temperature, and nutrients on growth dynamics of seagrasses: A review. Journal of Experimental Marine Biology and Ecology, The Biology and Ecology of Seagrasses 350, 144–175. https://doi.org/10.1016/j.jembe.2007.06.016

Lentz, S.J., Helfrich, K.R., 2002. Buoyant gravity currents along a sloping bottom in a rotating fluid. Journal of Fluid Mechanics 464, 251–278. https://doi.org/10.1017/S0022112002008868

MacDonald, D.G., Geyer, W.R., 2005. Hydraulic Control of a Highly Stratified Estuarine Front. Journal of Physical Oceanography 35(3), 374–387. https://doi.org/10.1175/JPO-2692.1

MacDonald, D.G., Geyer, W.R., 2004. Turbulent energy production and entrainment at a highly stratified estuarine front. Journal of Geophysical Research: Oceans 109. https://doi.org/10.1029/2003JC002094

Macdonald, R.W., Carmack, E.C., 1991. The role of large-scale under-ice topography in separating estuary and ocean on an Arctic shelf. Atmosphere-Ocean 29, 37–53. https://doi.org/10.1080/07055900.1991.9649391

Macdonald, R.W., Paton, D.W., Carmack, E.C., Omstedt, A., 1995. The freshwater budget and under-ice spreading of Mackenzie River water in the Canadian Beaufort Sea based on salinity and 18O/16O measurements in water and ice. Journal of Geophysical Research: Oceans 100, 895–919. https://doi.org/10.1029/94JC02700

McCabe, R.M., MacCready, P., Hickey, B.M., 2009. Ebb-Tide Dynamics and Spreading of a Large River Plume. Journal of Physical Oceanography 39(11), 2839-2856. https://doi.org/10.1175/2009JPO4061.1

Mcroy, C.P., 1969. Eelgrass under Arctic Winter Ice. Nature 224, 818–819. https://doi.org/10.1038/224818a0

Milliman, J.D., Farnsworth, K.L., 2013. River Discharge to the Coastal Ocean: A Global Synthesis. Cambridge University Press.

Moksnes, P.-O., Eriander, L., Infantes, E., Holmer, M., 2018. Local Regime Shifts Prevent Natural Recovery and Restoration of Lost Eelgrass Beds Along the Swedish West Coast. Estuaries and Coasts 41, 1712–1731. https://doi.org/10.1007/s12237-018-0382-y

Morales Maqueda, M.A., Willmott, A.J., Biggs, N.R.T., 2004. Polynya Dynamics: A Review of Observations and Modeling. Reviews of Geophysics 42. https://doi.org/10.1029/2002RG000116

Muench, R.D., Morison, J.H., Padman, L., Martinson, D., Schlosser, P., Huber, B., Hohmann, R., 2001. Maud Rise revisited. Journal of Geophysical Research: Oceans 106, 2423–2440. https://doi.org/10.1029/2000JC000531

Murphy, G.E.P., Dunic, J.C., Adamczyk, E.M., Bittick, S.J., Côté, I.M., Cristiani, J., Geissinger, E.A., Gregory, R.S., Lotze, H.K., O'Connor, M.I., Araújo, C.A.S., Rubidge, E.M., Templeman, N.D., Wong, M.C., 2021. From coast to coast to coast: ecology and management of seagrass ecosystems across Canada. FACETS 6, 139–179. https://doi.org/10.1139/facets-2020-0020

Nash, J.D., Moum, J.N., 2005. River plumes as a source of large-amplitude internal waves in the coastal ocean. Nature 437, 400–403. https://doi.org/10.1038/nature03936

Nejrup, L.B., Pedersen, M.F., 2008. Effects of salinity and water temperature on the ecological performance of *Zostera marina*. Aquatic Botany 88, 239–246. https://doi.org/10.1016/j.aquabot.2007.10.006

Nof, D., 1988. Eddy-wall interactions. Journal of Marine Research 46(3), 527–555

Nurser, A.J.G., Bacon, S., 2014. The Rossby radius in the Arctic Ocean. Ocean Science 10, 967–975. https://doi.org/10.5194/os-10-967-2014

O'Donnell, J., 2010. The dynamics of estuary plumes and fronts, in: Valle-Levinson, A. (Ed.), Contemporary Issues in Estuarine Physics. Cambridge University Press, Cambridge, pp. 186–246. https://doi.org/10.1017/CBO9780511676567.009

Osadchiev, A., Medvedev, I., Shchuka, S., Kulikov, M., Spivak, E., Pisareva, M., Semiletov, I., 2020. Influence of estuarine tidal mixing on structure and spatial scales of large river plumes. Ocean Science 16, 781–798. https://doi.org/10.5194/os-16-781-2020

Osadchiev, A., Zavialov, P., 2019. Structure and Dynamics of Plumes Generated by Small Rivers, in: Estuaries and Coastal Zones - Dynamics and Response to Environmental Changes. IntechOpen. https://doi.org/10.5772/intechopen.87843

Prinsenberg, S.J., 1980. Man-Made Changes in the Freshwater Input Rates of Hudson and James Bays. Canadian Journal of Fisheries and Aquatic Sciences 37, 1101–1110. https://doi.org/10.1139/f80-143

Pritchard, M., Huntley, D.A., 2006. A simplified energy and mixing budget for a small river plume discharge. Journal of Geophysical Research: Oceans 111. https://doi.org/10.1029/2005JC002984

Reed, A., 1996. Goose use of the coastal habitats of northeastern James Bay. Occasional paper, Environment Canada, Canada Wildlife Service.

Reimnitz, E., Toimil, L., Barnes, P., 1978. Arctic continental shelf morphology related to sea-ice zonation, Beaufort Sea, Alaska. Marine Geology 28, 179–210. https://doi.org/10.1016/0025-3227(78)90018-X

Ridenour, N.A., Hu, X., Sydor, K., Myers, P.G., Barber, D.G., 2019. Revisiting the Circulation of Hudson Bay: Evidence for a Seasonal Pattern. Geophysical Research Letters 46, 3891–3899. https://doi.org/10.1029/2019GL082344

Rippeth, T.P., Simpson, J.H., 1996. The frequency and duration of episodes of complete vertical mixing in the Clyde Sea. Continental Shelf Research 16, 933–947. https://doi.org/10.1016/0278-4343(95)00022-4

Robertson, A.I., Mann, K.H., 1984. Disturbance by ice and life-history adaptations of the seagrass *Zostera marina*. Marine Biology 80, 131–141. https://doi.org/10.1007/BF02180180

Rogowski, P., Terrill, E., Chen, J., 2014. Observations of the frontal region of a buoyant river plume using an autonomous underwater vehicle. Journal of Geophysical Research: Oceans 119, 7549–7567. https://doi.org/10.1002/2014JC010392

Roy, D., Messier, D., 1989. A review of the effects of water transfers in the La Grande Hydroelectric Complex (Québec, Canada). Regulated Rivers: Research & Management 4, 299–316. https://doi.org/10.1002/rrr.3450040308

Salo, T., Pedersen, M.F., Boström, C., 2014. Population specific salinity tolerance in eelgrass (*Zostera marina*). Journal of Experimental Marine Biology and Ecology 461, 425–429. https://doi.org/10.1016/j.jembe.2014.09.010

Schmidt, A.L., Wysmyk, J.K.C., Craig, S.E., Lotze, H.K., 2012. Regional-scale effects of eutrophication on ecosystem structure and services of seagrass beds. Limnology and Oceanography 57, 1389–1402. https://doi.org/10.4319/lo.2012.57.5.1389

Schulze, L.M., Pickart, R.S., 2012. Seasonal variation of upwelling in the Alaskan Beaufort Sea: Impact of sea ice cover. Journal of Geophysical Research: Oceans 117. https://doi.org/10.1029/2012JC007985

Shiklomanov, I.A., Shiklomanov, A.I., Lammers, R.B., Peterson, B.J., Vorosmarty, C.J., 2000. The Dynamics of River Water Inflow to the Arctic Ocean, in: Lewis, E.L., Jones, E.P., Lemke, P., Prowse, T.D., Wadhams, P. (Eds.), The Freshwater Budget of the Arctic Ocean. Springer Netherlands, Dordrecht, pp. 281–296. https://doi.org/10.1007/978-94-011-4132-1_13

Simpson, J.H., 1997. Physical processes in the ROFI regime. Journal of Marine Systems 12, 3–15. https://doi.org/10.1016/S0924-7963(96)00085-1

Steiner, N., Azetsu-Scott, K., Hamilton, J., Hedges, K., Hu, X., Janjua, M.Y., Lavoie, D., Loder, J., Melling, H., Merzouk, A., Perrie, W., Peterson, I., Scarratt, M., Sou, T., Tallmann, R., 2015. Observed trends and climate projections affecting marine ecosystems in the Canadian Arctic. Environmental Reviews 23, 191–239. https://doi.org/10.1139/er-2014-0066

Taha, W., Bonneau-Lefebvre, M., Cueto Bergner, A., Tremblay, A., 2019. Evolution From Past to Future Conditions of Fast Ice Coverage in James Bay. Frontiers in Earth Science 7. https://doi.org/10.3389/feart.2019.00254

Turschwell, M.P., Connolly, R.M., Dunic, J.C., Sievers, M., Buelow, C.A., Pearson, R.M., Tulloch, V.J.D., Côté, I.M., Unsworth, R.K.F., Collier, C.J., Brown, C.J., 2021. Anthropogenic pressures and life history predict trajectories of seagrass meadow extent at a global scale. Proceedings of the National Academy of Sciences 118, e2110802118. https://doi.org/10.1073/pnas.2110802118

Unsworth, R.K.F., Butterworth, E.G., 2021. Seagrass Meadows Provide a Significant Resource in Support of Avifauna. Diversity 13, 363. https://doi.org/10.3390/d13080363

Weeks, W.F., 2010. On sea ice. Fairbanks, AK: University of Alaska Press.

Whitney, M.M., Garvine, R.W., 2006. Simulating the Delaware Bay Buoyant Outflow: Comparison with Observations. Journal of Physical Oceanography 36(1), 3–21. https://doi.org/10.1175/JPO2805.1

Winsor, P., Björk, G., 2000. Polynya activity in the Arctic Ocean from 1958 to 1997. Journal of Geophysical Research: Oceans 105, 8789–8803. https://doi.org/10.1029/1999JC900305

Yan, Y., Yang, Z., Liu, Q., Sun, T., 2010. Assessing effects of dam operation on flow regimes in the lower Yellow River. Procedia Environmental Sciences, International Conference on Ecological Informatics and Ecosystem Conservation (ISEIS 2010) 2, 507–516. https://doi.org/10.1016/j.proenv.2010.10.055

Yankovsky, A.E., Chapman, D.C., 1997. A Simple Theory for the Fate of Buoyant Coastal Discharges. Journal of Physical Oceanography 27(7), 1386-1401.

Yankovsky, A.E., Hickey, B.M., Münchow, A.K., 2001. Impact of variable inflow on the dynamics of a coastal buoyant plume. Journal of Geophysical Research: Oceans 106, 19809–19824. https://doi.org/10.1029/2001JC000792

Yuan, Y., Horner-Devine, A.R., Avener, M., Bevan, S., 2018. The role of periodically varying discharge on river plume structure and transport. Continental Shelf Research 158, 15–25. https://doi.org/10.1016/j.csr.2018.02.009

Chapter 3 Under-ice hydrography of the La Grande River plume in relation to a ten-fold increase in wintertime discharge

This manuscript has been published in the peer-reviewed Journal of Geophysical Research: Oceans. Since publication it has been edited and adapted for this thesis. The citation for this manuscript is as follows:

Peck, C.J., Kuzyk, Z.Z.A., Heath, J.P., Lameboy, J., Ehn, J.K. (2022) 'Under-ice hydrography of the La Grande River plume in relation to a ten-fold increase in wintertime discharge', Journal of Geophysical Research: Oceans, e2021JC018341. Available at: https://doi.org/10.1029/2021JC018341

3.1 Abstract

A large under-ice plume forms because of the regulated winter discharge from the La Grande River hydroelectric complex (NE James Bay, Canada), which is among the largest winter discharges in the circumpolar north. In 2016–2017, field campaigns were completed to characterize the under-ice plume's structure, extent, and short-term dynamics related to tides, weather, and discharge. Amid concerns of the freshwater's impact on eelgrass, the lateral spreading of the under-ice plume into inshore areas was also assessed. When discharges averaged 4,800 $m^3 s^{-1}$ throughout the January–March periods, the freshwater influence of the La Grande River extended more than 100 km north along the James Bay coast, diluting the ambient surface waters of James Bay to salinity <25 PSU. The core area of the under-ice plume, defined as the area with a highly stratified water column and surface layer of salinity <5 PSU, extended 30–35 km north and >20 km south of the river mouth, producing an under-ice plume more than three times larger than in 1976, when the river's natural winter discharge was ~460 $m^3 s^{-1}$. The plume's extent was stable throughout the January–March 2016–2017 period and the size of the core area was not significantly larger than during winter survey periods in 1984–1987 when discharge was ~30% higher. This stability appears to be due to the coastal geometry and width of the landfast ice cover, under which the plume can spread with limited mixing. Inshore salinity was approximately 5–10 PSU lower in winter than in the open-water period. The seasonal duration of reduced salinity at eelgrass habitats will depend on landfast ice duration as well as river discharge magnitude.

3.2 Introduction

Rivers that discharge into coastal environments covered by landfast sea ice tend to form large, highly stratified under-ice plumes because of the absence of direct wind forcing under a continuous landfast sea-ice cover (Ingram, 1981; Ingram & Larouche, 1987a, 1987b). These winter plumes can be ecologically significant affecting distributions of nutrients, contaminants, ice algae, and phytoplankton (Carmack & Macdonald, 2002; Dunton et al., 2006; Granskog et al., 2005a; Granskog et al., 2005b; Ingram et al., 1996; Kuzyk et al., 2008; Li & Ingram, 2007; Macdonald et al., 1998). The key factors that control the extent and vertical structure (stratification) of under-ice plumes are, aside from the ice, generally similar to those controlling open-water plumes (cf. Horner-Devine et al., 2015). River discharge, which introduces stratification and buoyancy, drives plume dispersion, whereas tidal flows and roughness elements such as the ice bottom enhance mixing, which works to break down stratification. The reduced wind-generated turbulence under the landfast ice cover tends to promote wider plume spreading for a similar level of discharge (Ingram & Larouche, 1987a; Kasper & Weingartner, 2012, 2015; Li & Ingram, 2007). The pressure ridge/rubble zone at the outer edge of the landfast ice (sometimes called 'stamukhi'), which is formed by opening and closing of the flaw lead and collisions between mobile pack ice and fast ice, may contribute to 'steering' a plume and/or confining it near the coast thereby playing a role in establishing the thickness of the plume (Kuzyk et al., 2008; Macdonald et al., 1995). However, to date, no studies of under-ice plume extent and structure exist that would allow for an assessment of temporal and spatial variations as a function of the combined effects of landfast ice morphology, tides, weather, and variations in discharge.

The La Grande River (LGR) in northeast James Bay, south of Hudson Bay (Canada), presently has a typical winter discharge averaging ~5,000 $m^3 s^{-1}$, which is greater than the winter discharge of any other river in the Arctic watershed except the Siberian Yenisei River (Shiklomanov & Shiklomanov, 2003). The LGR under-ice plume has been studied on several occasions since flow augmentation began in the late 1970s. In the winter of 1976, when the discharge was at natural (unregulated) levels (~460 $m^3 s^{-1}$), the plume spread out under the landfast ice as a thin layer with a very low salinity (<5) that covered about 200 km^3 along the coast mostly north of the river mouth (Freeman, 1982; Freeman et al., 1982; Ingram & Larouche, 1987a). Following the first phase of hydroelectric development, winter discharge increased to about 1,500 $m^3 s^{-1}$ in 1980 and 3,000 $m^3 s^{-1}$ in 1984, and consequently, the area within the 5 isohaline increased first to 650 km^2 and finally to 1,200 km^2 (Ingram & Larouche, 1987a). Additional development of the LGR occurred after 1984, including the partial diversion of the Rupert River in 2009 (Consortium

Genivar-Waska, 2017). However, since limited observations in the winters of 1989 (Messier et al., 1989) and 1993–1995 (Messier, 2002), no update to the description of the plume's structure and extent has been published. The time-dependent properties of LGR's winter plume, including variations in salinity and currents beneath the sea ice, on time scales of weeks to months, have received scarce attention in previous work, and the timing of plume spreading into the inshore eelgrass (*Zostera marina*) habitat has not been previously studied. Understanding the magnitude and causes of salinity variations along the northeast James Bay coast has emerged as a local research priority because major declines have occurred in the area's eelgrass meadows, which were once among the most extensive in North America (Lalumière et al., 1994).

The importance of eelgrass is globally recognized because of its critical ecological functions, e.g., nutrient recycling, sediment trapping, and carbon sequestration (Hemminga & Duarte, 2000). In northeast James Bay, the wildlife associated with the eelgrass beds, especially migratory waterfowl, have been integral to the way of life and subsistence economy of the Cree First Nations for millennia. Near the Cree Nation of Chisasibi, which is located at the LGR mouth, eelgrass meadows were flourishing and extremely productive during the 1970s (Curtis & Allen, 1976; Lalumière et al., 1994) but massively declined in the late 1990s and have failed to consistently recover (Consortium Genivar-Waska, 2017). Low salinity is of potential concern for the health of eelgrass because, although eelgrass can tolerate a wide range of salinity, prolonged exposure to very low salinity (<5 PSU) or fluctuating salinity in the range of 5–15 PSU is considered detrimental to their health (Kamermans et al., 1999; Moreno- Marín et al., 2018).

The Cree Nation of Chisasibi raised concerns that the increasing discharge would lead to larger deleterious impact on the coastal habitat and specifically on the eelgrass and geese habitats. We hypothesized that the stratified plume would have expanded northward with increased discharge, consistent with previously observed changes in the plume with increased discharge (Ingram and Larouche, 1987). A second aim of the study was to assess time-dependent changes in the plume, which could not be completed in previous studies that relied on just single salinity surveys per season. A third aim was determining the plume's influence on salinity at nearby inshore eelgrass habitat because previous sampling efforts had generally omitted the embayments where eelgrass is found. We did not expect to find that the very low salinity (<5 PSU) associated with the plume's stratified surface layer intruded into the inshore eelgrass habitat.

3.3 Materials and methods

3.3.1 Study area

James Bay represents the southernmost extension of Arctic waters in Canada (Ingram & Prinsenberg, 1998; Prinsenberg, 1986b). In general, the surface waters circulate cyclonically within James Bay, with saline inflow in the west and fresher outflow along the eastern side (Prinsenberg, 1982; Ridenour et al., 2019). During summer, the outflow from James Bay along the northeast coast consists of a relatively narrow coastal current, with surface velocities on the order of 15 cm s^{-1}. There is about ten times as much transport (outflow) as summer river runoff because of entrainment (Prinsenberg, 1982). The outflow is balanced by a broad, deep, and much slower inflow with velocities less than 5 cm s^{-1} (El-Sabh & Koutitonsky, 1977). With this two-layer circulation, James Bay can be considered to function as a large estuary. During winter, when the bay is ice-covered and river runoff is reduced, the magnitude of the inflow and outflow decreases. Offshore from the LGR mouth, monthly mean flows in the winter of 1980 were generally to the northwest with speeds ranging from 2 to 5 cm s^{-1} (Freeman, 1982). More recent measurements are not available but early workers predicted the doubling of flows in and out of James Bay due to the increase in winter runoff following the development of the LGR system (Prinsenberg, 1982).

Sea ice freeze-up in James Bay typically begins in December and breakup occurs in early June (Gagnon & Gough, 2005). There was a negative trend in ice breakup date in James Bay over the period of 1985–2009 (Galbraith & Larouche, 2011) and breakup date for landfast ice in James Bay shifted about five days earlier between 1980–1997 and 1998–2016 (Taha et al., 2019, Gupta et al. 2022). Taha and coworkers (2019) concluded that hydrological changes due to hydroelectric development had not appreciably affected the landfast ice extent in east James Bay while noting that warm water coming from the LGR causes breakup to occur earlier in this area than in the rest of the Bay.

3.3.2 Sampling

The data set comprises conductivity, temperature, and depth (CTD) measurements from both winter and summer seasons of 2016 and 2017, and time-series records of temperature, salinity, currents, and water levels for the ice-covered period (January–April) of 2016 and 2017. Based on previous observations of the under-ice LGR plume extent (Ingram and Larouche 1987a; Messier 2002), sampling locations were distributed between the LGR mouth and Cape Jones at the northern tip of the coastline, representing an expanse of approximately 110 km (Figure 3.1). CTD casts were collected along several across-shore sections similar to previous surveys and a few samples also were collected south of the river mouth. In addition to past scientific work, the knowledge of members of the Cree Nation of Chisasibi guided the research in redirecting attention from along-shore plume characteristics (2016) to across-shore characteristics and influence on salinity at eelgrass beds (2017). Cree knowledge filled gaps in background scientific knowledge of the site-specific circulation, bathymetry, and sea ice. Cree research partners also made the field work possible by assisting with site selection, safety, and logistics. The trapline numbers used by the local Cree First Nation (CH1 at LGR mouth, CH3 at Paul Bay, CH4 at Bay of Many Islands, and CH5, CH6 and CH7 along the north coast to Cape Jones; Figure 3.1) are used for nearby mooring locations for ease of discussion.

Data collection was carried out during six field campaigns: January, April, and August 2016, and January, April, and August 2017. A total of more than 150 CTD casts were collected opportunistically during these campaigns (see locations in Figure 3.1) with many locations being revisited during several campaigns. CTD casts collected during January and April field campaigns are considered representative of ‘winter’ (ice-covered) conditions and those collected during August are considered representative of ‘summer’ (open water) conditions. During winter, sampling sites on the landfast ice were accessed by snowmobile. CTD casts were conducted by deploying the instrument through a hole bored with an auger through the ice, which was typically ~80-100 cm thick. During the summer, the sites were accessed by freighter canoe and the CTDs were deployed over the side of the canoe. Two CTD instruments were regularly used: a Castaway by Sontek and an Ocean Seven 304 plus by Idronaut. The accuracies of the Castaway CTD as stated by the manufacturer are ±0.05°C for temperature, 0.25% ±5 µS/C for conductivity, and ±0.1 for salinity. The accuracies of the Idronaut CTD as stated by the manufacturer are ±0.002°C for temperature and ±0.003 mS cm^{-1} for conductivity. Often both instruments were used at the same time providing redundancy and backup, and they showed good agreement (Figure S3.1). However, the Castaway was more widely used across the two years of study and will provide the majority of the CTD data for this study. The CTD profiles were processed in MATLAB to retain only the downcast and remove anomalous readings that occurred, particularly in the winter when instruments were cold or warm from transport and needed time to adjust to the temperature of the water. During winter, instruments were transported from site to site in warmed or water-filled coolers to prevent icing. The upcast would occasionally be used if the instruments record during downcast showed unrealistically cold temperatures.

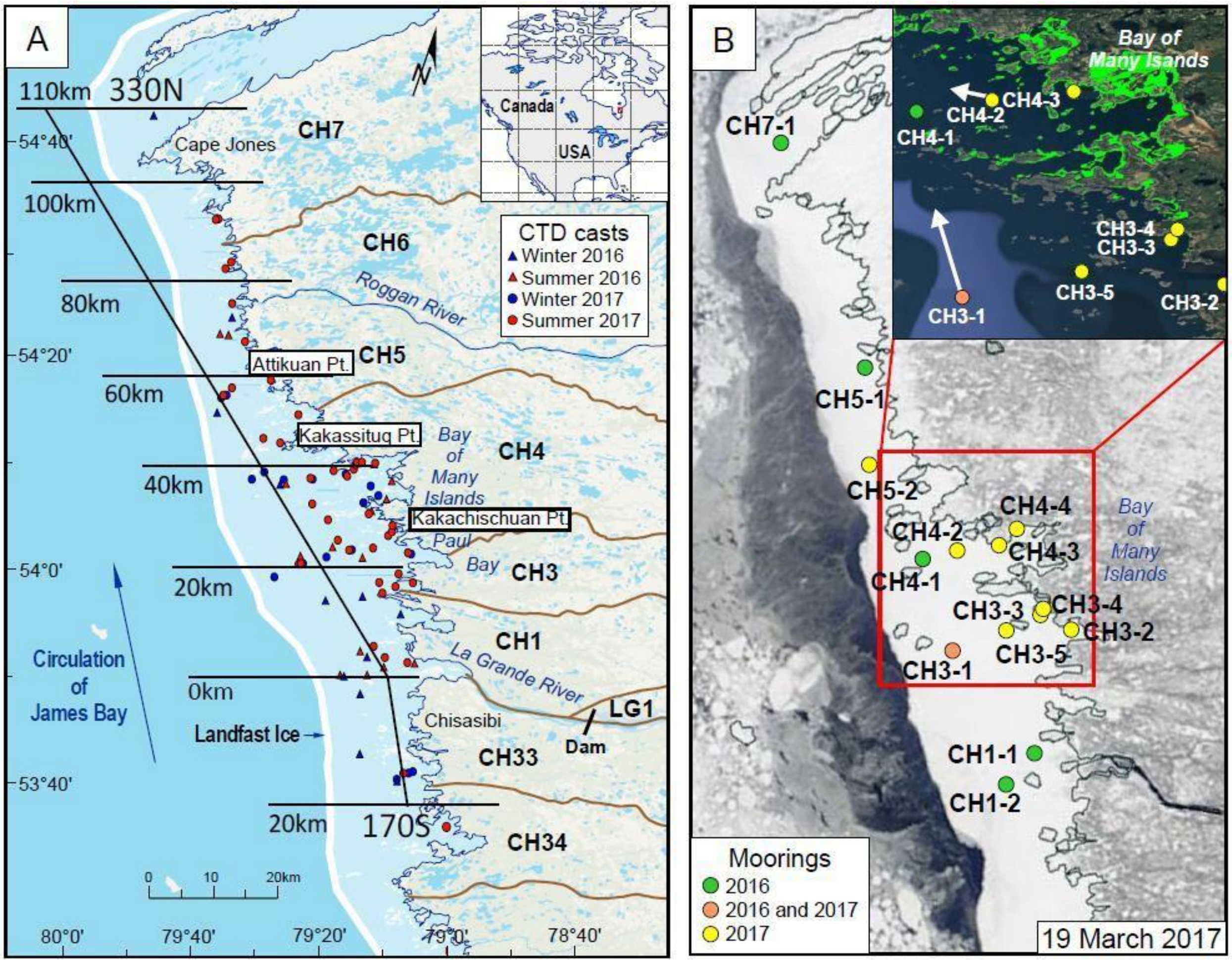

Figure 3.1: Map of the study area in northeast James Bay showing (A) CTD and mooring stations and background circulation and distance from the river mouth on bearings 330°N and 170°S, taken from Ingram and Larouche (1987a). Panel B shows a MODIS satellite image of the area for 19 March 2017. The band of white ice along the coast corresponds to the landfast ice. The mobile ice pack is located offshore of the landfast ice, with black areas of open water and light-grey areas of new ice intermixed with white thicker floes. The inset in B shows an important area of eelgrass habitat (Bay of Many Islands) with eelgrass cover as mapped in 1996 shaded green. Arrows show mean surface currents recorded during January–April periods (see Table 3.1 for details).

A total of 15 ice-tethered moorings were deployed under the landfast ice cover in the study area during the winters of 2016 and 2017 (Figure 3.1). Six moorings were deployed (and recovered) in winter 2016: two (CH1-1, CH1-2) near the LGR mouth and the remainder (CH3-1, CH4-1, CH5-1, CH7-1) arrayed northwards along the main axis of the plume (Figure 3.1). Nine moorings were deployed (and recovered) in winter 2017: one at the 2016 CH3-1 location; four (CH3-2, -3, -4, and -5) shoreward of CH3-1, roughly perpendicular to the axis of the plume; three (CH4-2, CH4-3, CH4-4) shoreward of the 2016 CH4-1 mooring location; and finally, one (CH5-2) slightly south of the 2016 CH5-1 mooring location (Figure

3.1). Note that moorings CH3-4 and CH4-4 were placed in eelgrass beds in Paul Bay and the Bay of Many Islands, respectively. The planned repeat deployment at CH1-1 near the mouth of LGR could not be conducted in 2017 due to unsafe ice conditions, and thus CH3-1 represents the sole location with records for both winters.

All the moorings included, at minimum, a conductivity and temperature sensor (CT) and a pressure sensor (P). Instruments from a number of different manufacturers were used and deployed at various heights in the water column (see Table S3.1): In-Situ Aqua TROLL 100 for CT; In-Situ Aqua TROLL 600 for CT and P; JFE Advantech (formerly Alec Electronics) Compact-CT for CT; Onset HOBO U24-002-C for CT; and Onset HOBO U20L for P. Nortek Aquadopp 600 kHz Acoustic Doppler Current Profilers (ADCP) were installed on moorings CH1-1 and CH1-2 in winter 2016, and CH3-1 and CH4-2 in winter 2017. In 2016, the ADCPs were deployed near the surface in a downward-looking orientation. However, the CH1-2 mooring accumulated frazil ice during the deployment, limiting the usefulness of data that could be obtained. To avoid any potential frazil ice in 2017, the ADCPs were installed in an upward-looking orientation near the seafloor. Additional pressure sensors were anchored to the bottom at each mooring location to record water level variations due to tides and weather, and one pressure sensor recorded in the air at CH3-1 to allow correction for local atmospheric pressure variations. Tidal harmonic analyses were conducted on water level data using the T-Tide MATLAB package (Pawlowicz et al., 2002) after first correcting for atmospheric pressure variations. The salinity time series data required no postprocessing as it showed the daily and monthly variations well and contained little notable noise. It also showed the difference between those moorings within the plume and outside very well. The data from CH3-1 in 2016 did need to be processed to better show the river plume properties as there were large salinity variations in the record over the tidal cycle. It was determined that the sensor depth was at the plume-seawater interface which caused the large change with the tide. Thus, to show the plume salinity, we retained only the low salinity values recorded during low tide.

The deployments lasted between 83 and 86 days in winter 2016 and between 67 and 69 days in winter 2017. Deployment and recovery dates of all the moorings are given in Table 3.1 and configurations in Table S3.1. Comparison of mooring salinity data and CTD data is given in Figure S3.2.

Table 3.1: Near-surface salinity statistics calculated for 15 locations within the various sectors of the winter La Grande plume using the continuous records obtained from CT sensors tethered beneath the ice (depths of ~1.5–3 m). The moorings are ordered from south to north starting at the station closest to the mouth of the LGR (CH1-1). See Figure 3.1 for details.

Mooring	Long	Lat	Bottom Depth	Start date	End Date	Salinity (PSU)		
	(W)	(N)	(m)			Avg (SD)[1]	Min.	Max.
Plume core area								
CH1-1	79.18	53.85	22	27/01/2016	05/04/2016	0.7 (± 0.3)	0.1	1.9
CH1-2	79.24	53.82	25	27/01/2016	05/04/2016	0.3 (±0.2)	0.1	2
CH3-1 (2016)[1]	79.35	54.00	17	29/01/2016	07/04/2016	3.0 (±2.4)	1	15.7
CH3-1 (2017)	79.35	54.00	17	25/01/2017	19/04/2017	0.7 (±0.8)	0.1	12.8
CH3-2	79.06	54.01	6	28/01/2017	21/04/2017	1.6 (±0.3)	0.8	2.2
CH3-3	79.12	54.04	8	28/01/2017	22/04/2017	1.7 (±0.4)	0.7	3.1
CH3-4	79.11	54.04	2	28/01/2017	24/04/2017	1.9 (±0.4)	0	7.3
CH3-5	79.22	54.02	16	28/01/2017	21/04/2017	0.5 (±0.4)	0.1	1.9
Frontal area								
CH4-1	79.4	54.12	10	30/01/2016	07/04/2016	11.3 (±2.3)	5.6	17.5
CH4-2	79.32	54.13	11	26/01/2017	20/04/2017	10.9 (±1.5)	4.4	13.9
CH4-3	79.22	54.14	8	26/01/2017	20/04/2017	11.0 (±1.5)	5	13.9
CH4-4	79.19	54.15	2	26/01/2017	20/04/2017	11.6 (±0.8)	9.6	13.6
North coast sector – Far field region								
CH5-1	79.52	54.38	6	30/01/2016	06/04/2016	19.6 (±1.9)	15.8	23.5

CH5-2	79.55	54.26	7	06/02/2017	25/04/2017	18.0 (±1.6)	12.6	22.9
CH7-1	79.72	54.70	17	01/02/2016	02/04/2016	25.8 (±0.6)	21.4	27.3

[1] Statistics were calculated after filtering the raw record to remove high salinities recorded during high tide (see Methods for details).

3.3.3 Additional data sources

For interpretation of the winter mooring records, wind speed and direction and atmospheric pressure data were obtained from the nearest coastal Environment and Climate Change Canada (ECCC) weather station at Wemindji airport, located about 88 km south of Chisasibi. Wind rose diagrams showing the prevailing wind direction and speed (km h^{-1}) for the mooring deployment periods in 2016 and 2017 are shown in Figure S3.4. Hydro-Québec provided daily discharge data for the LGR at the LG1 dam/generating station located about 40 km from the river mouth (Figure 3.1). Historical discharge data are provided in Figure S3.5.

3.4 Results

3.4.1 Sea ice, river discharge, and meteorological conditions

The icescape in the study area during the winters of 2016 and 2017 is shown in Figure 3.1. The landfast ice varied from 10 to 30 km wide and was at its maximum width in late January of each year. The landfast ice was wide, approximately 20–25 km, for the first 40 km stretch of coast nearest the LGR mouth (from Tees Bay to Kakachischuan Point; Figure 3.1) in March 2017 (Figure 3.2). To the north of that area, beyond Bay of Many Islands, the landfast ice narrowed to only 5–10 km (Figure 3.2). Seaward of the landfast ice edge, a flaw lead irregularly opened and closed as the mobile pack ice of James Bay was moved about by winds and with the passage of storms through the study area (see, for example, Figure S3.3). The outer boundary of the landfast ice appeared ridged and rough when viewed from the surface of the landfast ice, consistent with mechanical deformation resulting from collisions of the pack ice and landfast ice. In 2017, the landfast ice around the LGR mouth was thin and unsafe in comparison to 2016 when it was possible to travel and deploy moorings (CH1-1) in this area. The average thickness of the landfast ice in April across all mooring sites was also thinner in 2017 at 74 cm ±17 cm (n=13) compared to 2016 at 90 cm ±14 cm (n=10). During both 2016 and 2017, the LGR discharge averaged 4,800 m^3 s^{-1} in January, February, and March, and 3,960 m^3s^{-1} during April (Hydro-Québec, personal communication, 2019). However, the short-term temporal discharge pattern varied between the two years as controlled by weather and hydroelectric regulation (Figure 3.3). For example, the second half of February 2016 saw the highest weekly-averaged flows, whereas in 2017 the flows peaked in early February and then stayed low throughout the second half of the month (Figure 3.3). Aside from the LGR, the next largest river in the study area is the Roggan River, located north of Bay of Many Islands, which has a winter discharge of about 64 $m^3 s^{-1}$ (i.e., 1–2% of LGR; P. del Giorgio, personal Communication, 2019).

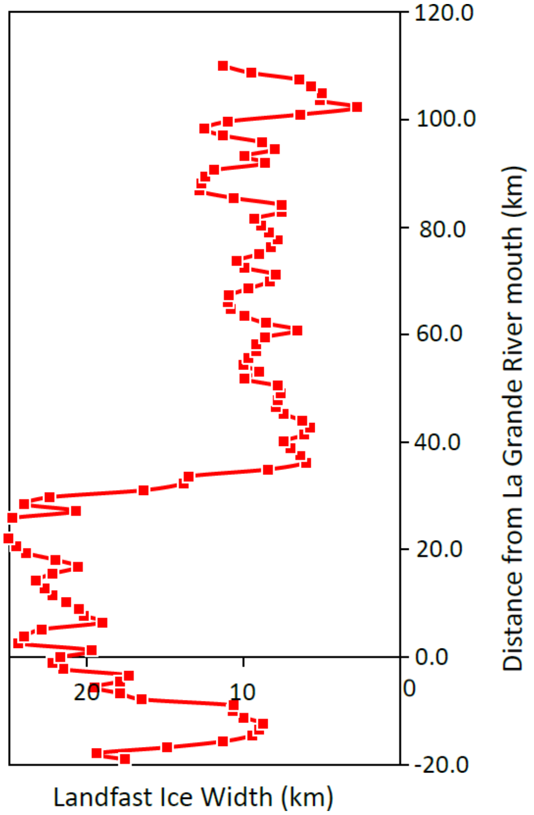

Figure 3.2: Width of the landfast ice along the coast from about 20km south of the LGR mouth (-20km on y-scale) northward to just past Cape Jones (~100km). Distances are marked on Figure 3.1 and follow roughly shore-parallel bearings (330N, 170S). Widths were calculated in Google Earth from MODIS images as the difference between the maximum ice width (30 March 2017) and early freeze-up width (30 November 2016).

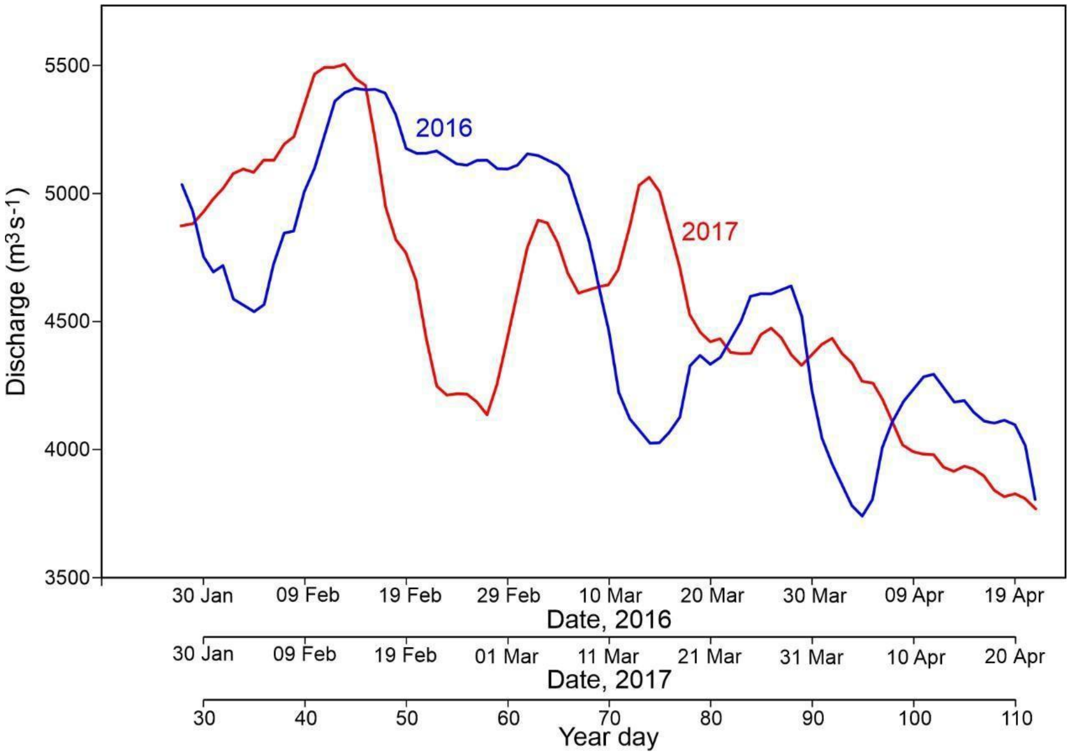

Figure 3.3: Weekly averaged discharge for the LGR as recorded at LG1 for the 2016 (blue) and 2017 (orange) winter study periods.

Winds and atmospheric pressure measured along the northeast James Bay coast at the Wemindji airport during winters 2016 and 2017 are shown in Figure 3.4. Atmospheric pressures measured at the CH3-1 mooring (instrument placed on a tower above the sea ice) closely agreed with the record from the Wemindji airport. Notable storms occurred around 25 February 2016 and 8–11 March 2017 (Figure 3.4). The prevailing wind direction during the mooring deployment period was south, southwest in 2016 and southeast in 2017. The average wind speed varied little between the months on record, varying between 14–15 km h^{-1} and 10–13 km h^{-1} for 2016 and 2017, respectively. While average wind speeds were similar between the years, the maximum wind speed was 10 km h^{-1} higher in 2016 than in 2017 (Figure S3.4). The air temperature was slightly different between the two years. On average, 2016 was 3.25°C colder during the winter and 1.97°C warmer during summer than 2017. The coldest month also varied, with it being March in 2016 (-21.19°C) and January in 2017 (–18.85°C). The summer months were largely the same with only a one- or two-degree difference between the two years.

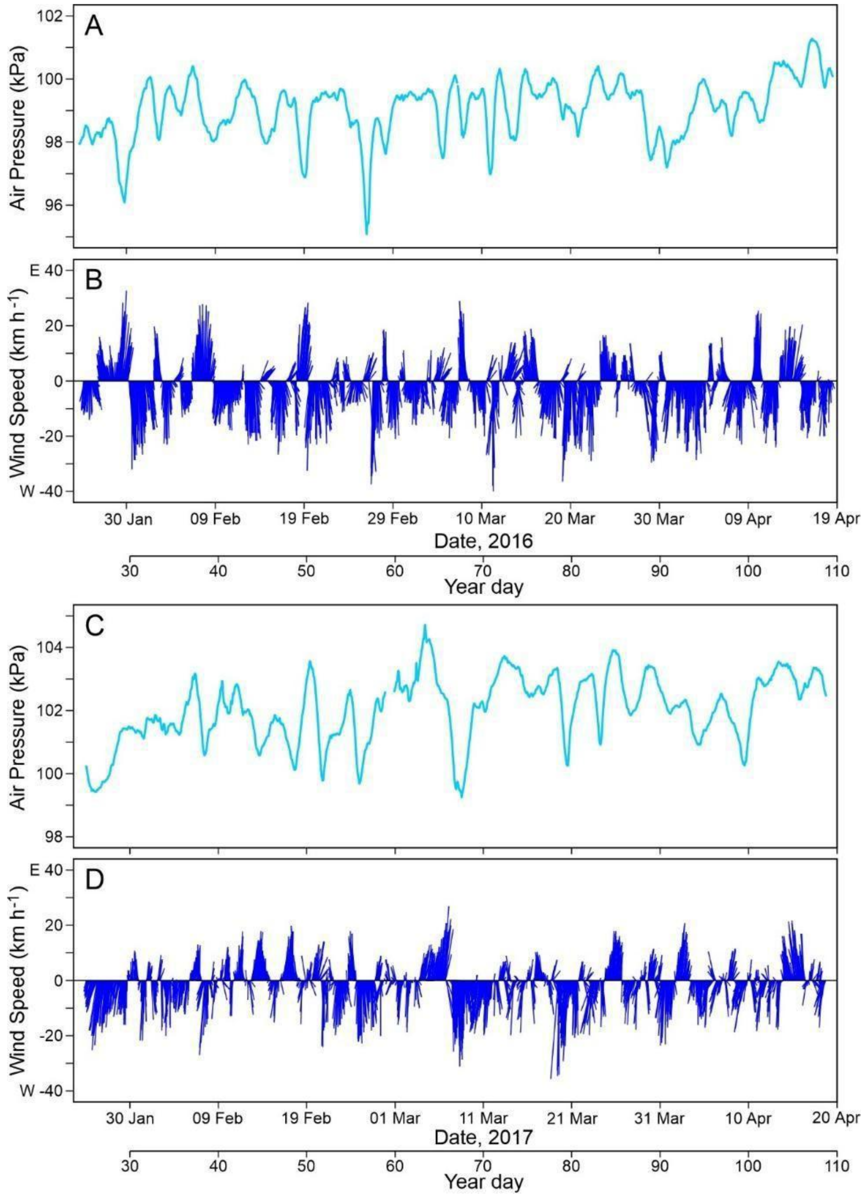

Figure 3.4: Environmental data including A) atmospheric pressure, and B) wind velocity and direction for the winter period of 2016 and C) atmospheric pressure, and D) wind velocity and direction for the winter period of and 2017. Data were collected at the Wemindji airport.

3.3.2 Water levels and tidal analysis

Water level data from two under-ice moorings (CH1-1 and CH4-2) are shown in Figure 3.5. Tidal analysis showed that the dominant tidal constituent at all locations was the semidiurnal M2 at about 0.5 m amplitude. There were significant contributions from other semidiurnal, diurnal and shallow water constituents, with S2 at 0.16 m and N2 at 0.10 m amplitudes being the two largest, resulting in a noticeable neap-spring tidal cycle. The tidal range at CH1-1 was about 1.5 m during the spring cycle and

0.8–1.0 m during the neap cycle (Figure 3.5a). The shallower site CH4-2 in Bay of Many Islands had slightly larger tidal range of 1.8 m during the spring cycle and 0.6–1.0 m during the neap cycle (Figure 3.5b). The residual water levels (red shaded areas in Figure 3.5) reveal that high-water level events exceeding 1.0 m above the recorded mean water level occurred at CH1-1 on 21 and 28 February 2016 (Figure 3.5a) and at CH4-2 on 10 March 2017 (Figure 3.5b). The two high-water level events in 2017 were preceded by low-water events that were more than a meter below the mean and associated with the passage of winter storms.

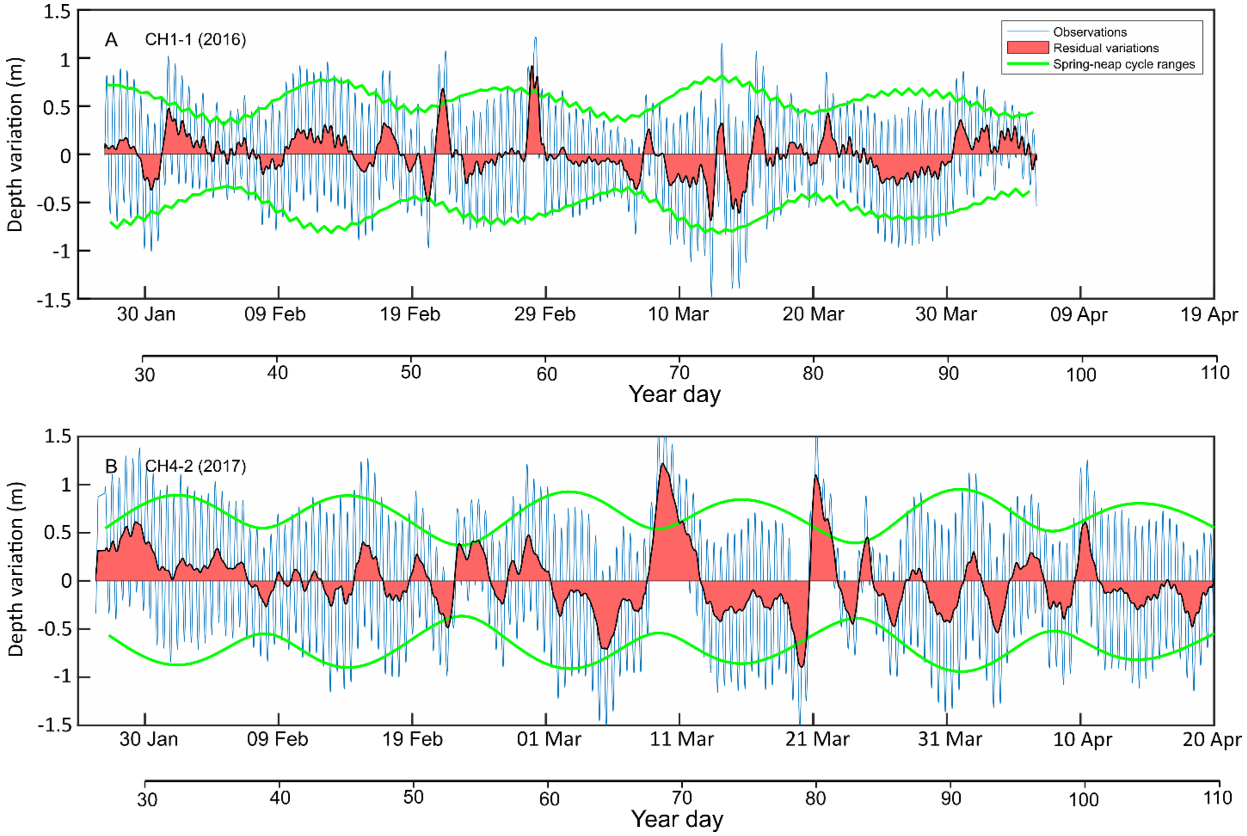

Figure 3.5: Observed water level changes (blue lines) and tidal predictions of tidal ranges (green lines) for A) CH1-1 and B) CH4-2. Tidal predictions were calculated using the T-tide package in MATLAB (Pawlowicz et al. 2002). Red shading show residual variations in water level after subtracting the tidal component.

3.4.3 Current velocity profiles

Progressive vector plots in Figures 3.6–3.8 show the direction and magnitude of the currents at various water depths over the winter period at the same three locations as the variations in water level (CH1-1, CH3-1, CH4-2). During winter 2016, at CH1-1 nearest the river mouth, the near-surface current, measured at 4.5 m depth or about 4.1 m beneath the ice bottom, was generally fast-flowing with an average velocity of 16.7 cm s^{-1} in a north-northwesterly direction (Figure 3.6a). However, there were significant short-term variations in surface current velocities and an overall correspondence between these velocity variations and changes in river discharge (Figure 3.6b). One example is the gradual increase in maximum plume velocities from the beginning of the record through to about YD 55 when peak flows exceeded 20 cm s^{-1}. This increasing trend spanning several weeks reached a maximum of 25 cm s^{-1} on YD 55 (24 February 2016) and was coincident with increasing river discharge. More rapid responses of the core of the plume to changes in river discharge also occurred. For example, several peaks in plume velocity lagged just a day or two behind peaks in daily discharge (measured at LG-1), and intervals of lower plume velocity similarly lagged brief minima in daily discharge (Figure 3.6). The attribution of cause and effect is made complicated by some coincident changes in atmospheric pressure, sea level, and wind speed and direction (Figures 3.4, 3.5, and 3.6).

The evidence for a seasonal thickening of the plume at this location (CH1-1 in winter 2016) in response to sustained high river discharge is provided by the currents at 5.5 m water depth. The flow at 5.5 m was initially weak and towards the south (i.e., opposite direction to the river plume). However, from YD 43 (12 February) onwards, the 5.5 m flow showed similar behavior and direction to the 4.5 m depth, albeit with slower current speeds (Figure 3.6). The storm around YD 58 (28 February) briefly halted the flow at this 5.5 m layer, and briefly slowed down the plume to 13 cm s^{-1} at 4.5 m. We observed a slight change in the average plume direction following the storm (Figure 3.6a). Flows at intermediate depths, i.e., at 6.5 m and 7.5 m depth, at CH1-1 were generally towards the south, with the highest average velocity of 5.9 cm s^{-1} at 7.5 m. Flows decreased with further depth and gradually turned eastward towards the river mouth, possibly steered by the deeper channel. Flows at the deepest water depths were southeasterly and very slow (~0.5 cm s^{-1}; Figure 3.6).

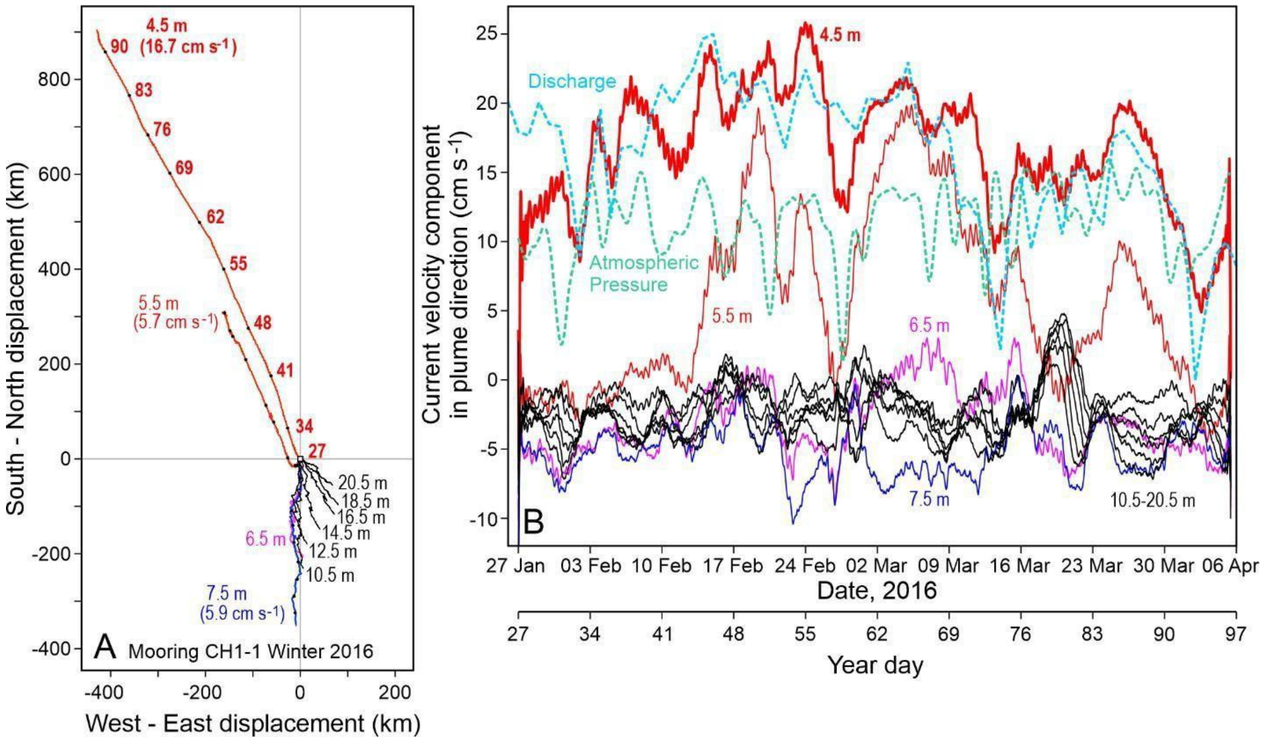

Figure 3.6: (A) Progressive vector diagram of currents at CH1-1 during winter 2016. The vectors are labeled with water depth and average current speed. The black filled circles along the lines show Year Days (weekly intervals). Panel B shows along-plume current velocities for various water depths. The blue dashed line shows normalized daily river discharge (courtesy Hydro-Québec), and the green dashed line shows atmospheric pressure as recorded at the Wemindji airport. For magnitude of discharge and atmospheric pressure see figures 3 and 4 respectively.

During winter 2017, at CH3-1 just north of the river mouth, the near-surface current flowed in a northwesterly direction at an average velocity of 7.6 cm s^{-1} (Figure 3.7a). At greater water depths at CH3-1, the currents weakened and flowed in a westerly direction except at the bottom (14.1 m water depth), where the current flowed slowly (0.5 cm s^{-1}) in an easterly direction (Figure 3.7a). At 6.1 m depth, the flow was almost perpendicular to the direction of the surface plume. The surface current record at CH3-1 shows that the current can change speed and direction over very short time scales. This occurred around YDs 54 (23 Feb 2017), 67 (8 Mar 2017), and 79 (20 Mar 2017) (Figure 3.7b). On YD 54, the surface current changed from 12 cm s^{-1} away from the river mouth to 2 cm s^{-1}towards it. At intermediate depths at this mooring, there was a noticeable change in the current direction around YD 67, following the passage of the 8 March 2017 storm, such that the mean flow thereafter was rotated about 45 degrees to the right (more westward or northward depending on depth) (Figure 3.7).

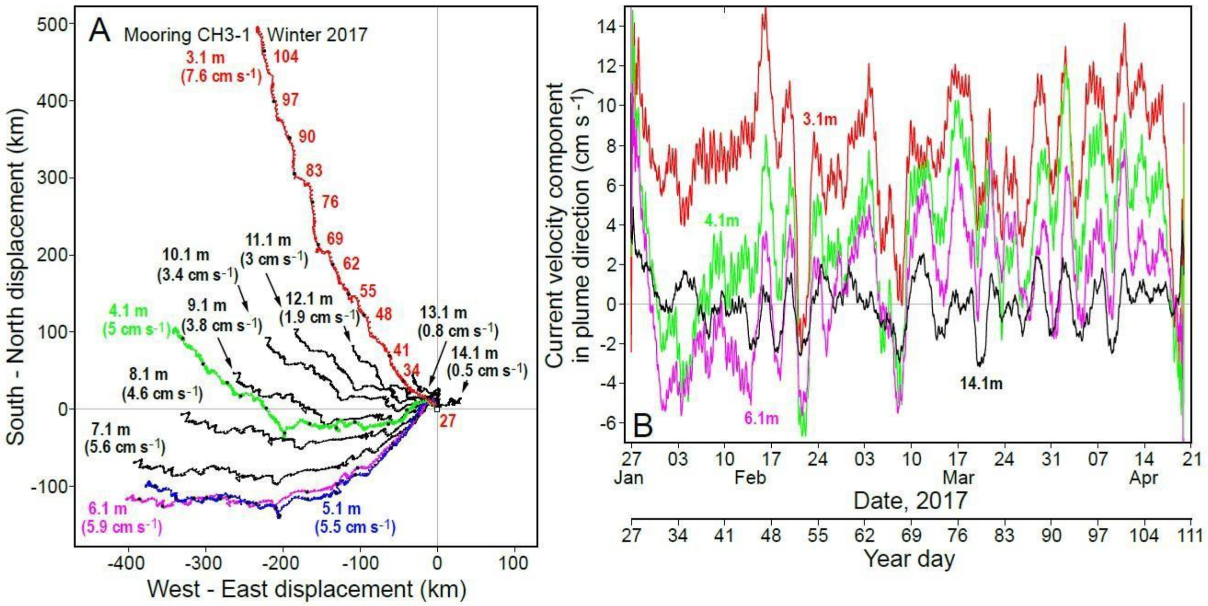

Figure 3.7: (A) Progressive vector diagram of currents at CH3-1 during winter 2017. The vectors are labeled with water depth and average current speed. The black filled circles along the lines show Year Days (weekly intervals). Panel B shows along-plume current velocities for various water depths.

At CH4-2 within Bay of Many Islands, during winter 2017, the surface and intermediate waters flowed west or west-northwest while only the bottom water layers at 9.6 m moved in a southeasterly direction towards the coast (Figure 3.8). The bottom flow was relatively fast (1.4 cm s^{-1}); however, local bottom topography may have affected the currents at this location within Bay of Many Islands where the bathymetry remains uncharted. The currents suggest that there was an anti-cyclonic circulation within the outer Bay of Many Islands area with the mainly westward flow at the CH4-2 needing to be compensated by eastward flow further south in Bay of Many Islands. The small back-and-forth movement in the vectors (Figure 3.8a) reflect the daily tidal oscillations. At CH4-2, they indicate a horizontal displacement of around 2 km per tidal cycle on top of the mean flow of 3.5 cm s^{-1}or about 3 km per day. Because the Bay of Many Islands is over 20 km wide, numerous tidal cycles would be required for flushing.

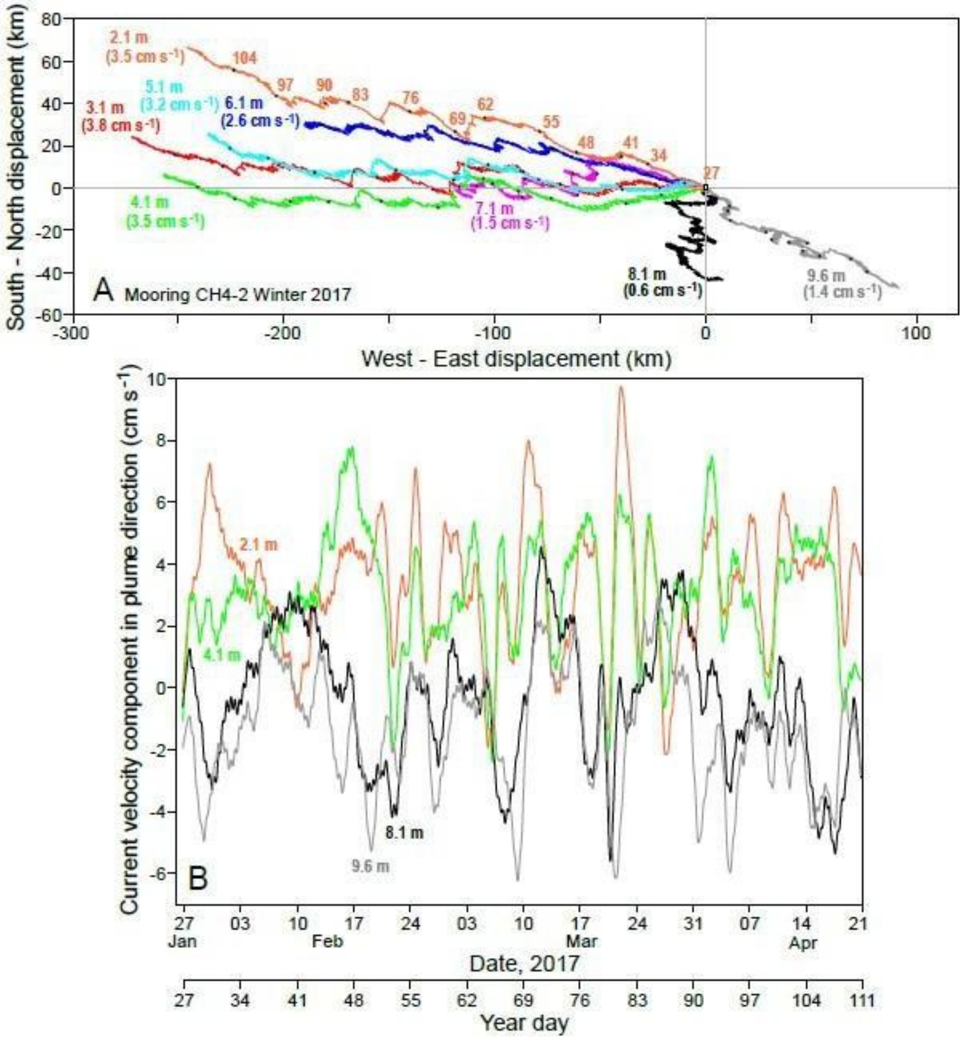

Figure 3.8: (A) Progressive vector diagram of currents at CH4-2 during winter 2017. The vectors are labeled with water depth and average current speed. The black filled circles along the lines show Year Days (weekly intervals). Panel B shows along-plume current velocities for various water depths.

3.4.4 CTD casts

The coastal waters spanned a wide salinity range of 0–25 PSU during the winter months (January, February, March, April) and 0–23 PSU during the summer months (August, September) (Figure 3.9). The frequency distributions of the salinity data were different between seasons, with multiple modes in winter (one at 0–2 PSU, another at 12–13 PSU, and a third at 24–25 PSU; lower inset in Figure 3.9) but with a strong peak near 21–22 PSU in summer (upper inset in Figure 3.9). These differences reflect the differences in water column structure between the ice-covered winter season and the open-water summer. The highest salinity found in summer was <23 PSU, while during winter, the salinity reached >25 PSU at the northern end of the study area reflecting brine input from sea-ice formation and reduced freshwater contribution in offshore waters. The temperature of the coastal waters was slightly above the freezing point across the entire salinity range during winter, in contrast to a wide range of about 5–17.5°C during summer (Figure 3.9).

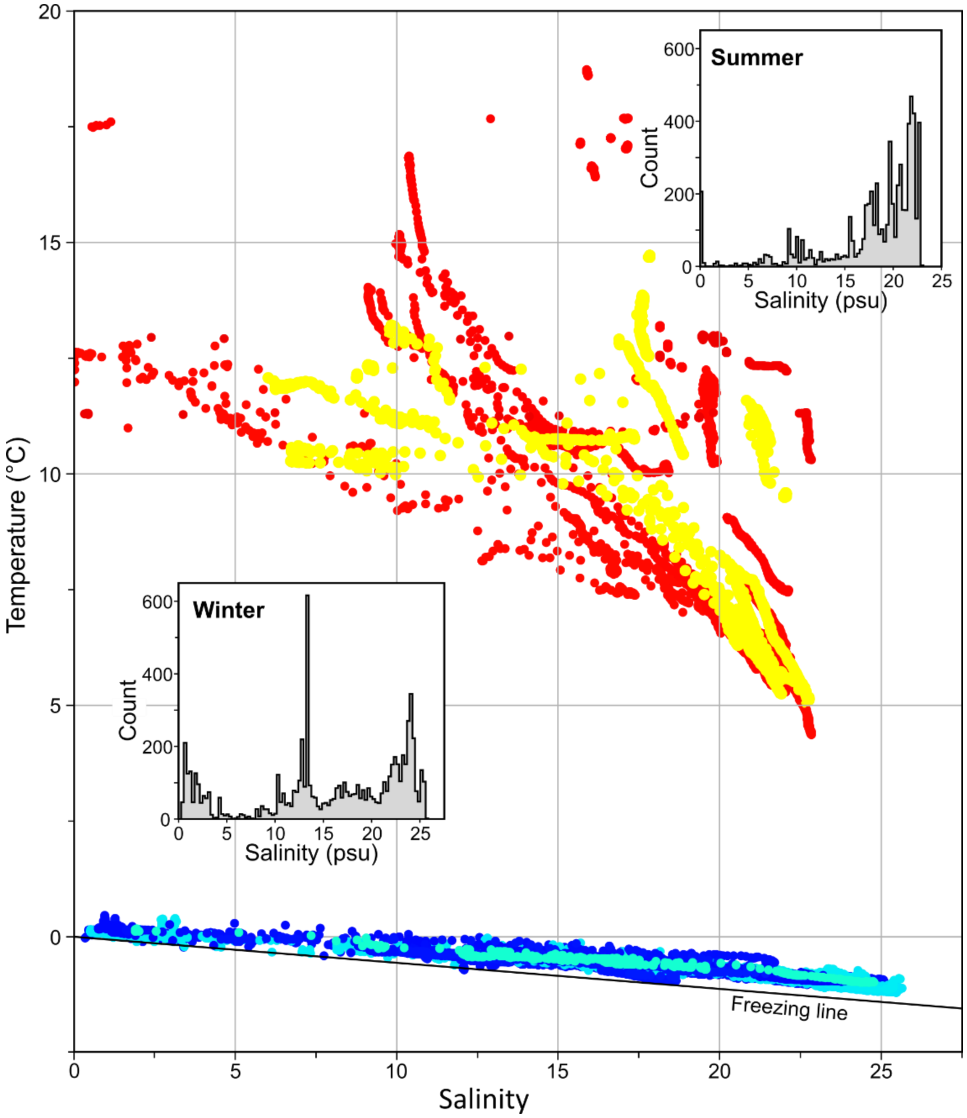

Figure 3.9: Temperature-salinity relationships for winter (Blue dots: January/February. Turquoise dots: March/April) and summer months (Yellow dots: August. Red dots: September) of 2016–2017. Insets show frequency distributions for salinity for the two respective periods. The data represent all CTD casts collected during 2016–2017.

Figures 3.10a and 3.10b show surface salinity distributions in the study area combined for 2016 and 2017 for winter and summer periods, respectively, based on 85 CTD profiles. During winter, there was an area of very low surface salinity (<5 PSU) both north and south of the LGR mouth (Figure 3.10a). This low salinity (0–5 PSU) area, which we estimate to have an area extent of about 1,200 km^2, is referred to as the ‘plume core area’ (following Messier et al., 1989). South of the river mouth, the plume core area extended to the southern limit of the sampling (~20 km from the LGR mouth). To the north of the river mouth, the plume core area extended about 25–30 km north along the coast to around Kakachischuan Point. Further north, in Bay of Many Islands, the surface salinity was about 10–15 PSU during winters 2016–2017 (Figure 3.10a). Further north still, beyond Kakassituq Point, the winter surface salinity was in the range of 15–20 PSU except at a single station located close to the Roggan River, where the surface salinity was <5 PSU(Figure 3.10a). One station sampled north of Cape Jones (properly in southern Hudson Bay) had a surface salinity near 25 PSU (Figure 3.10a).

Vertical salinity profiles within the plume core area during winters 2016 and 2017 showed a highly stratified two-layer water column structure with a very low salinity (0–5 PSU) surface layer, approximately 2 to 5 m thick, right under the ice, and a very sharp pycnocline overlying saltier water (salinity 20–25 PSU) (Figure 3.10c). In a sectional plot of the plume core near Paul Bay (Figure S3.6a), the plume thickness varies slightly from west to east, with the thickness portion in the center, where the 10 isohaline lies at 4 m depth, a slightly thinner portion towards shore, where the 10 isohaline lies between 3 and 4 m depth, and the thinnest portion towards the ice edge, where the 10 isohaline lies just below 3 m depth. In the area near Bay of Many Islands, vertical salinity profiles showed weaker stratification, which implies gradual mixing as the plume propagated further into the bay. The salinity ranged from 8–12 PSU in the surface layer to 13–20 PSU in the deeper portion of the water column between depths of 10 m and the bottom (Figure 3.10c and see Figure S3.6b). The Bay of Many Islands sector represents the frontal region where the highly stratified La Grande plume undergoes strong mixing with the background seawater (Freeman, 1982; Ingram & Larouche, 1987a; Messier et al., 1989). At CH7-1, in the northernmost sector of the study area, the vertical salinity profile showed weak stratification and a relatively high salinity from 25 to 28 PSU (Figure 3.10a, upper inset).

Surface salinity distributions during the summers of 2016 and 2017 (open water conditions; Figure 3.10b) were markedly different compared to those in winter. During summer, there was only a ~10 km region adjacent to the LGR mouth with very low surface salinity (0–5 PSU). Due to greater vertical mixing between freshwater and seawater and weaker vertical stratification during summer (compare Figure 3.10d to 3.10c), almost every location sampled repeatedly during both winter and summer was saltier at the surface during summer, despite the “background salinity” being lower during summer than winter (23 PSU vs. 25 PSU; Figure 3.9). The only exceptions to this general trend were sites located close to small streams that had significant flow during summer but negligible flow during winter. These smaller streams have an important local influence within embayments. However, despite the contribution of local rivers, surface salinities in Bay of Many Islands (CH4) were significantly higher during the summers of 2016 and 2017 (15–20 PSU) than during the corresponding winters (8–12 PSU).

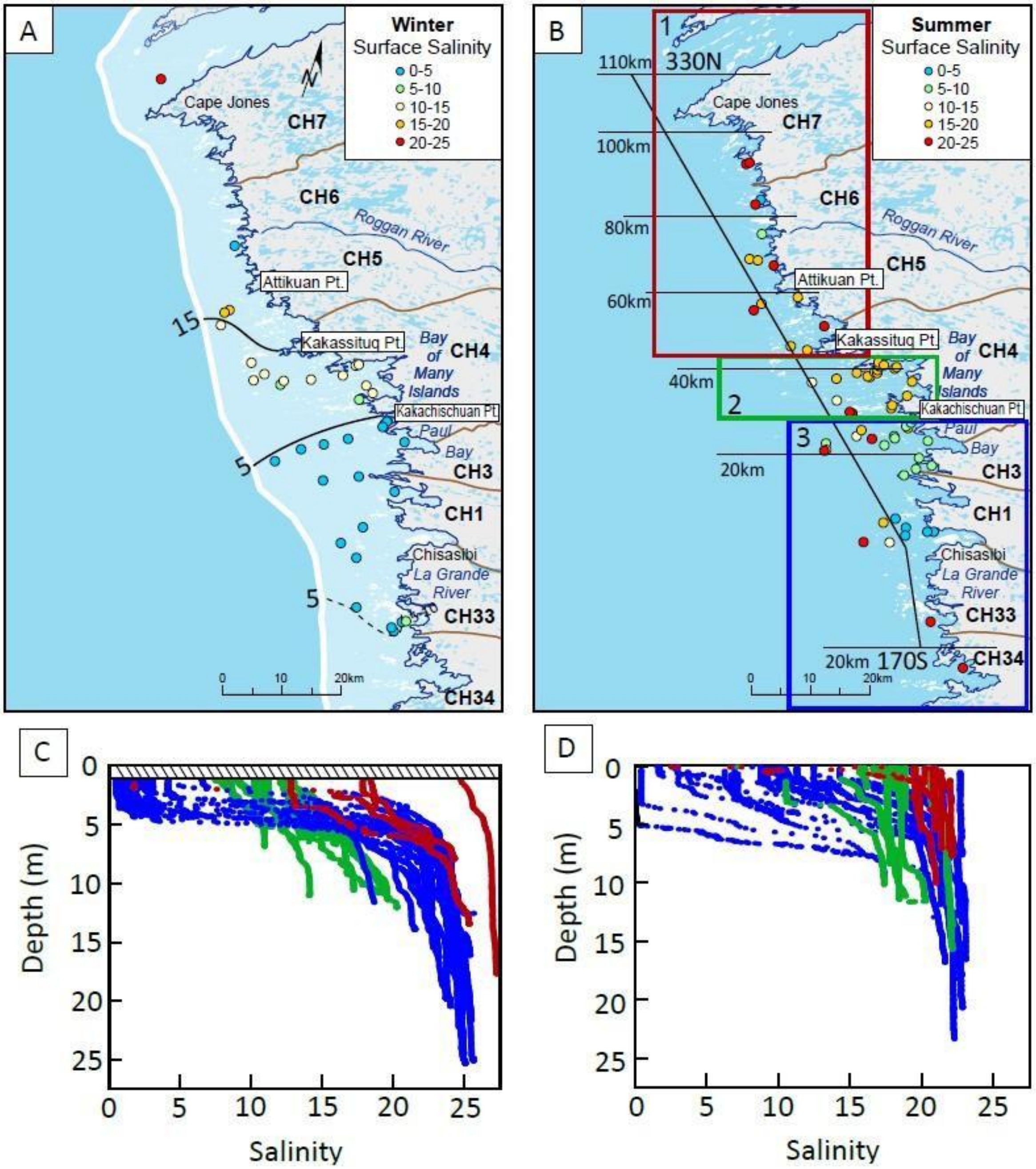

Figure 3.10: Salinity distributions from CTD data. Panel A shows surface salinity distribution along the coast during winter months, and panel B shows summer months. In panel A, the white line indicates the approximate position of the landfast ice edge and in panel C, the hatching represents the landfast sea ice (exaggerated in scale) that overlies the water column. Panels C and D show vertical salinity profiles for winter and summer, respectively, with colors corresponding to the locations of the casts within three sectors of the coast (red, green, and blue boxes labeled 1, 2, 3 in panel B, correspond with the same locations in panel A).

3.4.5 Salinity time series

i) Winter Baselines

The salinity time series records for surface waters immediately beneath the landfast sea ice (depths of ~1.5–3 m) at 15 locations for winters 2016 and 2017 are shown in Figure 3.11 and summarized statistically in Table 3.1. For the plume core area (including the LGR mouth CH1 to the Paul Bay CH3 sector), the surface salinity recorded by the moorings was generally fresh (<3 PSU). Both at the CH1-1 and CH1-2 moorings, there were no deviations in the salinity recorded by the surface sensor greater than 1– 2 PSU regardless of discharge variations and surface salinity changes <0.5 PSU were associated with the tidal cycle (Figure 3.11a). Mooring CH1-1 (2016) was located within a deep channel near the LGR mouth (Figure 3.1), where the water column remained highly stratified by the under-ice plume. The deepest sensor at 20 m depth was characterized by salinities between 25 and 27 PSU with semidiurnal tidal variations of about ±0.5 (Figure 3.12a). The average water flow at that depth was towards the LGR (Figure 3.6).

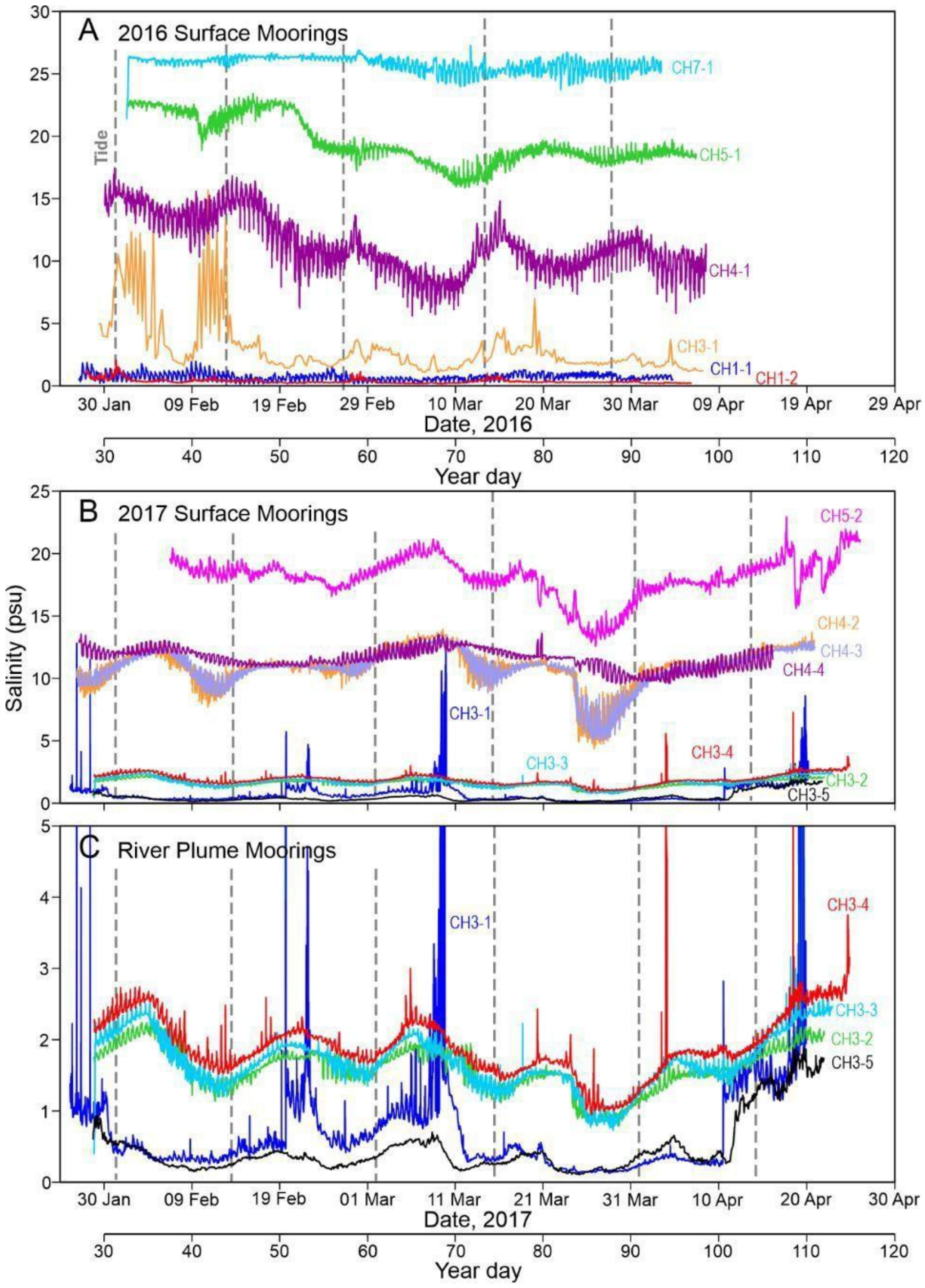

Figure 3.11: Salinity records for CT sensors tethered beneath the ice (depths of ~1.5–3 m) in 2016 (A), 2017 (B). Panel C shows an enlargement of the low-salinity portion of the time series for moorings close the river mouth in 2017. Note the change in the y-axis scale for panel C. The dashed vertical lines represent the spring tide peak.

For the Bay of Many Islands sector (CH4), records from four moorings yielded average salinities of about 11 PSU. For the north coast sector, the two sensors within the CH5 sector (Table 3.1) yielded average salinities of 18.1 PSU and 19.6 PSU, respectively, and further increased to 25.8 PSU at CH7-1, located between Cape Jones and Long Island (Figure 3.1). This latter value is about one unit higher than the average salinity recorded in 2015 at Cape Jones (Eastwood et al., 2020). The relatively small standard deviations of all the individual salinity records show that plume structure remained constant during the landfast ice-covered periods. The only exception was the record from mooring CH3-1 (2016), which displayed large salinity variations on a daily and spring-neap tidal cycle. We attribute these strong tidal variations to the sensor having been placed at too great a depth in the water column such that it was periodically lowered through the halocline into the saltier subsurface waters on each tidal cycle. Even after filtering the CH3-1 (2016) record to remove saline portions of the daily cycle (Figure 3.11; see Methods for details), the standard deviation remained higher than for other records, and the average salinity notably higher than for the 2017 record at the same location (Table 3.1).

The salinity time series (Figures 3.11 and 3.12) generally revealed three types of variability: (i) seasonal evolution related to the dispersion of riverine influx and regional hydrography; (ii) regular oscillations associated with the tidal cycle (both semi-diurnal and spring-neap); and (iii) abrupt short-duration changes associated with the passage of weather systems. Moorings from the same sectors of the coast (mooring series) generally showed similar variability. Tidal oscillations were most discernable in the surface salinities of the CH4, CH5, and CH7 series of moorings, whereas abrupt, short-duration increases in surface salinity from very fresh conditions characterized the CH1–CH3 moorings. The magnitudes of the time-dependent surface salinity variations within the different sectors were similar during the two winters; for example, there was about a 7-unit salinity variation at CH4-1 in 2016 (Figure 3.11a) and at CH4-2 and CH4-3 in 2017 (Figure 3.11b). A few salinity variations affected multiple sectors simultaneously or in short succession such as the freshening event in late March 2017, which was evident in CH3 series moorings, CH4 series moorings, and CH5-2 (Figure 3.11b). Similarly, in 2016, a freshening trend in early March showed a reversal towards more saline conditions beginning at around 11 March in moorings from the CH3, CH4, CH5, and CH7 sectors (Figure 3.11a).

The influence of weekly and longer variations in river discharge in the frontal region was evidenced by the gradual freshening at the CH4, CH5, and CH7 moorings from February through March 2016 (Figure 3.11a). This seasonal freshening is remarkable because it opposes the typical increase in salinity in high-latitude coastal waters due to brine input from sea ice formation (Eastwood et al., 2020). We attribute this trend to the accumulation of freshwater in the system during extended periods (week or longer) of high discharge from the LGR (Figure 3.3). The absence of a seasonal trend (neither a seasonal increase nor decrease) at the CH4 and CH5 moorings during winter 2017 may be linked to a difference in the discharge compared to 2016 (Figure 3.3). The subtle freshening trend at CH7-1 (the northernmost mooring) during early March 2016 (Figure 3.11a) indicates that the influence of the La Grande wintertime discharge reaches into southern Hudson Bay. Fluctuations in salinity over each semidiurnal tide cycle at CH7-1 also indicate river plume influence (i.e., the influence of vertical salinity stratification in the near-surface layer).

The three moorings that included current and water level measurements in addition to time series of salinity at multiple depths (i.e., CH1-1 (2016), CH3-1 (2017), and CH4-2 (017)) permitted a more detailed examination of the estuarine circulation (Figure 3.11b). Generally, the water columns at the three sites remained stratified and relatively stable throughout the landfast ice-covered period despite atmospheric and tidal forcing and the variations in LGR discharge (Figure 3.12). However, a few events in each mooring record bear pointing out.

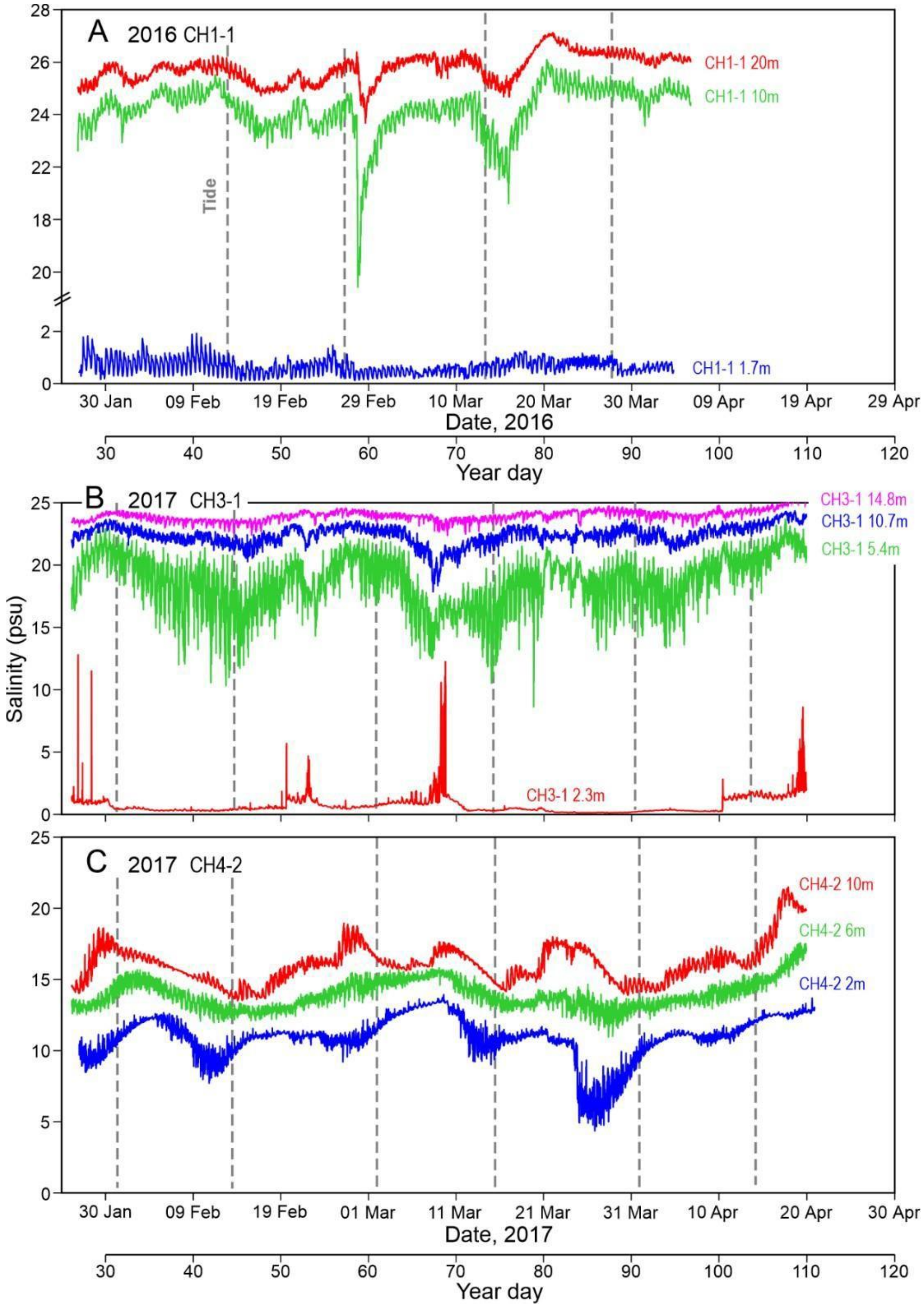

Figure 3.12: Salinity records for CT sensors placed at multiple water depths for mooring sites CH1-1 (A), CH3-1 (B), CH4-2 (C). Note the change in the y-axis scale for panel A. The dashed vertical lines represent the spring tide peak.

ii) Short-Duration Events at CH1-1 (2016)

The most pronounced of these events was the major winter storm of 25–29 February 2016 (YD 56–60), when an abrupt decrease in salinity from 24 PSU to ~20 PSU occurred at 10 m water depth concurrent with a ~2 PSU decrease in salinity at 20 m depth (Figure 3.12a). The surface salinity changed very little, being already near zero, but there was a pronounced decrease in the velocity of the plume and even the subsurface layer flowed inshore towards the river mouth (Figure 3.6). The subsurface salinities returned to their initial states within a few days, although the return was more gradual than the initial abrupt drop. The winter storm that backed up the river water near the river mouth in this way was very powerful with westerly wind speeds of 45 km h^{-1} and gusts reaching 85 km h^{-1} (Figure 3.4). This freshening event coincided with the largest observed (within our study) decreases in atmospheric pressure (Figure 3.4a) and a ~1 m increase in the water level around 27 February 2016. The storm and the responses of coastal waters in western Hudson Bay have been described in detail (Dmitrenko et al., 2021). For the LGR plume, the intense winter storm came at a time when river discharge was high and there was a spring tide (Figure 3.3). A later freshening event centered on 15 March 2016 at CH3-1 (2016), with a less abrupt and smaller magnitude decrease in salinity at 10 m and 20 m (Figure 3.12a), did not correspond to an unusual atmospheric pressure decrease but did coincide with large variations in sea level (Figure 3.5a) and a slowing down of plume current speeds at CH1-1 (2016).

iii) Short-Duration Events at CH3-1 (2017)

At CH3-1 in 2017 (Figure 3.12b), the most significant short-term decrease in subsurface salinity occurred around the 8 March 2017 storm event, during which we recorded a 1.5 m increase in water level over a few days (Figure 3.5b). During this event, there was a partial breakdown in water column stratification due to mixing, with the salinity at 5.4 m and 10.7 m depths decreasing while the salinity at the surface increased (Figure 3.12b). The salinity peak of 12 in the surface layer on 9th September occurred more than a day behind the salinity minima at 5.4 m and 10.7 m depths, which may have been a consequence of the estuarine circulation pattern (Figure 3.7). The salinity at all depths returned to previous levels within a few days as the storm passed. Overall, the observations at CH3-1 generally support previous work showing that wind forcing on areas with mobile ice (i.e., coastal flaw lead) can still transfer wind stress to the water column below landfast ice (Buckley et al., 1979; Dmitrenko et al., 2020; Dmitrenko et al., 2021; Kasper & Weingartner, 2012; Schulze & Pickart, 2012). However, the rapid return to pre-storm conditions highlights the dominance of the LGR discharge within the core plume area.

iv) Short-Duration Events at CH4-2 (2017)

At CH4-2 (2017), water column stratification was maintained throughout the record and the salinity difference between the surface and bottom layers varied between 3–6 PSU (Figure 3.12c). The impact of the 8 March storm was not as abrupt as at the more exposed CH3-1 but may have resulted in the highest average water column salinity of the high discharge winter period. The higher water column salinity recorded during the second half of April 2017 was likely a result of reduced discharge (Figure 3.3) and/or the breakup of landfast ice (Figure S3.3).

The largest and most abrupt surface freshening event observed in the frontal region was between 24 to 31 March 2017, when salinity at CH4-2 and CH4-3 decreased from 11 to 5 PSU for several days before returning to ~11 (Figure 3.11b). This event preceded and appeared to intensify the increase in stratification expected for the less dynamic neap tide period and indeed a salinity difference of ~11 PSU between surface and bottom was briefly observed (Figure 3.12c). The timing also coincided with a period of high river discharge between 12–20 March 2017 (YD 71–79; Figure 3.3) and strong westerly winds (17 March had the strongest wind speeds of the 2017 winter; Figure 3.4d). The currents experienced a reversal in direction on ~20 March and then a strong intensification to reach the largest current speeds of the winter (~10 cm s^{-1}; Figure 3.8). Immediately thereafter there was an abrupt decrease in surface salinity and concurrent freshening of near-bottom waters (at 10 m depth). We interpret this event as resulting from the advance of the LGR plume front into Bay of Many Islands, and while wind forcing appears to have been required, we note that sustained high river discharge may have been necessary preconditioning for the magnitude of the salinity drop. In 1980, a flushing time of about 12 days was estimated for the "highly stratified region" of the LGR winter plume (Freeman, 1982), which is similar to our river mouth-Paul Bay sector. This 12-day lag roughly matches the delay between the beginning of the period of increased river discharge and the low surface salinity anomaly at CH4-2.

Interestingly, the decrease in salinity at CH4-2 and CH4-3 between 24 to 31 March 2017 did not translate into a corresponding decrease at CH4-4, which is an adjacent inshore site supporting some of the most abundant eelgrass beds in James Bay. Thus, it appears that the tidal-driven mixing in the narrow and shallow channels had a protective effect by hindering the fresher surface waters from reaching the eelgrass beds without mixing with subsurface water.

3.5 Discussion

3.5.1 Under-ice plume structure and extent compared to past observations

The horizontal structure of the LGR under-ice plume during winters 2016 and 2017 consisted of three sectors or zones: (i) a plume core area of very low surface salinity (<5 PSU) and strong stratification stretching north from the river mouth to Paul Bay and Point Kakachischuan (CH3) and south to at least CH3-3; (ii) a frontal region where salinity increased rapidly across a short horizontal distance in the Bay of Many Islands sector (CH4 to Point Attikuan in CH5); and (iii) a large region of freshwater influence extending all along the northeast coast of James Bay in which surface salinity was notably diluted (Figure 3.10a). The same sectors have been previously observed, although some of the northern boundaries shifted northward between 1976, 1980, and 1987 with increases in winter river discharge as discussed further below (Freeman, 1982; Freeman et al., 1982; Ingram & Larouche, 1987a; Messier et al., 1989; Messier, 2002). Although our time series data show minor variations in surface salinity within each sector between January and April (Figure 3.11, Table 1), the overall picture that emerges is of an extremely stable plume structure, both throughout the period of landfast ice cover each year (2016 and 2017) and between the two years. We attribute this to the LGR discharge remaining relatively high (averaging 4,800 $m^3 s^{-1}$ from January–March, and slightly below 4,000 $m^3 s^{-1}$ in April of both 2016 and 2017; see Figure S3.5) and the landfast sea ice cover remaining intact. This apparent stability of the plume throughout winter agrees with previous findings for high discharge conditions (Messier et al., 1989; Messier, 2002). Nevertheless, our observations are the first to continuously record estuarine conditions for spans of several months. This wintertime plume is best classified as a rotational prototypical plume due to the LGR mouth being perpendicular orientation to the coast and the influence of the Coriolis effect, which causes northward deflection of the freshwater along the coast (Figure 2.2) (Horner-Devine et al., 2015). The presence of landfast ice enhances stratification and lateral spreading, reinforcing the rotational characteristics. In contrast, during the ice free summer the LGR is more transient and less stratified, with greater vertical mixing, resembling a non-rotational with the core of the plume constrained to the mouth of the LGR.

The dynamics of the LGR under-ice plume and the changes in its extent were studied several times during the February–March periods of 1976–1984, as winter discharge was modified by the first phase of La Grande development and winter discharge increased from 460 $m^3 s^{-1}$ (natural conditions in 1976), to 1,750 $m^3 s^{-1}$ (1980) and then 3,000 $m^3 s^{-1}$ (1984) (Ingram & Larouche, 1987a). Another survey was conducted during February–March 1987 when discharge exceeded 4,000 m3s-1at times of peak power production and averaged about 3,700 m^3 s^{-1} (Messier et al., 1989). In Figure 3.13, we compare the plumes during winters 2016 and 2017, when February discharge averaged 5,040 m^3 s^{-1} and 4,900 m^3 s^{-1} respectively, to these previous published observations. Following the previous workers, we show surface salinity as a function of distance from the LGR mouth (Figure 3.13). Although comparison of the salinity of the surface layer in Figure 3.13 shows that the increases in discharge have grown the overall region of influence of the LGR during winter as defined by measurable dilution of surface waters, and also the brackish region contained by the 20 isohaline, a striking result is that there is no conspicuous northward expansion of the plume core area relative to 1987 in the 2016–2017 data set, despite a 30% increase in winter discharge.

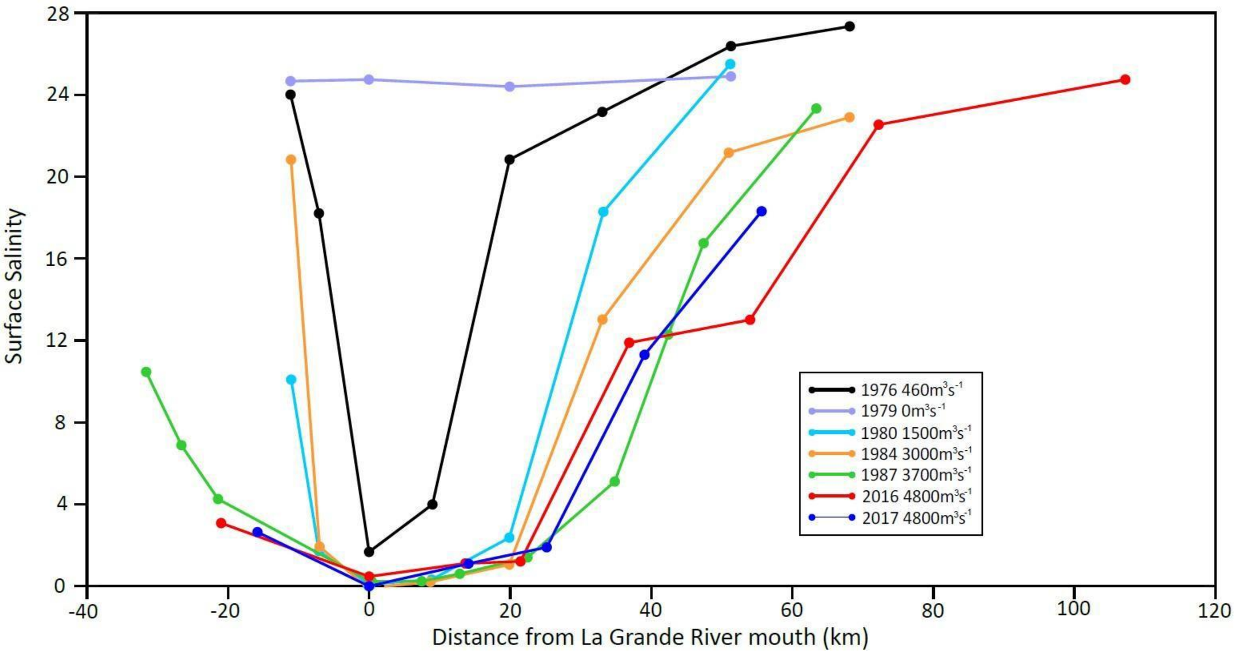

Figure 3.13: Surface salinity as a function of distance from the LGR mouth during winters 1976, 1979, 1980, 1984, 1987, 2016 and 2017, after Ingram and Larouche (1987a) (Years 1976, 1979, 1980, 1984) and Messier et al. (1989) (Year 1987) and based on CTD data from winters 2016 and 2017. Mean LGR discharges for February of each respective year are shown in the legend. Distance is measured from the LGR mouth along the bearings shown on Figure 3.1.

With no conspicuous northward expansion of the plume core area, one wonders whether the thickness of the plume would have increased by 30% to accommodate the increased winter discharge. Freeman (1982) described the plume as varying in thickness from 2 to 5 m and noted that increasing the discharge generally increased the thickness of the plume. A thickness of 2 m is rare in our observations especially those from late January to early April (we do not have observations from February or March to compare directly with those given in Freeman (1982) and other early works). In their Figure 4, Messier et al. (1989) showed a plume thickness of about 4-5 m depth, depending on distance from the river mouth and proximity to shore and the ice edge. We do not have the same data distribution as Messier et al. (1989). However, comparing CTD casts and a section at Paul Bay in the core plume area in 2017 (Figure S3.6a) with the Baie des Oies section shown by Messier et al. (1989) in their Figure 3.4b, we conclude that the thickness of the plume has remained unchanged, at an average of about 4 m (Figure S3.6a). The 10 isohaline lies between 4 and 5 m depth in the Baie des Oies section shown in Messier et al. (1989), which compares well with the 4 m depth of the isohaline in our Paul Bay section, considering that the Baie des Oies section is closer to the river mouth than our Paul Bay section. We note that another source of variation is that our data were collected earlier and later in the season than that of Messier et al. (1989).

We also do not know the variation in discharge during the weeks leading up to the sampling presented in the Messier et al. (1989) work. Nevertheless, from the similarity in the areal extent of the core of the plume, and the plume's apparent thickness, despite the 30% increase in discharge, we conclude that the majority of the freshwater discharge does not remain in the core area of the plume under present conditions. Based on simple freshwater budget calculations that assume a plume thickness of 4 m, mean plume salinity of 2 PSU, ambient salinity of 28 PSU, and 110 days of mean winter discharge into the ice-covered coastal area (Table 3.2), only 7% of the cumulative winter discharge for 2016 and 2017 is needed to "fill up" the core plume area (~1,200 km^2), which takes only about 10 days at mean winter discharge. The core area is based on the 5 isohalines, which in turn was determined by the CTD casts (Figure 3.10). The southern isohaline is an estimate based on the data we had available. More than 90% of the cumulative discharge over the winter period must therefore be transported either north, south or offshore of the core area. This reflects a rapid rate of freshwater flushing or turnover in the core plume area compared to 1976, when the percentage of winter discharge retained in the core plume area of 200 km2 would have been almost double (17%) what it was in 2016 and 2017. Most striking in Table 2 is that a constant mean winter discharge of 460 m^3 s^{-1}, which was the natural discharge in winter 1976 (Ingram & Larouche, 1987a), would have taken about 19 days to "fill up" the core plume area of 200 km^2, compared to the ~10 days it takes now to fill the core plume area of ~1,200 km^2. These estimates should be used with caution because of the simplifying assumptions (uniform plume thickness of 4 m, mean salinity values of 2 PSU and 28 PSU). If there is seasonal thickening of the plume and/or variation from one month to another with variations in discharge, then this is another source of error in the times estimated in Table 3.2. Assuming the results are reasonable despite these potential errors, the implication is that the freshwater turnover rate in the core plume area under recent winter discharges is much faster (higher) than under natural winter conditions, which has implications for renewal rates of nonconservative properties like river- derived nutrients.

Table 3.2: Freshwater budget calculations based on simplifying assumptions that during each year the mean winter river discharge continued for a period of 110 days (ice-covered period), plume thickness was uniformly 4 m, mean salinity of the plume was 2, and mean salinity of the ambient waters was 28. Mean winter LGR discharge and core plume area varied each year according to Ingram and Larouche (1987a) for 1976, 1979 and 1980, and Messier et al. (1989) for 1984 and 1987. Data for 2016 and 2017 are from the present study.

Year	Mean discharge ($m^3 s^{-1}$)	Plume core area (km^2)	Area fill-up time (days)	River water retained in core area	River water lost from core area
1976	460	200	19	17.00%	83.00%
1979	0	n/a	0	0.00%	0.00%
1980	1750	650	16	14.5%	85.5%
1984	3000	1200	17	15.6%	84.4%
1987	3700	1200	14	12.7%	87.3%
2016	5035	1200	10	9.3%	90.7%
2017	4900	1200	10	9.6%	90.4%

Southward expansion of the plume in winters 2016 and 2017, relative to winters 1976, 1980, and 1984, is apparent in Figure 3.13. Observations in Messier et al., (1989) indicate that southward spreading of the plume core had begun in 1987. The southern spreading showed a similar trend as the spreading in the north with the salinity increasing after 20 km but reaching a higher salinity more quickly. A salinity of 11 is found at 30 km which in 1980 was found at 10 km south of the river mouth. This finding was confirmed in monitoring undertaken in winters 1993 and 1995, when the discharge was around 4,400–4,600 $m^3 s^{-1}$ after the commissioning of the La Grande-2-A and La Grande-1 generating stations (Messier, 2002). Without continuous time-series data available from the past, it remains unknown if the under-ice plume spreads southward gradually throughout winter or abruptly, for example, in response to weather events or change in density gradient due to build-up of river runoff at the river mouth.

Offshore (westward) plume expansion past the landfast ice edge cannot be evaluated with our 2016–2017 data, which are limited to the landfast ice-covered zone. However, observations by Messier et al. (2002) that took place seaward of the landfast ice edge in February 1993 and 1995 showed that the westward extension of the plume was closely related to ice concentration and wind forcing, with more open-water conditions in 1995 promoting more rapid mixing and smaller westward expansion compared to 1993. In idealized numerical simulations, frictional coupling of a buoyant under-ice plume with the landfast ice cover slowed down the offshore spreading of the plume causing the plume to be thicker than when the ice is absent (Kasper & Weingartner, 2015). Based on the modelling results, changes in the position of the ice edge are inferred to be quite important for the evolution of a plume because freshwater leaking beyond the ice edge into the open water areas formed a fast-flowing, buoyant, ice-edge jet that would not preserve the strong stratification observed under the ice cover. A notable shortcoming of the idealized simulations is the absence of under-ice topography in the form of deep ice keels, which would add significant drag and serve to further confine a plume along the coast.

An increase in the overall region of influence of the LGR during winter with increasing wintertime discharge, as was predicted from observations of plume expansion during 1976–1984 (Ingram & Larouche, 1987a), is supported by the observations during winter 2016/2017. These workers measured dilution of surface waters by the La Grande plume at 70 km north of the river mouth in 1984 and estimated the full northward dilution extent in 1984 at 110 km, based on linear extrapolation of the 1976 and 1984 data. During winter 2016, we measured a surface salinity of 25–26 PSU at mooring CH7-1 at 100 km north of the river mouth (Table 3.1), which is about 1–3 units lower than under natural conditions where a salinity of about 28 PSU was typical for the winter surface outflow in northeast James Bay (El- Sabh & Koutitonsky, 1977; Prinsenberg, 1986a; 1986b). A previous study (Eastwood et al., 2020) reported observations of a mean salinity of 25 PSU (range 23–26 PSU) at a site about 5 km southwest of CH7-1 during February–March 2015. Thus, the region of freshwater influence of the La Grande in winter presently reaches to southern Hudson Bay. The rate at which the freshwater is transferred into the offshore marine system also must have increased, in keeping with the higher rates of freshwater loss from the plume core area, and the larger boundary along which this transfer occurs. Comparing the salinity of the surface layer at distances of ~40 to 80 km north of the river mouth (Figure 3.13) also leads to the conclusion that there has been an increase in the size of the brackish water area with the recent increases in winter discharge. The excess 4,000 $m^3 s^{-1}$ (or ~43 km^3 over January to April) of wintertime freshwater input will have downstream effects on the southern Hudson Bay marine system (Eastwood et al., 2020).

The input of buoyancy in winter will tend to increase water column stability, reduce deep-water ventilation, and reduce nutrient replenishment to the euphotic surface layer across the region of freshwater influence in southern Hudson Bay and James Bay.

3.5.2 The role of the landfast ice cover in freshwater-marine coupling

A unique aspect of the present data set is its large number of moorings monitoring changes in salinity of the under-ice plume in the different sectors of the landfast ice-covered coastal domain. Despite the overall stability of the under-ice plume structure, both seasonal and short-term dynamics (daily to weekly time scales) were observed throughout winter, which affected surface salinity, subsurface salinity and water levels, the tidal cycle, and flow velocities, as presented in section 3. The critical role of the landfast ice cover in maintaining the plume structure is highlighted by the large difference between ice covered and open water conditions (Figure 3.9).

In the core area of the plume, the salinity of the surface layer was controlled by the combination of discharge and sea ice extent as described above, with short-term storm-related events only briefly perturbing the stratification and salinity of the surface layer. The strong westerly winds during storms pushed mobile sea ice and, through the transfer of wind stress, accumulated water up against the coast, as observed elsewhere (St-Laurent et al., 2011). This resulted in accumulation of buoyant discharge near the river mouth and the accumulation of more saline offshore waters at the moorings, particularly CH3-1. Evidently the storms created conditions beneath the landfast ice cover, 10–20 km away from the floe edge, in which freshwater was more readily mixed to deeper depths (Figure 3.12a, b).

The stability of the northward limit of the plume core despite the discharge increase supports the notion that landfast ice extent, which has not changed notably during recent decades (Taha et al., 2019, Gupta et al. 2022), is a key control on under-ice plume structure, as discussed in general terms by past workers. The 20–25 km width of the landfast ice (Figure 3.2) in the coastal area off the LGR mouth allows the freshwater plume to expand largely unmixed until it reaches the floe edge. The position of the floe edge has remained roughly constant between the 1980s and recent years (compare Figure 3.1 with the 1980 ice edge (Freeman, 1982)) probably because it is stabilized by offshore islands and reefs. The abrupt narrowing of the landfast ice zone at Kakachischuan Point about 35 km north of the river mouth (Figure 3.2), which reflects the coastal geometry, appears to control the northward extent of the plume core area. Comparing Figure 3.2 and Figure 3.13, the narrowing of the landfast ice zone can be seen to coincide with the breakdown in stratification and increase in surface salinity beginning in the Bay of Many Islands (CH4) sector. Were it not for the coastal geometry and narrowing of the landfast ice limiting the northward spreading of the unmixed plume, we expect the area extent of the core plume area would have expanded well beyond 1100–1200 km^2 after 1980, as discharge was increased, like the increase in area extent that occurred between 1976 and 1987 (Table 3.2). This also means the vertical salinity gradient within Bay of Many Islands, which we found to include a low salinity of 8-10 PSU at the surface and steady increase with depth to as much as 20 PSU near the bottom in some places (Figure S3.6b), has remained unchanged since 1987 and the winter measurements reported by Messier et al. (1989).

According to the above scheme, provided the landfast ice cover remains roughly the same in the future, we would not expect to find increases in the area occupied by the stratified plume core even in the face of higher winter discharge. This projection contradicts the area-discharge relationships proposed based on observations during the early years of plume core expansion (Ingram & Larouche, 1987a). The result from that early study appears to be representative of a period when the winter freshwater discharge did not exceed the accommodation space provided by the area of the landfast ice platform found immediately north of the La Grande River mouth (Figure 3.2). Given projections of warming, or potential human activities (such as icebreaker use), it is more likely that the landfast ice extent and persistence are reduced in the future, in which case we would expect the wintertime plume core area to decrease from its present size.

Indirect evidence of the importance of the landfast ice floe edge in limiting offshore plume spreading and influencing under-ice plume structure is found in the increases in salinity late in the mooring period in 2017 following an early partial breakup of the landfast ice in April 2017 Typically, breakup occurs mid-May in the area of the La Grande estuary (Taha et al., 2019; Gupta et al., 2022). A MODIS satellite image from 16 April 2017 captured large sections of the outer portion of the landfast ice breaking off and moving westward into the flaw lead (Figure S3.3). CH3-1 and CH3-5 both showed immediate abrupt increases in salinity after 10 April 2017 that we suspect relate to the under-ice plume spilling out into the flaw lead after the rough outer ice edge broke off. We do not know enough about the properties of the outer edge of the landfast ice (i.e., keel depth) to deduce if it acts like a barrier, channeling or blocking under-ice flows, like the stamukhi zone on the Mackenzie shelf (Carmack & Macdonald, 2002; Macdonald & Carmack, 1991; Macdonald et al., 1995) or whether the major role of the landfast ice is limited to preventing direct wind mixing of underlying waters (Ingram, 1981; Ingram & Larouche, 1987a). The event highlights the potential in this setting for storm-driven changes in the extent of a thinner and weaker future landfast ice cover to lead to premature dispersal of plume waters into the lead.

3.5.3 Implications for salinity at inshore eelgrass habitat

The northeast coast of James Bay was once known for extensive eelgrass meadows, which were found all along the coast except at the river mouths and achieved, in many areas, high density and biomass (Lalumière et al., 1994). Massive and unprecedented eelgrass losses were observed in the spring of 1999 (Dickey, 2015) and limited recovery of the eelgrass occurred during subsequent decades. For example, in 2019, mean eelgrass vegetative shoot density was 213.49 ± 12.96 m^{-2}, which is significantly lower than (less than half) the mean value of 537.02 ± 38.26 m^{-2} in 1995 (Leblanc et al., 2023). Similarly, mean eelgrass aboveground biomass was 35.94 ± 3.26 g dry weight m^{-2} in 2019 compared to 185.31 ± 13.27 g dry weight m^{-2} in 1995. Mean shoot lengths of the eelgrass were 43.88 ± 0.90 cm (range of 11.3–104.9 cm) and 41.65 ± 1.00 cm (range of 13.9–99.2 cm) in 2019 and 2020, respectively. In contrast, the shoots of "the most vigorous" eelgrass sampled between 1986 and 1991 reached 2.5 m length (Lalumière et al., 1994). The cause(s) of the massive eelgrass decline, and the limited recovery are the focus of a comprehensive research program that began in 2017 and concluded in 2023.

Altered salinity is widely recognized as a factor that can severely impact eelgrass health. Eelgrass populations tolerate a wide range of salinity (typically 5–35 PSU), but experiments show that lowering the salinity to which eelgrass is exposed decreases plant production, regardless of the initial salinity it was exposed to (Salo et al., 2014). Both laboratory and field studies show that chronic exposure to salinity below 10–15 PSU can negatively affect eelgrass growth, reproduction, and survival (Nejrup & Pedersen, 2008; Salo et al., 2014; Zhang et al., 2022). Specifically, prolonged exposure (>4–6 weeks) to salinities below 10 PSU has been shown to reduce photosynthetic efficiency, increase metabolic stress, and impair carbohydrate storage, which is key to overwintering survival (Biebl & McRoy, 1971; Touchette, 2007). Because exposure to very low salinity (<5 PSU) or extended periods of moderately low salinity (5–15 PSU) are considered detrimental to eelgrass, it is relevant to consider the extent to which the La Grande plume influences salinity in eelgrass habitat and whether detrimental conditions could be brought about by the changes in the La Grande winter plume.

The eelgrass habitats that we focused on in winter 2017 were those in inner Paul Bay represented by the CH3- series mooring array, and those in Bay of Many Islands represented by the CH4- series mooring array. These areas possess different habitat characteristics. While Paul Bay is open to the plume core area, the approach to the eelgrass habitats in inner Bay of Many Islands (CH4-4 mooring location; Figure

3.1) is protected by islands so to reach this area, the plume would have to flow through narrow passages between islands in which mixing would occur. Cree land-users described to us that there are fast flows and open water in the passages between the islands near Point Kakashishuan in CH4 in winter (C. Sealhunter, personal communication). Thus, we suspect that enhanced vertical mixing between the fresh surface plume and underlying salty waters in the constricted passages caused surface salinities to increase rapidly over a short horizontal distance along the southern limit of Bay of Many Islands. The surface flow at mooring CH4-2 down to a depth of more than 7 m was towards the west (Figure 3.8), which is consistent with the plume flowing westward out of Bay of Many Islands at this latitude and suggests the notion of a counter-clockwise surface circulation within Bay of Many Islands. the winter salinity averaged 11.6 PSU (±0.8) at CH4-4 because of its greater distance from the river mouth and greater degree of protection from the unmixed plume along the inner Bay of Many Islands shoreline. The islands force vertical mixing of fresh plume waters with underlying salty waters as the plume flows north into Bay of Many Islands, which prevents the stratified core of the plume from reaching the CH4-4 area. Time series salinity data obtained at an eelgrass bed in inner Bay of Many Islands (CH4-4) showed similar salinity variations to those at outer Bay of Many Islands sites (CH4-2 and CH4-3), but the negative salinity anomalies at CH4-4 were very muted and there was an overall lag in the salinity changes (Figure 3.11). Both inner Bay of Many Islands (site of CH4-4) and the channels that connect to outer Bay of Many Islands (CH4-2 and CH4-3 locations) are shallow, so our data suggest that the fresher plume fronts that invaded CH4-2 and CH4-3 did not reach CH4-4 unmixed. The winter salinity was thus much more stable and higher at the eelgrass bed than for surface waters at the adjacent deeper locations in the outer Bay of Many Islands. The question in terms of eelgrass habitat quality is simply whether the mean winter salinity in this area of inner Bay of Many Islands (11.6 PSU) is too low to support healthy eelgrass beds. According to Salo et al. (2014), long-term exposure to 10–15 PSU can reduce eelgrass biomass and reproductive output even when temperature and light are adequate. Given that CH4-4 was exposed to this salinity range for several months, the conditions may allow survival but still limit seasonal regrowth. The expansion of the winter plume with increased LGR winter discharge during development (1980s and 1990s) likely posed a stress on the eelgrass by lowering the salinity relative to natural conditions.

Time series data obtained at a mooring placed directly in an eelgrass bed in Paul Bay (CH3-4) showed long exposure to low salinity as a result of the winter plume of the LGR with the winter salinity at CH3-4 hovering around 1.9 PSU (±0.4). This reflects its close proximity to the plume core area and unprotected location along the open shoreline of Paul Bay. In contrast to CH4-4, the low constant salinity at CH3-4 demonstrates that the very fresh surface waters of the winter plume spread unchecked into Paul Bay presumably compromising its ability to support perennial beds of eelgrass based on the known salinity tolerances of eelgrass as described above. While Salo et al. (2014) found that the critical salinity levels for growth differed among different eelgrass populations and can be quite low, it is important to note that the salinity in this area was much higher before the LGR development and expansion of the winter plume. The CH3-4 mooring, which was located in a small eelgrass bed (~3 m water depth) in a small inlet at the north end of Paul Bay, showed slightly higher mean salinity than the other CH3- series of moorings (1.9 vs. 0.5–1.7 PSU; Table 3.1) but very similar temporal patterns of salinity variation on daily and weekly time scales (Figure 3.11b). These values are far below known thresholds for sustained eelgrass survival and fall within the range (0–5 PSU) where photosynthetic stress and mortality are observed within weeks (Nejrup and Pedersen, 2008). Previous studies focused on the spreading of the plume in an alongshore direction and especially northwards thus made an important omission when they neglected to mention the possibility of lateral spreading into inshore areas containing eelgrass and alterations to the salinity therein.

3.6 Conclusions

The under-ice plume of the La Grande River in NE James Bay was studied during ice-covered conditions in winters 2016 and 2017, when the regulated river discharge averaged 4,800 m^3 s^{-1} or about ten-times the natural (unregulated) winter flows. As expected, the winter plume was significantly larger than the plume that forms during ice-free conditions because the landfast sea ice limits direct wind forcing However, when the winter plumes of 2016–2017 were compared to the observations from the early phase of river development (1976–1987), it was determined that the core area of the plume, characterized by very low surface salinity (<5 PSU) and a highly stratified water column, had not significantly expanded northward relative to the winters of 1984 or 1987, despite a ~30% increase in winter discharge. Neither the plume core nor the salinity 5–20 PSU frontal region showed significant northward expansion. We propose that the position of the frontal zone, where maximum mixing occurs, is determined primarily by coastal geometry and the associated narrowing of the landfast ice about 35 km north of the river mouth. The increased winter discharge between 1987 and 2016-2017 appeared to be accommodated by faster freshwater turnover in the core of the plume and a general increase in the region of freshwater influence, including the southward expansion of the under-ice plume against background flows.

The under-ice plume's influence on inshore eelgrass habitat depended on the proximity to the mouth of the river and the degree of protection offered by islands, which prevented penetration of the highly stratified plume front. Two studied inshore areas in embayments that host eelgrass showed influence of the LGR plume. Comparing the observed salinities to literature values, we conclude that the very low to moderately low salinities to which the eelgrass in these areas are exposed as a result of the expanded LGR plume could be negatively impacting eelgrass growth.

The mooring records highlight the remarkable stability of the plume structure under the landfast ice cover. The strongest winter storms during the observation period (25–29 February 2016 and 7–11 March 2017), accompanied by major storm surges and landfast ice accretion, only affected the plume salinity temporarily. Soon after the passing of the storms, the strong stratification was reinstated. If the landfast ice cover melts or undergoes early breakup, the freshwater distribution in the early part of the eelgrass growing season would dramatically change.

The extent to which the plume spreads southward gradually or intermittently as result of wind forcing is largely unknown, as is the loss of freshwater past the landfast ice edge. Knowing the extent of the under-ice plume spreading to the south would further help us assess the influence of river runoff on salinity at southern eelgrass beds and better constrain the freshwater balance. Mooring deployments south of the river mouth and beyond the landfast ice edge would provide the required time series to better show how the under-ice river plume spreads over the course of the winter than the occasional CTD casts alone.

3.7 References

Biebl, R., McRoy, C.P., 1971. Plasmatic resistance and rate of respiration and photosynthesis of *Zostera marina* at different salinities and temperatures. Marine Biology 8, 48–56. https://doi.org/10.1007/BF00349344

Buckley, J.R., Gammelsrød, T., Johannessen, J.A., Johannessen, O.M., Røed, L.P., 1979. Upwelling: Oceanic Structure at the Edge of the Arctic Ice Pack in Winter. Science 203, 165–167. https://doi.org/10.1126/science.203.4376.165

Carmack, E.C., Macdonald, R.W., 2002. Oceanography of the Canadian Shelf of the Beaufort Sea: A Setting for Marine Life. Arctic 55, 29–45.

Curtis, S., Allen, L., 1976. Waterfowl ecology of the Quebec coast of James Bay, in: Proceedings of the James Bay Environment 1976 Symposium. Environment Canada, Canada Wildlife Service, Ottawa, Canada, pp. 701–724.

Dickey, M.-H., 2015. Status of eelgrass beds on the east coast of James Bay. Internal Environment Canada Report.

Dmitrenko, I.A., Kirillov, S.A., Babb, D.G., Kuzyk, Z.Z.A., Basu, A., Ehn, J.K., Sydor, K., Barber, D.G., 2021. Storm-driven hydrography of western Hudson Bay. Continental Shelf Research 227, 104525. https://doi.org/10.1016/j.csr.2021.104525

Dmitrenko, I.A., Myers, P.G., Kirillov, S.A., Babb, D.G., Volkov, D.L., Lukovich, J.V., Tao, R., Ehn, J.K., Sydor, K., Barber, D.G., 2020. Atmospheric vorticity sets the basin-scale circulation in Hudson Bay. Elementa: Science of the Anthropocene 8, 049. https://doi.org/10.1525/elementa.049

Dunton, K.H., Weingartner, T. and Carmack, E.C., 2006. The nearshore western Beaufort Sea ecosystem: circulation and importance of terrestrial carbon in arctic coastal food webs. Progress in Oceanography, 71(2-4), pp.362-378. https://doi.org/10.1016/j.pocean.2006.09.011

Eastwood, R.A., Macdonald, R.W., Ehn, J.K., Heath, J., Arragutainaq, L., Myers, P.G., Barber, D.G., Kuzyk, Z.A., 2020. Role of River Runoff and Sea Ice Brine Rejection in Controlling Stratification Throughout Winter in Southeast Hudson Bay. Estuaries and Coasts 43, 756–786. https://doi.org/10.1007/s12237-020-00698-0

El-Sabh, M.I., Koutitonsky, V.G., 1977. An Oceanographic Study of James Bay before the Completion of the La Grande Hydroelectric Complex. Arctic 30, 169–186.

Gagnon, A.S., Gough, W.A., 2005. Trends in the Dates of Ice Freeze-up and Breakup over Hudson Bay, Canada. Arctic 58, 370–382.

Galbraith, P.S., Larouche, P., 2011. Reprint of "Sea-surface temperature in Hudson Bay and Hudson Strait in relation to air temperature and ice cover breakup, 1985–2009." Journal of Marine Systems, The Hudson Bay System 88, 463–475. https://doi.org/10.1016/j.jmarsys.2011.06.006

Granskog, M. A., Ehn, J., Niemelä, M., 2005. Characteristics and potential impacts of under-ice river plumes in the seasonally ice-covered Bothnian Bay (Baltic Sea). Journal of Marine Systems 53, 187–196. https://doi.org/10.1016/j.jmarsys.2004.06.005

Granskog, Mats A., Kaartokallio, H., Thomas, D.N., Kuosa, H., 2005. Influence of freshwater inflow on the inorganic nutrient and dissolved organic matter within coastal sea ice and underlying waters in the Gulf of Finland (Baltic Sea). Estuarine, Coastal and Shelf Science 65, 109–122. https://doi.org/10.1016/j.ecss.2005.05.011

Gupta, K., Mukhopadhyay, A., Babb, D.G., Barber, D.G., Ehn, J.K., 2022. Landfast sea ice in Hudson Bay and James Bay: Annual cycle, variability and trends, 2000–2019. Elementa: Science of the Anthropocene 10, 00073. https://doi.org/10.1525/elementa.2021.00073

Hemminga, M.A., Duarte, C.M., 2000. Seagrass Ecology. Cambridge University Press.

Horner-Devine, A.R., Hetland, R.D., MacDonald, D.G., 2015a. Mixing and Transport in Coastal River Plumes. Annual Review of Fluid Mechanics 47, 569–594. https://doi.org/10.1146/annurev-fluid-010313-141408

Ingram, R.G., 1981. Characteristics of the Great Whale River plume. Journal of Geophysical Research: Oceans 86, 2017–2023. https://doi.org/10.1029/JC086iC03p02017

Ingram, R.G., Larouche, P., 1987a. Variability of an under-ice river plume in Hudson Bay. Journal of Geophysical Research: Oceans 92, 9541–9547. https://doi.org/10.1029/JC092iC09p09541

Ingram, R.G., Larouche, P., 1987b. Changes in the under-ice characteristics of La Grande Rivière plume due to discharge variations*. Atmosphere-Ocean 25, 242–250. https://doi.org/10.1080/07055900.1987.9649273

Ingram, R.G., Wang, J., Lin, C., Legendre, L., Fortier, L., 1996. Impact of freshwater on a subarctic coastal ecosystem under seasonal sea ice (southeastern Hudson Bay, Canada). I. Interannual variability and predicted global warming influence on river plume dynamics and sea ice. Journal of Marine Systems, The Coastal Ocean in a Global Change Perspective 7, 221–231. https://doi.org/10.1016/0924-7963(95)00006-2

Kamermans, P., Hemminga, M.A., de Jong, D.J., 1999. Significance of salinity and silicon levels for growth of a formerly estuarine eelgrass (*Zostera marina*) population (Lake Grevelingen, The Netherlands). Marine Biology 133, 527–539. https://doi.org/10.1007/s002270050493

Kasper, J.L., Weingartner, T.J., 2015. The Spreading of a Buoyant Plume Beneath a Landfast Ice Cover. Journal of Physical Oceanography 45, 478-494. https://doi.org/10.1175/JPO-D-14-0101.1

Kasper, J.L., Weingartner, T.J., 2012. Modeling winter circulation under landfast ice: The interaction of winds with landfast ice. Journal of Geophysical Research: Oceans 117. https://doi.org/10.1029/2011JC007649

Kuzyk, Z.A., Macdonald, R.W., Granskog, M.A., Scharien, R.K., Galley, R.J., Michel, C., Barber, D., Stern, G., 2008. Sea ice, hydrological, and biological processes in the Churchill River estuary region, Hudson Bay. Estuarine, Coastal and Shelf Science 77, 369–384. https://doi.org/10.1016/j.ecss.2007.09.030

Lalumière, R., Messier, D., Fournier, J.-J., Peter McRoy, C., 1994. Eelgrass meadows in a low Arctic environment, the northeast coast of James Bay, Québec. Aquatic Botany 47, 303–315. https://doi.org/10.1016/0304-3770(94)90060-4

Leblanc, M.-L., O'Connor, M.I., Kuzyk, Z.Z.A., Noisette, F., Davis, K.E., Rabbitskin, E., Sam, L.-L., Neumeier, U., Costanzo, R., Ehn, J.K., Babb, D., Idrobo, C.J., Gilbert, J.-P., Leblon, B., Humphries, M.M., 2023. Limited recovery following a massive seagrass decline in subarctic eastern Canada. Global Change Biology 29, 432–450. https://doi.org/10.1111/gcb.16499

Li, S.S., Ingram, R.G., 2007. Isopycnal deepening of an under-ice river plume in coastal waters: Field observations and modeling. Journal of Geophysical Research: Oceans 112. https://doi.org/10.1029/2006JC003883

Macdonald, R.W., Carmack, E.C., 1991. The role of large-scale under-ice topography in separating estuary and ocean on an Arctic shelf. Atmosphere-Ocean 29, 37–53. https://doi.org/10.1080/07055900.1991.9649391

Macdonald, R.W., Paton, D.W., Carmack, E.C., Omstedt, A., 1995. The freshwater budget and under-ice spreading of Mackenzie River water in the Canadian Beaufort Sea based on salinity and 18O/16O measurements in water and ice. Journal of Geophysical Research: Oceans 100, 895–919. https://doi.org/10.1029/94JC02700

Macdonald, R.W., Solomon, S.M., Cranston, R.E., Welch, H.E., Yunker, M.B., Gobeil, C., 1998. A sediment and organic carbon budget for the Canadian Beaufort Shelf. Marine Geology 144, 255–273. https://doi.org/10.1016/S0025-3227(97)00106-0

Messier, D., Lepage, S., Margerie, S. de, 1989. Influence of ice cover on the extent of the La Grande River plumes (James Bay). Arctic (Journal of the Arctic Institute of North America); (Canada) 42:3.

Messier, D. (2002) 'Suivi environnemental des projets La Grande-2-A et La Grande-1. Le panache de La Grande Rivière', Hydro Québec Production, pp. 5–6.

Moreno-Marín, F., Brun, F.G., Pedersen, M.F., 2018. Additive response to multiple environmental stressors in the seagrass *Zostera marina* L. Limnology and Oceanography 63, 1528–1544. https://doi.org/10.1002/lno.10789

Nejrup, L.B., Pedersen, M.F., 2008. Effects of salinity and water temperature on the ecological performance of *Zostera marina*. Aquatic Botany 88, 239–246. https://doi.org/10.1016/j.aquabot.2007.10.006

Pawlowicz, R., Beardsley, B., Lentz, S., 2002. Classical tidal harmonic analysis including error estimates in MATLAB using T_TIDE. Computers & Geosciences 28, 929–937. https://doi.org/10.1016/S0098-3004(02)00013-4

Prinsenberg, S.J., 1986a. Chapter 9 Salinity and Temperature Distributions of Hudson Bay and James Bay, in: Martini, I.P. (Ed.), Elsevier Oceanography Series, Canadian Inland Seas. Elsevier, pp. 163–186. https://doi.org/10.1016/S0422-9894(08)70902-4

Prinsenberg, S.J., 1986b. Chapter 10 The Circulation Pattern and Current Structure of Hudson Bay, in: Martini, I.P. (Ed.), Elsevier Oceanography Series, Canadian Inland Seas. Elsevier, pp. 187–204. https://doi.org/10.1016/S0422-9894(08)70903-6

Ridenour, N.A., Hu, X., Sydor, K., Myers, P.G., Barber, D.G., 2019. Revisiting the Circulation of Hudson Bay: Evidence for a Seasonal Pattern. Geophysical Research Letters 46, 3891–3899. https://doi.org/10.1029/2019GL082344

Salo, T., Pedersen, M.F., Boström, C., 2014. Population specific salinity tolerance in eelgrass (*Zostera marina*). Journal of Experimental Marine Biology and Ecology 461, 425–429. https://doi.org/10.1016/j.jembe.2014.09.010

Schulze, L.M., Pickart, R.S., 2012. Seasonal variation of upwelling in the Alaskan Beaufort Sea: Impact of sea ice cover. Journal of Geophysical Research: Oceans 117. https://doi.org/10.1029/2012JC007985

Shiklomanov, I.A., Shiklomanov, A.I., 2003. Climatic Change and the Dynamics of River Runoff into the Arctic Ocean. Water Resources 30, 593–601. https://doi.org/10.1023/B:WARE.0000007584.73692.ca

Shiklomanov, I.A., Shiklomanov, A.I., Lammers, R.B., Peterson, B.J., Vorosmarty, C.J., 2000. The Dynamics of River Water Inflow to the Arctic Ocean, in: Lewis, E.L., Jones, E.P., Lemke, P., Prowse, T.D., Wadhams, P. (Eds.), The Freshwater Budget of the Arctic Ocean. Springer Netherlands, Dordrecht, pp. 281–296. https://doi.org/10.1007/978-94-011-4132-1_13

St-Laurent, P., Straneo, F., Dumais, J.-F., Barber, D.G., 2011. What is the fate of the river waters of Hudson Bay? Journal of Marine Systems, The Hudson Bay System 88, 352–361. https://doi.org/10.1016/j.jmarsys.2011.02.004

Taha, W., Bonneau-Lefebvre, M., Cueto Bergner, A., Tremblay, A., 2019. Evolution From Past to Future Conditions of Fast Ice Coverage in James Bay. Frontiers in Earth Science 7. https://doi.org/10.3389/feart.2019.00254

Touchette, B.W., 2007. Seagrass-salinity interactions: Physiological mechanisms used by submersed marine angiosperms for a life at sea. Journal of Experimental Marine Biology and Ecology, The Biology and Ecology of Seagrasses 350, 194–215. https://doi.org/10.1016/j.jembe.2007.05.037

Zhang, Y.-H., Yu, B., Liu, Y.-C., Ma, W., Li, W.-T., Zhang, P.-D., 2022. The influence of decreased salinity levels on the survival, growth and physiology of eelgrass *Zostera marina*. Marine Environmental Research 182, 105787. https://doi.org/10.1016/j.marenvres.2022.105787

3.8 Supplementary material

Here we present extra figures and tables that are not integral to the paper but still provide useful and important information. The figures included show, in Figure S3.1, comparison of salinity profiles obtained by the Castaway and Idronaut sensors; in Figure S3.2, comparison of the average salinity recorded by CT sensors and that recorded by CTD profiles at the mooring sites; in Figure S3.3, images of changes in the landfast ice; in Figure S3.4, the prevailing wind direction and speed for the mooring deployment periods; in Figure S.35, average monthly discharge of the La Grande River and annual discharge during historic periods, and, in Figure S3.6, section plots of salinity made using CTD casts. Table S3.1 shows the meta data for all the moorings including the instruments that were used and the configuration.

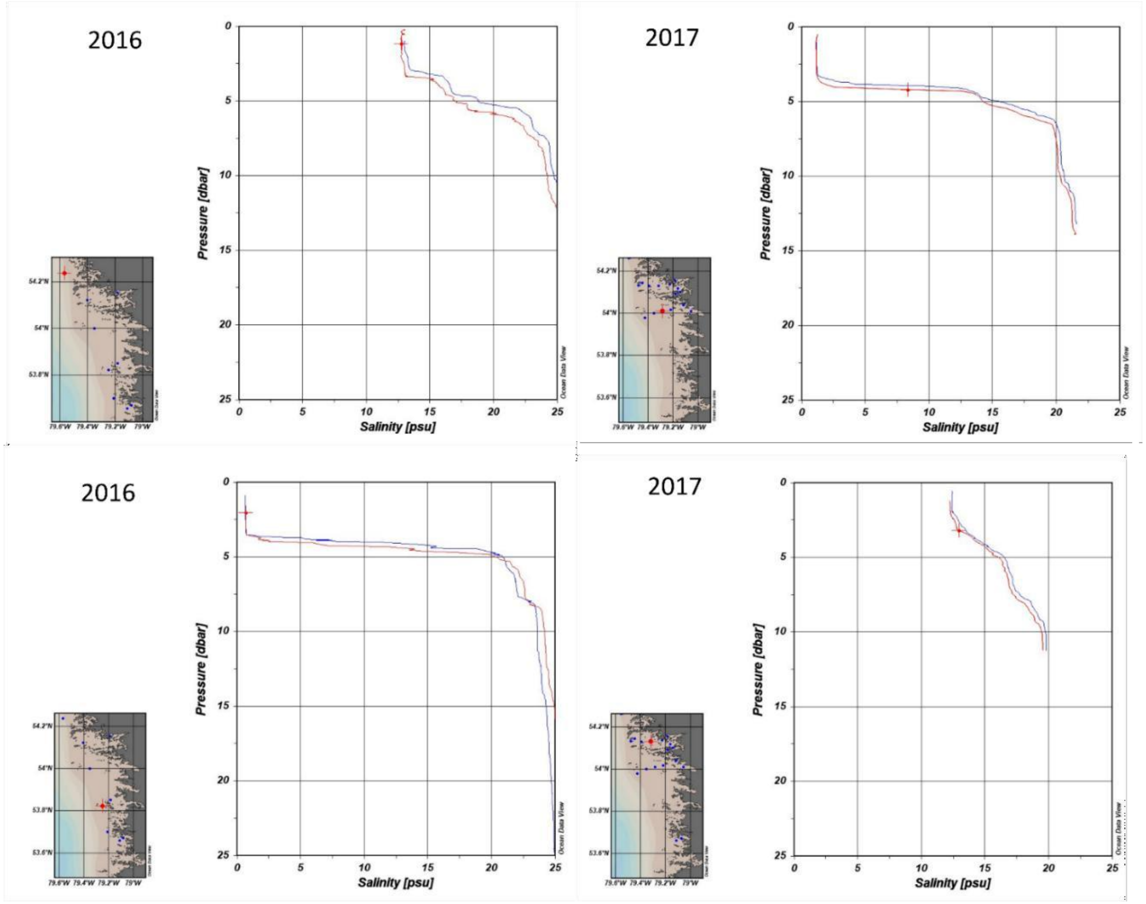

Figure S 3.1: Comparison of salinity profiles from Idronaut (blue) and Castaway (red) CTDs at selected stations during winter 2016 and 2017 before adjusting for minor pressure differences.

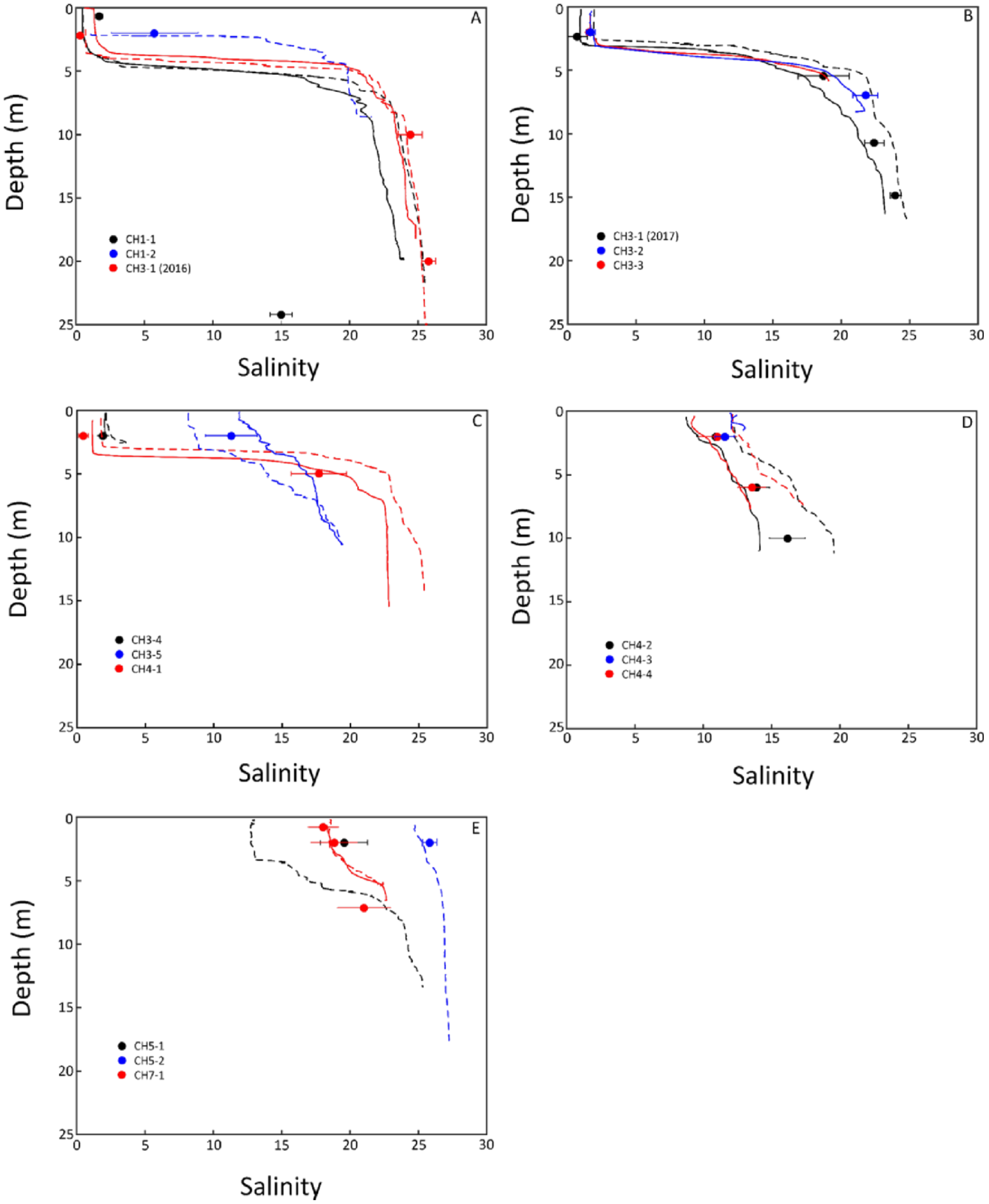

Figure S 3.2: Average salinity as recorded at multiple depths by CT sensors placed on moorings (filled circles with horizontal bars showing standard deviation) compared to salinity obtained from CTD casts during mooring deployment (-) and recovery (--). Panel A shows moorings closest to LGR, panels B and C show moorings near traplines CH3 and CH4, panel D shows moorings within Bay of Many Islands, and panel E shows moorings north of Bay of Many Islands.

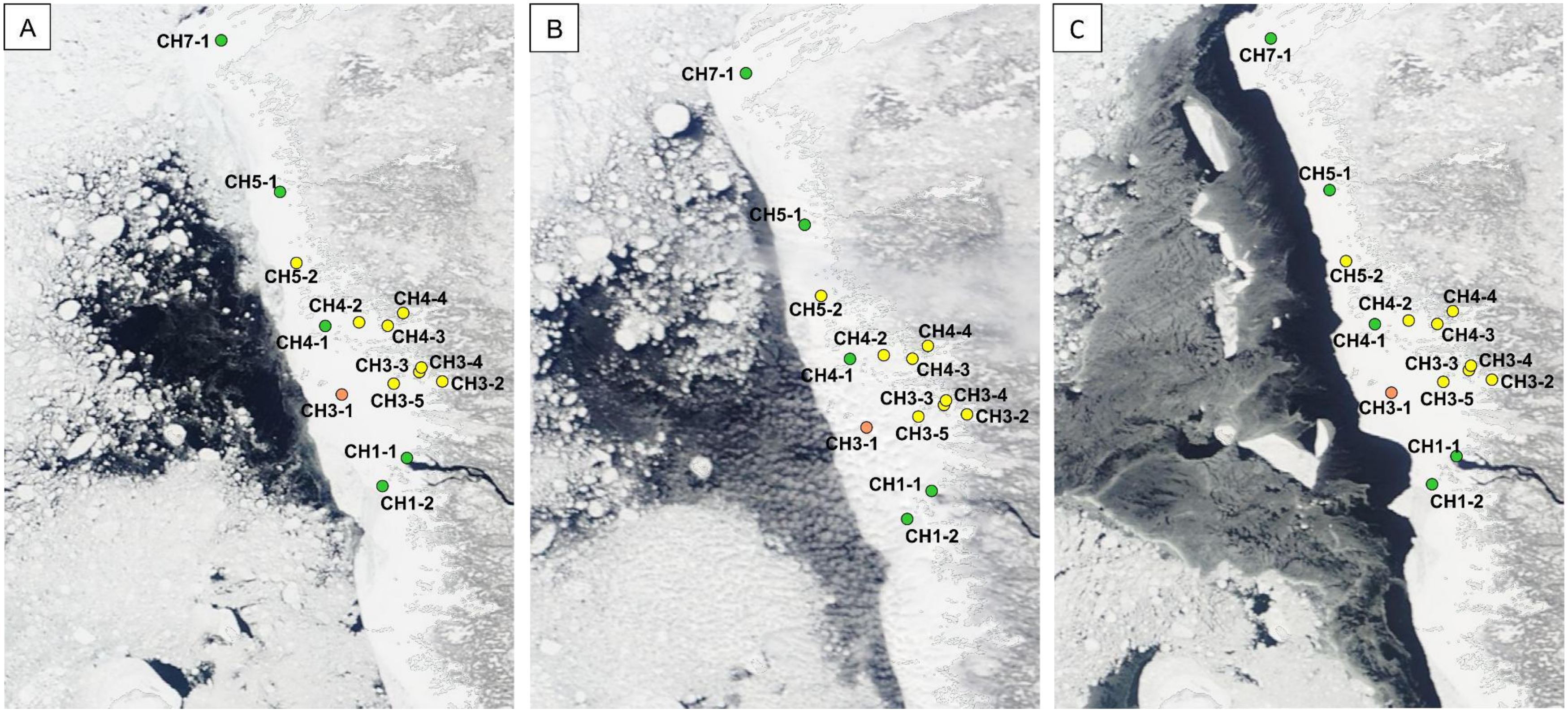

Figure S 3.3: MODIS satellite image from (A) 10th April, (B) 14th April, (C) 16th April 2017, showing a landfast breakup event and expansion of the flaw-lead, which corresponded to increases in salinity in the mooring records shown in Figure 3.12

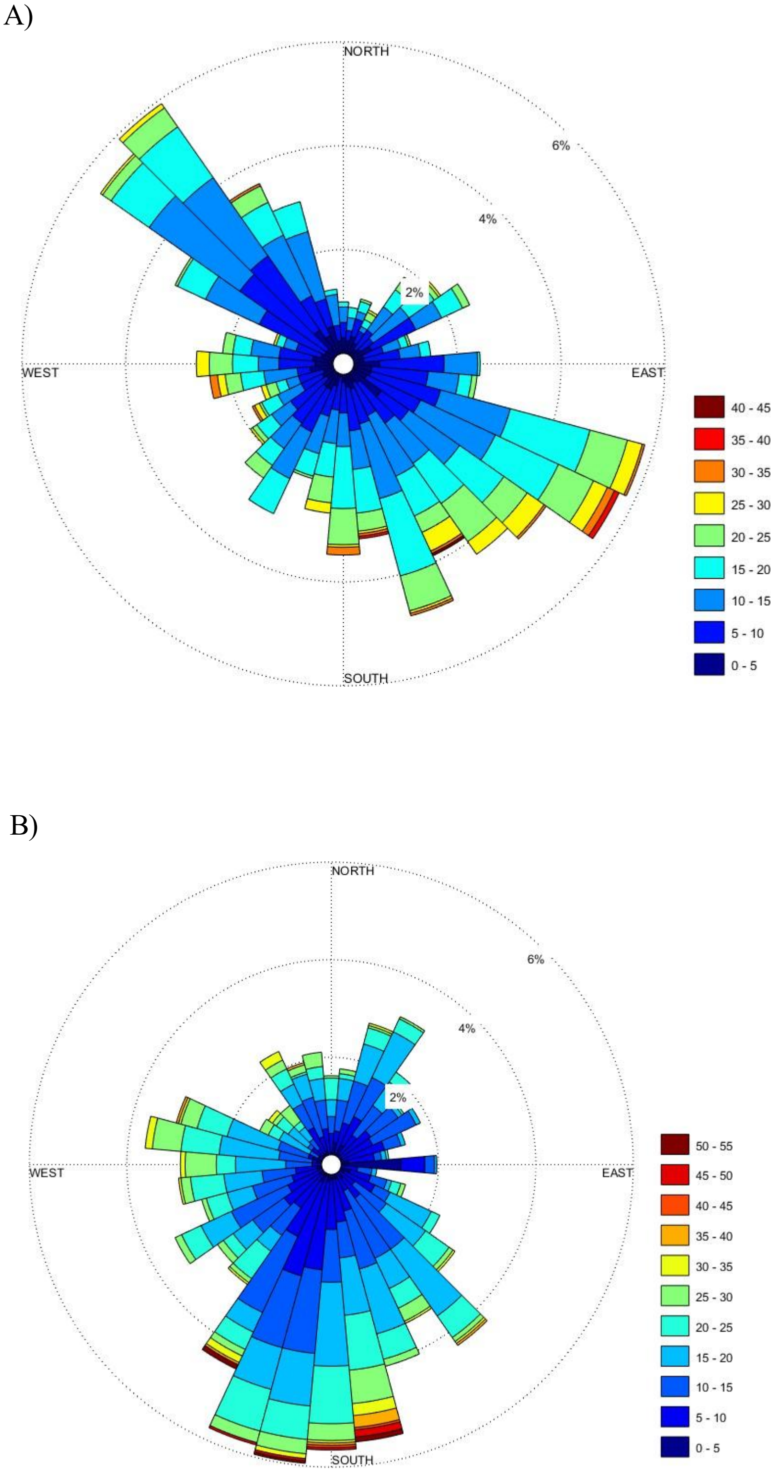

Figure S 3.4: Wind rose diagrams showing the prevailing wind direction and speed (km h^{-1}) for the mooring deployment periods in 2016 (a) and 2017 (b).

A)

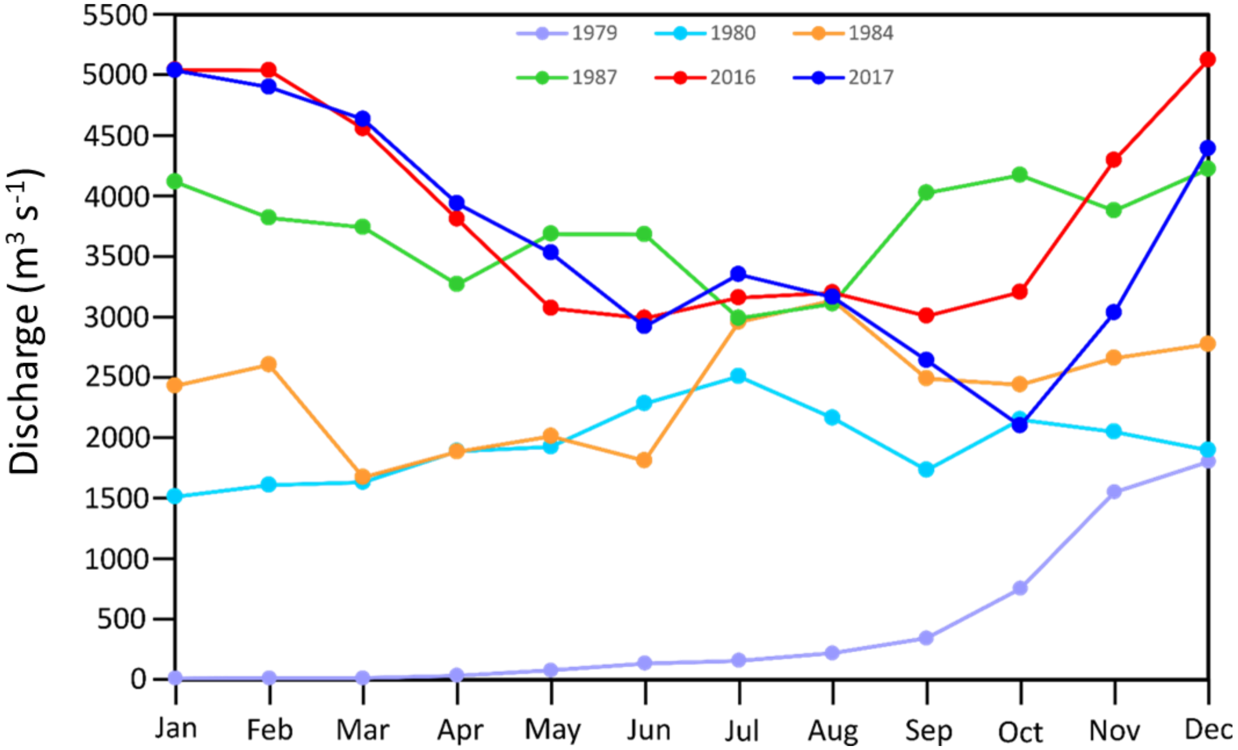

B)

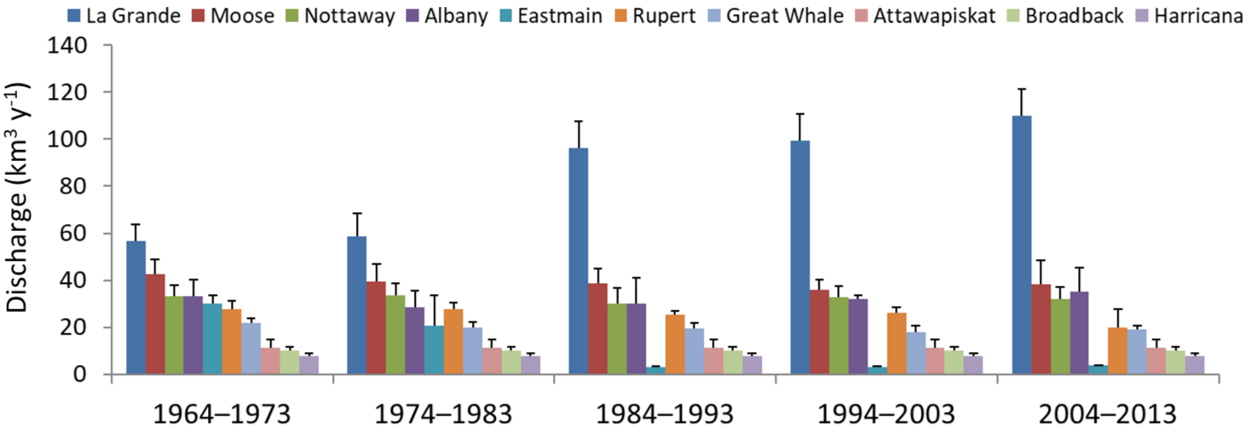

Figure S 3.5: (A) Average monthly discharge (m^3 s^{-1}) of the La Grande River during filling of the LG-2 reservoir in 1979 (purple) and subsequent years of flow augmentation and regulation, including 1980 (light blue), 1984 (orange), 1987 (green), 2016 (red), and 2017 (blue). Discharge for 1979, 1980, and 1984 was taken from Messier et al. (1986) and discharge for 1987 was taken from Messier (2002). Discharge for 2016 and 2017 discharge were provided by Hydro Québec (personal communication). Plot in (B) shows mean annual discharge (km^3 y^{-1}) for La Grande and other rivers in the region for various historical time periods based on data provided in Déry et al. (2016).

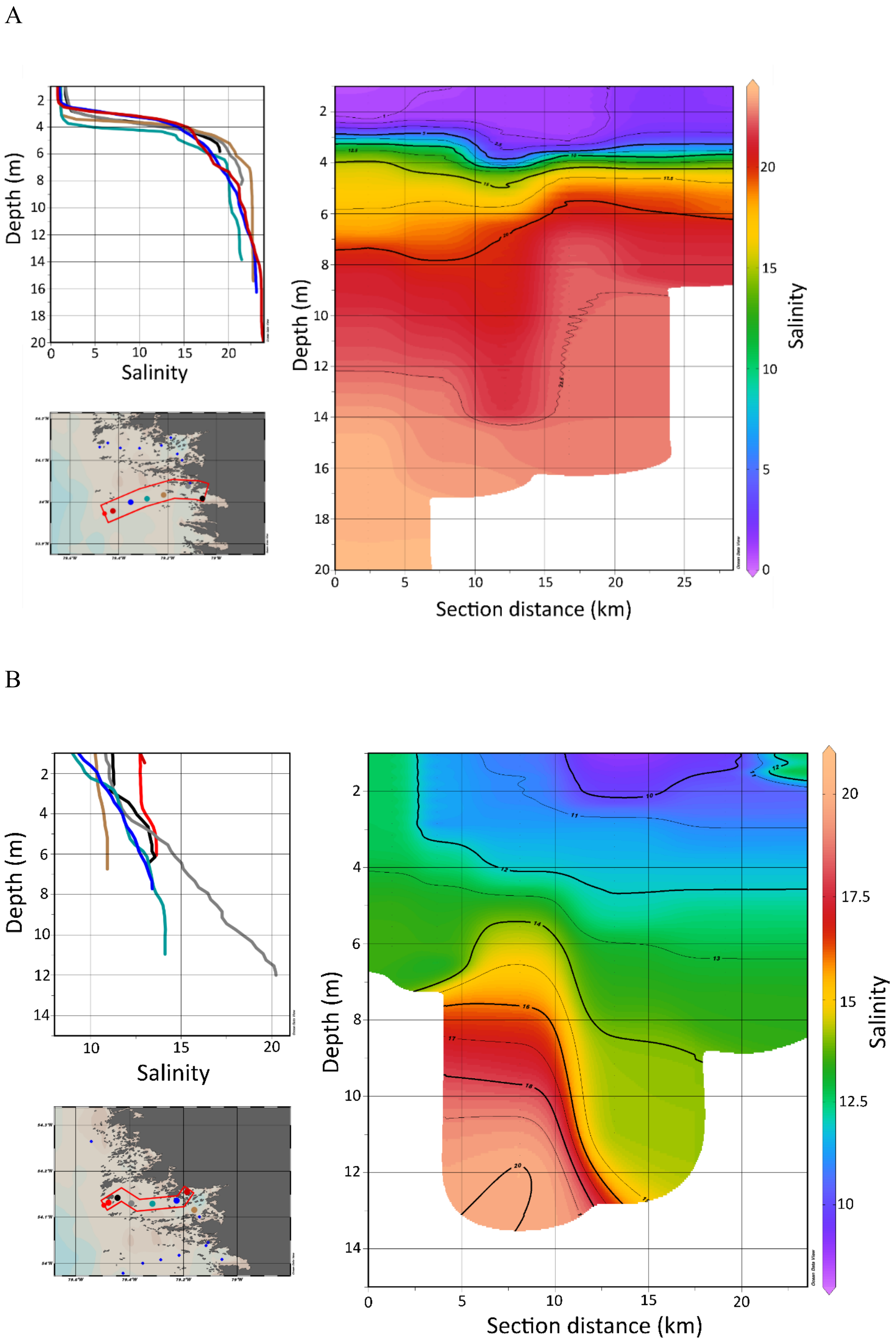

Figure S 3.6: Section plots of salinity at (A) Paul Bay and (B) Bay of Many Islands using 2017 CTD data. Each section plot goes from west to east and includes the CTD casts shown on the inset vertical profile plots and maps.

Table S 3.1: Meta data for all moorings indicating the instruments used and the water depth they were placed at on the taut, ice-tethered mooring line. Alec CT, WQMX, Aquatroll and Insitu devices measured conductivity and temperature. Acoustic Doppler Current Profilers (ADCPs) were deployed on two moorings in 2016. An RBR or Hobo pressure sensor was typically placed on the bottom at each mooring site.

Station ID	Longitude (Degrees N)	Latitude (Degrees N)	Instrument type (Serial Number)	Depth (meters)
2016				
CH1-1	-79.18	53.85	WQMx	1.7
			ADCP (088630)	3
			Alec CT (1588)	5
			Alec CT (1591)	10
			Alec CT (1517)	15
			Alec CT (1571)	20
			RBR Pressure Sensor (19175)	22
CH1-2	-79.25	53.82	ADCP (P22512-1)	2.5
			Alec CT (1585)	2.2
			Alec CT (1587)	10
			Alec CT (1590)	20
			RBR Pressure Sensor (19174)	25
CH3-1	-79.35	54.00	Insitu (435517)	2
CH4-1	-79.40	54.79	Insitu (435017)	2
CH5-1	-79.52	54.39	Insitu (435780)	2
CH7-1	-79.72	54.70	Aquatroll (435504)	2
			Insitu (435182)	5

Station ID	Longitude (Degrees N)	Latitude (Degrees N)	Instrument type (Serial Number)	Depth (meters)
			Insitu (435519)	8
			Insitu (435271)	11
2017				
CH3-1	-79.35	54.00	ADCP (P22512-1)	14.87
			Alec CT (1585)	14.87
			Insitu (435780)	2.35
			Insitu (435517)	5.45
			Insitu (435519)	10.72
			Pressure Sensor (11016874)	Air
CH4-2	-79.31	54.13	ADCP (088630)	10
			Alec CT (1571)	6
			Alec CT (1588)	10
			Pressure Sensor (20049576)	6
			WQMx	2
CH4-3	-79.22	54.14	Hobo (20036682)	2
			Hobo (20036684)	6
			Pressure sensor (11016877)	6
CH4-4	-79.19	54.15	Aquatroll (435504)	1
			Pressure Sensor (110168711)	1.5
CH3-2	-79.06	54.01	Hobo CT (20036679)	2

Station ID	Longitude (Degrees N)	Latitude (Degrees N)	Instrument type (Serial Number)	Depth (meters)
CH3-3	-79.11	54.0	Hobo CT (20036681)	2
			Hobo CT (20036680)	7
			Pressure Sensor (109063781)	7
CH3-4	-79.11	54.05	Hobo CT (20036683)	1.2
			Pressure Sensor (10868701)	1.9
CH3-5	-79.22	54.02	Insitu (435182)	2
			Insitu (435017)	5
			Pressure Sensor (10868709)	5
CH5-2	-79.54	54.26	Alec CT (1579)	0.8
			Alec CT (1568)	2.0
			Alec CT (1590)	7.14
			Pressure Sensor (20049575)	7.14

Chapter 4 On the upcoast intrusion of the La Grande River under-ice plume under wind forcing

This manuscript has been submitted to the peer-reviewed Continental Shelf Research and has been accepted with major revisions. The citation for this manuscript is as follows:

Peck, C.J., Kuzyk, Z.A., Kirillov, S., Neumeier, U., Rabbitskin, E., Ehn, J.K. (2025) 'On the upcoast intrusion of the La Grande River under-ice plume under wind forcing.' Continental Shelf Research. (Accepted)

4.1 Abstract

The La Grande River (LGR) is a regulated river that releases approximately 5000 m^3 s^{-1} during the winter months, making it the largest in Northern Canada and the second largest winter flow discharge among the pan-Arctic rivers. The discharge creates a substantial under-ice plume beneath the 10-20 km wide landfast ice cover along the northeastern coast of James Bay, Canada. The under-ice plume preferentially flows northward along the coast before dispersing into the upper ocean. However, previous observations suggest an unexpected southward flow against the mean background circulation. To document the duration and intensity of the southward under- ice plume extent and investigate the forcing conditions, bottom-mounted moorings were deployed in four shallow coastal inlets. Salinity, temperature, and current velocities were recorded at near-bottom depths of 3-4 m for a one-year duration from August 2019 to August 2020. The onset of landfast ice coverage in December 2019 was found to immediately allow the under-ice plume area to expand significantly under the regulated high-flow conditions due to reduced wind-driven mixing. Two freshwater intrusion events were observed in winter 2020. The strongest, in February, followed persistent westerly winds and caused a salinity decrease at three moorings south of the river mouth, lasting about 20 days. Salinity increased to normal once the winds relaxed. These results show that wind forcing over James Bay can indirectly influence LGR discharge dispersion along the coast, despite the large and immobile landfast ice. Noting that 9 out of 40 winters from to 1983-2022 were found to experience similar wind conditions as 2020, we conclude that the combination of sustained high winter river discharge, landfast ice, and westerly wind forcing can enhance the southward reach of the LGR freshwater plume, with potential implications for eelgrass ecosystems that are intolerant of low salinity.

4.2 Introduction

River runoff acts as a source of both momentum and buoyancy when it enters saline oceanic water. Initially, the buoyancy of fresh river water is often sufficient to overcome the forces that drive vertical mixing, such that a stratified river plume is formed on the surface (Kourafalou et al., 1996). The direction of flow, thickness, and size of a river plume are determined by external factors, such as coastal geometry, discharge rate, tides, the Coriolis effect, coastal background circulation, and wind-driven mixing (Chao, 1988; Chapman and Lentz, 1994; Garvine, 1995; Fong and Geyer, 2001; Yankovsky et al., 2001; García Berdeal et al., 2002; Halverson and Pawlowicz, 2008; Li and Zhong, 2009; O'Donnell, 2010; Horner-Devine et al., 2015). Under weak wind forcing, buoyancy can drive a plume to spread evenly out from the river mouth, forming an anticyclonically circulating bulge, but then generally flow along the coast as dictated by the buoyancy forcing and Coriolis effect (Horner-Devine et al., 2015).

However, wind forcing can quickly modify a plume's size and flow direction (Otero and Ruiz-Villarreal, 2008). Offshore wind generally promotes the surface water layers, including river plumes, to flow away from the coast, while water in the bottom layer flows towards the coast (Fewings et al., 2008; Jurisa and Chant, 2013). With onshore winds and continued river discharge, the river plume tends to converge and build up against the shore, forcing deeper waters to move offshore (Fewings et al., 2008). This results in a thicker plume, which deepens the pycnocline and increases the along-shore freshwater transport (Chao, 1988; Fong and Geyer, 2001). However, this process is affected by shallow bathymetry and complex coastal geometry, such as islands and channels, and has not been observed for river plumes propagating beneath a sea ice cover.

Immobile landfast sea ice that ubiquitously forms along high-latitude coasts during winter blocks direct wind mixing, allowing for a larger spatial extent of under-ice river plumes compared to open water conditions under similar levels of river discharge (Ingram, 1981; Ingram and Larouche, 1987a; Li and Ingram, 2007; Kasper and Weingartner, 2015). The spreading of under-ice river plumes may further be hindered or steered by ice roughness features, such as pressure ridges or rubble zones (Macdonald and Carmack, 1991; Macdonald et al., 1995; Kuzyk et al., 2008). However, in the case of level landfast sea ice, an under-ice plume can spread largely unmixed until it reaches the floe edge, after which the river water presumably mixes quickly with ambient seawater and disperses into the ocean surface layer (Kasper and Weingartner, 2012).

A few observational studies in Hudson Bay that included time-series observations of under-ice river plumes have shown that wind forcing occurring at a significant distance from the floe edge can still impact under-ice plume dynamics and structure (Ingram and Larouche, 1987b; Messier, 2002; Peck et al., 2022, Chapter 3). In particular, winter storms have been shown to temporarily speed up estuarine two-layer circulation and reduce the stratification of the under-ice plume (Messier, 2002; Peck et al., 2022, Chapter 3). A recent study of the La Grande River (LGR) plume on the northeast coast of James Bay during the winters of 2016 and 2017 revealed occasions when low-salinity (<5 PSU) surface waters were found up to 20 km south of the mouth of the LGR, against the prevailing circulation of James Bay (Peck et al., 2022, Chapter 3). The movement of a river plume against the prevailing ocean circulation, described as ‘upcoast intrusion’ hereafter, has been shown in numerous numerical models (Chapman and Lentz, 1994; Garvine, 1999; Yankovsky, 2000) but rarely observed (Beardsley et al., 1985), and is generally driven by wind forcing. To the best of our knowledge, there are no previous observational datasets showing the upcoast movement of an under-ice river plume, which is isolated from direct wind forcing by landfast ice.

Here, we follow up on the observations of Peck et al. (2022, Chapter 3) to further characterize the upcoast intrusion of the LGR plume opposite to the direction of the mean circulation (i.e., southward along the NE coast of James Bay). We used a new year-long salinity and temperature dataset obtained in 2019-2020 from four coastal moorings and CTD data to characterize the upcoast extent of the LGR under-ice plume throughout the landfast ice-covered winter period. We then examined wind forcing and discharge in relation to short-term salinity variations observed in coastal embayments south of the LGR River mouth. This study contributes to a large multidisciplinary effort called the Coastal Habitat Comprehensive Research Project (CHCRP), motivated by concerns of the coastal Cree First Nations regarding the environmental factors affecting the health of seagrasses (*Zostera marina* or eelgrass). Cree Nation research partners contributed to the study design (site selection) and fieldwork and reviewed this manuscript.

4.3 Methods

4.3.1 Study area

This study focused on the eastern coast of James Bay, north and south of the village of Chisasibi, located at the mouth of the La Grande River (Figure 4.1). The northeast James Bay coast is complex, with numerous islands, embayments, and nearshore water depths reaching approximately 20 m. The circulation in Hudson and James Bay is generally cyclonic (Figure 4.1), and an increase in the speed of cyclonic winds, such as during large storms associated with a low sea level pressure system over Hudson Bay, has a positive effect on the strength of cyclonic circulation, enhancing onshore transport (Prinsenberg, 1986). James Bay experiences an annual ice cover with the sea ice developing in late November along the western and southern coastlines. In mid-May, the landfast ice begins to break up around the mouth of the LGR earlier than the rest of the bay because of the river discharge (Taha et al., 2019). By examining satellite imagery from Sentinel-2 (ESA), we determined that landfast ice was formed around December 14, 2019, and the breakup period began on June 16, 2020.

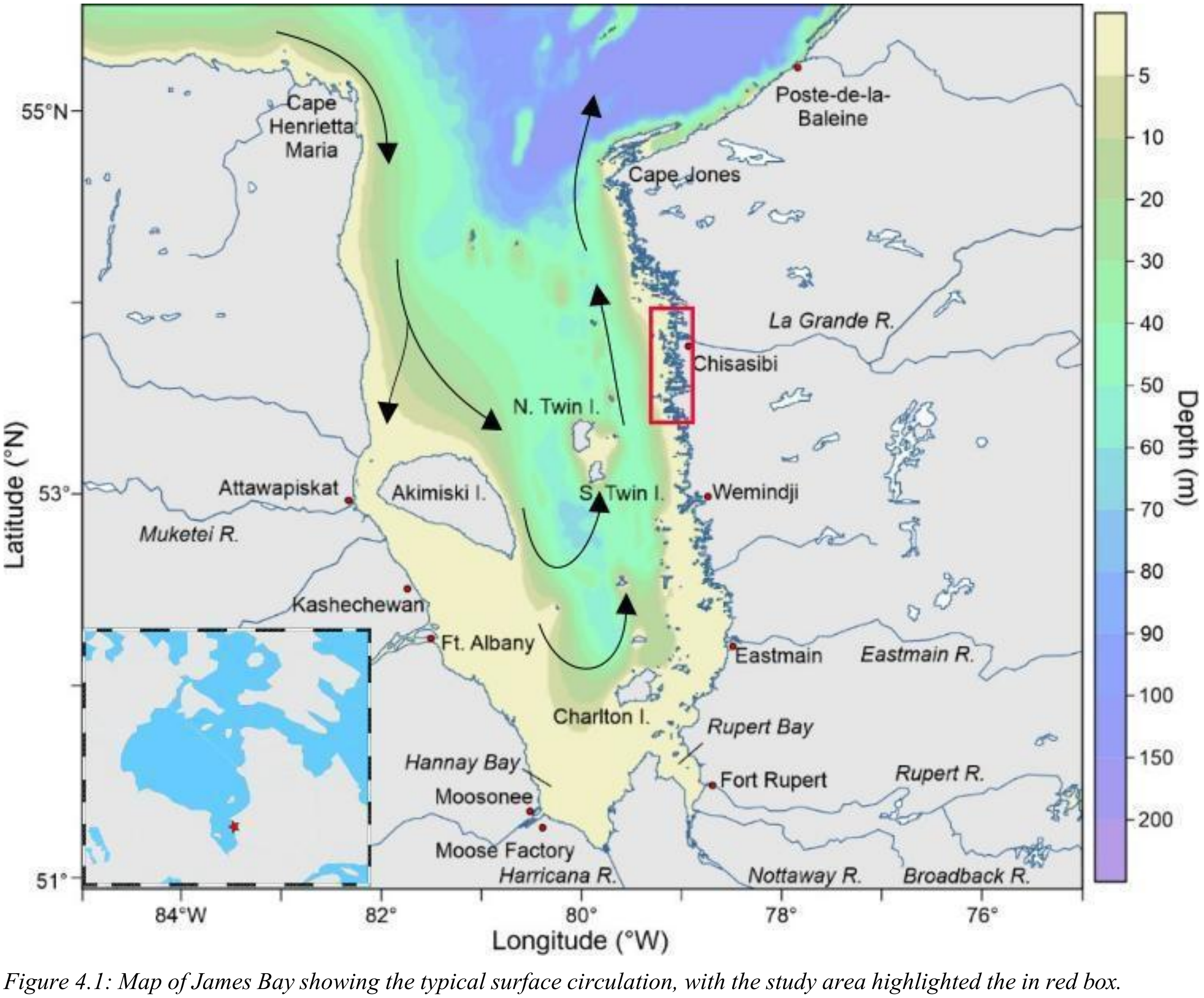

Figure 4.1: Map of James Bay showing the typical surface circulation, with the study area highlighted the in red box.

The increase in the size of the under-ice plume of the LGR has been relatively well documented, as the LGR underwent several phases of hydroelectric development that ultimately increased its winter discharge ten-fold from 460 $m^3 s^{-1}$ (1976) to 4800 $m^3 s^{-1}$ (2017) (Ingram and Larouche, 1987a; Messier, 2002). In 1976, before the hydroelectric development of the LGR, the core area of the under-ice plume (<5 salinity) was constrained close to the river mouth (Figure 4.2). After the development, the plume extended to both the north and south of the river mouth, but generally northwestward (Figure 4.2). Recently, Peck et al. (2022) characterized the horizontal and vertical structure of the LGR under-ice plume for the first time since 1987, showing that the highly stratified core area of the under-ice plume (low salinity <5) covered approximately 1200 km^2 during the winters of 2016 and 2017, when discharge during January-March averaged 4800 $m^3 s^{-1}$. The core area of the plume generally extends northward alongshore from the river mouth for approximately 35 km, following the mean circulation of James Bay. However, the core area of the plume did not enlarge towards the north with the most recent increases in discharge, owing to constraints from the coastal geometry that reduced the width of landfast ice and enhanced tidal-driven mixing. The discharge is thus dispersed more readily past the landfast ice edge into offshore James Bay. However, the under-ice plume was also observed to extend southward of the river mouth against the background circulation (Peck et al., 2022, Chapter 3).

4.3.2 Observations

The dataset consists of records obtained from four bottom-mounted moorings deployed in coastal inlets harboring eelgrass beds at average depths of 2.8 m (CH3), 3.7 m (CH33) and 2.9 m (CH37) (Figure 4.2, right panels).The moorings were labeled according to coastal trapline designations provided by the Cree Trapper's Association: the most southerly site is called CH37; the most northerly site and the only site north of the river mouth is called CH3; and between these locations and to the south of the river mouth, we had two other moorings, CH33 and CH34 (Figure 4.2). CH3 is located close to Paul Bay, 15 km north of the river mouth. The CH37 mooring was located 40 km south of the La Grande River mouth and 11 km north of the relatively small Castor River (mean annual discharge 48 $m^3 s^{-1}$) (Figure 4.2). The moorings remained in the water from August 2019 to September 2020.

The moorings consisted of two loggers attached to a stainless-steel frame: one Onset HOBO U24-002-C to record temperature and salinity, and one Onset HOBO U20L to record pressure (or depth). The accuracies of the Onset HOBO U24-002-C conductivity and temperature instruments used on the moorings were 3% of the reading or ±50 μS/cm and ±0.1 at 25°C, respectively. Approximately a meter away from the moorings, a Lowell Industries TCM-1 tilt current meter was attached to a rock-bag anchor. Unfortunately, the pressure logger at CH34 malfunctioned such that no data was recorded.

Owing to the circumstances associated with the global pandemic in 2020, the vertical profiles of conductivity, temperature, and depth (CTD) could not be collected during the winter of 2020 or at the time of mooring recovery. Here, we refer to the CTD measurements collected during the field campaigns in January-March 2019 and June-September 2019 (Figure 4.2). The CTD used for the vertical casts was a Castaway made by SonTek. The accuracies of the Castaway CTD, as stated by the manufacturer, are ±0.05°C for temperature, 0.25% ±5 µS/C for conductivity, and ±0.1 for salinity.

4.3.3 Additional data sources

The research presented here was conducted as part of the broader Eeyou Coastal Habitat Comprehensive Research Project (CHCRP), which aimed to improve the understanding of the environmental factors affecting eelgrass (*Zostera marina*) and the effects of a generalized decline in eelgrass on geese, and consequently, Cree hunting. The river team within the project installed new water level gauges on ten rivers of eastern James Bay and analyzed the discharge data collected by Hydro-Québec (see de Melo et al., 2022). The river team and Hydro-Québec provided discharge data for the eleven rivers shown in Figure 4.6 Additional information on the project can be found online: https://www. eeyoucoastalhabitat.ca.

In addition to the discharge data for the La Grande River provided by the CHCRP, we used wind velocity data obtained from ERA5 reanalysis products (10 m wind velocity) to interpret the mooring records. The ERA5 reanalysis data interrogation was conducted on one grid point (53.8°N and 79.6°W), and the data were found to be comparable to those from the Wemindji airport weather station. The freeze and melt evolution dates were estimated using satellite imagery (Sentinel-2 and MODIS) and mooring records.

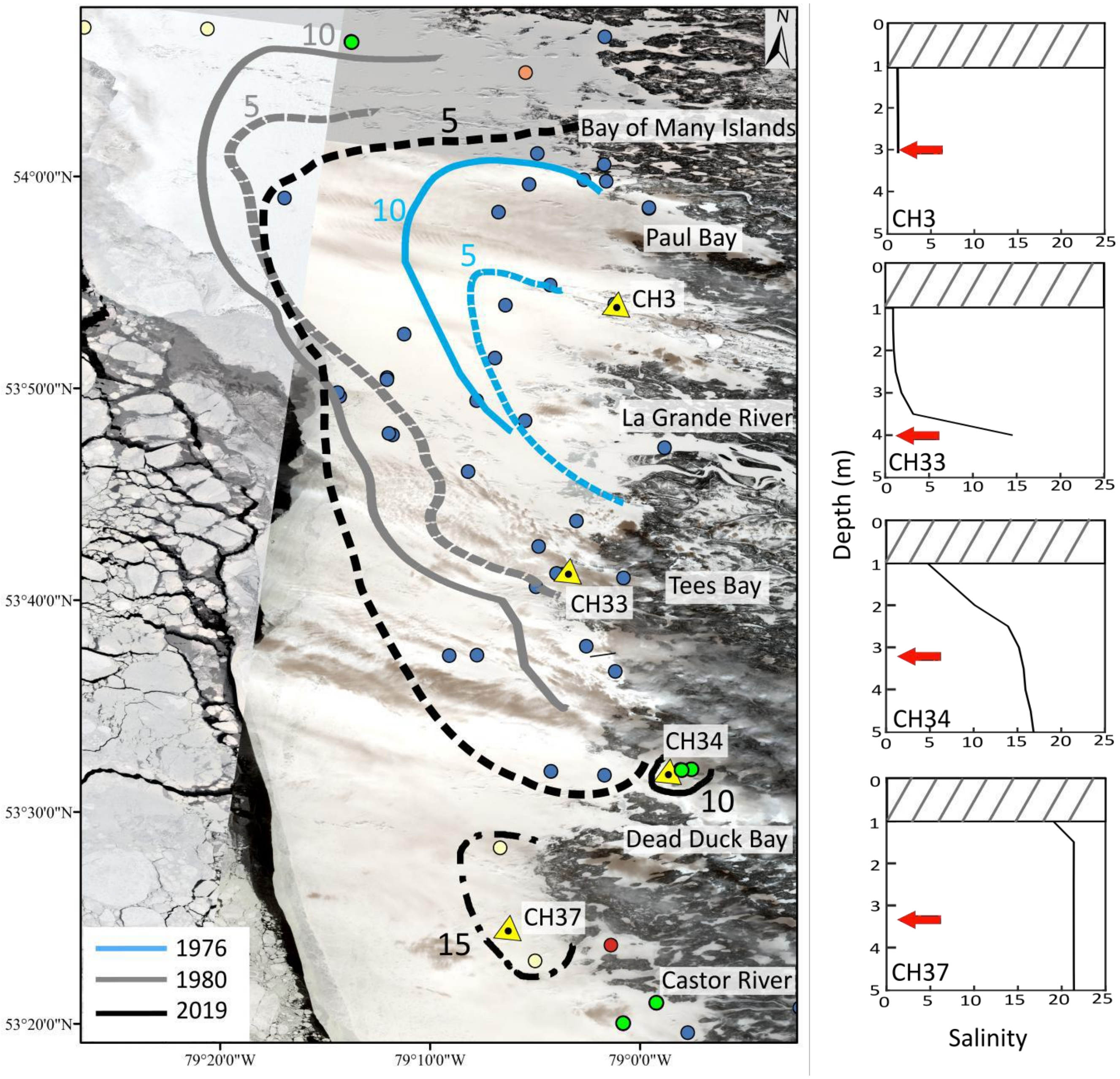

Figure 4.2: Map of the study area in northeast James Bay (see Fig. 4.1) around the La Grande River mouth showing the mooring locations (triangles) and under-ice plume extent based on CTD casts (colored circles) from 2019. The surface salinity under the ice is indicated by the following colors: blue- 0-5PSU, Green- 5-10 PSU, Yellow- 10-15 PSU, Red- 15-20 PSU. Salinity contours (5 and 10 PSU) were included from 1976 and 1980, based on Department of Fisheries and Oceans' Marine Environmental Data Section Archive data. The ice image is a Sentinel-2 true-color image for 1 March 2019 and shows the landfast ice extent for the coast. Right hand panels show the average under-ice salinity profile for each mooring location: CH3, CH33, CH34, and CH37 in winter 2019.

4.4 Results

4.4.1 CTD data

CTD profiling was performed to characterize the plume thickness and spatial extent. The plume extent in 2019 was similar to that in 2016 and 2017 (cf., Peck et al., 2022, Chapter 3), with the core area of the plume (salinity 0-5 PSU), extending approximately 30 km north and south of the river mouth. In relation to the coastline and moorings, the northern extent of the core area of the plume reached the southern end of the Bay of Many Islands, and the southern limit was located between Tees Bay and Dead Duck Bay (Figure 4.2). The average under-ice salinity profiles at moorings CH3 and CH33 clearly show a surface layer of <5 PSU, ~ 2-3 m thick (Figure 4.2, right panels), which was present under the landfast ice throughout the core area of the plume. At CH33, the CTD data revealed a distinct two-layered structure of the water column, with salinity increasing from approximately 2 PSU in the surface layer to approximately 15 PSU at a depth of 4 m. Outside the core area of the plume, the surface salinity increased rapidly in a frontal zone (Figure 4.2). At mooring CH34, which was positioned in this frontal zone, the average surface salinity was slightly above 5 PSU, and the water column was weakly stratified (Figure 4.2, right panel). Mooring CH37, which was located approximately 10 km south of CH34, had, on average during the winter period, a well-mixed water column with a salinity of approximately 21 PSU.

4.4.2 Annual time series of temperature

The temperature and salinity time series recorded by the four moorings are shown in Figure 4.3. A 24-hour moving average filter was applied to the data in Figure 4.3, to remove semidiurnal tidal variations. The filtering primarily eliminated minor fluctuations, with no significant periods of low salinity being excluded. The yearlong mooring record captured an expected annual cycle in water temperature starting with a i) fall cooling period, ii) winter conditions with temperatures at or near the freezing point, and iii) spring-summer heating period until annual maximum temperatures were reached in August.

When the CH3 and CH34 moorings were deployed in late August, the water temperature was approximately 12°C and decreased to approximately 8°C in early October when CH33 and CH37 were deployed (Figure 4.3a). A rapid cooling phase commenced in October, during which the recorded temperatures were almost the same at the four moorings. By the second week of November, ~4-5 weeks before ice freeze-up commenced, the water temperatures stabilized to close to their salinity-derived freezing points. Throughout November and the first half of December, CH3 and CH33 temperatures underwent oscillations that ranged from approximately –0.5°C to +2°C. The periods with lower temperatures were closely related to lower salinity, and vice versa, pointing to an influence from river discharge (Figures 4.3b and 4.4). These values correspond to temperature variations from 0 to 2.5°C above the freezing point. Temperatures at the more saline southern sites, CH34 and CH37, remained relatively more stable and closer (within 0.7°C) to the local seawater freezing points. Major variations in temperature stopped at all mooring sites after ice freeze-up occurred on 14 December 2019.

The ice breakup period began on 20 May 2020 and lasted approximately a month. During this period, the water temperature increased owing to increasing solar heating and a reduction in the albedo effect because the near-shore ice melted and offshore leads opened up. The ice breakup was complete by 16 June 2020. At all sites, the water temperature at 3-4 m depth steadily increased after the sites became ice-free and reached summer temperatures above 8-10°C by mid-July (Figure 4.3a).

4.4.3 Annual time series of salinity

In September and October, the salinity was above 20 at CH34 and CH37 and varied between approximately 10 and 18 PSU at the other two sites (Figure 4.3b). During November and early January, the salinity remained relatively constant at CH34, increased at CH37, and fluctuated at CH3 and CH33. A freshening event around 11 November 2019, affected the latter two moorings located closest to the LGR. Water temperatures stabilized shortly after freeze-up in early December 2019. In contrast, salinity continued to vary following the development of landfast ice after 14 December, particularly at CH3 and CH33 near the mouth of the La Grande River. Further south, at CH34 and CH37, salinities declined significantly between late January and March 2020.

By the second half of March, the salinities at CH34 and CH37 had returned to early January levels. Particularly at CH37, located furthest away from the LGR, the salinity showed an increasing trend that is typically expected from brine release from sea ice growth in locations with little freshwater input. In April, an increase in salinity was recorded at the CH3 and CH33 mooring sites. From the ice melt onset on 20 May 2020 and throughout the summer months, June and July 2020, salinity continued to gradually decrease at all mooring sites, presumably associated with a combination of LGR, the arrival of freshwater from the smaller non-regulated rivers discharging into southern James Bay, and sea-ice meltwater (Guzzi et al., 2024).

Salinity variations at the four moorings (Figure 4.4a) highlight three major freshening events in November, January, and February, which will be described in more detail. While there are several decreases in salinity, especially at CH3, the three major events occurred at two or more moorings simultaneously. While there was a freshening event that occurred at CH3 and CH33 at the end of December, it was relatively short-lived and the salinity decrease was not as severe when compared to the other events. Therefore, this and other decreases can be described as minor freshening events. The first major freshening event started on 06 November 2019 before the development of landfast ice coverage, and involved a decrease in daily mean salinity at CH3 from 18.3 PSU to 5.0 PSU over nine days and a salinity decrease of 9 PSU two days later at CH33. The salinities of CH34 and CH37 were not affected.

The next two freshening events occurred when solid landfast ice cover was present. The second freshening event can be split into two parts with the second part being highlighted as the more severe because it affected all 4 mooring locations. The first part occurred on 05 January 2020, and lowered the salinity at the CH3 mooring site to approximately 1.5 PSU. The salinity then remained low, varying between 1 and 6 PSU for the next 100 days. The salinity at CH33 also decreased by 6 PSU before the second part of the freshening event. The second part of the freshening event occurred on 15 January 2020, and all four moorings reached their lowest salinity in January. The onset of freshening occurred sequentially, north to south, along the coast south of the river mouth, beginning with CH33 on 15 January 2020, and affecting CH34 and CH37 two weeks later. The salinity at CH33 decreased by 16 PSU and remained low for 16 days. The decrease was less severe at CH34 and CH37, with salinity decreasing by 5 PSU and 1 PSU, respectively, for a duration of only 5 days.

A subsequent more extensive freshening event was recorded at all moorings beginning in February 2020 (Figures 4.3b & 4.4a). It began on 03 February 2020 with the low salinity signal quickly spreading across the mooring array, with only a 4-day lag between CH33, CH34, and CH37 (Figure 4.4a). It was also more substantial than previous events particularly with salinity at CH33 decreasing from 16 to 1.7 PSU over five days. The salinity at CH34 decreased by 14 PSU over 20 days, whereas the salinity at CH37 decreased by 10 units over 15 days. After the minimum salinity was reached at each location, the salinity returned to previous levels. Similar to the freshening event, the transition to more saline conditions occurred quickly at CH33 (i.e., salinity increased by 14 PSU over 5 days), whereas it took 25 days for the salinity at CH34 and CH37 to return to previous levels.

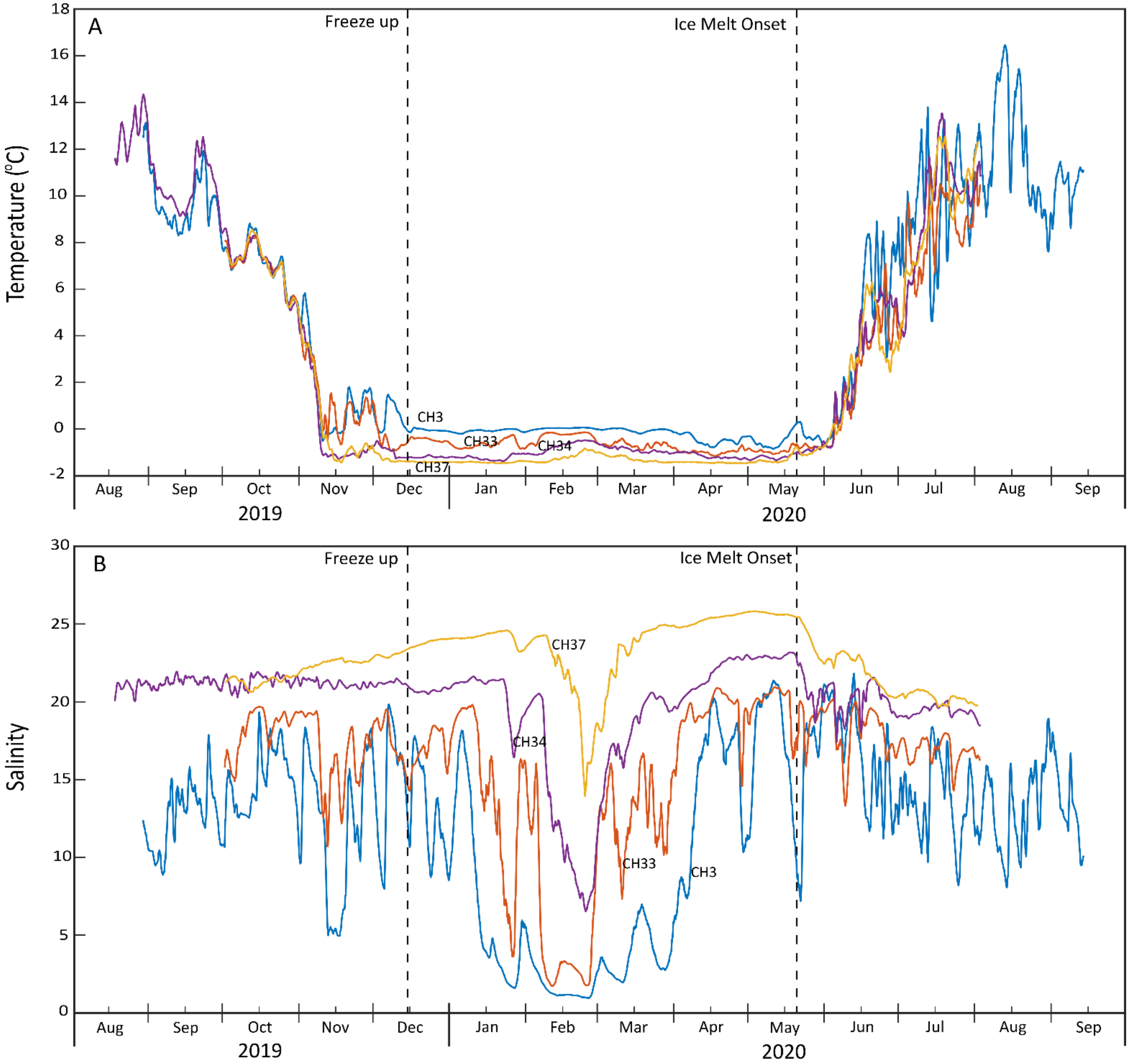

Figure 4.3: Annual records of temperature (A) and salinity (B) for all mooring locations. Values are averaged over 24 hours. The ice-covered and melt periods, as determined from Sentinel satellite images, are shown. Blue: CH3, Orange: CH33, Yellow: CH34, Purple: CH37.

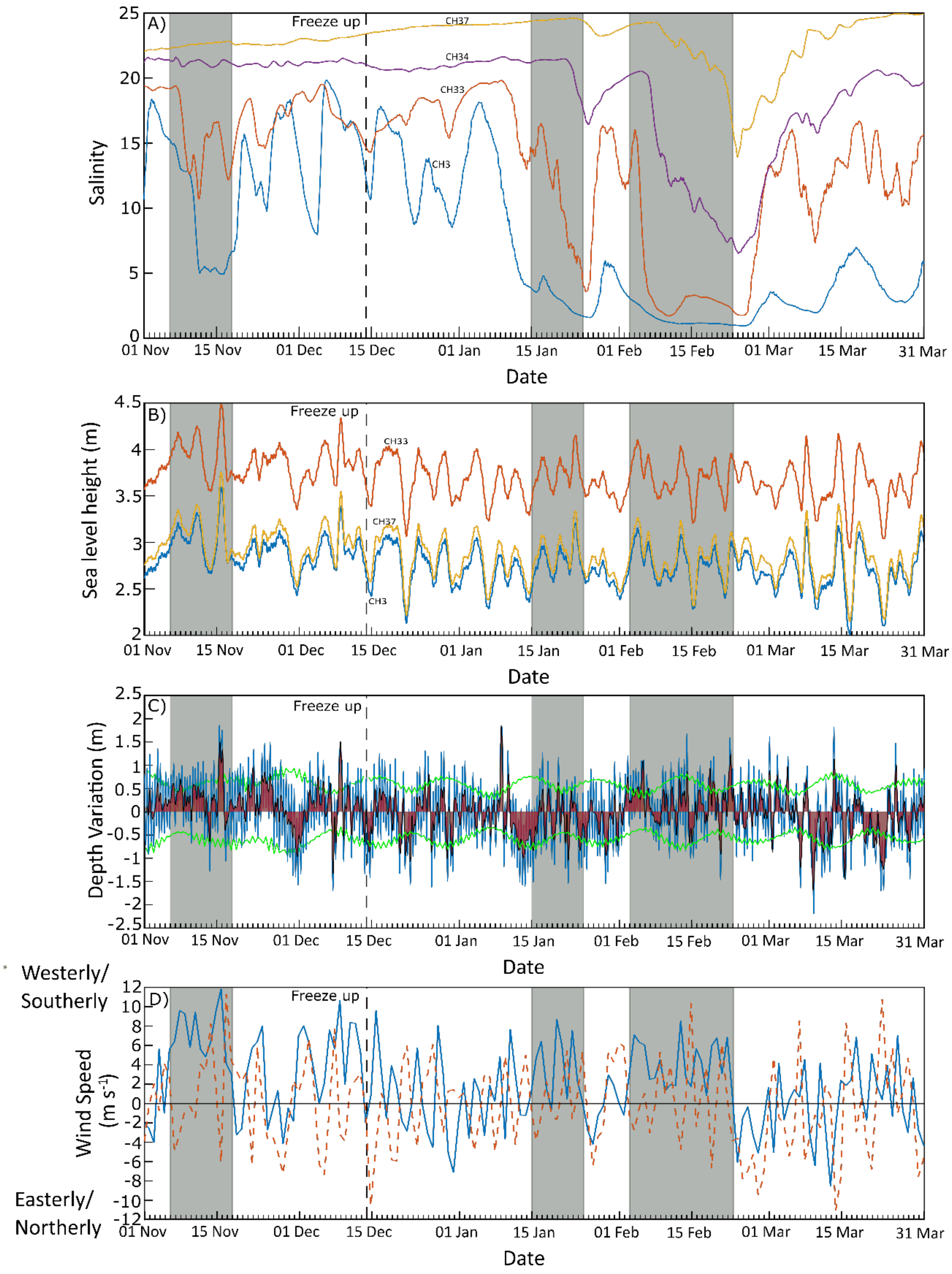

Figure 4.4: Daily averaged salinity (A) and daily averaged sea level height (B) for moorings CH3 (blue), CH33 (orange), CH37 (yellow). The pressure, spring-neap tidal range and residual variation for CH33 (C). Tidal analysis was conducted in T-Tide. Figure also shows wind velocity (D) in both U (blue) and V (orange dashed line) for the period of October 2019 to March 2020. Each panel shows the date on which the ice-covered period started and three freshening events are identified and shaded in grey, one in November, a second in January, and a third in February.

4.4.4 Recorded sea level variations

All mooring sites showed the same variation in sea level height throughout the record, with the tidal variation removed by a moving 24hour average (Figure 4.4c). Analyzing the raw pressure from CH33 with the MATLAB t_tide package (Pawlowicz et al., 2002) shows that the tidal range was approximately one meter across the entire record (Figure 4.4d). The relationship between U wind and sea level anomaly was quantified for CH33 and CH37 (Fig. 4.5). At CH33, U wind and sea level anomaly showed a moderate positive correlation ($r = 0.444$, $p = 0.016$) (Figure 4.5a), indicating that higher U wind speeds were generally associated with elevated sea levels. At CH37, the correlation was slightly weaker but still statistically significant ($r = 0.390$, $p = 0.037$) (Figure 4.5), suggesting a consistent but less pronounced association at this more southerly location. However, sea level height sometimes changes independently of the wind. During a period that included the February freshening event, the water depth at the mooring sites initially increased by about 0.75 m between 1 and 5 February, but then rose and sank several times during the following 15-day period without the wind changing in the east-west direction.

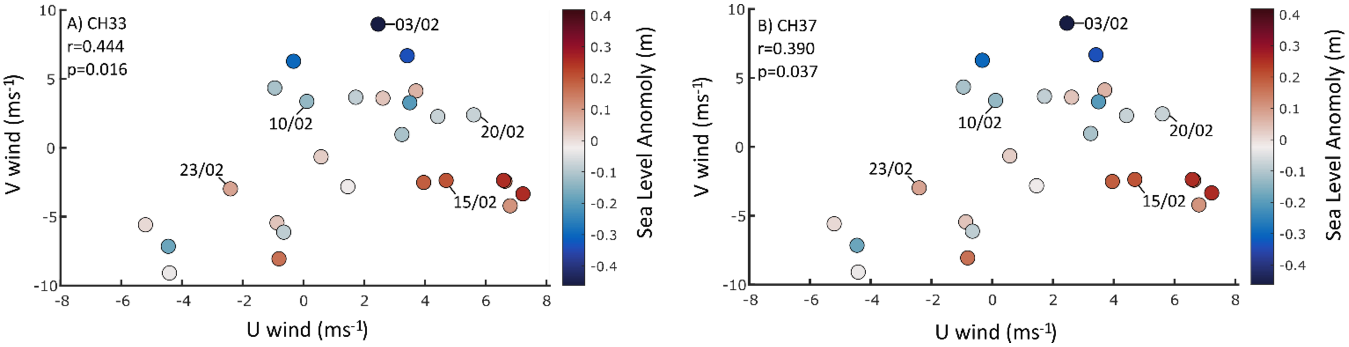

Figure 4.5: Relationships between the meridional/along shore (V) and zonal/across shore (U) wind components and daily averaged sea level anomaly (normalized to mean sea level height at each mooring) for CH33 (A) and CH37 (B). The dates for the onset and relaxation of the sustained wind period shown in Figure 4.4b are marked, along with the salinity peaks and lows during the sustained wind.

4.4.5 Wind speed during freshening events

The daily average wind speed data from the ERA5 reanalysis are shown in Figure 4.4b for the period spanning the three freshening events. The prevailing wind directions for the sample period were north-northwesterly and west-northwesterly (Figure S4.1). However, the wind speed in the region displays large variability and frequent changes in direction. For example, the monthly mean zonal wind component (U, or across shore) ranged from 3.5 m s^{-1} in November 2019 to 0.1 m s^{-1} in March 2020, but with standard deviations of 4.8 m s^{-1} and 3.9 m s^{-1}, respectively. For the meridional wind component (V, or along shore), monthly averages ranged between a northerly 3.0 m s^{-1} in October (standard deviation of 5.5 m s^{-1}) and a weak southerly –0.6 m s^{-1} in March (standard deviation of ± 5.2 m s^{-1}).

While the wind frequently changed direction, a consistent feature during all freshening events was the predominantly westerly wind. During the first freshening event, starting on 6 November 2019, the westerly wind had an average speed of 7.2 m s^{-1} and reached its highest peak of 11.8 m s^{-1} in the winter. For the second freshening event on 15 January 2020, the wind was blowing westerly reaching a peak of 8.7 m s^{-1}. During the third and largest freshening event on 3 February 2020, the westerly wind persisted uninterrupted for approximately 20 days (see shaded period in Figure 4.4). Daily average across-shore wind velocities during this period (3-23 February) were not exceptional but ranged between 0.8 m s^{-1} and 8.5 m s^{-1}; however, the absence of reversals in the U-component was notable.

4.4.6 Tilt current meters

Similar to the wind, the water currents were split into meridional and zonal components and expressed in Figure 4.6 as daily averages. The presence of landfast ice coverage has been shown to reduce wind-driven currents (Kasper and Weingartner, 2012). This is the case here, as the tidal amplitude does not decrease, but current speeds decrease during the ice-covered period as compared to the ice-free period at both mooring sites (Figure 4.6). For example, at mooring CH37, the range of current speed decreased from 6.7 cm s^{-1} in the ice-free period to 1.2 cm s^{-1} when ice cover was present. A small decrease in the average current speed was also observed. The largest of these was a decrease of 1.1 cm s^{-1} in the average U (across-shore) current component at mooring CH33 during the ice-covered period.

In the context of low variability in current speed, a few periods of higher flow during the ice-covered period stand out. There was a notable increase in the current speed at both moorings, coinciding with westerly winds and an increase in sea level height at the end of January, corresponding to the second freshening event at CH34 and CH37 (Figure 4.4a). Additionally, during the 20-day period of sustained wind in February 2020 (see section 3.4), the flow towards the west (away from shore) at CH33 intensified from -1.02 cm s^{-1} to -3.76 cm s^{-1} (Figure 4.6a). After the sustained wind subsided, the west-east current speed decreased but remained higher than before this period. The sustained westerly winds did not have the same impact on the current speeds at mooring CH37; however, there was an increase in the variation of the currents at CH37 during the period of sustained westerly winds.

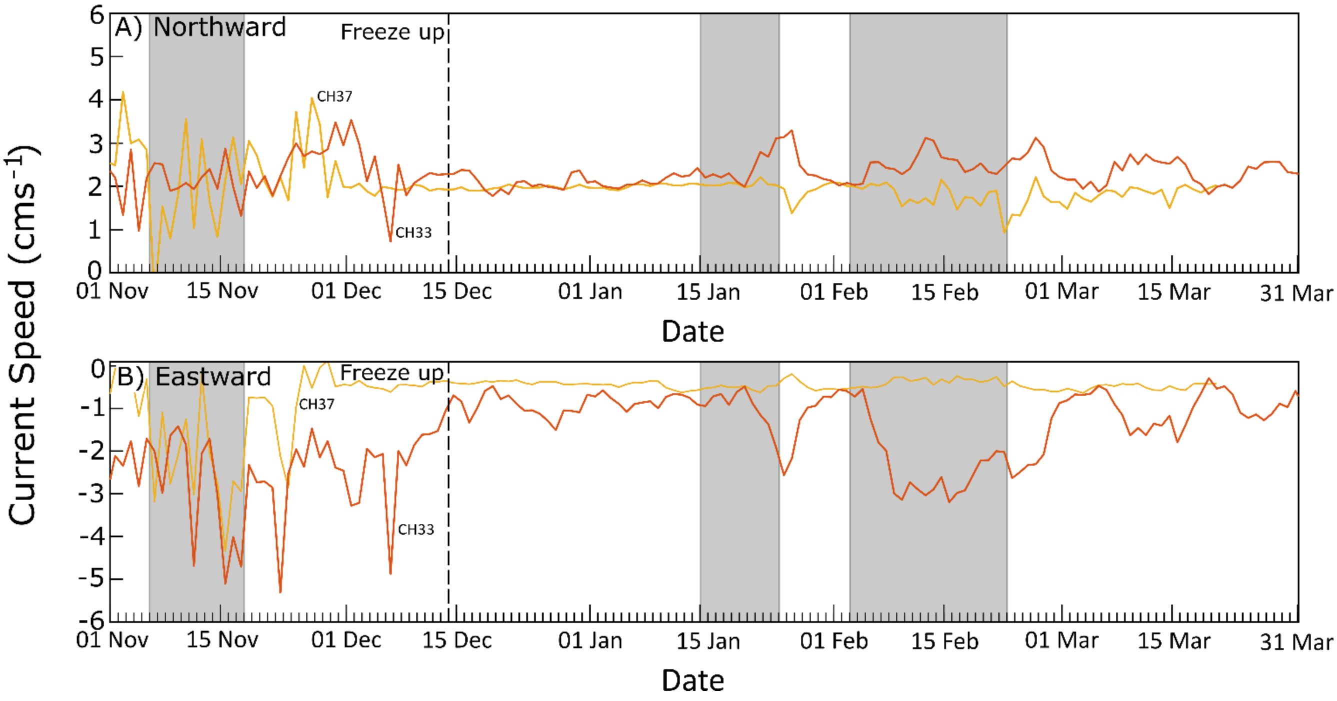

Figure 4.6: Daily averaged current velocity for the Northward (A)or the along shore component; high values at times approaching 4 cm s-1 indicate flow towards the north. eastward (B) current or across shore component; Low values at times approaching -5 cm s-1 indicate strong currents flowing towards the east and the shoreline Each panel shows the date on which the area became ice covered and highlights the 3 freshening events shown in Figure 4.

4.4.7 River discharge

The combined discharge for ten rivers (Figure 4.7 and Table SI4.1) with outlets in east James Bay south of the LGR show a boreal/subarctic discharge pattern that is typical of naturally unregulated rivers (McClelland et al., 2004; Dery et al., 2018). The combined discharge of the rivers to the south of the LGR was low and declined from November to March, with a weekly average of 1250 ± 280 $m^3 s^{-1}$, and in late April, began to rapidly increase to reach a peak of 6420 $m^3 s^{-1}$ during the spring freshet in mid-May. The LGR discharge, on the other hand, increased from ~2580 $m^3 s^{-1}$ to 5110 $m^3 s^{-1}$ in early November before ice freeze-up and then remained above 4500 $m^3 s^{-1}$ until the end of February (Figure 4.7).

Note that all three freshening events occurred during the period of elevated wintertime discharge >4500 $m^3 s^{-1}$ from the LGR. The mid-November freshening events observed at CH3 and CH33 (Figures 4.3a and 4.4a) commenced immediately after the November increase in LGR discharge. The overall average discharge of the LGR during the entire ice-covered period of 2019-2020 was 3760 $m^3 s^{-1}$ (±1250 $m^3 s^{-1}$ standard deviation). During the winter months, the LGR comprised between 70% and 80% of the total discharge into James Bay from the eleven sampled rivers. Therefore, the LGR is the predominant source of freshwater in the area during the mid-winter freshening events. Only during the spring freshet in May–early June did the LGR contribution decrease to below 30% of the total river discharge to eastern James Bay. The period of lowest observed discharge (~2000-3000 $m^3 s^{-1}$) from the LGR occurred in late March to May (immediately before and during spring freshet) and coincided with the general increase in salinity at all four moorings to their annual maximum values (Figure 4.3b).

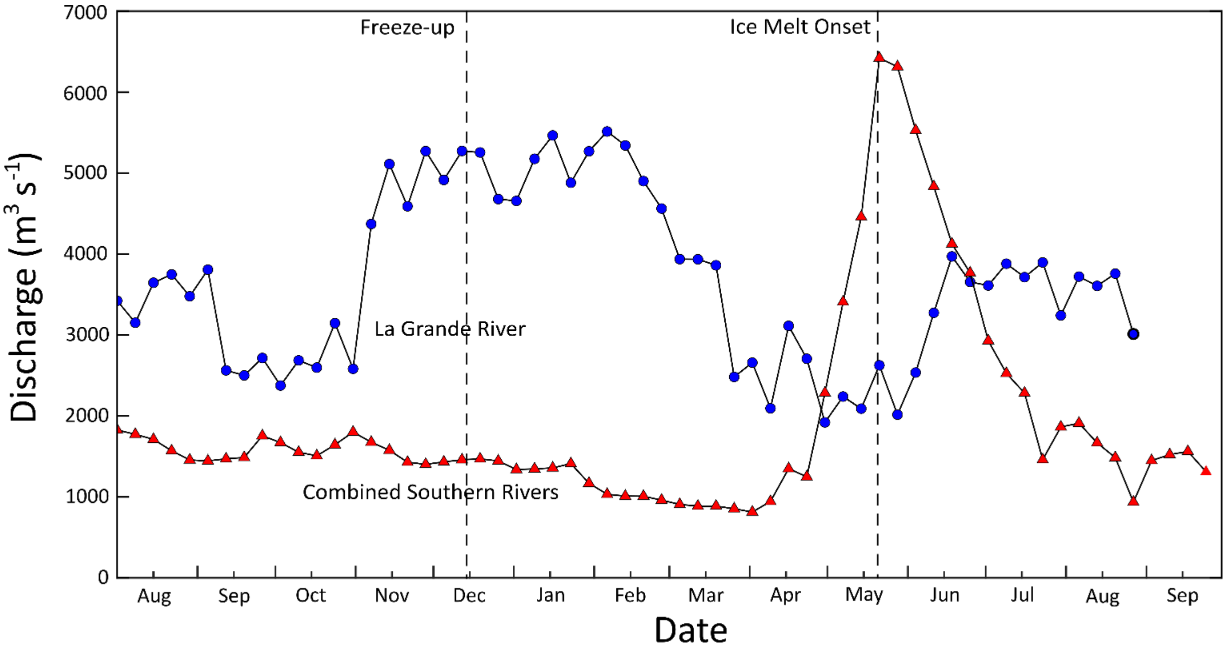

Figure 4.7: Weekly averaged discharge for the La Grande River (LGR) (blue) and combined discharge for 10 rivers on the east coast of James Bay south of La Grande (red) for the duration of the mooring deployments from August 2019 to August 2020. The dashed lines denote the dates of landfast sea ice freeze-up and melt onset.

4.5 Discussion

In a natural Arctic/subarctic coastal system, freshwater input into the coastal waters is minimal during winter when temperatures are below freezing, and the salinity steadily increases throughout the ice-covered period due to brine rejection from sea ice formation (El-Sabh & Koutitonsky, 1977; Prinsenberg 1986). However, the high discharge of the regulated LGR and the spreading of the plume, there are areas of the coast that are freshened throughout the winter months (cf., Eastwood et al., 2020). The under- ice plume of the LGR is usually assumed to flow northward or ‘down coast’ from the river mouth into northeast James Bay due to James Bay's cyclonic circulation. However, observations following the initial phases of the LGR hydroelectric development that raised the winter discharge from 460 to 4600 m^3 s^{-1} revealed that the under-ice plume also began to expand southward (Messier et al., 1989; Messier, 2002). Our own CTD sampling and time series data collected in winter 2019 further confirmed the upcoast expansion of the plume in the offshore area of the landfast ice-covered zone with, on average, the 5 PSU isohalines located approximately 25 km south of the 1976 position and 15 km south of the 1980 position (Figure 4.2). The CTD measurements only provide a snapshot of the plume at one point in time, while the four bottom-mount moorings deployed from August 2019 to August 2020, presented above, show that the plume’s extent evolved throughout the winter period.

4.5.1 Analysis of observed freshening events

The mooring data showed that the coast freshened on three separate occasions throughout the winter months, 06 November 2019, 05 January 2020, 03 February 2020, that coincided with sustained westerly winds (Figure 4.4). This section examines the specific environmental conditions: river discharge, wind forcing, ice dynamics, and coastal bathymetry, that contributed to the observed freshening event The first freshening event occurred before ice freeze-up and impacted only CH3 north of the river mouth and CH33 immediately south of the river mouth. At this time of year, the LGR plume expanded in response to the increase in LGR discharge from autumn levels of ~2600 m^3 s^{-1} to winter levels of >5000 m^3 s^{-1} (Figure 4.7). The second and third freshening events occurred in midwinter, when the landfast ice cover was well established and impacted all four moorings. The LGR discharge remained high throughout this period (Figure 4.7) and, from previous studies, the plume was likely at its full winter extent (Ingram and Larouche, 1987; Messier, 2002; Peck et al., 2022, Chapter 3). As with the first freshening event, there was a sustained westerly wind with the wind lasting 20 days for the third and most severe freshening event. Inspection of satellite imagery shows that before the third freshening event, there was a narrow

(~2 km at the widest point) open lead along the landfast ice edge with pack ice seaward with several holes and channels present (Figure 4.8a). During the period of sustained westerly wind (maximum wind speed 8.5 m s^{-1}), the mobile pack ice in James Bay was pushed up against the outer edge of the landfast ice (Figure 4.8b). Salinity at CH33 began to decrease on 4 February, just one day after the onset of sustained westerly winds on 3 February, followed by CH34 on 6 February and CH37 on 8 February, indicating a rapid and sequential southward intrusion of the plume in response to remote wind forcing (Figure 4.4a). After the westerly wind stopped on 23 February and became predominantly easterly and northerly (Figure 4.4d), the pack ice dispersed, allowing the lead to reopen and was 30-40 km at its widest point with very little pack ice present (Figure 4.8c), and salinity returned to normal at all moorings south of the river mouth (i.e., CH33, CH34, and CH37; Figure 4.4a).

Thus, we propose that the shoreward movement of the mobile pack ice resulting from the sustained winds in early February set up shoreward movement of the water column under the landfast ice and pushed the LGR plume up against the coast, including the coastal inlets where the moorings were located. This is similar to how a plume reacts to onshore winds in open water conditions (Fewings et al., 2008), except that here the wind forcing of surface waters is indirect, occurring tens of kilometers away in the flaw lead and area of mobile pack ice, rather than acting directly on the plume. Westerly wind action can be transferred into the water column through mobile pack ice and can impact the circulation of water under landfast ice (Schulze and Pickart, 2012). Strong westerly winds in the James Bay region are typically associated with cyclones traversing eastward over central Hudson Bay. These systems generate widespread onshore and alongshore winds across the bay, leading to coastal storm surges and elevated sea levels (Dmitrenko et al., 2021). Similar patterns were observed during the 2019–2020 winter season, where concurrent peaks in westerly wind speed and sea level height increases were recorded at multiple moorings (Figure 4.4), supporting the notion of onshore water mass displacement.

Focusing on the third event, there was a 0.5 m rise in water level at the start of the 20-day sustained wind (Figure 4.4b) and the local westward currents at CH33 increased by 2 m s^{-1} and remained increased throughout the 20-day period (Figure 4.5b). This increased offshore flow at the bottom is typical of downwelling, with surface water flowing towards the coast and likely kept the plume in the inlets. It is not clear why salinity remained low at CH37 in late February, as the currents only marginally increased during the period of sustained wind (Figure 4.5) but the LGR discharge remain high throughout February.

While onshore transport due to westerly wind forcing is supported by concurrent increases in sea level at all moorings and enhanced westward bottom currents at CH33, the sequential timing of freshening across the southern moorings suggests that the freshwater signal may have propagated along the coast. Under typical conditions, onshore flow increases sea surface height along the eastern coast of James Bay, establishing a cross-shelf pressure gradient that drives northward coastal currents a pattern recorded at mooring CH33 (Figure 4.6a) and consistent with regional cyclonic circulation (Dmitrenko et al., 2021). This mechanism suggests that westerly winds would more likely enhance northward, not southward, plume propagation. However, during the February 2020 event, the progression of salinity decreases from CH33 to CH34 and CH37 show a southward displacement of the plume along the coast. While there is a north-westerly component of the wind during the freshening event it is unlikely to overcome the enhanced northerly coastal current. The water flow along the east coast of James Bay is very complex such that delays and variations in freshening at the more southerly moorings could be caused by the local bathymetry and tidal dynamics at each mooring site. The embayments at CH34 and CH37 contain more islands and have narrower entrances (Figure 1) which could have slowed the propagation of the plume.

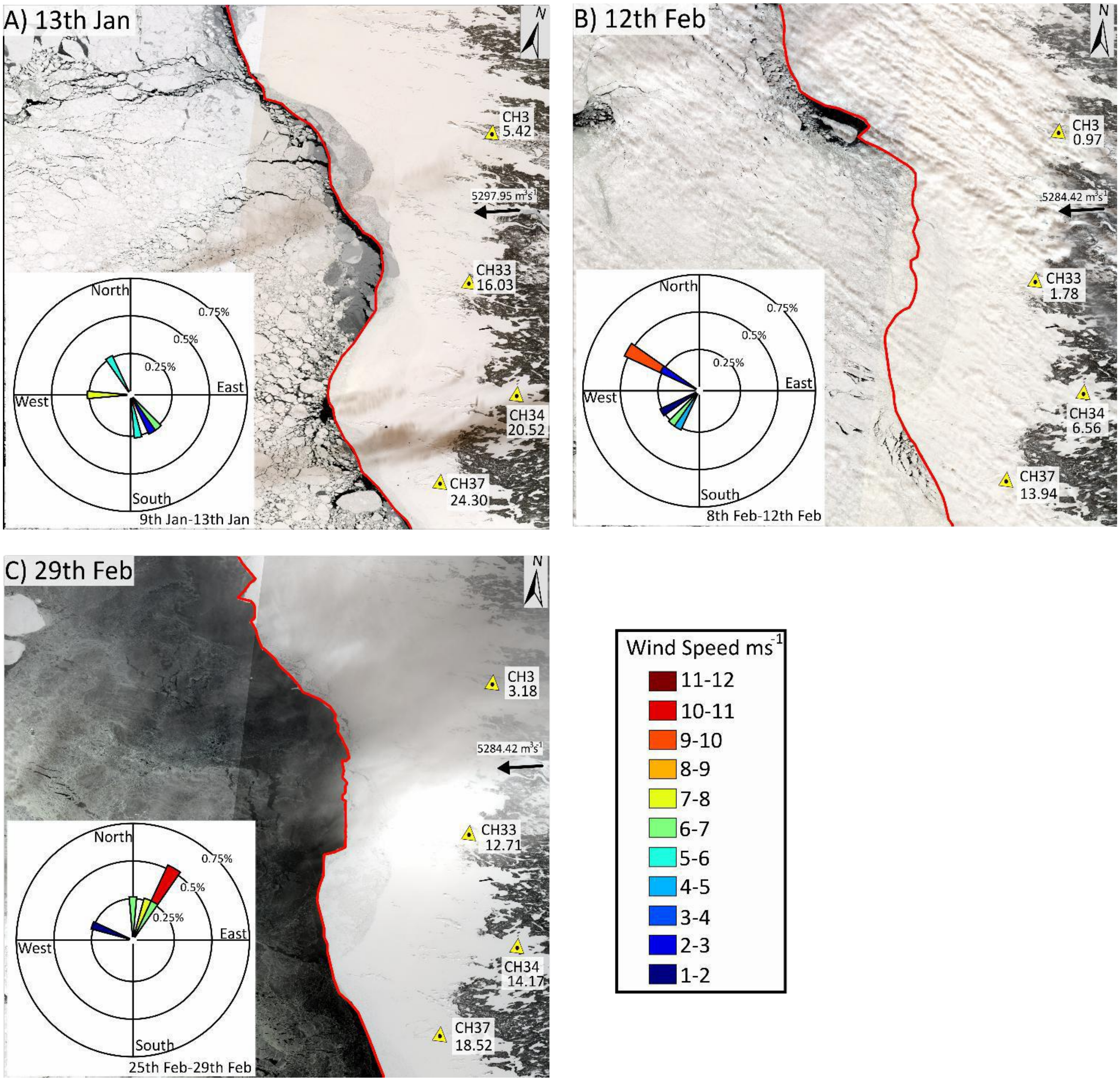

Figure 4.8: Satellite images of the land fast in various states. A) shows typical ice, discharge and wind conditions with the mobile pack ice closing a lead at the land fast edge. B) Shows the pack ice being pushed up against the land fast ice edge during the sustained westerly wind show in Figure 4.5b. C) Shows the westerly wind subsiding and the pack ice retreating to open water as a large flaw lead opens.

4.5.2 Historical occurrence of LGR plume intrusions

Given that these freshening events only occurred during winter when LGR is the only significant freshwater source, it is evident that a high LGR discharge is a prerequisite for the events to occur, and that landfast ice facilitates an expanded area of freshening as it enables the LGR plume to extend further along the coast (Ingram and Larouche 1987; Peck et al., 2022, Chapter 3). Thus, LGR plume intrusions south of the river mouth were presumably exceedingly rare or did not occur at all before increases in wintertime discharge occurred. It is important to consider how similar events of persistent wind forcing, favorable for upcoast freshening, have occurred on the northeast coast of James Bay during the past decades or if the winter of 2019-2020 was anomalous. The core area of the LGR under-ice plume (i.e., surface salinity <5 PSU) has remained at ~1200 km^2 since 1984, despite an increase in river discharge from 3000 m^3 s^{-1} to 5000 m^3 s^{-1} (Ingram and Larouche, 1987; Peck et al., 2022, Chapter 3). The landfast ice extent has also shown little change in width (~20-45 km) and persistence since 1978 (Taha et al., 2019; Gupta et al., 2022). With the LGR plume and landfast ice extent remaining relatively constant since 1984, it is likely that freshwater intrusions of the LGR under-ice plume occurred not only in 2020 but also during other winters with persistent westerly wind events.

ERA5 reanalysis wind data from 1983 to 2020 were analyzed to detect every event when the 5-day average westerly wind of ≥2 m s^{-1} lasted 20 days or more (Figure 4.9). In total, nine persistent wind events, such as the one in February 2020, were detected for 40 winters (January-March) from 1983 to 2022, or 1 out of 4-5 winters (22.5%). The inclusion of all months in the analysis suggests that persistent wind events occur every other year. No statistical trend or pattern could be discerned; however, we note that periods between events vary widely, from two years in a row in 1993 and 1994, to eight consecutive years without events (1995-2002 and 2006-2013). The 1993 event coincided with the previous time when the under-ice plume was investigated and observed to spread southward (Messier, 2002). The mean westerly wind speed during winter events generally ranged between 3.6 m s^{-1} and 4.9 m s^{-1}, i.e., roughly double the 2 m s^{-1} criteria used for their detection, indicating that these events are significant and observable periods. With the high wintertime discharge from the LGR expected to continue and the landfast ice extent likely to remain similar during winter months, we expect the freshwater intrusions of the LGR plume to continue to occur along the coast in the near future.

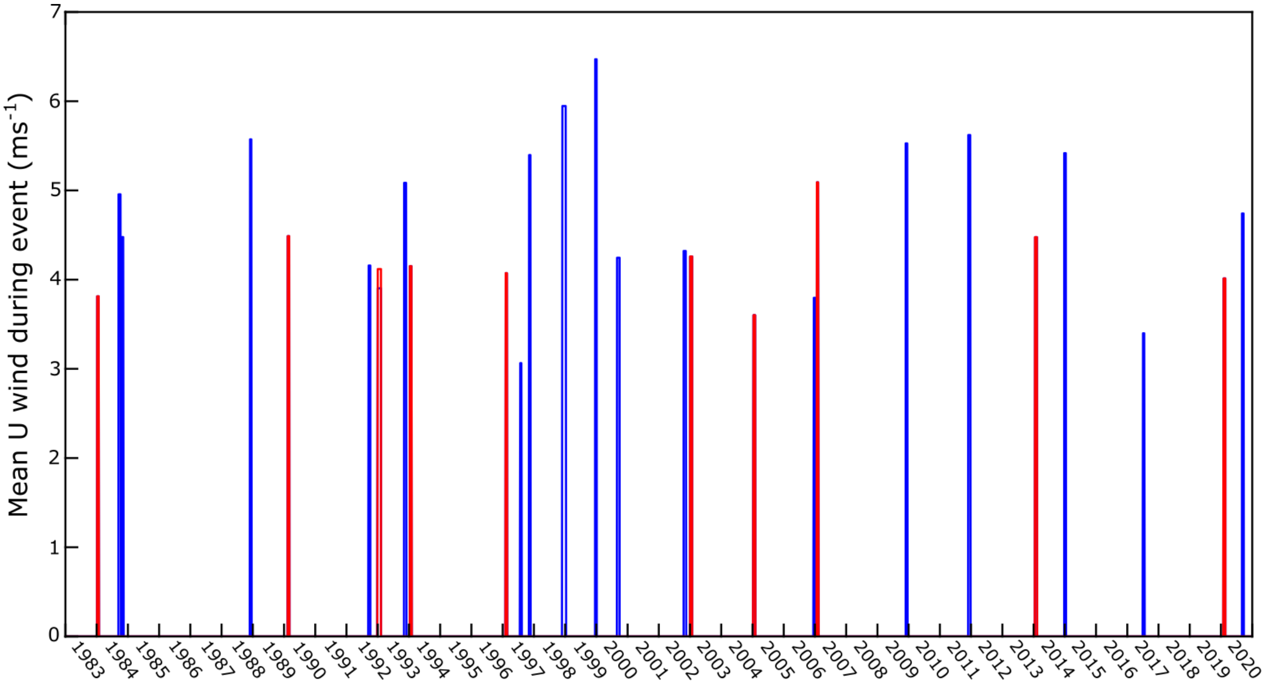

Figure 4.9: Wind events lasting 20 days with a 5-day average U wind of ≥2 m s^{-1} from 1983 to 2022 throughout each year (blue) and during January, February and March (red). Wind data was retrieved from ERA5 reanalysis data.

This dataset clearly shows that the plume expanded to the south, and certain weather events can push the plume into shallow coastal areas. While little is known about the impact of low salinity on eelgrass during the winter, it is known that prolonged periods of salinity of <15 PSU is below the optimal threshold for eelgrass growth (Nejrup and Pedersen, 2008). The movement of the plume to the south of the LGR could potentially affect eelgrass bed habitats that were previously thought to be unaffected by the influence of the plume. This should be considered when monitoring these habitats or before any future eelgrass restoration takes place.

Observations from other Arctic and subarctic systems provide useful context for interpreting the LGR plume's winter behavior. Under-ice plumes are often larger than in open-water conditions because they are protected from wind-driven mixing. In Alaska's Stefansson Sound, under-ice plumes persist and spread along the coast, but their movement is steered and limited by bathymetric channels and the stamukhi zone of the landfast ice (Okkonen and Laney, 2021), similar to the LGR plume described by Peck et al. (2022). Another recent example is in the Kara Sea, where the Ob–Yenisei plume developed an intense buoyancy-driven coastal current below sea ice. It spread hundreds of kilometers into the Laptev Sea despite being isolated from direct wind forcing, with plume motion preconditioned by autumn convection and enhanced by pressure gradients. In contrast, while the LGR plume also extends further under ice, our results show that winds acting through mobile pack ice can displace the plume, revealing an additional mechanism that may influence winter plume pathways and should be considered in other settings.

4.6 Conclusions

In a natural Arctic/subarctic coastal system, the salinity of seawater is expected to increase during winter owing to a reduction in runoff and sea ice growth. However, the mooring records from close to the LGR revealed a significant freshwater influence from the regulated LGR. The intrusion of the LGR under-ice plume into the southern areas of the coast may have negative implications for eelgrass habitats previously thought not to be affected by the enhanced LGR discharge. On average, with a larger southern extent, the LGR under-ice plume can now invade bays that were previously salty throughout the winter.

Three key conditions were found to be necessary for freshwater intrusion of the LGR plume: (1) the high winter discharge of the LGR (> 4000 $m^3 s^{-1}$), (2) the presence of a continuous cover of landfast ice, and (3) persistent westerly wind forcing. While northwesterly winds are typical of the region, our analysis indicates that events with sustained westerly winds ($\geq$2 $m s^{-1}$) of 20 days or more, which enabled the LGR under-ice plume intrusion southward to CH37, have only occurred nine times in the past 40 years. The periods with sustained westerly winds, when the plume was observed to reach furthest south, were also when the offshore James Bay waters were maximally ice-covered. It is therefore evident that the transfer of motion from the wind to the ocean was strong enough, despite the presence of mobile sea ice and the 10-20 km wide fringe of immobile landfast ice, to force the LGR under-ice plume to flow southward along the coast into embayments with eelgrass habitats.

4.7 References

Beardsley, R.C., Limeburner, R., Yu, H., Cannon, G.A., 1985. Discharge of the Changjiang (Yangtze River) into the East China Sea. Continental Shelf Research, 4, 57–76. https://doi.org/10.1016/0278-4343(85)90022-6

Chao, S.Y., 1988. Wind-driven motion of estuarine plumes. Journal of Physical Oceanography 18(8), 1144-1166.

Chapman, D.C., Lentz, S.J., 1994. Trapping of a coastal density front by the bottom boundary layer. Journal of Physical Oceanography 24(7), 1464-1479.

de Melo, M.L., Gérardin, M.-L., Fink-Mercier, C., del Giorgio, P.A., 2022. Patterns in riverine carbon, nutrient and suspended solids export to the Eastern James Bay: links to climate, hydrology and landscape. Biogeochemistry 161, 291–314. https://doi.org/10.1007/s10533-022-00983-z

Déry, S.J., Stadnyk, T.A., MacDonald, M.K., Koenig, K.A., Guay, C., 2018. Flow alteration impacts on Hudson Bay river discharge. Hydrological Processes 32, 3576–3587. https://doi.org/10.1002/hyp.13285

Dmitrenko, I.A., Kirillov, S.A., Babb, D.G., Kuzyk, Z.Z.A., Basu, A., Ehn, J.K., Sydor, K., Barber, D.G., 2021. Storm-driven hydrography of western Hudson Bay. Continental Shelf Research 227, 104525. https://doi.org/10.1016/j.csr.2021.104525

Eastwood, R.A., Macdonald, R.W., Ehn, J.K., Heath, J., Arragutainaq, L., Myers, P.G., Barber, D.G., Kuzyk, Z.A., 2020. Role of River Runoff and Sea Ice Brine Rejection in Controlling Stratification Throughout Winter in Southeast Hudson Bay. Estuaries and Coasts 43, 756–786. https://doi.org/10.1007/s12237-020-00698-0

El-Sabh, M.I., Koutitonsky, V.G., 1977. An Oceanographic Study of James Bay before the Completion of the La Grande Hydroelectric Complex. Arctic 30, 169–186.

Fewings, M., Lentz, S.J., Fredericks, J., 2008. Observations of Cross-Shelf Flow Driven by Cross-Shelf Winds on the Inner Continental Shelf. Journal of Physical Oceanography 38(11), 2358–2378. https://doi.org/10.1175/2008JPO3990.1

Fong, D.A., Geyer, W.R., 2001. Response of a river plume during an upwelling favourable wind event. Journal of Geophysical Research: Oceans 106, 1067–1084. https://doi.org/10.1029/2000JC900134

García Berdeal, I., Hickey, B.M., Kawase, M., 2002. Influence of wind stress and ambient flow on a high discharge river plume. Journal of Geophysical Research: Oceans 107, 13-1-13–24. https://doi.org/10.1029/2001JC000932

Garvine, R.W., 1999. Penetration of buoyant coastal discharge onto the continental shelf: A numerical model experiment. Journal of Physical Oceanography 29(8), 1892-1909.

Garvine, R.W., 1995. A dynamical system for classifying buoyant coastal discharges. Continental Shelf Research, Nearshore and Coastal Oceanography 15, 1585–1596. https://doi.org/10.1016/0278-4343(94)00065-U

Gupta, K., Mukhopadhyay, A., Babb, D.G., Barber, D.G., Ehn, J.K., 2022. Landfast sea ice in Hudson Bay and James Bay: Annual cycle, variability and trends, 2000–2019. Elementa: Science of the Anthropocene 10, 00073. https://doi.org/10.1525/elementa.2021.00073

Guzzi, A.C., Ehn, J.K., Michel, C., Tremblay, J.-É., Heath, J.P., Kuzyk, Z.Z.A., 2024. Influence of altered freshwater discharge on the seasonality of nutrient distributions near La Grande River, northeastern James Bay, Québec. Elementa: Science of the Anthropocene 12, 00133. https://doi.org/10.1525/elementa.2023.00133

Halverson, M.J., Pawlowicz, R., 2008. Estuarine forcing of a river plume by river flow and tides. Journal of Geophysical Research: Oceans 113. https://doi.org/10.1029/2008JC004844

Horner-Devine, A.R., Hetland, R.D., MacDonald, D.G., 2015. Mixing and Transport in Coastal River Plumes. Annual Review of Fluid Mechanics 47, 569–594. https://doi.org/10.1146/annurev-fluid-010313-141408

Ingram, R.G., 1981. Characteristics of the Great Whale River plume. Journal of Geophysical Research: Oceans 86, 2017–2023. https://doi.org/10.1029/JC086iC03p02017

Ingram, R.G., Larouche, P., 1987. Changes in the under-ice characteristics of La Grande Rivière plume due to discharge variations. Atmosphere-Ocean 25, 242–250. https://doi.org/10.1080/07055900.1987.9649273

Jurisa, J.T. and Chant, R.J., 2013. Impact of offshore winds on a buoyant river plume system. Journal of Physical Oceanography 43(12), 2571-2587.https://doi.org/10.1175/JPO-D-12-0118.1

Kasper, J.L. and Weingartner, T.J., 2015. The spreading of a buoyant plume beneath a landfast ice cover. Journal of Physical Oceanography 45(2), 478–494.https://doi.org/10.1175/JPO-D-14-0101.1

Kasper, J.L., Weingartner, T.J., 2012. Modeling winter circulation under landfast ice: The interaction of winds with landfast ice. Journal of Geophysical Research: Oceans 117. https://doi.org/10.1029/2011JC007649

Kourafalou, V.H., Oey, L.-Y., Wang, J.D., Lee, T.N., 1996. The fate of river discharge on the continental shelf: 1. Modeling the river plume and the inner shelf coastal current. Journal of Geophysical Research: Oceans 101, 3415–3434. https://doi.org/10.1029/95JC03024

Kuzyk, Z.A., Macdonald, R.W., Granskog, M.A., Scharien, R.K., Galley, R.J., Michel, C., Barber, D., Stern, G., 2008. Sea ice, hydrological, and biological processes in the Churchill River estuary region, Hudson Bay.

Estuarine, Coastal and Shelf Science 77, 369–384. https://doi.org/10.1016/j.ecss.2007.09.030

Li, M., Zhong, L., 2009. Flood–ebb and spring–neap variations of mixing, stratification and circulation in Chesapeake Bay. Continental Shelf Research, Physics of Estuaries and Coastal Seas: Papers from the PECS 2006 Conference 29, 4–14. https://doi.org/10.1016/j.csr.2007.06.012

Li, S.S., Ingram, R.G., 2007. Isopycnal deepening of an under-ice river plume in coastal waters: Field observations and modeling. Journal of Geophysical Research: Oceans 112. https://doi.org/10.1029/2006JC003883

Macdonald, R.W., Carmack, E.C., 1991. The role of large-scale under-ice topography in separating estuary and ocean on an Arctic shelf. Atmosphere-Ocean 29, 37–53. https://doi.org/10.1080/07055900.1991.9649391

Macdonald, R.W., Paton, D.W., Carmack, E.C., Omstedt, A., 1995. The freshwater budget and under-ice spreading of Mackenzie River water in the Canadian Beaufort Sea based on salinity and 18O/16O measurements in water and ice. Journal of Geophysical Research: Oceans 100, 895–919. https://doi.org/10.1029/94JC02700

McClelland, J.W., Holmes, R.M., Peterson, B.J., Stieglitz, M., 2004. Increasing river discharge in the Eurasian Arctic: Consideration of dams, permafrost thaw, and fires as potential agents of change. Journal of Geophysical Research: Atmospheres 109. https://doi.org/10.1029/2004JD004583

Messier, D., Lepage, S., Margerie, S. de, 1989. Influence of ice cover on the extent of the La Grande River plumes (James Bay). Arctic (Journal of the Arctic Institute of North America); (Canada) 42:3.

Nejrup, L.B., Pedersen, M.F., 2008. Effects of salinity and water temperature on the ecological performance of *Zostera marina*. Aquatic Botany 88, 239–246. https://doi.org/10.1016/j.aquabot.2007.10.006

O'Donnell, J., 2010. The dynamics of estuary plumes and fronts, in: Valle-Levinson, A. (Ed.), Contemporary Issues in Estuarine Physics. Cambridge University Press, Cambridge, pp. 186–246. https://doi.org/10.1017/CBO9780511676567.009

Okkonen, S.R., Laney, S.R., 2021. Optical, Structural and Kinematic Characteristics of Freshwater Plumes Under Landfast Sea Ice During the Spring Freshet in the Alaskan Coastal Arctic. Journal of Geophysical Research: Oceans 126, e2021JC017549. https://doi.org/10.1029/2021JC017549

Otero, P., Ruiz-Villarreal, M., 2008. Wind forcing of the coastal circulation off north and northwest Iberia: Comparison of atmospheric models. Journal of Geophysical Research: Oceans 113. https://doi.org/10.1029/2008JC004740

Peck, C.J., Kuzyk, Z.Z.A., Heath, J.P., Lameboy, J., Ehn, J.K., 2022. Under-Ice Hydrography of the La Grande

River Plume in Relation to a Ten-Fold Increase in Wintertime Discharge. Journal of Geophysical Research: Oceans 127, e2021JC018341. https://doi.org/10.1029/2021JC018341

Prinsenberg, S.J., 1986. Chapter 9 Salinity and Temperature Distributions of Hudson Bay and James Bay, in: Martini, I.P. (Ed.), Elsevier Oceanography Series, Canadian Inland Seas. Elsevier, pp. 163–186. https://doi.org/10.1016/S0422-9894(08)70902-4

Schulze, L.M., Pickart, R.S., 2012. Seasonal variation of upwelling in the Alaskan Beaufort Sea: Impact of sea ice cover. Journal of Geophysical Research: Oceans 117. https://doi.org/10.1029/2012JC007985

Taha, W., Bonneau-Lefebvre, M., Cueto Bergner, A., Tremblay, A., 2019. Evolution From Past to Future Conditions of Fast Ice Coverage in James Bay. Frontiers in Earth Science 7. https://doi.org/10.3389/feart.2019.00254

Yankovsky, A.E., 2000. The cyclonic turning and propagation of buoyant coastal discharge along the shelf. Journal of Marine Research 58(4), 585–607.

Yankovsky, A.E., Hickey, B.M., Münchow, A.K., 2001. Impact of variable inflow on the dynamics of a coastal buoyant plume. Journal of Geophysical Research: Oceans 106, 19809–19824. https://doi.org/10.1029/2001JC000792

4.8 Supplemental material

Table S 4.1: Locations for ten sampled rivers to the south of the La Grande.

River	Lat	Long
Castor	53.406	-78.834
Broadback	51.334	-78.822
Conn	52.382	-78.402
Eastmain	52.239	-78.133
Jolicoeur Sud	51.906	-78.560
Jolicoeur Nord	51.979	-78.481
Maquatua	53.014	-78.770
Nottaway	50.954	-78.305
Rupert	51.403	-78.515
Vieux-Comptoir	52.595	-78.624

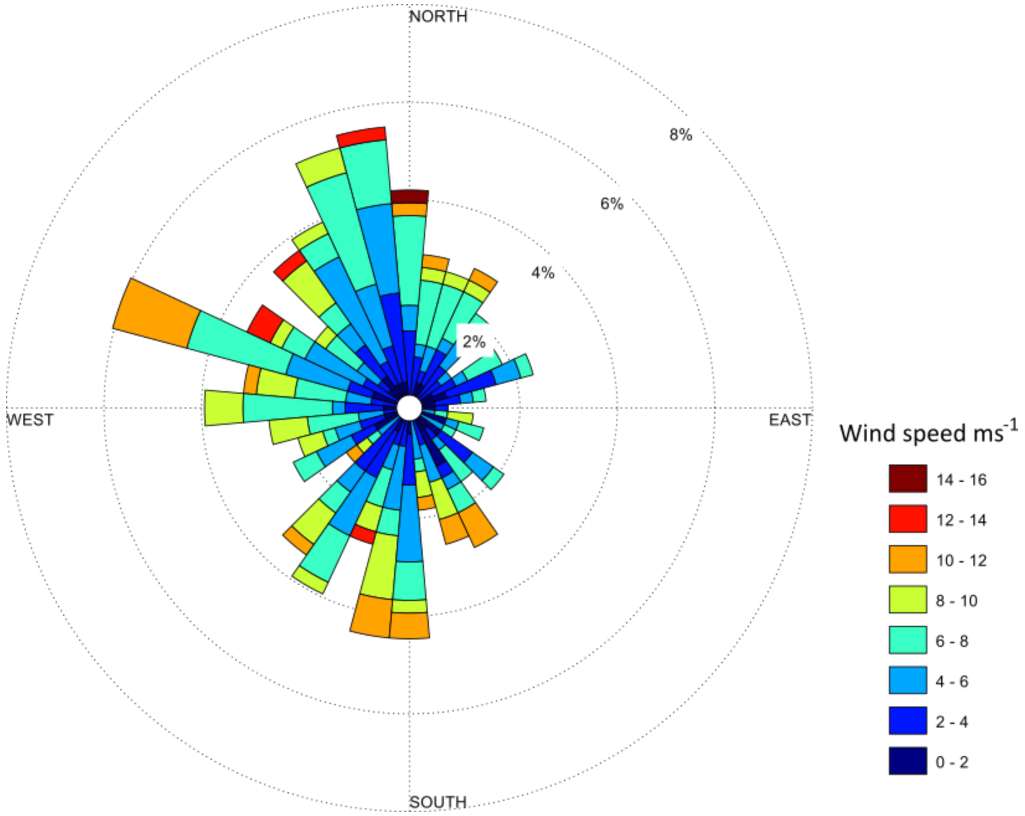

Figure S 4.1: Wind rose diagram showing the prevailing wind direction and speeds (m s^{-1}) for the sample area. Wind directions are labeled according to meteorological convention, where a northerly wind (N) blows from the north toward the south, a southerly wind (S) from the south toward the north, etc.

Chapter 5 Winter-to-summer transition in seawater salinity, temperature and light at eelgrass bed habitats in northeastern James Bay

This manuscript is being prepared for submission to the peer-reviewed journal Estuaries and Coasts. The citation for this manuscript is as follows:

Peck, C.J., Kuzyk, Z.A., O'Conner, M., Leblanc, M., Ehn, J.K. (in prep.) Winter-to-summer transition in seawater salinity, temperature, and light at eelgrass bed habitats in northeastern James Bay.

5.1 Abstract

Understanding the impacts of climate warming and extreme events on northern nearshore ecosystems requires observational data on seasonal changes in ice cover, salinity, temperature, and light. This study examines changes in these essential variables influencing eelgrass (*Zostera marina*) habitats in northeastern James Bay that are within the La Grande River (LGR) estuary, where growth conditions are at the tolerance limits for eelgrass. From March to August 2019, as the eelgrass ecosystem transitioned from ice-covered to ice-free open water, bottom-mounted moorings continually collected data to track salinity, temperature, and photosynthetically active radiation (PAR) at two locations with perennial eelgrass beds: CH4 (30 km north) and CH33 (10 km south of the LGR mouth). We hypothesized that salinity, temperature, and light would increase together with the onset of ice-free conditions while differences in the degree of LGR influence would modulate the seasonal patterns in a site-specific manner. During the ice-covered period, hydroelectric regulation of the LGR caused high freshwater discharge, which reduced salinity to 1 PSU at CH33 and 7 PSU at CH4. PAR was very low and likely limited eelgrass growth. In late May to early June, a sequence of melt-related events caused variations in salinity, temperature and PAR, starting with snow and ice surface melt (decrease in salinity, increase in PAR), followed by land drainage and initiation of local stream flow (decrease in both salinity and PAR), and finally ice melt (decrease in salinity and initiation of warming). Open-water conditions from 10 June onwards brought increased temperatures and elevated PAR levels. However, during the open-water period, overall, there was sufficient underwater light for eelgrass growth only 26% of the time at CH33 and 15% at CH4. Furthermore, CH33 experienced large tidal salinity fluctuations (changes of 15–20 PSU) because of oscillations between riverine and marine influences; this may have hindered eelgrass growth relative to the more stable environmental conditions at CH4. Overall, essential variables for

eelgrass habitats responded strongly to seasonal snow and ice melt and changes in river discharge, with local differences caused by proximity to small streams and the LGR. Variations in light were, at times, independent from water temperature and salinity, which highlights a need for dedicated study of potential drivers. The spring transition period is undergoing dramatic changes across the Arctic and subarctic in terms of timing and rate of freshening and warming, relative to when PAR becomes sufficient to support growth, thus potentially either improving or worsening eelgrass growth conditions. To support eelgrass conservation as coastal ecosystems undergo change, these results emphasize the importance of monitoring multiple essential variables across the winter to summer transition as they influence eelgrass health and growth at different times and conditions.

5.2 Introduction

High-latitude estuaries and nearshore habitats (e.g., seagrasses, kelp forests, salt marshes) support unique and productive ecosystems, which are culturally and socioeconomically important to northern communities and contribute to biodiversity and carbon storage (Krause-Jensen et al., 2020; Prentice et al., 2020; Kuzyk et al., 2023; Idrobo et al., 2024). However, northern nearshore habitats are characterized by large variations in environmental properties, such as surface state (frozen or unfrozen), salinity, temperature, nutrient concentrations, and sunlight levels, over the course of the year (Guzzi et al., 2024), many of which influence the growth, survival, and distribution of high-latitude vegetation (cf., Lalumiere et al. 1994). Variations in these properties, hereafter called essential variables because of their importance for plant growth, result from seasonal cycles of sea-ice cover, solar elevation, freshwater runoff, and weather events such as storms (cf. Harris et al., 2017; Carmack and Macdonald, 2002; Dunton et al., 2006). Site-specific differences arise due to coastal form and structure, which determine degree of connectivity between the coast and offshore, and the degree of shelter (cf., Moksnes et al., 2021; Harris et al., 2017). With rapid warming and sea-ice loss (Stroeve et al., 2024), increased river runoff, and earlier onset of spring freshets (Stadnyk et al., 2021), it is important to understand the variation experienced by these high-latitude ecosystems in relation to physical drivers and seasonal change. This baseline understanding of current temperature, light, and salinity regimes enables informed assessments of how nearshore habitats and their ecosystems may change (cf., Waldock et al., 2018; Steiner and Reader, 2024). Previous studies have investigated the impact of rivers and earlier sea ice melt on marine ecosystems on a larger scale, for example, on the Canadian Beaufort Shelf (Carmack and Macdonald, 2002), the Laptev Sea (Bareiss et al., 1999; Eicken et al., 2005), and the Arctic Ocean as a whole (Le

Fouest et al., 2013; Park et al., 2023). More limited investigation of hydrologic and biologic changes has been conducted in nearshore waters during the winter-spring transition (Ingram et al., 1996; Granskog et al., 2005a, 2005b; Kuzyk et al., 2008; Harris et al., 2017). However, the environmental conditions in which perennial, subtidal Arctic and subarctic seagrass populations survive, and grow, are known at only a very limited number of sites including Alaska, Arctic Russia, and West Greenland (Krause-Jensen et al., 2020). Understanding drivers of variations in essential variables is particularly crucial for seagrasses because they have been declining worldwide at an accelerated rate since the 1990s (Waycott et al. 2007). The threats and challenges to their recovery have varied both in space and time (cf., Krause-Jensen et al., 2021).

Eelgrass (*Zostera marina*) is the most common and widespread seagrass species in the Northern Hemisphere, with a wide latitudinal range, occurring between 40° N and 60° N (Murphy et al., 2021). Some of the high-latitude eelgrass ecosystems in Alaska and the Hudson Bay system are recognized as being among the largest in North America (McRoy, 1969; Lalumière et al., 1994). Eelgrass beds play a key ecological role in coastal ecosystems, as they stabilize and enrich the carbon content of sediments, and provide food resources and habitat for invertebrates, fish, and various migratory birds (Short et al., 2007; Murphy et al., 2021). While there have been studies on Arctic and subarctic eelgrass beds (Lalumière et al., 1994; Namba et al., 2024), there are very few that characterize habitat conditions under ice cover (McRoy, 1969, Olesen et al. 2015), and the drivers of variations in essential variables in these regions have received less attention than for temperate eelgrass populations.

Although eelgrass can survive short-term fluctuations in habitat conditions, long-term changes can negatively affect eelgrass productivity and resilience under the impact of ongoing and future warming. For example, eelgrass can tolerate a wide range of temperatures and salinities, but it grows best at stable high salinity (> 15 PSU) and temperature ranging from 10 to 25°C (Nejrup and Pedersen 2008). Intense recent warming is suspected of holding back full recovery of shallow eelgrass beds in the Western Baltic Sea, following a decline driven mostly by eutrophication (Krause-Jensen et al., 2020). Eelgrass has high requirements of light in order to grow, and changes in light conditions are often the causes of eelgrass declines (Phillips et al., 1983; Sand- Jensen and Borum, 1983; Moore et al., 1997). Light limitation is usually caused by increased turbidity (Schallenberg and Burns, 2004; McSweeney et al., 2017), but the ultimate drivers vary from phytoplankton blooms in nutrient-rich waters to wave-driven resuspension of bottom sediments or river- borne materials, such as eroded sediments or colored dissolved organic matter (CDOM) (Mayora et al., 2016). At high latitudes, the eelgrass growing season is shortened by low irradiance in the winter, and eelgrass beds must survive 5-6 months of low light conditions owing to the presence of snow-covered sea ice (Olesen et al., 2015; Namba et al., 2024). The ~1 m or more of sea ice typically found along the North American Arctic margin in late winter significantly reduces underwater photosynthetically active radiation (PAR) (Matthes et al., 2020). McRoy (1969, 1970) proposed that a depressed rate of respiration in winter may allow eelgrass to survive under the winter sea ice in Safety Lagoon, an embayment of the Bering Sea near Nome, Alaska, under conditions of extremely low light intensity and anoxic water. Nevertheless, plants retrieved from under the ice had new roots, rhizomes, and leaves that had grown since the previous September indicating that the plants were actively metabolizing, presumably responding to the onset of spring (McRoy, 1970).

The winter-to-summer transition, when both temperature and sunlight increase, is thus thought to be a critical period for high-latitude perennial eelgrass, which has survived the winter and is poised for spring growth (cf., Davis et al., 2024). With rising water temperatures, respiration demands increase, but eelgrass can cope if there is sufficient light for net primary production (Greve et al., 2003; Lee et al., 2007). It has been hypothesized that rising water temperatures and reduced ice cover may enable eelgrass to expand into higher latitudes (McRoy, 1969). However, recent research suggests that unusually warm conditions from winter to spring can negatively affect eelgrass by increasing energy expenditure beyond that supported by the available light and hence depleting carbon reserves (Sawall et al., 2021). Another study found that above-average summer temperatures were associated with a reduced likelihood of eelgrass presence in the subsequent year (Plaisted et al., 2022). Seasonal sea ice, combined with variable freshwater inputs from river runoff and a shifting photoperiod, further contributes to highly variable conditions for eelgrass growth throughout the year at high latitudes (McRoy, 1969; Lalumière et al., 1994).

This study examines variations in salinity, temperature, and underwater light in eelgrass bed habitats in northeastern James Bay during the seasonal transition from winter to summer. This works towards a larger goal of the Coastal Habitat Comprehensive Research Project (CHCRP) to investigate ‘What are the main factors affecting the current state of eelgrass along the eastern coast of James Bay?’ Eelgrass here has shown limited recovery since suffering a massive decline in the late 1990s (Leblanc et al., 2023). Research and monitoring activities conducted as part of the CHCRP showed that eelgrass in this region is not limited by nutrient availability (Davis et al., 2024), and that salinity, water temperature, and light are the primary drivers of eelgrass health. We hypothesized that salinity, temperature, and light would increase together with the onset of ice-free conditions while differences in the degree of LGR influence would modulate the seasonal patterns in a site-specific manner. In particular, we expected that the seasonal transition from ice-covered winter, through ice melt and breakup, followed by increased spring streamflow and the onset of the open-water period creates conditions that support eelgrass growth throughout the spring and summer. However, the quality of these conditions may vary across sites due to local environmental differences that affect one or more of the essential variables, with LGR discharge dominantly controlling salinity at nearby sites. This study is a first step towards establishing the hydrological baseline conditions along the east James Bay coast in terms of salinity, water temperature, and light at the onset of the eelgrass growing season and understanding the processes causing variations within the coastal habitat. Following recent work describing the LGR winter plume (Peck et al., 2022, Chapter 3) and the influence of extreme wind events on coastal salinity (Peck et al., 2025 (accepted), Chapter 4), we examined new time-series observations combining salinity, temperature, and photosynthetically active radiation (PAR) from bottom-mounted moorings deployed between March and August 2019, adjacent to eelgrass beds in approximately 4.5 m water depth along the northeast coast of James Bay. We describe the results from these moorings and use auxiliary data on air temperature, winds, and river discharge to explore the linkages to main drivers of variation and seasonal change. In particular, we sought to address how LGR influence on salinity, water temperature and PAR varies seasonally and on shorter time scales at two eelgrass habitat sites; assess whether spring freshet bringing peak flows to local streams would impact essential variables; and characterize the short-term disruptions in conditions caused by ice melt and breakup period in these eelgrass habitats.

5.3 Methods

5.3.1 Study area

The northeast coast of James Bay, which is part of the Cree traditional territory Eeyou Istchee, is a subarctic coastal area and part of Canada's Inland Seas (also referred to as the Hudson Bay complex). The coast supported some of the highest concentrations of eelgrass in North America (Lalumière 1988; Lalumière et al., 1994) prior to massive declines in both eelgrass cover and biomass during the 1990s (Leblanc et al., 2023). This region is not only influenced by seasonal landfast ice cover (December-May) but also by the inflow of a regulated river, the La Grande River (LGR), which has the second-highest winter discharge across the circumpolar Arctic watershed after the Yenisei River (Shiklomanov & Shiklomanov, 2003; Peck et al., 2022, Chapter 3). The LGR, together with smaller rivers along the coast, may also affect eelgrass health via changes in local salinity, water temperature, water clarity, or sea ice regimes (Aagaard and Carmack, 1989; Macdonald et al., 1995; Harms et al., 2000). During winter, freshwater inflow has a higher temperature than ambient seawater and can cause thinner ice around the river mouth and an earlier onset of sea ice melt (Dean et al., 1994). Openings in the ice cover in late winter allow additional sunlight to penetrate the water column, where it is available for phytoplankton and eelgrass primary production (Arrigo and van Dijken, 2015; Lewis et al., 2020). However, rivers with high sediment loads or colored dissolved organic matter (CDOM) absorb and reduce light availability (Blough and Del Vecchio, 2002).

The east coast of James Bay, much like the coastline throughout eastern Hudson Bay, Labrador, and Baffin Island, has a complex geometry and tides of approximately 1 m (Peck et al., 2022, Chapter 3), which modify the influence of river inflows on salinity, temperature, and light within many local embayments along the coast. For example, in northeast James Bay, the stratified winter LGR plume flows freely into open bays, maintaining its two-layer structure, whereas in other bays sheltered by offshore islands, the fresh surface layer becomes mixed with the underlying seawater in the narrow channels between islands (tidal straits), producing brackish, vertically mixed waters in the nearshore habitat (Peck et al., 2022, Chapter 3). The east coast of James Bay experiences annual ice cover, with landfast ice extending 10–20 km from the shore (Gupta et al., 2022; Diaz et al., 2024). Adjacent to the fast ice is a flaw lead, which may contain open water or concentrations of drifting pack ice depending on the wind (Gupta et al., 2022; Taha et al., 2019). Small polynyas sometimes open in the landfast ice where tidal flows are fast, e.g., in channels between islands.

Oceanographic studies of James Bay began in the 1970s, focusing on how hydroelectric development impacts water circulation and salinity. Early research suggested that cold, saline water from Hudson Bay enters the western part of James Bay, whereas warmer, low-salinity water exits on the eastern side (Prinsenberg, 1978). Away from the major rivers, the offshore James Bay water column is stratified and brackish during summer, whereas in winter, the water column becomes uniformly salty and well-mixed (Freeman, 1982). The region's anticlockwise circulation is driven by wind, freshwater inputs from rivers, and density differences between seawater and riverine water (Prinsenberg, 1978; Ridenour et al., 2019). Seasonal ice growth and melting further influence water properties (Prinsenberg, 1980, 1982).

The topography of James Bay is generally moderate, with more complex features along the eastern shore. The LGR, the largest river discharging into James Bay and indeed the whole Hudson Bay Complex, has been the subject of several detailed plume studies, both before and after the construction of the hydroelectric complex (Freeman et al., 1982; Ingram et al., 1986; Messier et al., 1989). Since hydroelectric development began in the late 1970s, the annual LGR discharge has doubled and the seasonal flow patterns have been strongly altered, with the highest flows now occurring in winter rather than during the spring freshet (Messier, 2002; de Melo et al., 2022). The increased winter LGR discharge creates a large under-ice plume with very low salinity (<5 PSU) that extends over approximately 1,200 km^2 (Messier et al., 1989; Peck et al., 2022, Chapter 3). The effects of the additional freshwater discharge during winter months are detected as far away as the Belcher Islands in southern Hudson Bay, illustrating the extensive influence of the LGR on the region's oceanography (Ingram and Larouche, 1987; Eastwood et al., 2020). More recent studies, as part of the Coastal Habitat Comprehensive Research Program (CHCRP), revealed that the under-ice plume remains relatively stable throughout winter, as long as river discharge is high and landfast ice remains intact (Peck et al., 2022, Chapter 3; Kuzyk et al., 2023).

Since dam and reservoir development, LGR discharge is several degrees warmer during winter and cooler during summer compared to natural conditions (Messier et al. 1986). The water released from LG2 and LG1 dams has a lower suspended sediment content than before the hydropower developments, owing to sediments being trapped in the Robert Bourassa reservoir; as it flows towards the bay, the river water gradually becomes more turbid due to bank erosion but the sand fraction settles out in the delta around the river mouth while a smaller but unquantified amount of fines disperses into the bay (Tremblay et al., 2006). Concentrations of CDOM in the LGR are higher than in marine waters but lower than in adjacent unregulated rivers (Évrard et al., 2023).

The eelgrass ecosystem in the La Grande River region of northeastern James Bay extended across approximately 250 km^2 in the 1980s, supported a wide range of organisms, including fish and invertebrates, and attracted large numbers of migratory birds (Curtis & Allen, 1976; Lalumière et al., 1994; Reed et al., 1996). Today eelgrass remains but monitoring data show it is much less extensive than in the 1980s and 90s. A gradual decline in eelgrass occurred near the La Grande River in the 1980s, coinciding with the development of the LGR hydroelectric complex, followed by a drastic decline in the late 1990s that extended widely along the east coast (Leblanc et al., 2023). Almost 20 years after the decline, eelgrass has failed to recover in many locations; plants are shorter, many historic beds are no longer present, and the current surviving beds are generally less dense than pre-decline beds (Leblanc et al., 2023).

5.3.2 Data collection

This study focuses on new data collected from in-situ moorings deployed in two contrasting coastal embayments on the northeast coast of James Bay (Figure 5.1). The embayments are located to the north and south of the La Grande River mouth and are called the Bay of Many Islands (mooring CH4) and Tees Bay (mooring CH33), respectively. The Bay of Many Islands is a large, complex bay with many small islands and shoals. The northward-flowing LGR plume and seawater moving as part of James Bay's cyclonic background circulation pass through narrow inlets where tidal mixing can occur to reach the location of CH4 in the southeastern part of the Bay of Many Islands. The mooring site was located approximately 30 km north of the La Grande River mouth. Previously deployed moorings and conductivity-temperature-depth (CTD) data from winters 2016-2017 showed that the salinity in the Bay of Many Islands is typically approximately 11 PSU during the high LGR-flow period of February and March (Peck et al., 2022, Chapter 3). The mooring site CH33 in Tees Bay is located approximately 10 km south of the river mouth (Figure 5.1). It is much less protected from direct, unmixed inflow of fresh river plume or seawater, and the CTD data showed a salinity of <5 PSU during February and March 2016 and 2017 (Peck et al., 2022, Chapter 3). Both mooring sites had similar mean water depths (~4.5 m) and were located adjacent to eelgrass beds and within a few kilometers of small local rivers with seasonal flow (Table 1, Figure 5.1).

Table 5.1: Physical details of the two mooring deployment sites in March 2019.

Mooring	Distance LGR	Distance local river	Mean Water depth	Latitude (°N)	Longitude (°W)	Deployment length
CH4	30 km	4.0 km	4.6 m	54.092	-79.131	140 days
CH33	10 km	3.6 km	4.5 m	53.728	-79.096	136 days

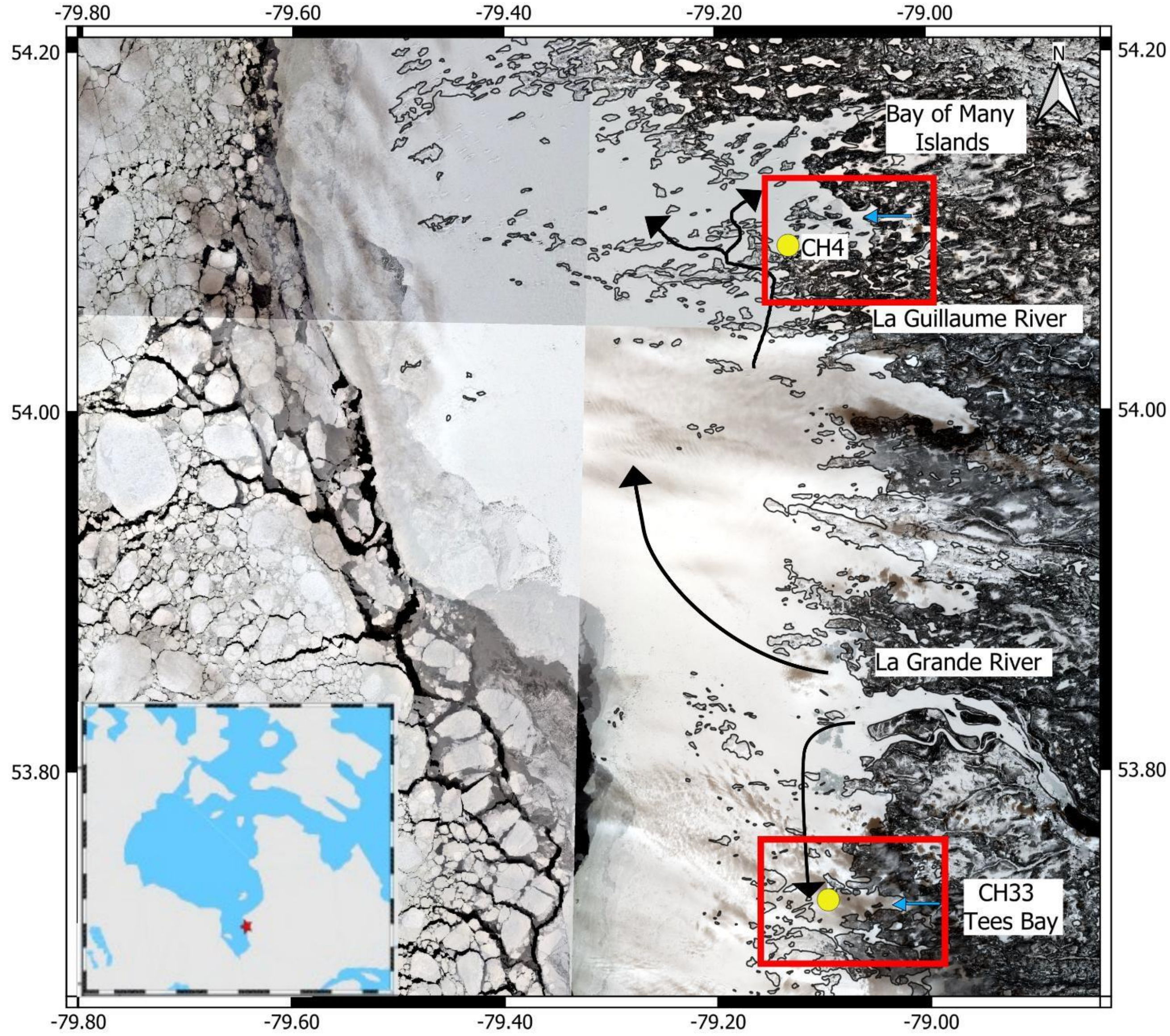

Figure 5.1: Map of the study area in northeast James Bay, off the southern end of Hudson Bay, showing the two mooring locations, CH4 and CH33. The black arrows represent the expected movement of the La Grande River (LGR) plume in the direction of the moorings based on observations during winter 2016 and 2017 presented in Peck et al. (2022) and Cree knowledge shared with the research team. Blue arrows represent flow from local rivers towards the mooring locations. The stream discharging near CH33 is unnamed; the stream discharging near CH4 is La Guillaume River. Red boxes indicate the areas used for the satellite images shown in Figure 5.2.

The two moorings, CH4 and CH33, were deployed on the seabed on 20 and 21 March 2019, respectively, by lowering them through openings made in the landfast ice, and recovered by Cree boaters on 7 August and 4 August 2019, respectively. The moorings were constructed on a simple frame with a weight at the bottom and a series of sensors attached to the central pole. Each mooring was equipped with an Onset HOBO and a RBR conductivity and temperature (CT) logger, an Onset HOBO pressure logger (which failed at CH33), and a Li-Cor LI-192 Underwater quantum sensor connected to a RBR solo data logger that measured and recorded PAR, respectively. It should be noted that the PAR values at CH4 do not reach 0, likely due to how the sensors are calibrated to compensate to the cold water conditions. Each PAR sensor had a ZebraTech hydrowiper to prevent fouling. The moorings were installed with a time-scheduled release system by Little Leonardo Corporation, which released a float to the surface 120 days after deployment. The pressure and CT sensors were mounted 0.6 m above the seabed while the PAR sensors were 1 m above the seabed.

5.3.3 Additional data and data processing

The auxiliary data used in this study include air temperature and wind data obtained from ERA5. The ERA5 reanalysis data for one grid point (53.8°N and 79.6°W) were analyzed and found to be comparable to those from the Wemindji airport weather station (53.0° N and 78.8°W, 93 km south of LGR). The percentage of cloud cover was also obtained from ERA5 reanalysis data at the same grid point. River discharge data for the LGR were obtained from Hydro-Québec (de Melo et al., 2022). MODIS satellite data were used to determine ice melt onset and breakup dates. Incident PAR values for land locations adjacent to CH33 and CH4 were obtained from the MODIS land product MCD18A2 version 6.2 (Wang, 2024), freely available via NASA Earthdata Search. The data were converted to mol day^{-1} m^{-2} by multiplying with the constant factor of 4.56 and adjusting the units. Grid locations containing data near the mooring locations were selected, and the PAR data available at 3-hour intervals were averaged to obtain daily mean values in local time (Eastern Daylight Time). As it was not possible to measure the PAR at the surface of the water in situ, the satellite-derived MODIS PAR was used as the surface irradiance input for estimating the PAR transmittance of the ice cover and water column. Tidal analysis on the data from the pressure sensors was conducted using the MATLAB toolbox known as T_Tide (Pawlowicz et al., 2002). The pressure sensor data was also corrected for atmospheric pressure changes. After this correction, the predicted tidal water depth variations were subtracted from the predicted variations due to the time to yield the residual water level variations that may be due to other processes, such as wind forcing. The solar elevation was obtained using the HEMIDAL model (Connan-McGinty et al., 2022).

5.4 Results and Discussion

5.4.1 Variations in ice cover, air temperature, wind, and cloud cover

In subarctic environments, ice cover is typically a dominant control on nearshore hydrography throughout winter and during the winter-summer transition. In this section, the evolution of the ice cover in the eelgrass habitat of northeast James Bay over March-August 2019 is described. The most readily obtained externally and remotely observed variables that are key drivers of environmental change at the local level, i.e., air temperature, wind, cloudiness, tides, and river discharge and cloud cover are also presented. This data will then be used to help explain the variations in the essential variables measured in the coastal waters (temperature, salinity and PAR).

Between March and August 2019, the nearshore ecosystem transitioned through four (ice) surface states. Satellite imagery (Figure 5.2) shows that solid landfast ice was present in each embayment and at the mooring sites continuously between mooring deployment on 20 and 21 March and mid May (Figure 5.2). During late April, there were very brief events of surface melting when air temperatures rose above 0°C but the surface state returned to white and high albedo (i.e., possibly from fresh snowfall) within a day or two.

Around 13 May, satellite images show the ice becoming discolored and opening up in places near the shoreline, especially near the outlets of local streams indicating the start of the melt period (Figure 5.2a & b). Average daily air temperatures had begun exceeding 0°C most days (Figure 5.3a), snow was melting both on land and on the surface of the ice, and areas of open water were appearing in the local streams. On 23 May, open water channels can be seen extending away from the shoreline in the bays (e.g., Figure 5.2c); our interpretation is that intense freshwater discharge from the local streams has melted some of the ice along the main flow pathways in the interior of the bays. Discharge levels in local streams, such as the Guillaume River that has its outlet near CH4 (Figure 5.1), rose abruptly after 13 May peaking on 15 May, after having been very low throughout the months of March and April (Figure 5.4b). Despite open-water channels having formed in front of the local streams by 23 May, the coastal bays were still mainly covered by landfast ice, albeit melting, for approximately another two weeks. However, around 2 June, satellite imagery shows that the ice breakup period had begun. There was mostly open water at the mooring sites on that day but still extensive ice slightly offshore (Figures 5.2g & h). On 9 June, satellite imagery shows mostly open water throughout the bays. From 9 June onward, the minimum daily air temperature was above 0°C (Figure 5.3a), supporting our conclusion from the satellite imagery that the majority of the ice in the embayments had melted, and that the “open-water period” at CH4 and CH33 had begun (Figure 5.2g & h). Based on the above description, we consider 20 March – 12 May to represent an “ice-covered” period, 13 May – 1 June as the “melt” period during which there was surface melt and some openings in the ice but still a fairly intact ice cover, 2-8 June as the “ice breakup” period, and 9 June onwards as the “open water period”.

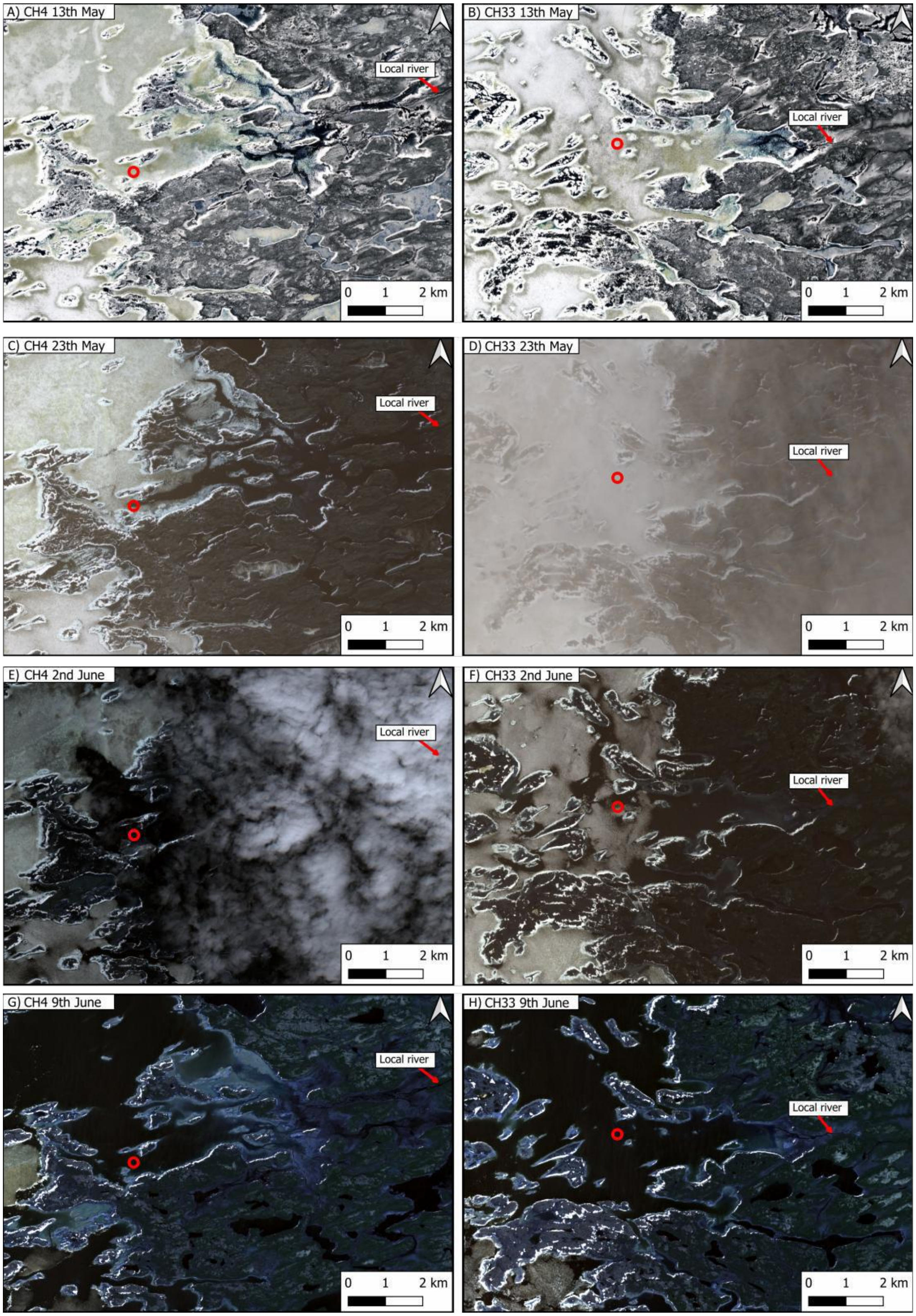

Figure 5.2: Sentinel 2 true-color satellite images with the locations for moorings CH4 (A, C, E, G) and CH33 (B, D, F, H) showing the state of landfast ice at various dates throughout the winter-to-summer transition.

Wind speed and direction are known to impact both the ice and surrounding waters in northeast James Bay, affecting near-shore salinity even under landfast ice cover (Peck et al., 2025 (accepted), Chapter 4). The prevailing wind in the area comes from the northwest and this direction also accounts for some of the strongest winds. The March-August 2019 record shows a strong wind event on 27 April when the winds reached velocities of 10 m s^{-1}, blowing in a southeast direction towards the land (Figure 5.3b, Figure S5.1). Aside from this event, the winds showed strong oscillations in both U and V components over the sampling period (Figure 5.3b).

Water depth at the mooring sites varied both with wind forcing and the tide. Based on pressure records, the tidal range for CH4 was approximately 1 m during spring tide and 0.4 m during neap tide (Figure 5.3c). These are substantial ranges in relation to the mean water depth of 4.6 m at this location (Table 5.1). There was very little change in water levels outside of the inferred tidal variations, apart from 29 April, when a peak followed the strong wind event of 27 April, and 2 May, when recorded air pressure rose to over 1030 mbar during a neap tide period (not shown). We note that the two moorings had similar mean water depths of 4.5–4.6 m (Table 5.1), and previous studies found similar average tidal ranges at the two locations (Peck et al., 2022, Chapter 3).

In addition to solar elevation (i.e., season and time of day), cloud cover strongly influences surface incident and transmitted PAR (Figure 5.3d). ERA5 cloud data were consistent across both mooring sites, so only CH33 data are shown. On average, the study area experienced 78% cloud cover during the ice-covered period (20 March – 1 June) and 84% during the ice break-up and open-water period (2 June – 10 August), though coverage varied frequently. Incident PAR remained low and variable, with only a weak, statistically non-significant increase with rising solar elevation between 21 March and 21 June (summer solstice) ($p>0.06$; $R^2<0.078$; Figure 5.3e). Cloud cover correlations with incident PAR were similarly weak (CH33: $R^2 = 0.041$, $p = 0.051$; CH4: $R^2 = 0.041$, $p = 0.052$ in winter), with only marginal significance. These results show that the effect of cloud cover on PAR is not well represented by linear models using ERA5 data. This is partly because the ~20 km spatial resolution of ERA5 cannot resolve the fine-scale cloud variability that impacts surface irradiance at the mooring sites.

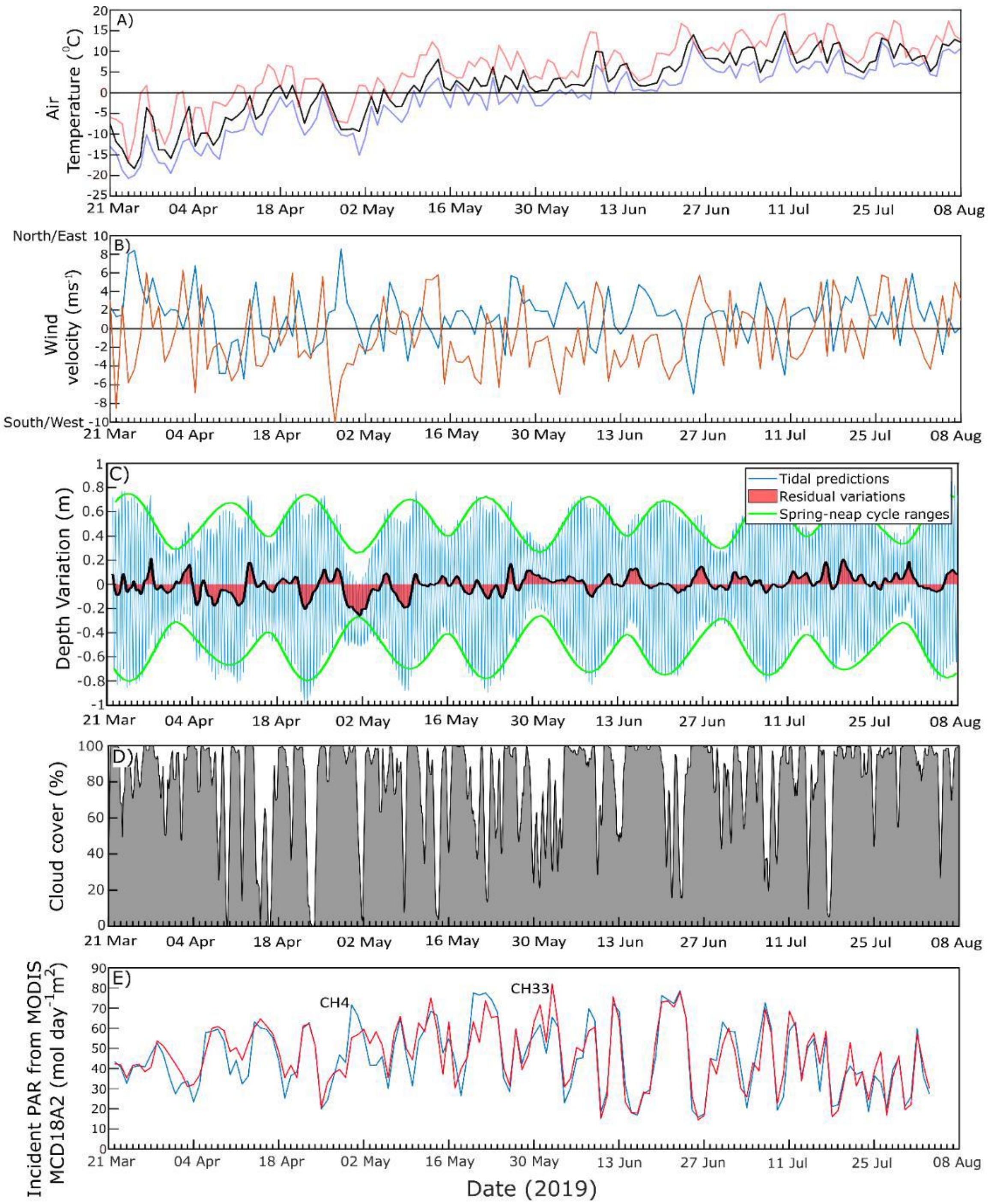

Figure 5.3: Daily average of air temperature (black), maximum daily temperature (red), minimum daily temperature (blue) from ERA5 reanalysis data (A). Wind velocity (B) in both U/West to East (blue) and V/South to North (orange) directions for the sample period from ERA5 reanalysis data. Water depth variations (C) observed at CH4 (blue line), tidal oscillations (green line), and the residual water level (red shading). Hourly cloud cover from ERA5 reanalysis data (D) for the CH33 location. Surface incident PAR (E) at CH33 (red) and CH4 (blue) taken from the MODIS product MCD18A2.

5.4.2 Influence of river discharge and water dynamics on salinity and temperature at the eelgrass sites

Seasonal variation in river discharge is a key driver of coastal water properties in northeast James Bay, particularly during the transition from winter to summer. In the nearshore environment, rivers not only inject freshwater, which alters salinity and temperature, but also deliver particulate matter and coloured dissolved organic matter (CDOM) that degrade the underwater light climate. CDOM preferentially absorbs UV and blue wavelengths, reducing short-wavelength PAR. Suspended particulate matter absorption spectrum is similar to CDOM but with less wavelength dependence, and furthermore attenuates light through backscattering (Blough and Del Vecchio, 2002; Novak et al., 2022). During late March and early April 2019, the regulated La Grande River (LGR) reached peak discharges of approximately 4000 $m^3 s^{-1}$ (Figure 5.4a), the highest observed during the measurement period. By mid-April, discharge declined to ~3000 $m^3 s^{-1}$, remained steady for several weeks, and then dropped to a minimum of ~1500 $m^3 s^{-1}$ by late May. In contrast, local unregulated rivers such as La Guillaume remained frozen through most of the winter and only began contributing freshwater during the spring freshet, peaking at ~150 $m^3 s^{-1}$ in the second week of May (Figure 5.4b). These contrasting discharge regimes high winter flow from LGR and delayed spring input from local streams strongly influence the seasonal patterns of salinity and temperature at the eelgrass monitoring sites.

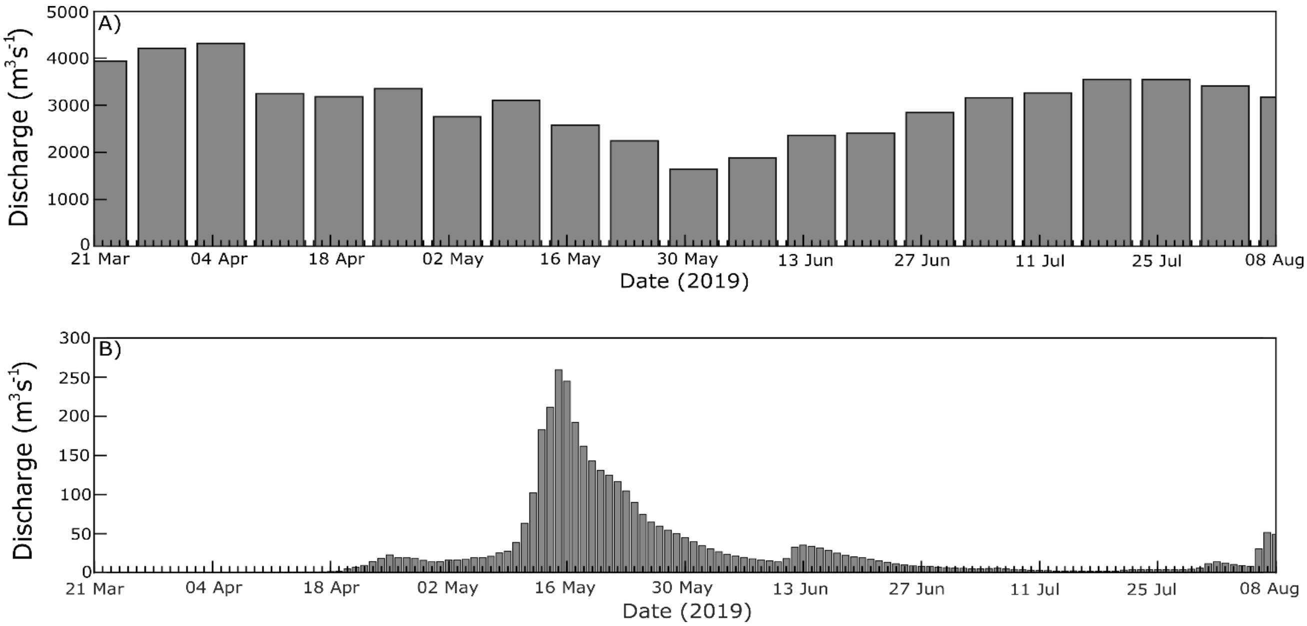

Figure 5.4: Weekly averaged discharge from the regulated La Grande River (A) and daily discharge from the unregulated river La Guillaume (B) throughout the sample period. Note the order of magnitude difference in Y-axis scale between panels A and B. (River discharge data for the La Grande was obtained from Hydro-Québec and the discharge data for the Guillaume river was obtained from de Melo et al., (2022)).

During the ice-covered winter period, the regulated La Grande River has its highest discharge (Figure 5.4a), while smaller local rivers are mostly frozen (Figure 5.4b). As a result, river discharge exerts the strongest seasonal influence on coastal water properties in northeast James Bay during winter and early spring. Typically, high-latitude coastal oceans experience increased salinity in winter due to reduced river input and brine rejection from sea-ice formation (e.g., El-Sabh & Koutitonsky, 1977; Prinsenberg, 1986). However, in this study, an average decrease in salinity was observed during the ice-covered period compared to the ice-free season (Table 5.2), highlighting the dominant influence of the La Grande River plume. This pattern was most pronounced at CH33, where the average winter salinity was nearly 9 PSU lower than the ice free average. But even at CH4, there was a 4.6 PSU different in the average salinity with lower values in winter. This reversal of the seasonal salinity regime typically observed in high-latitude coastal oceans is an indication that the dominant freshwater influence is the regulated LGR discharge (Peck et al., 2022, Chapter 3). As documented in previous studies, the combination of the high winter LGR discharge and reduced wind mixing and tides produces a highly stratified, very fresh (salinity<5 PSU) "core" plume area outside the river mouth (Messier, 2002; Peck et al., 2022, Chapter 3; Peck et al., 2025 (accepted), Chapter 4). During winters 2016 and 2017, for example, with LGR discharges averaging 4800 m^3 s^{-1}, the core of the plume extended under the ice cover across an area of ~1200 km^2 , which is a much larger area of low surface salinity than observed during summer regardless of discharge (Peck et al., 2022).

During the ice-covered period of March-April 2019, low salinities with high short-term variability were observed at both CH33 and CH4, with minimum values reaching 0.86 and 6.65, respectively (Table 5.2). These low salinities are attributed to the influence of the stratified core of the LGR plume, with CH33 experiencing more direct plume effects while tidal straights in the Bay of Many Islands mixed the plume with surrounding waters, reducing the plume's influence (Peck et al., 2022). Salinity at CH33 often persisted near 1 PSU for extended periods throughout late March and early April 2019 (Figure 5.5b). These very low winter salinities at CH33 reflect its close proximity to LGR and the fact that the 3–4 m thick LGR plume core moves southward into Tees Bay under the intact landfast ice cover without significant mixing (Messier, 2002; Peck et al., 2022, Chapter 3). CH4 was, on average, 1.2 PSU saltier than CH33, and, at times, nearly 10 PSU saltier than CH33 during the pre-melt period (Figure 5.5b). As the LGR plume moves northward through complex coastal topography and especially narrow tidal straits in the Bay of Many Islands, it mixes with surrounding waters, increasing salinity to >6 PSU (Peck et al., 2022, Chapter 3).

The effect of local streamflow on salinity and temperature at the mooring sites during the ice-covered period is relatively minor compared to LGR influence, with the exception of a sharp freshening at CH4 on 23 May, which we attribute to influx of freshwater from La Guillaume River at a time of relatively lower LGR discharge. The fairly extensive ice cover in the CH4 area at that time probably reduced the rate at which the streamflow mixed with local waters allowing the salinity to dip down to ~ 8.9. Before this sharp freshening event on 23 May, the LGR discharge had been declining throughout the second half of April, presumably related to decreasing demand for electricity for heating in southern Canada. The lower LGR discharge in late April and early May allowed salinity to begin increasing at both sites (Figure 5.5b). The record clearly shows an increase in salinity throughout May at CH33 alongside a steady LGR discharge decline. At CH4, it appears that the increase in salinity that started in the second week of April when LGR freshwater input decreased was interrupted briefly by the local stream's impact but then resumed in late May.

In early June, ice breakup briefly disrupted the trends driven by falling LGR discharge and brought short-term marked changes in both temperature and salinity at the mooring sites. Salinity, which had been rising throughout May to a peak of 22.6 PSU at CH33 and 16.5 PSU at CH4, fell sharply at breakup, reversing the April–May trend, with minima near 12.5 PSU occurring in the first few days of June (Figure 5.5b; Table 5.2). We suspect that local ice melt supplied most of the freshwater that accounts for these salinity decreases because by 2 June, local streamflow had fallen considerably from its peak levels (Figure 5.4b). The water temperature at both mooring locations, which had remained below 0°C during the ice-covered and melt periods from March to early June (Figure 5.5a), remained low at ~0.71 at CH4 and ~0.43 at CH33 during the end the melt period and beginning of breakup, most likely because of the increase of cold melt water. However, once the ice was gone, the water temperature increased rapidly. Although both moorings showed high short-term variability in salinity and temperature during March, April, and May, CH33 recorded larger semidiurnal salinity oscillations of as much as 15–20 PSU during the periods of 14–25 April and 1–22 May, while CH4 varied by <2 PSU. Comparing the water level changes against temperature and salinity changes at CH33 shows that temperature decreased and salinity increased with the rising tide and then the trend reversed during falling tide (Figure 5.6a & b). This pattern is interpreted as resulting from colder, saltier seawater entering the embayment, likely from a southerly or westerly direction on the flood tide, and undergoing mixing with local waters. During the ebb tide, when salinity at CH33 falls abruptly, it appears that buoyancy forcing allows the under-ice LGR plume to increase its southward flow to the CH33 location (Peck et al., 2025 (accepted), Chapter 4).

The low and highly variable salinity at CH33 during the ice-covered period contrasts sharply with the steady conditions observed during the summer ice free period, when salinity remained relatively high at both mooring sites, averaging 18.5 PSU at CH33 and 16.5 PSU at CH4 (Table 5.2) (Figure 5.6c & d). In the absence of ice cover, the La Grande River (LGR) plume mixes rapidly with James Bay waters, causing salinity to increase with distance from the river mouth (Peck et al., 2022). As a result, neither site experienced very low salinities typical of the stratified plume. On average, CH4 was fresher than CH33 during the ice free period, the reverse of the ice covered period, which we attribute to influence of the local La Guillaume River at CH4 in addition to influence of the mixed LGR plume. CH4 was also notably warmer on average compared to CH33 during the ice free period. Average water temperature during the ice free period was 9.89°C at CH4 (range: 2.11–13.92°C) and 5.10°C (range: 0.62–8.54°C) at CH33 (Figure 5.5a; Tables 5.2). The approximately 4°C- 5°C lower average and peak temperatures and the larger daily tidal cycle variations at CH33 during the ice free period (Figure 5.5a) are attributed to CH33 being more exposed to both offshore conditions and the LGR plume. CH33 is closer in proximity to the La Grande River mouth and thus more directly receives the cold summer LGR discharge, which is approximately 3°C colder in summer than it was prior to dam and reservoir development (Roche, 1985). In contrast, LGR waters have more time to warm before reaching CH4, and any local stream inputs at CH4 are likely warmer than LGR discharge, which is withdrawn from subsurface in the reservoir. 52

It is also interesting to note that the several multi-day freshening events that occurred at CH33 during the ice free period were sometimes associated with warming and, at other times, cooling. The most notable summer salinity variations were a 5.3 PSU drop from 20–22 June with a concurrent 4°C temperature rise; a 7.6 PSU drop from 21–24 July with a 1.6°C temperature rise followed by abrupt 3.3°C cooling; and a 2.3 PSU freshening on 7 July followed by 2.8°C cooling on 9–10 July. These variations support our interpretation that CH33 is more exposed than CH4 to both offshore conditions and the LGR plume and also, at times, influenced by discharge from local streams.

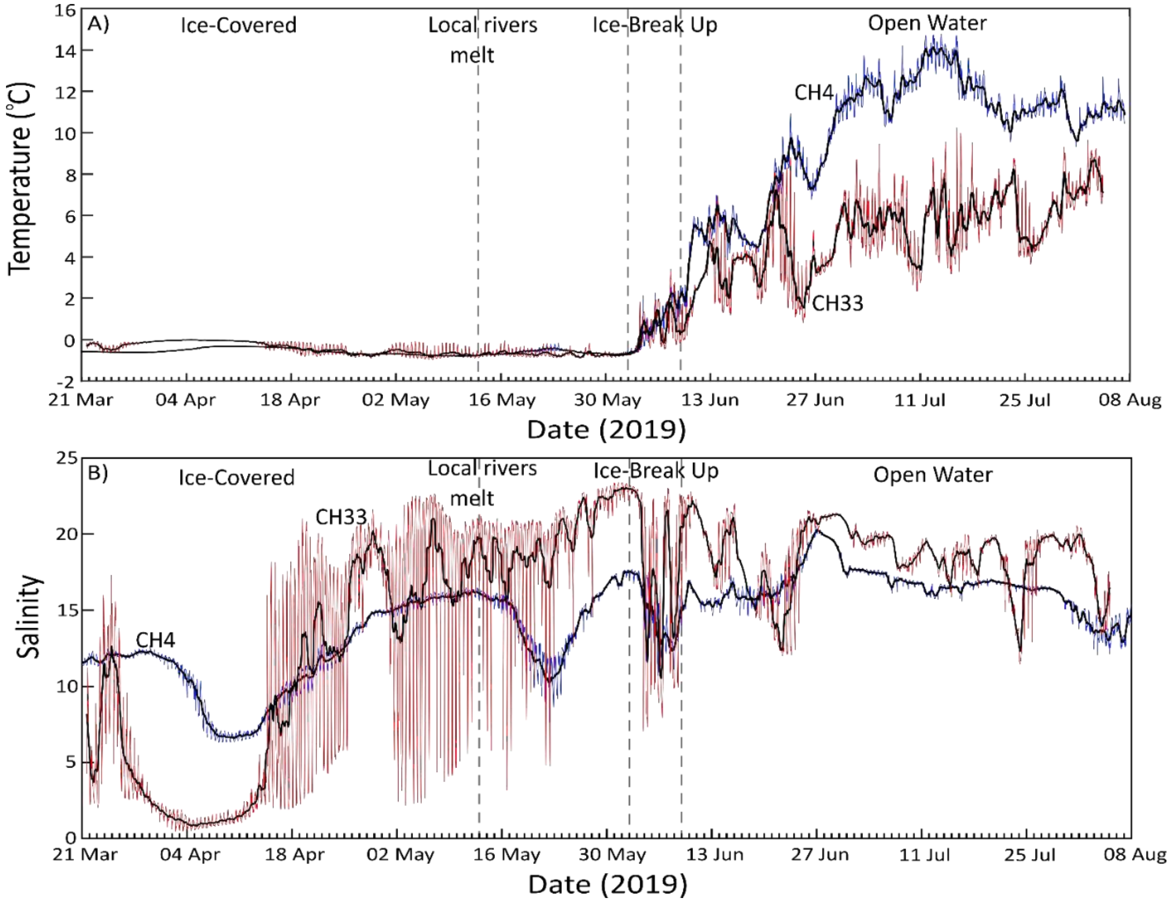

Figure 5.5: Hourly averaged water temperature (A) and salinity (B) for mooring CH33 (red) and CH4 (blue). The black lines represent the 12-hour running mean salinity and temperature.

Table 5.2: Summary statistics for water temperature (°C), salinity, and integrated daily PAR (mol day^{-1} m^{-2}) at the two mooring sites, CH4 and CH33, across the pre-melt ice covered period, ice melt and breakup periods (combined), and the open water period. Dates of ice melt and breakup (13 May – June 9) and open water (June 10 – August 8) were defined by examining satellite imagery and mooring records.

Mooring	Ice state	Parameter	Average	Stdev	Range	Min	Max
CH4	Covered	Temperature	-0.57	0.15	0.46	-0.79	-0.33
		Salinity	11.90	2.97	9.50	6.65	16.15
		PAR	0.11	0.17	0.68	-0.01	0.67
CH4	Melt	Temperature	-0.61	0.10	0.32	-0.74	-0.42
		Salinity	14.36	2.21	7.06	10.45	17.51
		PAR	0.12	0.15	0.44	-0.01	0.44
CH4	Break up	Temperature	0.71	0.96	2.53	-0.59	1.94
		Salinity	14.66	0.71	4.87	12.54	17.41
		PAR	14.66	1.73	0.44	0.03	0.47
CH4	Free	Temperature	9.89	2.92	11.81	2.11	13.92
		Salinity	16.47	1.42	6.87	13.18	20.06
		PAR	0.65	0.72	2.75	-0.01	2.75
CH33	Covered	Temperature	-0.38	0.26	0.79	-0.81	-0.02
		Salinity	9.55	6.72	19.20	0.86	20.06
		PAR	0.02	0.03	0.16	0.00	0.16
CH33	Melt	Temperature	-0.71	0.06	0.24	-0.83	-0.60
		Salinity	19.82	1.99	5.89	17.05	22.94
		PAR	0.17	0.11	0.35	0.02	0.38
CH33	Break up	Temperature	0.43	0.62	1.91	-0.66	1.25
		Salinity	17.48	3.03	8.82	13.92	22.74
		PAR	0.73	0.29	0.87	0.33	1.21
CH33	Free	Temperature	5.10	1.72	7.92	0.62	8.54
		Salinity	18.50	2.03	8.81	12.94	21.75
		PAR	1.38	1.08	3.93	0.06	3.99

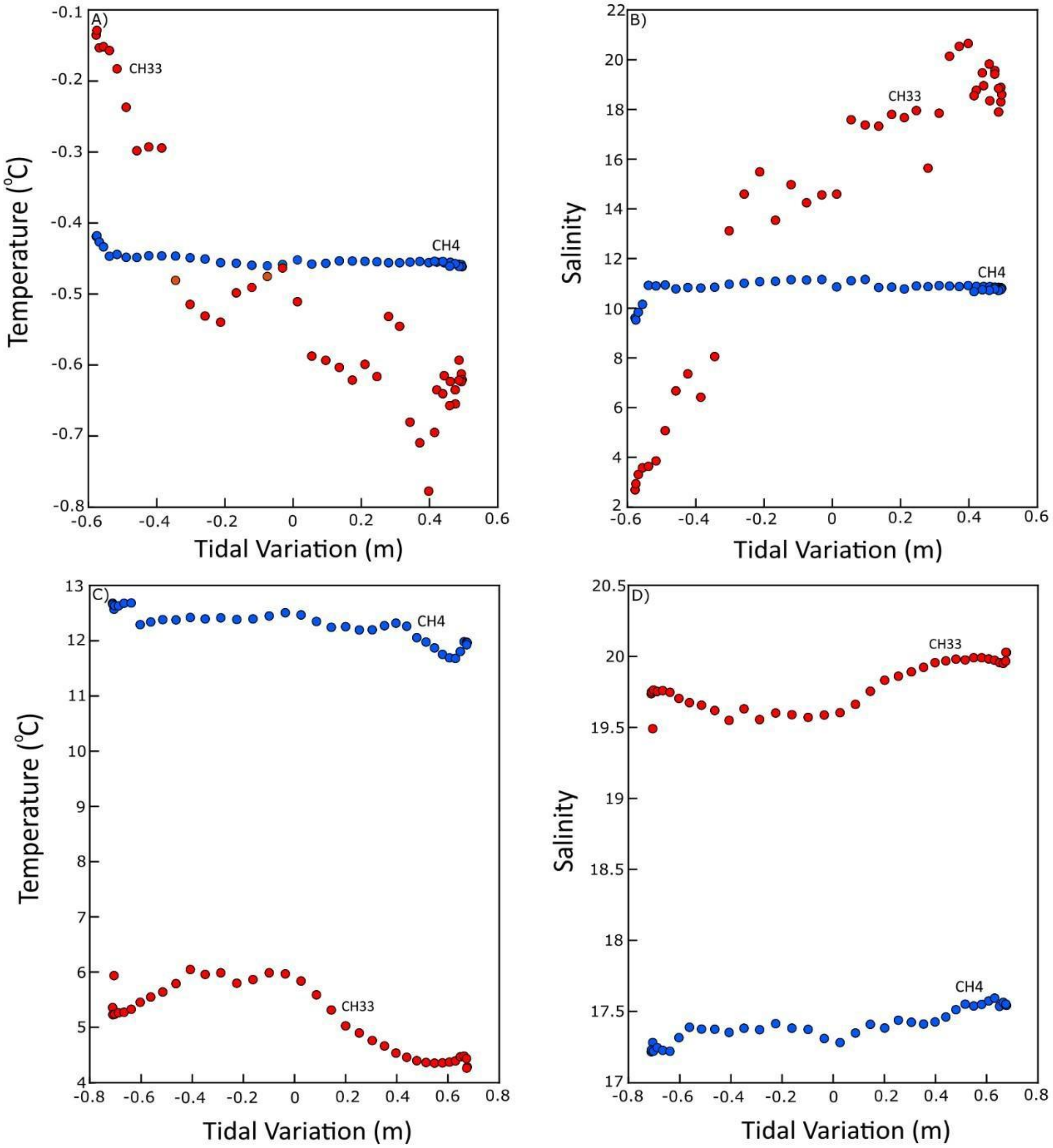

Figure 5.6: Example of temperature (a, c) and salinity (b, d) from CH33 (red) and CH4 (blue) against tidal range for half of a tidal cycle on 18 April (a, b) during period of high variability under landfast ice, and on 5 July (c, d) during steady conditions in the open water period.

5.4.3 Seasonal variation in PAR and controls on light climate

The stronger influence of LGR at CH33 compared to CH4 during winter made very little difference to the light climate in the eelgrass habitat, with hourly average PAR values generally remaining below 0.1 µmol s^{-1} m^{-2} at both sites throughout most of the ice-covered period (Figure 5.7), which aligns with typical under-ice PAR values beneath snow-covered, landfast sea ice prior to melt onset (Matthes et al., 2020). It should be noted that many of the averaged hourly PAR values during the night were negative.

However, it was negative by -0.06 (CH4) and -0.004 (CH33) which will have a negligible on the overall data relative to light compensation point for eelgrass. The average daily values were 0.11 and 0.02 µmol s^{-1} m^{-2} at CH4 and CH33 respectively. In late April, a brief event of surface melting and meltwater flooding reduced ice albedo, producing a brief 1–2 order of magnitude increase in PAR, which peaked at ~4 µmol s^{-1} m^{-2} at CH33 and ~7 µmol s^{-1} m^{-2} at CH4. It is possible that the lower peak in PAR at CH33 is explained by the stronger influence of the LGR plume, which contains more CDOM and suspended sediment than James Bay waters (Meilleur et al., 2023; Évrard et al., 2023). However, even if the LGR reduced under-ice PAR at CH33 in late April, it was probably inconsequential because the late-April increase in PAR was short-lived and followed by a reduction to <1 µmol s^{-1} m^{-2} that lasted from mid-May until ice breakup in early June. The interruption in the seasonal increase in PAR was linked to ice breakup in the small

Overall, local rivers seem to exert a disproportionately strong impact (relative to their discharge) on the light climate in the eelgrass habitat starting during the ice melt and breakup periods and persisting through summer. The low-light period that lasted from mid-May until early June may be linked, in the case of the CH4 mooring, to the influence of the CDOM-rich La Guillaume River. The period in which PAR persisted at <1 µmol s^{-1} m^{-2} coincides with the appearance of the ice-free channel extending from the river mouth to the mooring site (Figure 5.4c) and the low- salinity period at CH4 (Figure 5.5b). Notably, although PAR also dips low at CH33 in late May, it is not matched by a salinity decrease at this site, nor does the satellite imagery show clearly that local stream inflow has affected the ice cover at the CH33 site. Therefore, the low PAR observed at CH33 in late May remains unexplained.

In the open-water period, CH33 recorded consistently higher PAR than CH4, averaging 4.1 versus 1.7 mol day^{-1} m^{-2} (Table 5.2). From mid-June to mid-July, CH33 exhibited larger peaks, while CH4 showed persistently lower values. The lower summer values at CH4 likely are explained by continued influence from CDOM-rich local rivers. De Melo et al. (2022) found that the LGR consistently had the lowest dissolved organic carbon (DOC) and suspended sediment values among rivers with outlets along eastern James Bay. For La Guillaume River in particular, they report an average DOC concentration of 18.9 (5.0) mg L^{-1} compared to only 4.3 (0.3) mg L^{-1} in the LGR. Although La Guillaume River has low DOC exports to James Bay and La Grande River is the largest exporter of DOC, the close proximity of CH4 to La Guillaume River means that when the stream is not frozen, it exerts strong influence on the water properties at this site. During summer, La Guillaume River discharges about 21% of its total annual freshwater export, compared to only 2% during winter and 53% during spring (de Melo et al., 2022).

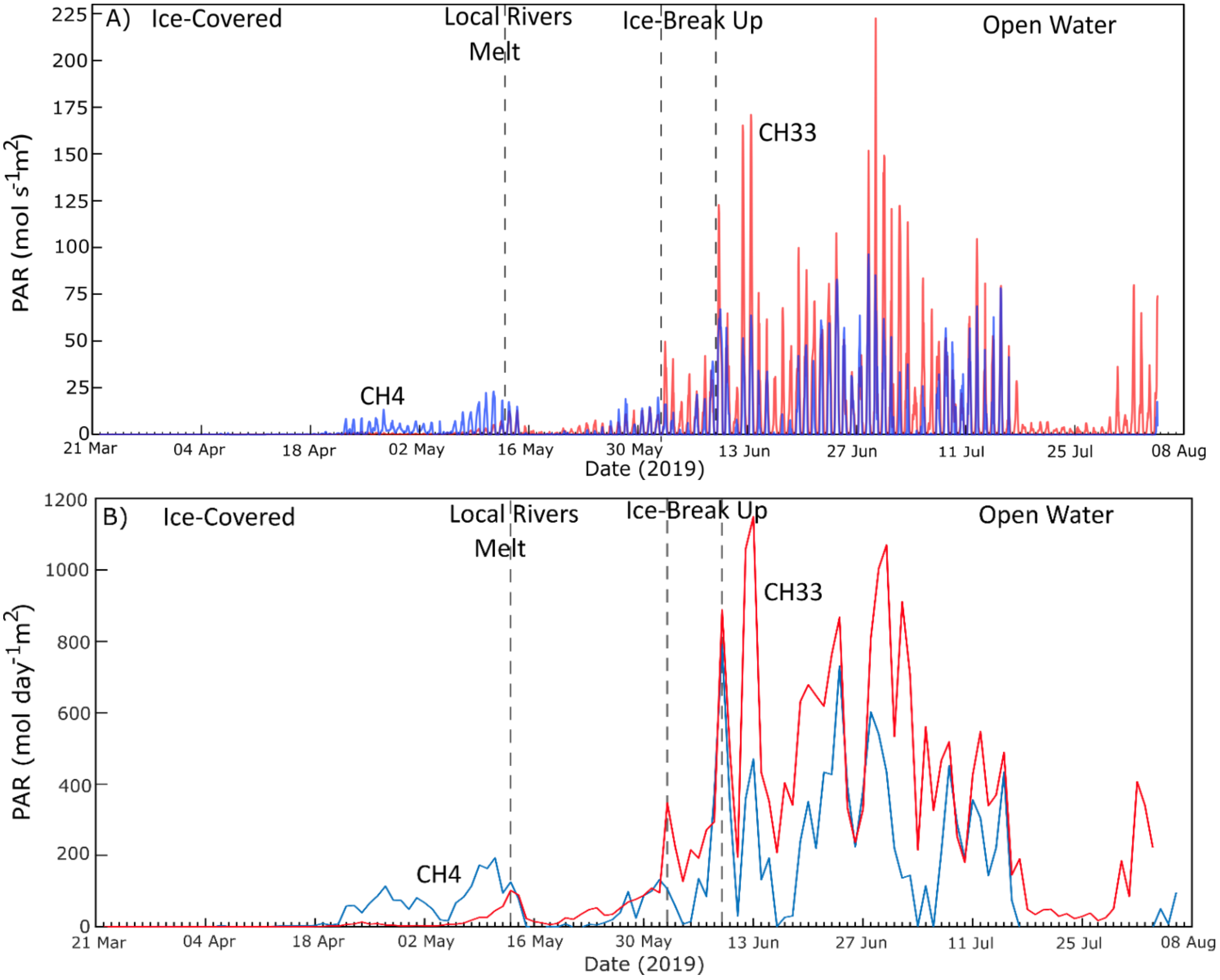

Figure 5.7: Hourly averaged (A) and integrated daily (B) PAR for the CH4 (4.6m) (blue) and CH33(4.5m) (red) moorings.

Ice breakup around 2-9 June marked a sharp rise in PAR, with daily values peaking on 9 June, when satellite imagery shows that most of the ice was gone from the embayments. The PAR hourly averages and integrated daily values on 9 June were among the highest recorded values at both sites (Figure 5.7). In the open-water period that followed, there were several dips in the integrated daily PAR, many of which lasted for several consecutive days. Most of these do not obviously match dips in salinity and temperature. Both moorings experienced a prolonged low-light period from 16 July to ~2 August, more severe at CH4 where almost no PAR was detected for over two weeks. There is no clear explanation for this simultaneous decrease. It could have been caused by an increase in turbidity or shading by eelgrass. But most likely, large benthic algal mats that have been observed in numerous field campaigns along the coast, lifting may have shaded the sensors. The mats sometimes lift up off the bottom and float in the water column and may have become entangled on the mooring superstructure so that even the action of the wiper on the PAR sensor had no effect (Figure S5.2); these mats could have also shaded the sensors.

Overall, we suspect that combination of cloud cover, water level, surface roughness, water optical properties (CDOM, turbidity), and possibly also algal matter influenced short-term PAR variability during the open water season (Figures 5.7). The percentage of incident PAR transmitted to 3.6 m depth (estimated from MODIS MCD18A2 incident PAR; Figure 5.8a), which was below 2% during the ice-covered period, increased to only 0–11% in open water (Figure 5.8b), still below the 12–18% required for northern eelgrass (Lee et al., 2007). Estimated bulk PAR diffuse attenuation coefficients were 2.93 m^{-1} during the pre-melt period (i.e., under snow-covered ice), 1.77 m^{-1} during ice melt, and 1.01 m^{-1} in open water. These values indicate that 3.6 m depth is at the lower light limit for eelgrass growth in northeast James Bay. Indeed, CHCRP eelgrass beds occur at shallower depths (Kuzyk et al., 2023). Assuming an attenuation coefficient of 1.0 m^{-1}, PAR at 2.5 m and 1.5 m depths would be ~3 and ~8 times higher, respectively, making them more suitable for eelgrass, though growth in shallower zones is limited by ~1 m thick winter ice.

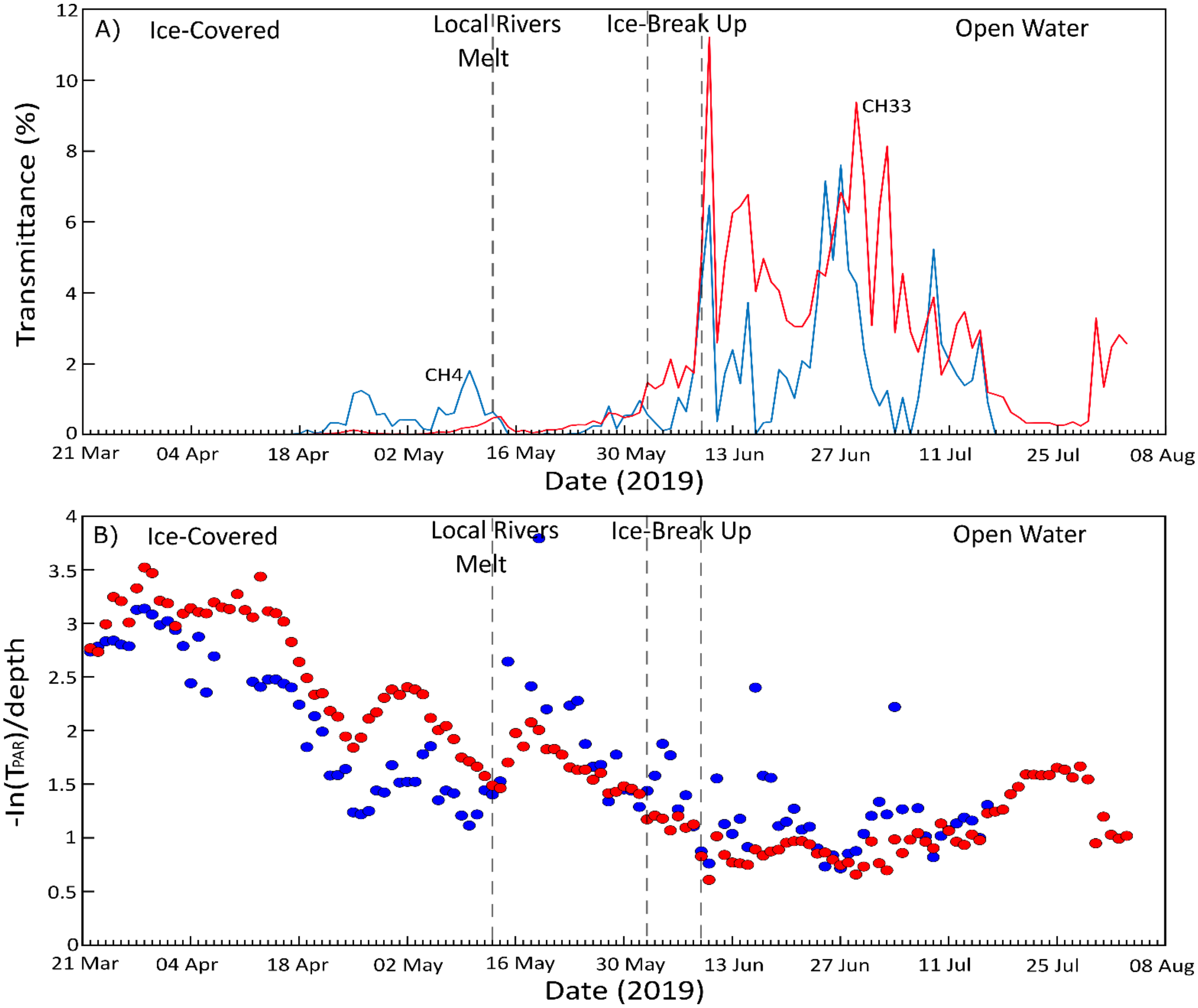

Figure 5.8: Transmittance estimated from daily average PAR from mooring observations and MODIS product MCD18A2 version 6.2 (A). Estimate of diffuse attenuation coefficient for PAR for the snow-ice-water column above the PAR sensors on the moorings (B). TPAR is the fraction of the daily average PAR at the moorings to the daily average surface incident PAR from the MODIS product MCD18A2 version 6.2. Distance above sensor to the surface was assumed be a constant at 3.6 m.

5.4.4 Implications for eelgrass beds

Eelgrass (*Zostera marina*) is highly sensitive to environmental conditions, with growth and survival closely tied to stable salinity, temperature, and light availability. Suboptimal salinity, particularly levels below 15 PSU or subject to frequent fluctuations, can disrupt osmotic balance, reduce photosynthetic efficiency, and impair carbon storage (Nejrup & Pedersen, 2008; Salo et al., 2014). Temperature extremes also pose challenges; growth slows significantly below 5°C, while prolonged exposure above 25–30°C can lead to physiological stress and dieback (Olesen et al., 1993; Phillips et al., 1983). Light limitation, especially when PAR falls below the compensation point (~30–60 μmol photons m^{-2} s^{-1}), restricts photosynthesis and biomass accumulation, making eelgrass vulnerable in turbid or ice-covered waters (Davis et al., 2024; Olesen et al., 2015). These factors often interact, compounding stress and reducing resilience in eelgrass habitats worldwide.

The observed data support the hypothesis that the transition from ice-covered winter months to the open-water period, which includes ice breakup, melt, and spring stream flows, leads to changes in the essential variables of salinity, temperature, and photosynthetically active radiation (PAR). These environmental shifts create suboptimal growing conditions for eelgrass in the spring. Salinity, temperature, and PAR levels varied significantly between the ice-covered, ice-breakup, and open-water periods, influencing the physiological and ecological responses of eelgrass. Regional freshwater sources like the LGR dominate coastal salinity and temperature gradients, while small local streams can contribute disproportionately to nearshore variability. These smaller inputs rapidly alter surface salinity and temperature in shallow eelgrass habitats during peak spring discharge (Hamman et al., 2017; Fraley et al., 2021). Moreover, the interaction between ice cover and freshwater discharge modulates light availability and mixing dynamics. Ice can constrain river plume spread, affecting freshwater mixing with coastal waters, while streamflow can accelerate ice melt and carve channels (Figure 5.2c), enhancing light penetration and altering under-ice conditions (Nghiem et al., 2014; Osadchiev et al., 2024).

Taking 15 PSU as the threshold (minimum) salinity for optimal eelgrass growth, during the ice-covered, breakup, and open-water periods, 44%, 87%, and 89% of the salinity records at CH33 were above the optimal threshold and 25%, 61%, and 82% at CH4, respectively. Compared to CH4, CH33 experienced larger fluctuations, especially during the ice-covered period, with standard deviations of 2.92 and 7.95, indicating high salinity variability. This can be attributed to the intermittent strong influence of LGR on salinity at CH33 (Figure 5.5b). Similar patterns were observed in subarctic eelgrass beds in Japan, where strong salinity gradients affected community structures, reducing invertebrate biomass and eelgrass productivity (Namba et al., 2024).

Eastern James Bay eelgrass is perennial and survives the ice-covered period with significantly slowed growth, relying on the carbon stored in its rhizomes (Wong et al., 2013; Olesen et al., 2015). This survival strategy aligns with observations in Greenland, where eelgrass remains dormant under ice but recovers biomass at higher summer temperatures (Olesen et al., 1993; Olesen et al., 2015). Experimental studies have shown that eelgrass can withstand low salinities (5-10 PSU or <15 PSU) for up to six weeks (Nejrup and Pedersen, 2008; Salo et al., 2014; Zhang et al., 2022). However, the effects of prolonged salinity fluctuations on eelgrass health and carbon storage are poorly understood. Baltic Sea studies suggest that eelgrass populations with frequent salinity variations develop greater plasticity, whereas those from stable environments may be more vulnerable to fluctuations (Salo et al., 2014). With this in mind, eelgrass at CH33 could be more resilient to high salinity fluctuations than at CH4. However, whether this resilience has developed remains uncertain. If local eelgrass populations have not fully adapted or if fluctuations exceed physiological thresholds during critical growth periods, salinity stress may still impair resilience by increasing energy demands for osmotic regulation and reducing carbon storage.

The temperature at CH33 was below the optimal range for eelgrass growth, averaging 5.2°C during the open-water period, with a maximum of 10.9°C in mid-July. In contrast, CH4 had an average open-water temperature of 9.1°C, generally above 10°C for most of July and August. Temperature is critical for flowering and seed maturation; typically, temperatures above 10°C are required (Phillips et al., 1983). This suggests that eelgrass beds at CH4 may have a higher reproductive capacity than those at CH33. A similar pattern was observed for eelgrass in Akkeshi Bay, Japan, where temperature influenced seed production and biomass (Namba et al., 2024). Eelgrass diebacks occur at temperatures above 25°C, although such extremes are rare in James Bay (CH33 max 22.44°C, CH4 14.85°C). This is in contrast to Baltic and Japanese eelgrasses, where warming trends increase physiological stress, potentially causing diebacks and shifting their distribution (Salo et al., 2014). The low temperatures in James Bay suggest that warming could extend the growing season without exceeding lethal thresholds, although the combined effects of warming and altered freshwater discharge remain unclear.

Continuous daytime PAR measurements are crucial for understanding macrophyte adaptation to light availability. For eelgrass to grow, PAR must exceed the compensation point at which photosynthesis matches respiration. A recent study found that the compensation points for two eelgrass beds in eastern James Bay ranged between 31 and 61 μmol m^{-2} s^{-1}, while the maximum production occurred between 224 and 260 μmol m^{-2} s^{-1}. The high light requirements for maximum growth and low compensation point indicate that these beds are not well adapted to low light (Davis et al., 2024). This aligns with findings from Greenland and the Baltic Sea, where light limitation constrains eelgrass productivity during winter ice cover (Olesen et al., 2015; Salo et al., 2014). Ice breakup and open-water periods are crucial for eelgrass growth in northeast James Bay, because PAR levels frequently exceed the compensation point and occasionally reach saturating irradiances. During daylight hours (05:00 to 20:00) between March and August 2017, the average hourly PAR exceeded the compensation point only 15% of the time at CH4 and 26% at CH33. This supports the notion that eelgrass in James Bay is light-limited rather than nutrient-limited (Davis et al., 2024), despite low nutrient concentrations (Guzzi et al., 2024).

Overall, these findings highlight the complex interactions between salinity, temperature, and light that shape eelgrass habitat conditions in James Bay. Comparisons with other eelgrass beds in the Arctic and Subarctic regions suggest that some adaptation to suboptimal conditions is possible, but extreme variability in salinity and light likely remain major stressor. However, potential climate-driven shifts, such as earlier ice melt breakup, may enhance light availability and stabilize salinity regimes during critical spring growth periods, potentially improving habitat suitability for eelgrass.

5.5 Summary and Conclusion

This study presents a unique in-situ dataset to investigate essential variables for eelgrass, investigating the seasonal transition period of essential variables in eelgrass ecosystems under ice-covered to ice-free conditions, which is a phase of the eelgrass annual cycle that has received very limited direct observation globally. For the first time in subarctic James Bay. We investigated seasonal changes in salinity, temperature, and underwater light (PAR) at two sites that differ in degree of protection/exposure, proximity to the largest regional source of freshwater, the regulated La Grande River (LGR), and proximity to local streams. Our findings highlight the complex environmental dynamics that influence essential variables for eelgrass health, particularly during the critical winter-to-summer transition period when eelgrass energy reserves are low after surviving a long dark winter. This could make the eelgrass especially vulnerable to early-season stressors that can have lasting effects on growth and resilience. Significant spatial and temporal variations in salinity, temperature, and light levels were observed between the two mooring sites (CH4 and CH33) caused by seasonality, rivers of various sizes, ice conditions, tidal cycles, and weather conditions. Examining the essential variables temperature, salinity, and PAR at each location revealed that the northern site (CH4), which was more protected, less influenced by the LGR plume but more strongly influenced by CDOM-rich local streams, had more optimal temperature and salinity conditions for eelgrass growth but less optimal light conditions were significantly less optimal than at the southern site compared to the more exposed and LGR-dominated CH33 site (CH33).. The average temperature and salinity at CH33 were outside the optimal ranges for eelgrass growth, particularly during the period of high LGR discharge and landfast ice cover, but also, in terms of temperature, extending into the eelgrass growth season. The data provide evidence that different factors may impact eelgrass health depending on season and location, as well as external forcing factors such as ice conditions, weather events, and river discharge.

We conclude from our PAR observations that eelgrass is unlikely to grow significantly at 3.6 m depth at either site. Given the ~1 m tidal range, ~1 m thick landfast ice, and significant light attenuation both under the ice and within the water column, we infer that perennial eelgrass habitat is presently limited to a very narrow depth band along the northeast coast of James Bay. These findings underscore the complexity of designing protection and restoration measures for eelgrass in these types of coastal environments where hydrological conditions can vary over relatively short distances and timescales. This also highlights the importance of understanding the hydrological dynamics for eelgrass survival and growth at the scale of individual bays and possibly beds if replanting efforts are considered, as they are in James Bay.. Ongoing monitoring and future research are needed to understand how interannual variability and changes in river discharge patterns and ice coverage due to climate change may impact these critical eelgrass ecosystems, with implications for the broader coastal ecosystem and the communities that depend on it.

5.6 References

Aagaard, K., Carmack, E.C., 1989. The role of sea ice and other fresh water in the Arctic circulation. Journal of Geophysical Research: Oceans 94, 14485–14498. https://doi.org/10.1029/JC094iC10p14485

Arrigo, K.R., van Dijken, G.L., 2015. Continued increases in Arctic Ocean primary production. Progress in Oceanography, Synthesis of Arctic Research (SOAR) 136, 60–70. https://doi.org/10.1016/j.pocean.2015.05.002

Bareiss, J., Eicken, H., Helbig, A., Martin, T., 1999. Impact of River Discharge and Regional Climatology on the Decay of Sea Ice in the Laptev Sea during Spring and Early Summer. Arctic, Antarctic, and Alpine Research 31, 214–229. https://doi.org/10.1080/15230430.1999.12003302

Blough, N.V. and Del Vecchio, R., 2002. Chromophoric DOM in the coastal environment. In: Hansell, D.A. and Carlson, C.A. (eds.) Biogeochemistry of marine dissolved organic matter. San Diego: Academic Press, pp. 509–546. https://doi.org/10.1016/B978-012323841-2/50012-9

Carmack, E.C., Macdonald, R.W., 2002. Oceanography of the Canadian Shelf of the Beaufort Sea: A Setting for Marine Life. Arctic 55, 29–45. https://doi.org/10.14430/arctic733

Connan-McGinty, S., Banas, N.S., Berge, J., Cottier, F., Grant, S., Johnsen, G., Kopec, T.P., Porter, M., McKee, D., 2022. Midnight Sun to Polar Night: A Model of Seasonal Light in the Barents Sea. Journal of Advances in Modeling Earth Systems 14, e2022MS003198. https://doi.org/10.1029/2022MS003198

Curtis, S., Allen, L., 1976. Waterfowl ecology of the Quebec coast of James Bay, in: Proceedings of the James Bay Environment 1976 Symposium. Environment Canada, Canada Wildlife Service, Ottawa, Canada, pp. 701–724.

Davis, K., Noisette, F., Ehn, J., Kuzyk, Z., Peck, C., O’Connor, M., 2024. Effects of light and water column nutrient availability on eelgrass *Zostera marina* productivity in Eeyou Istchee, eastern James Bay, Quebec. Marine Ecology Progress Series 738, 103–117. https://doi.org/10.3354/meps14605

de Melo, M.L., Gérardin, M.-L., Fink-Mercier, C., del Giorgio, P.A., 2022. Patterns in riverine carbon, nutrient and suspended solids export to the Eastern James Bay: links to climate, hydrology and landscape. Biogeochemistry 161, 291–314. https://doi.org/10.1007/s10533-022-00983-z

Dean, K.G., Stringer, W.J., Ahlnas, K., Searcy, C., Weingartner, T., 1994. The influence of river discharge on the thawing of sea ice, Mackenzie River Delta: albedo and temperature analyses. Polar Research 13, 83–94. https://doi.org/10.1111/j.1751-8369.1994.tb00439.x

Diaz, A., Kuzyk, Z.Z.A., Guzzi, A., Gupta, K., Papakyriakou, T., Ehn, J.K., 2024. Stable isotopes of landfast sea ice as a record of La Grande River under-ice plume dispersal. Arctic Science 10, 698–712. https://doi.org/10.1139/as-2024-0003

Dunton, K.H., Weingartner, T., Carmack, E.C., 2006. The nearshore western Beaufort Sea ecosystem: Circulation and importance of terrestrial carbon in Arctic coastal food webs. Progress in Oceanography, Structure and function of contemporary food webs on Arctic shelves: a pan-Arctic comparison 71, 362–378. https://doi.org/10.1016/j.pocean.2006.09.011

Eastwood, R.A., Macdonald, R.W., Ehn, J.K., Heath, J., Arragutainaq, L., Myers, P.G., Barber, D.G., Kuzyk, Z.A., 2020. Role of River Runoff and Sea Ice Brine Rejection in Controlling Stratification Throughout Winter in Southeast Hudson Bay. Estuaries and Coasts 43, 756–786. https://doi.org/10.1007/s12237-020-00698-0

Eicken, H., Dmitrenko, I., Tyshko, K., Darovskikh, A., Dierking, W., Blahak, U., Groves, J., Kassens, H., 2005. Zonation of the Laptev Sea landfast ice cover and its importance in a frozen estuary. Global and Planetary Change, Arctic Siberian Shelf Environments 48, 55–83. https://doi.org/10.1016/j.gloplacha.2004.12.005

El-Sabh, M.I. and Koutitonsky, V.G., 1977. An oceanographic study of James Bay before the completion of the La Grande Hydroelectric Complex. Arctic 30, 169–186. https://doi.org/10.14430/arctic2697

Évrard, A., Fink-Mercier, C., Galindo, V., Neumeier, U., Gosselin, M., Xie, H., 2023. Regulated vs. unregulated rivers: Impacts on CDOM dynamics in the eastern James Bay. Marine Chemistry 256, 104309. https://doi.org/10.1016/j.marchem.2023.104309

Fraley, K.M., Robards, M.D., Rogers, M.C., Vollenweider, J., Smith, B., Whiting, A. and Jones, T., 2021. Freshwater input and ocean connectivity affect habitats and trophic ecology of fishes in Arctic coastal lagoons. Polar Biology 44, 1–15. https://doi.org/10.1007/s00300-021-02895-4

Freeman, N.G., 1982. Measurement and modelling of freshwater plumes under an ice cover. PhD dissertation, University of Waterloo, Canada

Granskog, M. A., Ehn, J., Niemelä, M., 2005(a). Characteristics and potential impacts of under-ice river plumes in the seasonally ice-covered Bothnian Bay (Baltic Sea). Journal of Marine Systems 53, 187–196. https://doi.org/10.1016/j.jmarsys.2004.06.005

Granskog, Mats A., Kaartokallio, H., Kuosa, H., Thomas, D.N., Ehn, J., Sonninen, E., 2005(b). Scales of horizontal patchiness in chlorophyll a, chemical and physical properties of landfast sea ice in the Gulf of Finland (Baltic Sea). Polar Biology 28, 276–283. https://doi.org/10.1007/s00300-004-0690-5

Greve, T.M., Borum, J., Pedersen, O., 2003. Meristematic oxygen variability in eelgrass (*Zostera marina*). Limnology and Oceanography 48, 210–216. https://doi.org/10.4319/lo.2003.48.1.0210

Gupta, K., Mukhopadhyay, A., Babb, D.G., Barber, D.G., Ehn, J.K., 2022. Landfast sea ice in Hudson Bay and James Bay: Annual cycle, variability and trends, 2000–2019. Elementa: Science of the Anthropocene 10, 00073. https://doi.org/10.1525/elementa.2021.00073

Guzzi, A.C., Ehn, J.K., Michel, C., Tremblay, J.-É., Heath, J.P., Kuzyk, Z.Z.A., 2024. Influence of altered freshwater discharge on the seasonality of nutrient distributions near La Grande River, northeastern James Bay, Québec. Elementa: Science of the Anthropocene 12, 00133. https://doi.org/10.1525/elementa.2023.00133

Hamman, J., Nijssen, B., Roberts, A., Craig, A., Maslowski, W. and Osinski, R., 2017. The coastal streamflow flux in the Regional Arctic System Model. Journal of Geophysical Research: Oceans 122, 1683–1701. https://doi.org/10.1002/2016JC012323

Harms, I.H., Karcher, M.J., Dethleff, D., 2000. Modelling Siberian river runoff implications for contaminant transport in the Arctic Ocean. Journal of Marine Systems, 27, 95–115. https://doi.org/10.1016/S0924-7963(00)00062-2

Harris, C.M., McClelland, J.W., Connelly, T.L., Crump, B.C., Dunton, K.H., 2017. Salinity and Temperature Regimes in Eastern Alaskan Beaufort Sea Lagoons in Relation to Source Water Contributions. Estuaries and Coasts 40, 50–62. https://doi.org/10.1007/s12237-016-0123-z

Idrobo, C.J., Leblanc, M.-L., O'Connor, M.I., 2024. The "Turning Point" for the Fall Goose Hunt in Eeyou Istchee: A Social-Ecological Regime Shift from an Indigenous Knowledge Perspective. Human Ecology 52, 617–636. https://doi.org/10.1007/s10745-024-00499-0

Ingram, R.G., d'Anglejan, B.F., Lepage, S., Messier, D., 1986. Changes in current regime and turbidity in response to a freshwater pulse in the Eastmain estuary. Estuaries 9, 320–325. https://doi.org/10.2307/1351411

Ingram, R.G., Larouche, P., 1987. Changes in the under-ice characteristics of La Grande Rivière plume due to discharge variations*. Atmosphere-Ocean 25, 242–250. https://doi.org/10.1080/07055900.1987.9649273

Ingram, R.G., Wang, J., Lin, C., Legendre, L., Fortier, L., 1996. Impact of freshwater on a subarctic coastal ecosystem under seasonal sea ice (southeastern Hudson Bay, Canada). I. Interannual variability and predicted global warming influence on river plume dynamics and sea ice. Journal of Marine Systems, 7, 221–231. https://doi.org/10.1016/0924-7963(95)00006-2

Krause-Jensen, D., Archambault, P., Assis, J., Bartsch, I., Bischof, K., Filbee-Dexter, K., Dunton, K.H., Maximova, O., Ragnarsdóttir, S.B., Sejr, M.K., Simakova, U., Spiridonov, V., Wegeberg, S., Winding, M.H.S., Duarte, C.M., 2020. Imprint of Climate Change on Pan-Arctic Marine Vegetation. Frontiers in Marine Science 7. https://doi.org/10.3389/fmars.2020.617324

Krause-Jensen, D., Duarte, C.M., Sand-Jensen, K. and Carstensen, J., 2021. Century-long records reveal shifting challenges to seagrass recovery. Global Change Biology 27, 563–575. https://doi.org/10.1111/gcb.15440

Kuzyk, Z.A., Macdonald, R.W., Granskog, M.A., Scharien, R.K., Galley, R.J., Michel, C., Barber, D., Stern, G., 2008. Sea ice, hydrological, and biological processes in the Churchill River estuary region, Hudson Bay. Estuarine, Coastal and Shelf Science 77, 369–384. https://doi.org/10.1016/j.ecss.2007.09.030

Lalumière, R., Messier, D., Fournier, J.-J., Peter McRoy, C., 1994. Eelgrass meadows in a low Arctic environment, the northeast coast of James Bay, Québec. Aquatic Botany 47, 303–315. https://doi.org/10.1016/0304-3770(94)90060-4

Lemieux, C., Lalumière, R., & Laperle, M., 1999. Complexe La Grande.Suivi environnemental 1999. Les habitats côtiers de la baie James etla végétation aquatique de La Grande Rivière. Rapport présenté àla Direction Expertise et Support technique de production, UnitéHydraulique et Environnement Hydro-Québec, par le Groupe con-seil Génivar inc. 73 p. et annexes

Le Fouest, V., Babin, M., Tremblay, J.-É., 2013. The fate of riverine nutrients on Arctic shelves. Biogeosciences 10, 3661–3677. https://doi.org/10.5194/bg-10-3661-2013

Leblanc, M.-L., O'Connor, M.I., Kuzyk, Z.Z.A., Noisette, F., Davis, K.E., Rabbitskin, E., Sam, L.-L., Neumeier, U., Costanzo, R., Ehn, J.K., Babb, D., Idrobo, C.J., Gilbert, J.-P., Leblon, B., Humphries, M.M., 2023. Limited recovery following a massive seagrass decline in subarctic eastern Canada. Global Change Biology 29, 432–450. https://doi.org/10.1111/gcb.16499

Lee, K.-S., Park, S.R., Kim, Y.K., 2007. Effects of irradiance, temperature, and nutrients on growth dynamics of seagrasses: A review. Journal of Experimental Marine Biology and Ecology, The Biology and Ecology of Seagrasses 350, 144–175. https://doi.org/10.1016/j.jembe.2007.06.016

Lewis, K.M., van Dijken, G.L., Arrigo, K.R., 2020. Changes in phytoplankton concentration now drive increased Arctic Ocean primary production. Science 369, 198–202. https://doi.org/10.1126/science.aay8380

Macdonald, R.W., Paton, D.W., Carmack, E.C., Omstedt, A., 1995. The freshwater budget and under-ice spreading of Mackenzie River water in the Canadian Beaufort Sea based on salinity and 18O/16O measurements in water and ice. Journal of Geophysical Research: Oceans 100, 895–919. https://doi.org/10.1029/94JC02700

Matthes, L.C., Mundy, C.J., L. -Girard, S., Babin, M., Verin, G., Ehn, J.K., 2020. Spatial Heterogeneity as a Key Variable Influencing Spring-Summer Progression in UVR and PAR Transmission Through Arctic Sea Ice. Frontiers in Marine Science 7. https://doi.org/10.3389/fmars.2020.00183

Mayora, G., Devercelli, M., Frau, D., 2016. Spatial variability of chromophoric dissolved organic matter in a large floodplain river: control factors and relations with phytoplankton during a low water period. Ecohydrology 9, 487–497. https://doi.org/10.1002/eco.1651

Mcroy, C.P., 1969. Eelgrass under Arctic Winter Ice. Nature 224, 818–819. https://doi.org/10.1038/224818a0

McSweeney, J.M., Chant, R.J., Wilkin, J.L., Sommerfield, C.K., 2017. Suspended-Sediment Impacts on Light-Limited Productivity in the Delaware Estuary. Estuaries and Coasts 40, 977–993. https://doi.org/10.1007/s12237-016-0200-3

Messier, D., Ingram, R.G., Roy, D., 1986. Chapter 20 Physical and Biological Modifications in Response to LA Grande Hydroelectric Complex, in: Martini, I.P. (Ed.), Elsevier Oceanography Series, Canadian Inland Seas. Elsevier, pp. 403–424. https://doi.org/10.1016/S0422-9894(08)70913-9

Messier, D., Lepage, S., de Margerie, S., 1989. Influence of ice cover on the extent of the La Grande River plumes (James Bay). Arctic 42, 278–284. https://doi.org/10.14430/arctic1666

Moksnes, P.-O., Eriander, L., Infantes, E., Holmer, M., 2018. Local Regime Shifts Prevent Natural Recovery and Restoration of Lost Eelgrass Beds Along the Swedish West Coast. Estuaries and Coasts 41, 1712–1731. https://doi.org/10.1007/s12237-018-0382-y

Moore, K.A., Wetzel, R.L., Orth, R.J., 1997. Seasonal pulses of turbidity and their relations to eelgrass (*Zostera marina* L.) survival in an estuary. Journal of Experimental Marine Biology and Ecology 215, 115–134. https://doi.org/10.1016/S0022-0981(96)02774-8

Murphy, G.E.P., Dunic, J.C., Adamczyk, E.M., Bittick, S.J., Côté, I.M., Cristiani, J., Geissinger, E.A., Gregory, R.S., Lotze, H.K., O'Connor, M.I., Araújo, C.A.S., Rubidge, E.M., Templeman, N.D., Wong, M.C., 2021. From coast to coast to coast: ecology and management of seagrass ecosystems across Canada. FACETS 6, 139–179. https://doi.org/10.1139/facets-2020-0020

Namba, M., Abe, H., Ito, M.A., Nakaoka, M., 2024. The linkage between spatial and temporal variations in epifaunal and primary producer communities in eelgrass (*Zostera marina*) beds. Estuarine, Coastal and Shelf Science 296, 108574. https://doi.org/10.1016/j.ecss.2023.108574

Nejrup, L.B., Pedersen, M.F., 2008. Effects of salinity and water temperature on the ecological performance of *Zostera marina*. Aquatic Botany 88, 239–246. https://doi.org/10.1016/j.aquabot.2007.10.006

Nghiem, S.V., Hall, D.K., Rigor, I.G., Li, P. and Neumann, G., 2014. Mackenzie River discharge and Arctic sea ice cover. Geophysical Research Letters 41, 2014GL059705.

Novak, M.G., Mannino, A., Clark, J.B., Hernes, P., Tzortziou, M., Spencer, R.G., Kellerman, A.M. and Grunert, B., 2022. Arctic biogeochemical and optical properties of dissolved organic matter across river to sea gradients. Frontiers in Marine Science, 9, p.949034.https://doi.org/10.3389/fmars.2022.949034

Olesen, B., Krause-Jensen, D., Marbà, N., Christensen, P.B., 2015. Eelgrass *Zostera marina* in subarctic Greenland: dense meadows with slow biomass turnover in cold waters. Marine Ecology Progress Series 518, 107–121. https://doi.org/10.3354/meps11087

Olesen, B., Sand-Jensen, K., 1993. Seasonal acclimatization of eelgrass *Zostera marina* growth to light. Marine Ecology Progress Series 94, 91–99. https://doi.org/10.3354/meps094091

Osadchiev, A., Kuskova, E. and Ivanov, V., 2024. The roles of river discharge and sea ice melting in formation of freshened surface layers in the Kara, Laptev, and East Siberian seas. Frontiers in Marine Science 11, 1348450. https://doi.org/10.3389/fmars.2024.1348450

Park, J.H., Kim, S.-J., Lim, H.-G., Kug, J.-S., Yang, E.J., Kim, B.-M., 2023. Phytoplankton responses to increasing Arctic river discharge under the present and future climate simulations. Environmental Research Letters 18, 064037. https://doi.org/10.1088/1748-9326/acd568

Pawlowicz, R., Beardsley, B., Lentz, S., 2002. Classical tidal harmonic analysis including error estimates in MATLAB using T_TIDE. Computers & Geosciences 28, 929–937. https://doi.org/10.1016/S0098-3004(02)00013-4

Peck, C., Kuzyk, Z.Z.A., Kirillov, S., Neumeier, U., Rabbitskin, E., Ehn, J.K., 2025. On the Upcoast Intrusion of the La Grande River Under-Ice Plume Under Wind Forcing. https://doi.org/10.2139/ssrn.4968853

Peck, C.J., Kuzyk, Z.Z.A., Heath, J.P., Lameboy, J., Ehn, J.K., 2022. Under-Ice Hydrography of the La Grande River Plume in Relation to a Ten-Fold Increase in Wintertime Discharge. Journal of Geophysical Research: Oceans 127, e2021JC018341. https://doi.org/10.1029/2021JC018341

Phillips, R.C., McMillan, C., Bridges, K.W., 1983. Phenology of eelgrass, *Zostera marina* L., along latitudinal gradients in North America. Aquatic Botany 15, 145–156. https://doi.org/10.1016/0304-3770(83)90025-6

Plaisted, H.K., Shields, E.C., Novak, A.B., Peck, C.P., Schenck, F., Carr, J., Duffy, P.A., Evans, N.T., Fox, S.E., Heck, S.M., Hudson, R., Mattera, T., Moore, K.A., Neikirk, B., Parrish, D.B., Peterson, B.J., Short, F.T., Tinoco, A.I., 2022. Influence of Rising Water Temperature on the Temperate Seagrass Species Eelgrass (*Zostera marina* L.) in the Northeast USA. Frontiers in Marine Science 9. https://doi.org/10.3389/fmars.2022.920699

Prentice, C., Poppe, K.L., Lutz, M., Murray, E., Stephens, T.A., Spooner, A., Hessing-Lewis, M., Sanders-Smith, R., Rybczyk, J.M., Apple, J., Short, F.T., Gaeckle, J., Helms, A., Mattson, C., Raymond, W.W., Klinger, T., 2020. A Synthesis of Blue Carbon Stocks, Sources, and Accumulation Rates in Eelgrass (*Zostera marina*) Meadows in the Northeast Pacific. Global Biogeochemical Cycles 34, e2019GB006345. https://doi.org/10.1029/2019GB006345

Prinsenberg, S.J., 1986. Salinity and temperature distributions of Hudson Bay and James Bay. In: Martini, I.P. (ed.) Canadian inland seas. Elsevier Oceanography Series, vol. 44. Amsterdam: Elsevier, pp. 163–186. https://doi.org/10.1016/S0422-9894(08)70902-4

Prinsenberg, S. J. (1982). Present and future circulation and salinity in James Bay. Le Naturaliste Canadien, 109(4), 827–841.

Prinsenberg, S.J., 1980. Man-Made Changes in the Freshwater Input Rates of Hudson and James Bays. Canadian Journal of Fisheries and Aquatic Sciences 37, 1101–1110. https://doi.org/10.1139/f80-143

Reed, A., Canadian Wildlife Service (Eds.), 1996. Goose use of the coastal habitats of northeastern James Bay, Occasional paper / Canadian Wildlife Service. Environment Canada, Canada Wildlife Service, Ottawa, Ontario.

Ridenour, N.A., Hu, X., Sydor, K., Myers, P.G., Barber, D.G., 2019. Revisiting the Circulation of Hudson Bay: Evidence for a Seasonal Pattern. Geophysical Research Letters 46, 3891–3899. https://doi.org/10.1029/2019GL082344

Salo, T., Pedersen, M.F., Boström, C., 2014. Population specific salinity tolerance in eelgrass (*Zostera marina*). Journal of Experimental Marine Biology and Ecology 461, 425–429. https://doi.org/10.1016/j.jembe.2014.09.010

Sand-Jensen, K., Borum, J., 1983. Regulation of growth of eelgrass (*Zostera marina* L.) in Danish coastal waters. Journal of Marine Engineering and Technology 17, 15–21.

Sawall, Y., Ito, M., Pansch, C., 2021. Chronically elevated sea surface temperatures revealed high susceptibility of the eelgrass *Zostera marina* to winter and spring warming. Limnology and Oceanography 66, 4112–4124. https://doi.org/10.1002/lno.11947

Schallenberg, M., Burns, C.W., 2004. Effects of sediment resuspension on phytoplankton production: teasing apart the influences of light, nutrients and algal entrainment. Freshwater Biology 49, 143–159. https://doi.org/10.1046/j.1365-2426.2003.01172.x

Shiklomanov, I.A., Shiklomanov, A.I., 2003. Climatic Change and the Dynamics of River Runoff into the Arctic Ocean. Water Resources 30, 593–601. https://doi.org/10.1023/B:WARE.0000007584.73692.ca

Short, F., Carruthers, T., Dennison, W., Waycott, M., 2007. Global seagrass distribution and diversity: A bioregional model. Journal of Experimental Marine Biology and Ecology, The Biology and Ecology of Seagrasses 350, 3–20. https://doi.org/10.1016/j.jembe.2007.06.012

Stadnyk, T.A., Tefs, A., Broesky, M., Déry, S.J., Myers, P.G., Ridenour, N.A., Koenig, K., Vonderbank, L., Gustafsson, D., 2021. Changing freshwater contributions to the Arctic: A 90-year trend analysis (1981–2070). Elementa: Science of the Anthropocene 9, 00098. https://doi.org/10.1525/elementa.2020.00098

Steiner, N.S., Reader, C.M., 2024. Trends and Projections in Climate-Related Stressors Impacting Arctic Marine Ecosystems—A CMIP6 Model Analysis. Journal of Geophysical Research: Oceans 129, e2024JC020970. https://doi.org/10.1029/2024JC020970

Stroeve, J., Crawford, A., Ferguson, S., Stirling, I., Archer, L., York, G., Babb, D., Mallett, R., 2024. Ice-free period too long for Southern and Western Hudson Bay polar bear populations if global warming exceeds 1.6 to 2.6 °C. Communications Earth and Environment 5, 296. https://doi.org/10.1038/s43247-024-01430-7

Taha, W., Bonneau-Lefebvre, M., Cueto Bergner, A., Tremblay, A., 2019. Evolution From Past to Future Conditions of Fast Ice Coverage in James Bay. Frontiers in Earth Science 7. https://doi.org/10.3389/feart.2019.00254

Tremblay, C., Awashish, P., Craik, B., Berrouard, D., and Harvey, B., 2006. Report on the Eastmain-1-A and Rupert Diversion hydropower project : report by the Provincial Review Committee to the Administrator of Chapter 22 of the James Bay and Northern Quebec Agreement. Canada: N.

Waldock, C., Dornelas, M., Bates, A.E., 2018. Temperature-Driven Biodiversity Change: Disentangling Space and Time. BioScience 68, 873–884. https://doi.org/10.1093/biosci/biy096

Waycott, M., Collier, C., McMahon, K., Ralph, P., McKenzie, L.J., Udy, J. and Grech, A., 2007. Vulnerability of seagrasses in the Great Barrier Reef to climate change. In: Johnson, J.E. and Marshall, P.A. (eds.) Climate change and the Great Barrier Reef: a vulnerability assessment. Townsville, QLD: Great Barrier Reef Marine Park Authority and Australian Greenhouse Office, pp. 193–236. ISBN 978-1-876945-61-9

Wong, M.C., Bravo, M.A., Dowd, M., 2013. Ecological dynamics of *Zostera marina* (eelgrass) in three adjacent bays in Atlantic Canada. Botanica Marina 56, 413–424. https://doi.org/10.1515/bot-2013-0068

Zhang, Y.-H., Yu, B., Liu, Y.-C., Ma, W., Li, W.-T., Zhang, P.-D., 2022. The influence of decreased salinity levels on the survival, growth and physiology of eelgrass *Zostera marina*. Marine Environmental Research 182, 105787. https://doi.org/10.1016/j.marenvres.2022.105787

5.7 Supplementary Material

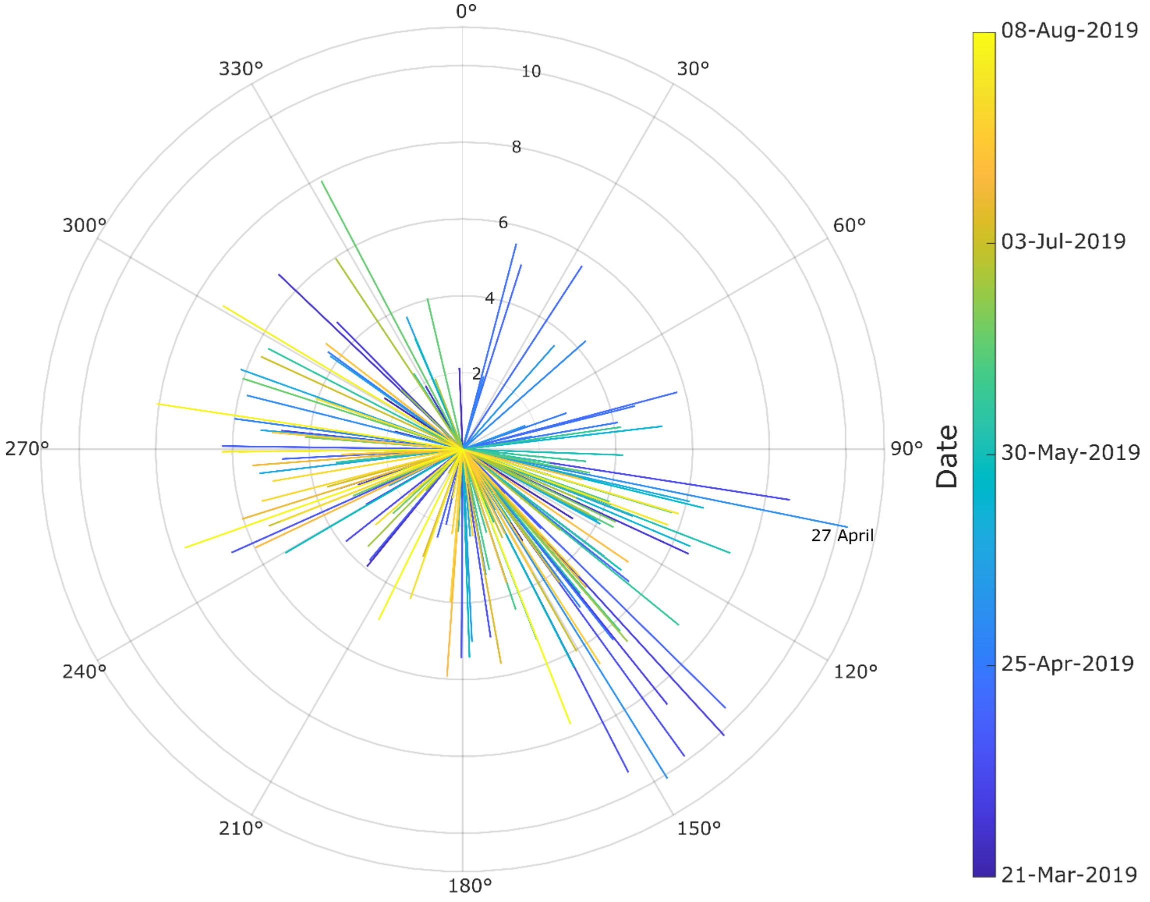

Figure S 5.1: Wind rose diagram showing the daily averaged wind direction and speeds (m s^{-1}) for the sample area and period. Each line represents a date.

Figure S 5.2: Example of large algal mats observed in the coastal waters of northeast James Bay

Chapter 6 Summary and Conclusions

6.1 Summary of major contributions

This thesis aims to answer three research questions in chapters 3 to 5, which contribute to the understanding of how river plumes behave in a seasonally ice-covered environment and how they impact habitat properties of importance to coastal ecosystems, as described below. The main conclusions of the thesis can be summarized as follows:

Research question 1: How has the La Grande River plume (LGR) changed in response to discharge regulation and changes in ice cover?

- Despite a 30% increase in winter discharge since the 1980s, the La Grande River plume has not significantly expanded northward. However, the extent of the plume spreading to the south has increased since the increase in regulated discharge.
- Persistent constraints on plume spreading include coastal geometry and stable landfast ice cover, indicating that with increased winter discharge, larger amounts of the freshwater are lost beyond the landfast ice edge.

Research question 2: What are the short-term drivers of variations in the LGR plume characteristics, especially horizontal extent along the coast?

- Short-term wind events were shown to temporarily break down the stratification under the landfast ice. Persistent westerly wind events can drive significant southward intrusions of the plume under landfast ice, extending its influence up to 25 km beyond historical limits.
- Plume behavior also varies with characteristics of the ice cover, discharge levels, and local bathymetry, with stratification and mixing dynamics influencing how far and how fast freshwater spreads along the coast.

Research Question 3: How does the influence of the LGR plume, local stream discharge, and evolution of the surface ice cover influence key eelgrass habitat properties during the seasonal transition from winter to summer?

- In situ observations during the winter-to-summer transition revealed large, and, at times, independent changes in salinity, temperature, and light availability, resulting from the interaction of multiple drivers. Causes of interruptions in the seasonal increase in photosynthetically active radiation (PAR) in late May, during the ice melt and breakup period, warrant further study because of the suggestion, in previous studies, that this is a critical period for eelgrass regrowth, as it follows a long period of negative carbon balance throughout winter.

- Site-specific differences showed that two areas influenced by the LGR plume to different degrees still both experienced salinity, temperature, and light conditions below optimal thresholds for eelgrass, emphasizing the need for localized monitoring and habitat-specific conservation strategies.

This research demonstrates how river discharge regulated for hydroelectric power generation, ice dynamics, and wind forcing collectively shape river plume behavior and habitat conditions in ice-covered coastal ecosystems. While previous models have acknowledged some of these drivers, they have largely failed to capture the complexity and variability of under-ice plume dynamics particularly the influence of wind forcing and time-dependent interactions between discharge and ice cover. These processes remain inadequately represented in current plume models, which often assume static or simplified conditions. The new observations presented in this thesis directly address these gaps by revealing how persistent wind events can significantly alter plume spreading beneath ice, and how seasonal changes in discharge and ice cover modulate salinity and light availability in critical habitats. These findings refine existing conceptual models of under-ice river plumes and highlight their sensitivity to environmental changes. Given the projected shifts in ice cover thickness and duration with climate warming, and potential changes to discharge regimes, understanding these interactions are crucial for habitat conservation and management—particularly for species like eelgrass that depend on stable salinity and light conditions.

This thesis builds on Cree land users' observations of environmental change in Eeyou Istchee, particularly the impacts of hydroelectric development on eelgrass and Canada geese. While Cree knowledge has linked the declines in goose presence and eelgrass health and extent to changes in La Grande River freshwater flow, this research quantifies the changes, adds to the observations related to seasonality and spatial variability, and identifies other factors that interact with LGR discharge to determine salinity and other essential variables at the eelgrass beds. The research also provides an explanation for unexpected changes that were observed, such as the plume expanding southward rather than northward with the 30% increase in winter discharge since the 1980s because of the constraints imposed by coastal geometry and landfast ice. Continuous observations allowed us to learn about the impact of other processes on the plume, such as how wind events drive plume intrusions beyond historical limits, which explain episodic changes observed by Cree hunters. The thesis reveals how seasonal transitions in ice cover and plume behaviour affect habitat properties like salinity, temperature, and light availability. Measurements show that plume-influenced areas often fall below optimal thresholds for eelgrass growth, reinforcing community concerns about habitat degradation. These findings complement traditional knowledge while providing insights into physical drivers of change, supporting localized monitoring and conservation strategies. By integrating scientific and Indigenous perspectives, the research contributes to understanding environmental change in subarctic coastal ecosystems. Detailed summaries of each of the main chapters and their findings are below.

Chapter 3 summary

Chapter 3 presents an updated assessment of the La Grande under-ice river plume. It addresses **Research Question 1** and interpreting the data revealed some insight into **Research Question 2**. The plume forms a region of freshwater influence (ROFI) extending over 100 km along the east coast of James Bay. The plume structure observed during the winters of 2016 and 2017 can be interpreted through the framework of near-field, mid-field, and far-field regions described in Chapter 2 (Figure 2.1). The data showed three distinct areas of the plume: (i) the core area, where salinity is low (<5 PSU) and the water column is highly stratified, and likely encompasses both the near-field and mid-field regions. This zone extends north to Paul Bay and Point Kakachischuan, reflecting the persistence of stratification and limited mixing under landfast ice (Figure 3.10); (ii) a frontal region, where salinity increases rapidly across a short horizontal distance in the Bay of Many Islands sector (CH4 to Point Attikuan in CH5), reflects the transition zone between mid-field and far-field dynamics, where mixing and lateral spreading dominate; and (iii) a large region of freshwater influence extending along the northeast coast of James Bay represents the far field, where surface salinity was notably diluted. Novel insights into the stability of this plume structure were gained using continuous wintertime salinity data obtained from moorings. To the best of our knowledge, this is the first time that continuous data have been obtained from an under- ice plume, as previous studies of this and other major Arctic river plumes have relied largely on CTD casts, which are snapshots in time and space (Ingram and Larouche 1987; Macdonald and Carmack, 1991; Messier, 2002).

Data from our mooring time series revealed that the plume structure under landfast ice was stable throughout winter, as long as the landfast ice extent remained constant and river discharge remained high (average winter discharge of 4800 m^3 s^{-1}). This stable plume could cause salinity at eelgrass habitats within the core area of the plume to remain low (5-10 PSU) throughout winter. Long exposure to low salinity (<5 PSU) can be detrimental to eelgrass growth (Nejrup and Pedersen, 2008).

Despite a 30% increase in winter LGR discharge in 2016/2017 compared to that in the 1980s, the plume's core area showed no significant northward expansion relative to the 1984 and 1987 observations. Remote sensing imagery suggests that the plume is constrained by coastal geometry and landfast ice cover which narrows 35-40 km north of the river mouth. With the maximum landfast ice extent not changing significantly over time (Taha et al., 2019; Gupta et al., 2022), the same constraints were likely applied to the plume in the 1980s (Ingram and Larouche 1987). With no significant increase in plume area, an increased winter discharge implies either an increased plume thickness or an increased freshwater turnover rate. A comparison of our CTD data with those of Messier et al. (1989) indicated no significant increase in thickness. Therefore, flushing rates have increased; a simple budget suggests that over 90% of the cumulative winter freshwater discharge is rapidly transported beyond the core plume area. Consequently, of the winter nitrate stocks of 22.5 mmol m^{-2} in the top 5 m of the water column (Guzzi et al., 2024), approximately only 2.25 mmol m^{-2} remains available for spring primary production.

The influence of the under-ice plume on inshore eelgrass habitats varied with distance from the river mouth and island protection. In Paul Bay, near the mouth of the LGR, freshwater-dominated inshore-waters maintained salinity below 5 PSU throughout winter, rising to 10 PSU in summer, potentially impacting eelgrass health (Lalumière et al., 1994; Dickey, 2015). The Bay of Many Islands experienced more stable, higher salinity (11–13 PSU) during ice-covered periods, increasing to 15–20 PSU in summer, due to turbulent mixing caused by narrow passages among islands. The sensitivity of eelgrass beds to prolonged low salinity during winter and the timing of these conditions relative to the eelgrass growth season remain important areas for further research, as shifts in ice dynamics and discharge patterns may alter habitat suitability (CGW, 2017; Taha et al., 2019; Gupta et al., 2022).

Chapter 4 summary

Land users of traplines south of the La Grande River (LGR) have observed changes to their coastal habitats, including a loss of eelgrass. In response, they requested scientific information on how and when the LGR plume might affect their traplines. Accordingly, Chapter 4 investigates how far south the plume can extend against the prevailing geostrophic circulation and addresses **Research Question 1 and 2**. In Chapter 4, the results of an observational study on the influence of strong wind events on a river plume under landfast ice cover are presented. Many 2D models treat ice as a slab that prevents atmosphere-ocean interaction and wind mixing of surface waters (Kasper and Weingartner, 2012; 2015). However, some observational studies have shown that wind events influence circulation in ice-covered waters (Dmitrenko et al., 2021).

A second motivation was the preliminary CTD data indicating that the LGR plume extends further south of the river mouth compared to the early 1980s following increased winter discharge (Ingram and Larouche, 1987). One hypothesis is that strong wind events influence the shape and extent of the plume. Historically, the winter LGR plume has spread northward owing to the bay's cyclonic circulation, causing a northward flow along the east coast of James Bay. The increase in winter discharge from 460 to 4,600 m^3s^{-1} following hydroelectric development has led to low salinities south of the river mouth in past studies (Messier et al., 1989; Messier, 2002; Peck et al., 2022, Chapter 3), indicating southward plume spreading.

To investigate this further, three moorings were deployed south of the LGR and one north of the river mouth from 2019 to 2020. Our continuous observations of salinity, water level, and other properties during winter 2020 confirmed the southward expansion of the LGR plume core, with the 5 PSU isohaline located as far as 25 km south of its 1976 position and 15 km south of its 1980 position. The plume was found further south than expected, with two freshening events significantly reducing the bottom salinity at all four mooring locations. The largest event lasted 20 days, coinciding with a sustained westerly wind pushing the plume inshore into shallow embayments. These observations were the first to show wind-driven processes affecting under-ice plume dynamics via mobile pack ice interactions (Schulze & Pickart, 2012; Fewings et al., 2008). Previously, it was believed that under-ice plumes were unaffected by wind forcing. For the southern intrusion of the LGR plume to occur on such scales (tens of kilometers), high winter discharge (> 4000 m^3 s^{-1}), continuous landfast ice north and south of the river mouth, and persistent westerly winds are required.

As the maximum extent of landfast ice cover along James Bay has not changed over time (Taha et al., 2019; Gupta et al., 2022), it is likely that upcoast intrusion has occurred since the LGR reached high discharge levels in the 1980s and developed a large (ca. 1200 km^2), very fresh, core plume area. The ERA5 reanalysis data from 1983 to 2022 revealed that prolonged westerly wind events, such as those in winter 2020 (≥2 m s^{-1} lasting 20 days or more), have occurred nine times in 40 winters, with no discernible trend in frequency. With a stable landfast ice extent (Taha et al., 2019; Gupta et al., 2022), high discharge, and persistent winds, intrusions of the plume into the southern areas of the coast are likely to occur in future winters, potentially affecting eelgrass habitats sensitive to low salinity (<15) (Nejrup & Pedersen, 2008). This could hinder eelgrass growth and restoration efforts in coastal habitats south of the river. The large spatial extent of the highly stratified LGR core plume area and its influence on previously unaffected coastal areas during persistent wind events underscore the importance of considering river plume dynamics in habitat monitoring and management strategies

Chapter 5 summary

Community members along the east coast of James Bay are concerned about the conditions in their region, particularly when it comes to the suitability for eelgrass and potential regrowth. Chapter 5 addresses **Research Question 3** and discusses how temperature, salinity, and light availability can vary between two coastal locations due to river influence and other factors. This chapter provides the first in situ observations of the winter-to-summer transition in eelgrass habitats in northeastern James Bay, a period that has not previously been directly measured in this region. Novel in situ records of salinity, temperature, and photosynthetically active radiation (PAR) in eelgrass habitats spanning the seasonal transition from winter to summer, analyzed together with remote sensing images, showed that both site-specific and regional factors explained the variation in habitat characteristics. The melt and transition period, particularly late April to early June, revealed rapid and complex changes in environmental conditions, including brief but significant increases in PAR, salinity reversals, and temperature shifts. These dynamics are critical for understanding eelgrass regrowth potential and are often overlooked in broader regional analyses**.** This is important because regional ice-melt trend analyses often overlook how the timing of ice melt can vary across small spatial scales and influence conditions within the water column.

In high-latitude coastal systems, salinity generally increases during winter as freshwater input decreases and brine is added from sea ice formation (El-Sabh & Koutitonsky, 1977; Prinsenberg, 1986). While this trend is observed at the mooring sites in eastern James Bay, high discharge and the large core plume area of the LGR continue to lower salinity in coastal embayments throughout winter and into early spring. Winter 2019-2020 observations from moorings at two locations, CH33 and CH4, south and north of the river mouth, respectively, showed that both sites experienced average salinity below the optimal threshold for eelgrass growth. The southern site (CH33) was more closer to the edge of the LGR plume, with salinity fluctuating between 15-20 PSU over tidal cycles. This contrasts with the more moderate salinity fluctuations at CH4, where mixing processes buffered the variations. The plume's thickness of 3-4 m under the landfast ice (Messier, 2002; Peck et al., 2022, Chapter 3), maintained at distances of 20 km south of the river mouth, allowed it to penetrate unmixed into shallow coastal embayments, impacting eelgrass beds. As the plume moved northward, mixing reduced the salinity to levels considered less harmful to eelgrass. The effects of persistent fresh pulses at CH33 on eelgrass health remain uncertain, given the limited winter growth of eelgrass.

Light availability, measured as PAR, is crucial for eelgrass growth, yet it is rarely measured in situ in nearshore habitats during the winter-to-summer transition period. These observations represent a novel contribution, as few studies have captured this critical seasonal window in Arctic or subarctic coastal environments, particularly in eelgrass habitats. Our PAR data indicated insufficient light levels for eelgrass growth during the ice-covered period, with the exception of a brief increase in light levels during the ice-melt phase in late April and early May. Cloud cover and water turbidity influenced PAR during the open-water period, with eelgrass at CH33 experiencing higher average light levels than CH4. Despite low nutrient concentrations (Guzzi et al., 2024), light limitation appears to be a critical factor for eelgrass growth in this region. Although the daily integrated PAR at CH33 often met the minimum requirements for growth, PAR that could support maximum growth rarely occurred, and CH4 had fewer instances of adequate light exposure (Davis et al., 2024). These findings underscore the complex interplay between salinity, temperature, and light in determining eelgrass health in the coastal habitat of eastern James Bay and stress the importance of understanding these dynamics for future eelgrass conservation and replanting efforts.

6.2 Limitations and recommendations for future work

This thesis provides new observations of under-ice river plumes and the influence of different interacting factors over different time scales in determining plume shape, extent, and intrusions into inshore eelgrass habitats. This thesis revealed how oceanographically complex the coast of James Bay is and how difficult it is to find direct links between influencing factors, such as wind, river output, tide, or temperature, and the response of the LGR plume.

Community based research

Conducting community-based research along the northeastern coast of James Bay has been a deeply collaborative and adaptive process. This research was initiated in response to concerns raised by local Cree communities about the noticeable decline in eelgrass along the coast. Their observations and questions prompted an independent study led by university researchers, aiming to better understand the environmental changes affecting these vital habitats. Community members played an essential role in facilitating fieldwork by providing transportation to remote data collection sites and, at times, offering accommodation in the more remote locations. Their local knowledge was invaluable in identifying ecologically significant areas and sharing historical insights into how the coastline has changed over time. This guidance not only enriched the scientific understanding of the region but also ensured that the research remained grounded in lived experience. In 2020 during the COVID-19 pandemic, when we were unable to travel, community members continued sampling, allowing data collection to proceed uninterrupted. At the same time, respectful engagement meant recognizing that some areas were not accessible due to local restrictions, which required flexibility and open communication. Overall, the research benefited immensely from the trust and expertise of the community, underscoring the importance of reciprocal relationships in environmental science, particularly in the Arctic/subarctic.

More observations of the plume and beyond

Despite numerous CTD casts and moorings, both bottom-mounted and ice-tethered mounted beneath the ice, the LGR plume is still not mapped well enough to create detailed salinity contours that encompass the inshore eelgrass habitat and intersect the shoreline. This is mostly because of the size of the plume, the complexity of the coastline and nearshore bathymetry with limited charting, and the limited sampling period in winter. This represents a critical data gap because much of the existing understanding of plume behavior is based on studies of open coastal waters or idealized models with linear, featureless coastlines. Eelgrass beds are particularly sensitive to salinity gradients, and without this information, it's challenging to assess or model their response to changing freshwater inputs. The addition of helicopter work to collect more CTD data and to deploy and recover an array of moorings in the winter at new and repeat locations, would provide valuable insights into these critical salinity dynamics and habitat monitoring.

With the advancement of marine robotics, it could be that an Autonomous Underwater Vehicle (AUV) could collect temperature and salinity data beneath the ice, over large areas. An AUV could also be used to sample the landfast ice edge and in the flaw lead to determine if the plume is advancing beyond the ice edge and determine how quickly it mixes with the surrounding waters. The AUV could also conduct missions at different depths or undulating flight paths to determine where the plume decreases in thickness as it extends away from the LGR mouth. To my knowledge, an AUV has not been used before in an under-ice plume, but this technology has been used in other locations in the Arctic with marginal ice zones, such as north of Svalbard (Johnsen et al., 2018) and offshore of Barrow, Alaska (Kukulya et al., 2010). However, large AUV surveys under ice cover have not been conducted owing to the challenges of underwater navigation. In a traditional AUV survey, the vehicle will surface frequently to establish a GPS fix before continuing the survey. The time between surfacing can be increased with the use of an internal navigation system (INS). An accurate INS uses the vehicle's orientation, heading, propeller speed, and speed over ground, gathered from a Doppler velocity logger (DVL), to calculate an approximate position. However, the longer the vehicle is under the surface (or under ice cover), the greater the error of the INS position; therefore, the vehicle still needs to surface to gather position data. One way to improve this is with the use of an ultrashort baseline acoustic positioning system (USBL), which can tell the AUV where it is relative to the USBL. These positioning systems can be deployed through the ice and can continuously update the internal navigation system of the AUV while collecting data. However, the AUV would still need to be kept at a safe distance below the ice to avoid collisions with pressure ridges and under-ice topography. With this in mind, it might be more practical to sample the under-ice plume using helicopter surveys and transition to using robotics in the open water where navigation becomes simpler.

In the summer, when the ice has melted, the task of mapping the LGR plume becomes simpler, as an AUV could be used in a more traditional way and deployed from a vessel. Another alternative to generate a detailed map of the plume is to use an Uncrewed Surface Vehicle (USV) to collect surface temperature and salinity data with an underway system and then collect CTD casts at specific locations along the coast. The use of robotic vehicles allows a large amount of data to be collected in an efficient manner. However, the scientists controlling the AUV and the USV still need to be present within a distance of a few kilometers to supervise the operations. Though Cree knowledge of the coast and its bathymetric features is unmatched by scientific data at the present time, collaborative efforts for such a long period would be difficult, so any autonomous vehicle will be flying "blind" and mitigation measures would need to be implemented to prevent vehicles running aground. Shoals are appearing at rates more rapid than hydrographic charts are updated because, in this region, post-glacial isostatic rebound still measures about 1-2 cm per year or higher (Pendea et al., 2010).

Numerical model

The plume dynamics along the coast of James Bay are complex, and it is difficult to understand the full picture from observational data alone with regards to how the different influences on the LGR plume interact. It is clear that a detailed numerical model would add to the understanding of the dynamics of the LGR plume along the coast. As mentioned in Chapter 2, several models of river plumes have been developed, but mostly for application to open-water conditions. The models that have been developed for or applied to under-ice plumes have not focused on how combined influences, such as coastal topography, discharge variations, wind, tide, etc., might interact to affect a plume's structure and extent. A numerical model should start with a simple box model with the current discharge, ice cover and ideally the background circulation. Once a baseline has been established, then complexity can be added to give a better representation of the processes along the coast. When adding to the model, using the most detailed bathymetry available is key, as it is a determining factor for how the plume behaves in shallow coastal regions. It is likely that more high-resolution bathymetry would need to be collected in order to get the best results. The model would also need to include largescale circulation of James Bay and the predicted tides for the area. It would then need a realistic landfast ice extent, which would be more accessible than other locations, as it has not significantly changed since the 1980s. The discharge would then be modified and could mimic the discharge conditions from the 1980s to the present to confirm how the plume's size and shape evolved with hydroelectric development. One could also follow the seasonal discharge pattern, decreasing it in the spring as the ice begins to melt. Wind forcing could then be introduced, but the model would have to include an area beyond the landfast ice edge to capture the movement of mobile pack ice and how that energy can transfer to the plume below the landfast ice. Local tides and discharge from smaller rivers would need to be introduced to obtain more accurate water column conditions at specific targets along the coast. When such a model is developed, it could provide further insight not only into the under-ice plume dynamics along the whole coast, but also into ecosystem studies; for example, it could be used in eelgrass replanting efforts by informing on the conditions in specific coastal embayments.

Eelgrass site monitoring

With the water column conditions changing so drastically along the coast on daily to seasonal time scales, I believe it would be useful to have long-term monitoring stations established along the coast at specific sites that could be maintained and accessed by the local community. These monitoring stations could consist of bottom-mounted moorings that monitor salinity, temperature, and light conditions throughout the year and communicate the data to the community via a wired connection to the shore. It would provide more continuous observations as the seasons transition and could be used to monitor the coast in future decades. This could provide information not only on the impact of the modified LGR plume but also on how the coast responds to a warming climate and extreme climate events. These stations would be of particular interest to the local communities along the coast, some of whom are eager to start replanting efforts of eelgrass. In addition to in situ moorings, remote sensing techniques such as satellite imagery and aerial surveys could provide valuable synoptic views of ice cover, plume extent, and turbidity patterns across the coast. These data would complement local monitoring by capturing spatial variability in surface conditions and helping to contextualize site-specific observations within broader regional trends. Remote sensing could also assist in identifying suitable replanting zones by tracking seasonal changes in water clarity and plume influence, especially in areas not easily accessible by boat or diver.

If replanting efforts were to begin, it is important to monitor the new shoots in relation to water properties (such as light and salinity) and assess them to see if growth has occurred or if the replanting has failed. To that end, the use of various automated bottom-mapping techniques could be very valuable. One technique is 3D photogrammetry, which provides detailed 3D models of habitats; it has been used successfully to monitor coral habitats (Ferrari et al., 2017, Rossi et al., 2020) and more recently for seagrass (Ventura et al., 2022). Another technique would be to use hydrographic mapping methods such as side-scan sonar (SSS), which is a well-known technique for habitat mapping and has been used to map seagrass (Mulhearn 2001; Montefalcone et al., 2014; Greene et al., 2018). Covering more areas in a shorter timescale than traditional monitoring techniques using scuba divers, SSS surveys can provide detailed maps of seagrass extent and information on the surrounding area. The equipment is also becoming cheaper and more accessible. With some training, community members could monitor eelgrass seagrass extent with a fish finder equipped with SSS.

6.3 Final thoughts

This research would not have been possible without the invitation and support of the Cree Nation of Chisasibi, whose knowledge, guidance, and participation were essential throughout the study. The community members transported the researchers up and down the coast in order to collect the data and often provided valuable insight on where to collect data and shared points of interest. Because of the effort of community members, we were able to continue to collect data throughout the COVID-19 pandemic, ensuring continuity in data collection when travel restrictions were in place. The collaborative nature of this work fostered mutual learning and capacity building, strengthening local stewardship of coastal ecosystems. While publishing these results in academic journals contributes to broader scientific understanding, it is equally important to ensure that findings are shared in accessible formats with the communities who live with and depend on these ecosystems. Reports, workshops, and co-developed outreach materials are essential for translating research into meaningful local action and policy.

The findings of these studies reveal the complexity and sensitivity of the northeastern James Bay ecosystem, particularly in relation to the combined effects of modified and regulated freshwater discharge, large- and small-scale ice dynamics, and wind forcing. The altered coastal hydrography caused by the La Grande River's increased winter discharge has far-reaching consequences for the coastal environment, affecting salinity, temperature, and light availability, which are critical factors for the health of nearshore species such as eelgrass. This thesis provides valuable insights into the physical processes that shape coastal habitat characteristics in this region and highlights the need for continued research and monitoring to mitigate the potential negative impacts of hydroelectric development and regulation. Although hydroelectric power is necessary to offset the use of fossil fuels in the fight against climate change, it is important to recognize that modified freshwater discharge can severely impact the surrounding coastal marine habitat. Therefore, any new developments or increases in freshwater output from existing hydroelectric dams should carefully consider the potential environmental impact beyond the river itself. Moving forward, adaptive management strategies that consider the complex interactions between freshwater inputs, seasonal transitions, and climate variability and change will be essential for preserving the ecological integrity of not only northeastern James Bay but also coastal habitats around the world.

6.4 References

CGW Consortium-Genivar-Waska., 2017. Eastmain-1-A and Sarcelle powerhouses and Rupert diversion: Follow up of eelgrass meadows on the northeast coast of Baie James (James Bay) – Study report 2014.

Davis, K., Noisette, F., Ehn, J., Kuzyk, Z., Peck, C., O'Connor, M., 2024. Effects of light and water column nutrient availability on eelgrass *Zostera marina* productivity in Eeyou Istchee, eastern James Bay, Quebec. Marine Ecology Progress Series 738, 103–117. https://doi.org/10.3354/meps14605

Dickey, M.-H., 2015. Status of eelgrass beds on the east coast of James Bay. Internal Environment Canada Report.

Dmitrenko, I.A., Kirillov, S.A., Babb, D.G., Kuzyk, Z.Z.A., Basu, A., Ehn, J.K., Sydor, K., Barber, D.G., 2021. Storm-driven hydrography of western Hudson Bay. Continental Shelf Research 227, 104525. https://doi.org/10.1016/j.csr.2021.104525

El-Sabh, M.I., Koutitonsky, V.G., 1977. An Oceanographic Study of James Bay before the Completion of the La Grande Hydroelectric Complex. Arctic 30, 169–186.

Ferrari, R., Figueira, W.F., Pratchett, M.S., Boube, T., Adam, A., Kobelkowsky-Vidrio, T., Doo, S.S., Atwood, T.B., Byrne, M., 2017. 3D photogrammetry quantifies growth and external erosion of individual coral colonies and skeletons. Scientific Reports 7, 16737. https://doi.org/10.1038/s41598-017-16408-z

Fewings, M., Lentz, S.J., Fredericks, J., 2008. Observations of Cross-Shelf Flow Driven by Cross-Shelf Winds on the Inner Continental Shelf. Journal of Physical Oceanography 38(11), 2358–2378. https://doi.org/10.1175/2008JPO3990.1

Greene, A., Rahman, A.F., Kline, R., Rahman, M.S., 2018. Side scan sonar: A cost-efficient alternative method for measuring seagrass cover in shallow environments. Estuarine, Coastal and Shelf Science 207, 250–258. https://doi.org/10.1016/j.ecss.2018.04.017

Gupta, K., Mukhopadhyay, A., Babb, D.G., Barber, D.G., Ehn, J.K., 2022. Landfast sea ice in Hudson Bay and James Bay: Annual cycle, variability and trends, 2000–2019. Elementa: Science of the Anthropocene 10, 00073. https://doi.org/10.1525/elementa.2021.00073

Guzzi, A.C., Ehn, J.K., Michel, C., Tremblay, J.-É., Heath, J.P., Kuzyk, Z.Z.A., 2024. Influence of altered freshwater discharge on the seasonality of nutrient distributions near La Grande River, northeastern James Bay, Québec. Elementa: Science of the Anthropocene 12, 00133. https://doi.org/10.1525/elementa.2023.00133

Ingram, R.G., Larouche, P., 1987. Changes in the under-ice characteristics of La Grande Rivière plume due to discharge variations*. Atmosphere-Ocean 25, 242–250. https://doi.org/10.1080/07055900.1987.9649273

Johnsen, G., Norli, M., Moline, M., Robbins, I., von Quillfeldt, C., Sørensen, K., Cottier, F., Berge, J., 2018. The advective origin of an under-ice spring bloom in the Arctic Ocean using multiple observational platforms. Polar Biology 41, 1197–1216. https://doi.org/10.1007/s00300-018-2278-5

Kasper, J.L., Weingartner, T.J., 2015. The Spreading of a Buoyant Plume Beneath a Landfast Ice Cover. Journal of Physical Oceanography 45(2), 478–494. https://doi.org/10.1175/JPO-D-14-0101.1

Kasper, J.L., Weingartner, T.J., 2012. Modeling winter circulation under landfast ice: The interaction of winds with landfast ice. Journal of Geophysical Research: Oceans 117. https://doi.org/10.1029/2011JC007649

Kukulya, A., Plueddemann, A., Austin, T., Stokey, R., Purcell, M., Allen, B., Littlefield, R., Freitag, L., Koski, P., Gallimore, E., Kemp, J., Newhall, K., Pietro, J., 2010. Under-ice operations with a REMUS-100 AUV in the Arctic, in: 2010 IEEE/OES Autonomous Underwater Vehicles. Presented at the 2010 IEEE/OES Autonomous Underwater Vehicles, pp. 1–8. https://doi.org/10.1109/AUV.2010.5779661

Lalumière, R., Messier, D., Fournier, J.-J., Peter McRoy, C., 1994. Eelgrass meadows in a low Arctic environment, the northeast coast of James Bay, Québec. Aquatic Botany 47, 303–315. https://doi.org/10.1016/0304-3770(94)90060-4

Macdonald, R.W., Carmack, E.C., 1991. The role of large-scale under-ice topography in separating estuary and ocean on anArctic shelf. Atmosphere-Ocean 29, 37–53. https://doi.org/10.1080/07055900.1991.9649391

Messier, D., Lepage, S., Margerie, S. de, 1989. Influence of ice cover on the extent of the La Grande River plumes (James Bay). Arctic (Journal of the Arctic Institute of North America); (Canada) 42:3.

Messier, D., 2002. Suivi environnemental des projets La Grande-2-A et La Grande-1. Le panache de La Grande Rivière, Hydro Québec Production, pp. 5–6.

Montefalcone, M., Rovere, A., Parravicini, V., Albertelli, G., Morri, C., Bianchi, C.N., 2014. Reprint of “Evaluating change in seagrass meadows: A time-framed comparison of Side Scan Sonar maps.” Aquatic Botany, Mediterranean Seagrasses - from genes to seascapes 115, 36–44. https://doi.org/10.1016/j.aquabot.2014.02.001

Mulhearn, P.J. (2001) Mapping seabed vegetation with side scan sonar. DSTO Technical Note DSTO-TN-0381. Melbourne: Aeronautical and Maritime Research Laboratory, Defence Science and Technology Organisation.

Nejrup, L.B., Pedersen, M.F., 2008. Effects of salinity and water temperature on the ecological performance of *Zostera marina*. Aquatic Botany 88, 239–246. https://doi.org/10.1016/j.aquabot.2007.10.006

Peck, C.J., Kuzyk, Z.Z.A., Heath, J.P., Lameboy, J., Ehn, J.K., 2022. Under-Ice Hydrography of the La Grande River Plume in Relation to a Ten-Fold Increase in Wintertime Discharge. Journal of Geophysical Research: Oceans 127, e2021JC018341. https://doi.org/10.1029/2021JC018341

Pendea, I.F., Costopoulos, A., Nielsen, C., Chmura, G.L., 2010. A new Shoreline displacement model for the last 7 ka from eastern James Bay, Canada. Quaternary Research 73, 474–484. https://doi.org/10.1016/j.yqres.2010.02.001

Prinsenberg, S.J., 1986. Chapter 9 Salinity and Temperature Distributions of Hudson Bay and James Bay, in: Martini, I.P. (Ed.), Elsevier Oceanography Series, Canadian Inland Seas. Elsevier, pp. 163–186. https://doi.org/10.1016/S0422-9894(08)70902-4

Rossi, P., Castagnetti, C., Capra, A., Brooks, A.J., Mancini, F., 2020. Detecting change in coral reef 3D structure using underwater photogrammetry: critical issues and performance metrics. Applied Geomatics 12, 3–17. https://doi.org/10.1007/s12518-019-00263-w

Schulze, L.M., Pickart, R.S., 2012. Seasonal variation of upwelling in the Alaskan Beaufort Sea: Impact of sea ice cover. Journal of Geophysical Research: Oceans 117. https://doi.org/10.1029/2012JC007985

Taha, W., Bonneau-Lefebvre, M., Cueto Bergner, A., Tremblay, A., 2019. Evolution From Past to Future Conditions of Fast Ice Coverage in James Bay. Frontiers in Earth Science 7. https://doi.org/10.3389/feart.2019.00254

Ventura, D., Mancini, G., Casoli, E., Pace, D.S., Lasinio, G.J., Belluscio, A., Ardizzone, G., 2022. Seagrass restoration monitoring and shallow-water benthic habitat mapping through a photogrammetry-based protocol. Journal of Environmental Management 304, 114262. https://doi.org/10.1016/j.jenvman.2021.114262